# Silicate melt under pressure:
# coordination changes and trace element partitioning

Eleanor Rose Mare

August 2017

A thesis submitted for the degree of Doctor of Philosophy of The Australian National University

# Declaration

This thesis contains the results of research done in the Research School of Earth Sciences, The Australian National University, between 2013 and 2017. I certify that this thesis contains no material which has been accepted or submitted for the award of any other higher degree or graduate diploma in any tertiary institution and to the best of my knowledge and belief, the thesis contains no material previously published or written by another person, except where otherwise acknowledged.

ERMare

Eleanor Rose Mare

Canberra

August 2017

# Acknowledgements

Firstly I would like to thank my supervisors, Hugh O'Neill and Andrew Berry. They have both been exceptionally supportive and encouraging supervisors, from helping me get to grips with a new research area, to reading drafts of my resume when I applied for jobs, and helping me make progress when I felt stuck. I am very grateful for all of their support. They have also provided helpful and detailed feedback on drafts of this thesis. Greg Yaxley and Jörg Hermann, my advisors, have also provided valuable advice and support.

I spent a lot of time in the Experimental Petrology Lab over the years and am very grateful for the technical support from Dean Scott and David Clarke; I have learned a great deal from them. I also thank Robert Rapp for his help with the multi-anvil. He very kindly ran a couple of multi-anvil experiments for me when I was very busy preparing for a beamtime. I have also appreciated the advice received from many other staff and students in the Petrology group over the years, in particular the later-year students who were here when I arrived: Jeremy Wykes, Mike Jollands, Paolo Sossi, Prokopiy Vasilyev and Tarun Whan (Tazz). Tazz was also my first office-mate and made me feel very welcome.

I have enjoyed many fruitful conversations with Charles Le Losq, who is one of the few other people in the department directly interested in silicate melt structure. Charles has helped me to get a better understanding of my NMR results, and I am also very grateful for the time he spent adapting some scripts to do some clever fitting of some of my spectra.

Several people have provided technical support in the other labs around RSES: Jung-Woo Park, Mike Jollands, Peter Tollan and James Tolley with the LA-ICPMS; Ulli Troitzch in the XRD labs; Robert Rapp with the electron microprobe; Penny King and Jörg Hermann in the IR lab; and Hui Juan Li, Laure Gauthiez-Putallaz, Morgan Williams and Melanie Sieber with the SEM. I am grateful for all of their assistance.

I also acknowledge the facilities, and the scientific and technical assistance of the Australian Microscopy & Microanalysis Research Facility at the Center for

Advanced Microscopy, ANU. In particular, I thank Hua Chen and Frank Brink for their assistance.

I also thank my collaborators at the University of St Andrews, Sharon Ashbrook and Nasima Kanwal. I spent two months in Sharon's research group and learned a great deal. In particular, I must thank Nasima in particular for her patience in explaining many aspects of NMR spectroscopy to me, for running many experiments, and for performing fits to all of the $^{27}$Al spectra presented in this thesis. This is an enormous amount of work and I am very grateful to her. Both Sharon and Nasima have contributed to revisions of Chapter 3 of this thesis. I also thank Daniel Dawson, Scott Sneddon, Robert Moran and Joseph Hooper for their assistance and friendship during my time in St Andrews.

The UK 850 MHz solid-state NMR Facility used in this research was funded by EPSRC and BBSRC (contract reference PR140003), as well as the University of Warwick including via part funding through Birmingham Science City Advanced Materials Projects 1 and 2 supported by Advantage West Midlands (AWM) and the European Regional Development Fund (ERDF). Collaborative assistance from the 850 MHz Facility Manager (Dinu Iuga, University of Warwick) is acknowledged.

All of the X-ray absorption spectroscopy for this thesis was was undertaken on the X-ray Absorption Spectroscopy beamline at the Australian Synchrotron, part of ANSTO. I gratefully acknowledge assistance from the beamline scientists there, including Chris Glover, Peter Kapen and Bernt Johannessen.

Thanks also to Daniel Neuville for performing a $T_g$ analysis on one of my samples, a crucial piece of information for interpreting my results!

I received financial support throughout my candidature from several awards. The Australian Government Research Training Program Scholarship (formerly Australian Postgraduate Award) and the Jaeger Supplementary Scholarship covered my living costs, and the extra financial support has made life a little easier during the last few years. My travel to and accommodation in St Andrews was funded by an Australian Bicentennial Award. I attended Goldschmidt 2016 (Japan) thanks to the Vice-Chancellor's Travel Grant, and I was awarded a fully funded place at the Cheiron School 2014 (Japan). Hugh O'Neill's research funding also enabled me to attend several small conferences and workshops, and I am very grateful for all of these opportunities.

Thanks also to Josephine Magro, Maree Coldrick, Mary Hapel and Joy McDermot for administrative support over the years, and for making me feel so welcome. Josephine and Maree in particular have been very supportive in the final stages of my write-up. I also thank Brian Harrold for the lunchtime walks, teas, and all the fruitcake!

I am also very grateful to the Research Skills and Training team at the ANU, for providing writing days and evenings (funded by the Postgraduate and Research Students Association, PARSA). They kindly allowed me to attend all of their sessions over the last month or two of my write-up stage. I found these sessions enormously helpful, in speeding up my progress and making the whole experience more fun!

The sense of community at RSES is very strong and this is part of the reason I have enjoyed my time here so much; I have met so many great people. Firstly, my officemates over the years: Tazz Whan, Rachel Stott, Johanna Sommer, Ting Chen, Laura Miller, and Melanie Sieber. I am very grateful for their friendship and support. Secondly, I'd like to thank everyone who has done writing sessions with me in the last few months, including Louise Schoenveld, Kate Holland, Ali Kimbrough, Melanie Sieber, Laura Miller, Jennifer Wurtzel, Hannah James and Kelsie Long. Some days the only way I have mustered up the energy to write is because they were there with me, and I am very thankful for that. Thirdly, the many friends and friendly faces who I have met either at morning teas, or lunches, or just generally around. There are too many to name, but they include the officemates and writing buddies already mentioned, along with: Kathryn Hayward, Mari Rosa Scicchitano, Jess Aimes, Rose Manneau, Shayne Lakey, Suzette Timmerman, Peter Tollan, Bianca Kallenberg, Oscar Branson, Tim Jones, Chris Renggli, Michael Annenburg, Patrick Goodarzi, James Tolley, Jon Powell, Marija Mustac, Tanja Pejic, Philipp Brandl, Leonardo Baeza, Ilya Bobrovsky, Antony Burnham, Mimi Chen, Christopher Cline II, Laure Gauthiez-Putallaz, Rhys Hawkins, Piers Koefoed, Charles Le Losq, Jennifer Prichard, Jo Stephenson, Jo Ward, Patrick Carr, Joelle Ducommun, Nick Farmer, Katie Harazin, Liane

Loiselle, Jessica Lowczak, Matthew Valetich, Brendan Hanger, and Emmanuel David, and many others.

I also acknowledge my new colleagues and friends at the University of St Andrews. In particular, my supervisor, Sami Mikhail, has been very supportive. Matthew Warke, Tim Kinnaird, Elyse Allender, Adi MacArtney and others have been very welcoming and I am grateful for their friendship.

There are a few other people outside of RSES who have made the last few years really enjoyable. Firstly, my fantastic housemates: Kat Owen, Rachel Stott, and Mya Anumarlapudi and Simone Cilia. Simone made me feel immediately at home in Woodlands Cottage, Dunino, and Kat and Mya have helped out a lot over the last month of my thesis-writing, by cooking me delicious food when I had no energy left to cook myself! Secondly, two close friends deserve a special mention: Tom Meumann and Kat Owen. Tom has been a very good friend to me for many years. I'm very grateful to him for providing me with a listening ear and a cup of tea on so many occasions. Kat has also been a wonderful friend for the 4.5 years that we have lived together. A great deal has happened in that time and I'm glad to have been able to share so much of it with her. I really appreciate her warmth, encouragement and support.

Lastly, I'd like to thank my uncle and aunt, Bill and Maria Young, who were like second parents to me when I moved to Canberra; and, of course, my immediate family, Sarah, David and James Mare, who are unceasingly supportive.

# Abstract

Many geochemical models of magmatic processes, such as the formation of the Earth's metallic core, are based on trace element partition coefficients. Fundamental to these models is an understanding of how partition coefficients vary with pressure. The main objective of this thesis is to explore one factor that controls the pressure-dependence of partitioning: the coordination environment (i.e. the number of bonded oxygens) of cations in silicate melt.

Changes in the coordination number of major elements, Si and Al, are well known to occur in natural melts with pressure, but similar changes have been demonstrated for only a few trace elements: Ni, Co and Lu. In this work, coordination environments of Ge were Ga were studied. X-ray absorption spectroscopy of aluminosilicate glasses was used to show that both Ge and Ga begin to change their coordination from about 1 GPa, and this change is not yet complete at 10 GPa.

In glasses quenched from high-pressure melts, Ge and Ga average coordination increased rapidly between 4 and 5 GPa, suggesting that a change in major element coordination might influence the coordination of both trace elements. To assess this possibility, nuclear magnetic resonance spectroscopy was used to determine changes in the local environments of major elements in the same or similar glasses to which Ge and Ga coordination was studied. Al coordination changed rapidly between 4 and 5 GPa, as had been observed for Ge and Ga. In particular, the Ga and Al average coordination numbers correlate well. These observations indicate that changes in the coordination of major elements may indeed influence the coordination of trace elements.

The effect of a Ge coordination change on partitioning was determined by conducting olivine-melt partitioning experiments up to 4.5 GPa. The results show that Ge becomes more incompatible with increasing pressure, whereas if no coordination change took place, the opposite behaviour would be expected. However, existing models are insufficient to describe the effect of coordination changes on partitioning behaviour.

The observed coordination changes of $Ge^{4+}$ will be relevant in models of the Earth's core formation only if $Ge^{4+}$ is the stable species at the reducing conditions of the magma ocean at that time (below the iron-wüstite oxygen buffer, IW). However, previous work has indicated the possibility of $Ge^{2+}$ stability in silicate melts around these conditions. This was tested using X-ray absorption spectroscopy of glasses quenched from melts prepared at varying oxygen fugacity. The spectra show that the $Ge^{4+}$–$Ge^{2+}$ transition occurs over the range ΔIW +2 to ΔIW -2. Olivine-melt partitioning experiments indicate that $Ge^{2+}$ is highly incompatible, in contrast to $Ge^{4+}$, which has a partition coefficient close to one.

# Contributions

The key contributions made by this thesis are as follows:

- The first observations of pressure-induced coordination changes of $Ge^{4+}$ and $Ga^{3+}$ when dissolved as trace cations in silicate melts; this extends the so-far limited work on trace element coordination changes

- A discussion of the effect of coordination changes on trace element partitioning

- The first evidence to suggest that major element coordination changes may influence those of trace elements

- The first spectroscopic evidence for the stability of $Ge^{2+}$ in silicate melts at low oxygen fugacity, and the first constraints on the olivine–melt partitioning of this species (which indicate that it is highly incompatible)

# Table of Contents

# List of Figures

# List of Tables

# List of Equations

# Chapter 1: Overview

Silicate liquids have been involved with much of the chemical differentiation and ongoing evolution of the Earth, and other planetary bodies. Earth is a relatively large planet, at least in comparison to the other rocky planets in our solar system, and so it can sustain very high pressures in its interior. At very high pressures, the structure and properties of silicate liquids are known to change. Yet we are only beginning to understand these changes and their consequences for planetary evolution.

This thesis is concerned with how pressure-induced changes in the structure of silicate liquids may affect the distribution of trace elements. Trace elements (elements of low abundance in a system) are widely used to test and refine our models of large-scale magmatic processes. Presently, the strength of our models is hampered by an incomplete understanding of how trace elements behave in silicate liquids at high pressures. The behaviour of trace elements is fundamentally tied to the structural changes that may occur in silicate liquids with pressure. Therefore, the objective of this thesis is to explore these structural changes and their effect on the behaviour of trace elements.

In this introductory chapter, I begin with an overview of the importance of silicate liquids in the Earth. I then discuss the geochemical constraints that we have on major magmatic processes that have occurred during Earth's history, and show that understanding the behaviour of trace elements at high pressure is key to these models. Next I provide an overview of the structure of silicate liquids and the changes that occur with pressure, and explain how these changes may affect trace elements. I then describe how I will build on previous work in this thesis, and provide a justification for the approach I have taken. Finally I set out the research questions and the structure of the thesis.

## 1.1 The importance of silicate melts in the Earth

The importance of silicate liquids in planetary evolution cannot be understated. For example, magma oceans are thought to have formed on several planetary bodies during their early history, as a result of the energetic collisions that led to planetary accretion (Taylor and Norman 1992). These magma oceans would have enabled efficient segregation of metal and silicate to form planetary cores, and the subsequent crystallisation of the silicate magma could have profound influences on the differentiation of the silicate part of planets (Carlson et al. 2014). In the Earth, layers of neutrally buoyant melt may still exist in the mantle, and these melt layers may influence the distribution of volatile and incompatible trace elements (Tauzin et al. 2010). Furthermore, in geologically active planets such as the Earth and Venus, ongoing melting in the upper mantle and crust fundamentally influences the evolution of the planetary surfaces and their atmospheres (Ryan and Chauvel 2014; Mikhail and Heap 2017).

The best evidence that we have for a magma ocean on the early Earth comes from two geophysical arguments. The first argument is that the energetic nature of planetary accretion would have generated a great deal of heat. For example, the moon-forming impact should have led to extensive melting on the proto-Earth (Cameron and Benz 1991; Tonks and Melosh 1993; Elkins-Tanton 2012; de Vries et al. 2016). The second argument is that the process of core formation appears to have been so efficient that it must have occurred in a magma ocean. If there was no magma ocean, molten metal could not have percolated through a solid silicate matrix without leaving some residual metal behind. No metal is seen in the rocks of the upper mantle, so it is assumed that metal-silicate segregation must have occurred in a magma ocean, where the process would be more efficient (e.g. Stevenson 1990; Shannon and Agee 1996; Bagdassarov et al. 2009).

A remnant of this magma ocean may still exist in the lower mantle, although this is highly controversial. Seismic studies have observed an ‘ultra-low velocity zone’ (ULVZ) at the base of the lower mantle, which could be explained by partial melt (Williams and Garnero 1996), and the mantle geotherm may well cross the solidus at these depths (Fiquet et al. 2010). However, other studies have suggested that partial melting is not needed to explain the observations, and instead these zones might be comprised of iron-rich (Mg,Fe)O crystals (Wicks et al. 2010; Bower et al. 2011). Still other studies propose that these zones might contain metallic liquid (Zhang et al. 2016) or subducted banded iron formations (Dobson and Brodholt 2005). Overall it is impossible to say with any certainty what these zones represent (Yu and Garnero 2018), and whether a remnant of the magma ocean exists is unknown.

However, a layer of partial melt above the transition zone in the mantle is far more well established. The basis for this is a low seismic velocity layer at about 350 km depth (Revenaugh and Sipkin 1994; Tauzin et al. 2010). It is widely accepted that this 'low velocity layer' is due to the presence of around 1 vol% partial melt (Tauzin et al. 2010; Hier-Majumder and Courtier 2011; Hier-Majumder et al. 2014; Freitas et al. 2017). The presence of melt can be explained by the fact that transition zone minerals can store far more water than upper mantle minerals. Any water released by transition zone minerals will lower the solidus of the upper mantle peridotite and cause partial melting (Hirschmann 2006; Freitas et al. 2017).

Magmatism is also responsible for the generation of the Earth's crust, with continental crust produced by hydrous melting at subduction zones and oceanic crust produced by decompression melting of the mantle at mid-ocean ridges. In turn, oceanic crust subducts and is eventually recycled back into the mantle (Carlson et al. 2014). The process of plate tectonics is the only way by which the atmosphere, hydrosphere and biosphere interact with the deep Earth, and this is fundamentally influenced by magmatism (Ryan and Chauvel 2014).

## 1.2 Geochemical constraints on magmatic processes

Geochemistry can be used to test and refine our understanding of the magmatic processes that have shaped the Earth. In particular, trace element partitioning is a valuable tool. Trace elements are typically defined as elements present in a system at concentrations of less than 0.1 wt%. Their low abundance means that their distribution usually does not affect the outcome of a process. This, combined with the wide range of behaviours exhibited by different elements, means that the distribution of trace elements within a system can provide valuable information (Blundy and Wood 2003). The distribution of trace elements between phases are quantified by their 'partition coefficients', and the partition coefficient of any given trace element could vary with pressure, temperature, oxygen fugacity and the chemical composition of both phases (Righter et al. 2014; Wood and Blundy 2014).

For many years, metal–silicate partition coefficients of siderophile ('iron-loving') trace elements have been used as evidence for core formation in a deep magma ocean. This began with the observation that Ni and Co are in a chondritic ratio in the upper mantle, despite having very different metal–silicate partition coefficients at ambient pressure (e.g. Jones and Drake 1986). When Li and Agee (1996) observed that Ni and Co partition coefficients changed with pressure at different rates, they extrapolated their results to obtain a pressure of around 30 GPa for metal–silicate equilibration in a magma ocean. They postulated that this pressure corresponded to the deepest part of the magma ocean, where metallic droplets would pool and equilibrate with the silicate melt, before sinking through the solid mantle below as metal diapirs. Because this inference required extrapolating from lower to higher pressures, many subsequent studies have attempted to measure partition coefficients at ever-higher pressures. Recent studies involving many siderophile elements model the equilibration pressure as being 40–50 GPa (Bouhifd and Jephcoat 2003; Wood et al. 2006; Kegler et al. 2008; Cottrell et al. 2009; Bouhifd and Jephcoat 2011; Siebert et al. 2011; Mann et al. 2012; Siebert et al. 2012; Blanchard et al. 2015; Fischer et al. 2015; Laurenz et al. 2016).

Do these studies provide proof that core formation occurred in the presence of a very deep magma ocean? There are two key issues that complicate the interpretation of these results. Firstly, despite predicted pressures of around 40–50 GPa for the base of the magma ocean, few studies have reported partitioning experiments at pressures exceeding 25 GPa; the few higher-pressure experiments reported are limited to Ni, Co, V and Cr partitioning (Bouhifd and Jephcoat 2003; Bouhifd and Jephcoat 2011; Siebert et al. 2012; Fischer et al. 2015). Therefore, many models of core formation in the Earth are based on extrapolating data measured at <25 GPa to twice that pressure. Secondly, it has been widely discussed in recent years that metallic cores began forming in planetesimals in the first 1–2 million years of the solar system, before these planetesimals accreted to form planets (see Halliday 2013). Therefore, siderophile trace element distributions in the Earth record a complex history of metal–silicate exchange in both the early planetesimals and the growing proto-Earth. The distributions will depend on (a) the extents of metal–silicate equilibration in the planetesimal (Tomkins et al. 2013) and (b) how efficiently the cores of these planetesimals equilibrated with the silicate part of the proto-Earth (Rubie et al. 2015). The latter in turn depends on the depth and longevity of the terrestrial magma ocean (de Vries et al. 2016). Unravelling the process of core formation, and the nature of the magma ocean will require more sophisticated models that can account for all of these factors, as well as a better understanding of trace element partitioning at very high pressures.

If a deep and long-lived magma ocean did exist on the early Earth, it might have left behind other geochemical tracers in addition to the signature of core formation recorded by siderophile elements. Many studies have tried to find evidence of mantle hetereogeneities resulting from the fractional crystallisation of a magma ocean. There is abundant petrological evidence for a magma ocean on the Moon, for example (Smith et al. 1970; Wood et al. 1970; Taylor and Norman 1992; Wieczorek et al. 2006; Warren and Taylor 2014), but similar evidence for the Earth is surprisingly scarce. Only a few studies have claimed to have found evidence in the form of isotopic anomalies of Xe, Nd, He and Ne (Labrosse et al. 2007; e.g. Coltice et al. 2011; Mukhopadhyay 2012; Guitreau et al. 2013; Pető et al. 2013; Peters et al. 2018).

There are several reasons why finding geochemical evidence for silicate differentiation in an early magma ocean is so difficult. Firstly, the dynamics and behaviour of a deep magma ocean are not easy to predict. For example, would it crystallise starting from the bottom (Carlson 1994; Walter and Trønnes 2004; Carlson et al. 2014), or from the middle (Stixrude et al. 2009)? And when it starts to crystallise, do the crystals remain entrained in the rapidly convecting magma, or do they segregate from the melt enabling fractional crystallisation? How and where fractional crystallisation would begin will depend on a complex interplay involving the density contrast between minerals and melts (which depends on the compressibility of both phases), the rate of crystal nucleation and growth, the viscosity of the melt, and the cooling rate of the magma ocean (which will depend on whether there is a primitive crust or atmosphere) (Abe 1997; Walter and Trønnes 2004; Elkins-Tanton 2012; Carlson et al. 2014). Predicting the chemical signatures that would result from the crystallisation of a magma ocean is therefore difficult when we don't have a good consensus on how this occurred. Furthermore, determining phase relations, element partitioning and isotope fractionation at appropriate pressures and temperatures is experimentally challenging. Finally, mantle convection may well have erased most heterogeneities within 100 m.y. (Coltice and Schmalzl 2006), although it is possible that crystal piles at the base of the magma ocean may have survived to the present day (Carlson et al. 2014).

Overall, there are many unknowns when it comes to understanding the earliest evolution of the Earth. The segregation of the Earth's metallic core and the subsequent crystallisation of its magma ocean are arguably some of the most dramatic events that the Earth has ever experienced. If we are to model these processes, we must better understand the properties of silicate liquids, and the partitioning of trace elements, at very high pressures.

## 1.3 The effect of pressure on trace element partitioning

As described in the previous section, understanding the pressure–dependence of trace element partitioning is of fundamental importance for modelling large-scale magmatic processes that have influenced the Earth's evolution. Many studies of metal–silicate partitioning at high pressures have shown that trace element partition coefficients *do* depend on pressure, and in different ways for different elements (e.g. Siebert et al. 2011). In contrast, the pressure-dependence of trace element partitioning between silicate minerals and silicate melts has been less well studied. Partly this is because the high temperatures required make these experiments more technically challenging, and it can be difficult detangle the relative effects of melt composition, pressure and temperature. A few studies that have investigated olivine–melt partitioning at very high pressures include Taura et al. (1998), Imai et al. (2012), and Suzuki et al. (2012) – these authors performed experiments up to 14, 10 and 20 GPa respectively. From a thermodynamic point of view, the exchange equilibrium between a trace element component in two coexisting phases should depend on pressure, because smaller volumes will be favoured at higher pressures (e.g. Capobianco and Watson 1982). However, there is no successful model that can predict the variation of trace element partition coefficients as a function of pressure.

The best predictive model developed for trace element partitioning so far is known as the 'lattice strain model', which was developed by Blundy and Wood (1994) and was built on earlier work by Onuma et al. (1968) and Brice (1975). This model is based on the concept of trace cations substituting onto particular crystal lattice sites in a mineral, with the compatibility depending on the relative 'match' between the trace cation and the lattice site in terms of size and charge (a concept first described by Goldschmidt 1937). Although this approach has been very successful for describing the variation in trace element partitioning at low pressures, it does not account well for changes with increasing pressure. For example, the data of Imai et al. (2012), when fit to a lattice strain model, imply that the lattice sites in olivine become more elastic with increasing pressure. This is not expected, nor reasonable, and Imai et al. (2012) argue that this apparent ‘softening’ of the lattice sites is more likely to be related to a structural change in the melt. Indeed, beyond the initial attempts of Imai et al. (2012), the melt is largely ignored in the lattice strain models, and the partition coefficients are assumed to be completely controlled by the crystallographic sites. However, as will be described next, we have a wealth of evidence to suggest that there are dramatic changes in the structure of silicate melts with pressure, which could affect trace element partitioning in unknown ways.

## 1.4 Silicate melt structure

Our understanding of the structure of silicate glasses and melts has come a long way since Zachariasen (1932) proposed the continuous random network model for pure $SiO_2$ glass. In this model, $SiO_2$ in the glassy state is composed of the same basic structural units as are found in quartz – that is, tetrahedral units comprising one Si bonded to four oxygens. Each tetrahedral unit is connected to another by sharing an oxygen at the corner, and in glasses, the Si–O–Si bond angles are variable, leading to rings and cages containing different numbers of tetrahedral units. Eight decades after this model was proposed, this structure was directly imaged by Huang et al. (2012) using scanning transmission electron microscopy.

Pure $SiO_2$ liquid is a simple system, and is not particularly relevant to natural magmatic liquids. For one thing, pure $SiO_2$ liquid is highly viscous, because any flow requires breaking some of the strong covalent Si–O–Si bonds (Bottinga and Weill 1972). Natural liquids contain additional elements such as Al, Ca, Mg, Fe, Na, K and Ti, as well as $CO_2$ and water. Cations such as $Ca^{2+}$ and $Mg^{2+}$ form weaker, ionic bonds with oxygen, and are said to ‘break up’ the tetrahedral network, thereby known as ‘network modifiers’. The main ‘network formers’ are $Si^{4+}$ and $Al^{3+}$. $Al^{3+}$ needs another cation for charge balancing in order for it to bond with four oxygens, so in some glasses, like pure $SiO_2$–$Al_2O_3$ systems, $Al^{3+}$ acts as a network modifier (Bottinga and Weill 1972; Mysen et al. 1982). However, in natural compositions, there are sufficient network-modifying cations available for charge-balancing, as well as to act as network modifiers. Liquid compositions containing more network modifiers are therefore less viscous, because the network modifiers enable the liquid to flow with less breakage of the strong covalent bonds between tetrahedral units.

A commonly-used parameter to describe melt structure is NBO/T, the ratio of non-bridging oxygens (NBO) to tetrahedrally coordinated cations (T) (Mysen et al. 1982). Bridging oxygens (BO), also known as bonding oxygens, are oxgyens that bridge between two tetrahedral units. NBO are oxygens which bond with only one tetrahedral unit, and provide weak bonds with network modifying cations. Therefore, a higher ratio of NBO/T means a composition with more network modifiers; pure $SiO_2$ has a theoretical NBO/T of 0, whereas basaltic melts have NBO/T of 0.6–0.9 (Mysen et al. 1982). The concept of NBO/T has been a useful tool to describe melt structure at ambient pressure, where the main control on structure is composition. However, pressure is now known to cause structural changes that are not well-encompassed by the concept of NBO/T. In particular, the coordination numbers of cations increase with pressure.

Waff (1975) was the first to propose that pressure-induced coordination changes of cations might occur in melts. This was proposed on the basis of comparison with crystal phase transitions with pressure: for example, when sodium and calcium feldspars transform into pyroxene and garnet structures, Al changes its coordination from four-fold to six-fold. Waff (1975) suggested that similar transitions were likely to occur in melts, and would have important consequences for melt density and viscosity. This prediction inspired a number of studies to search for experimental evidence for such coordination changes. However, the initial studies found no evidence (Fleet et al. 1984; Hochella and Brown 1985), most likely because (a) the pressures studied were not high enough, and (b) the compositions studied were NBO-poor, and we now know that coordination changes occur more readily in more NBO-rich compositions (Stebbins 2016). However, the late 1980's and early 1990's, unambiguous evidence for the pressure-induced coordination change of Al and Si was found using nuclear magnetic resonance (NMR) spectroscopy (Stebbins and McMillan 1989; Xue et al. 1989; Yarger et al. 1995).

Since these initial studies, a lot of research has been done to investigate structural changes of silicate melts with pressure, using a variety of techniques (Stebbins 2016). The emerging picture is that liquids accommodate initial compression by mechanisms such as shrinking of the inter-tetrahedral bond angles, and the reduction of bond lengths (Wang et al. 2014). When pressure increases further, the coordination of cations begins to change, and this proceeds gradually over a very wide pressure range (Guillot and Sator 2007; Sanloup et al. 2013; Wang et al. 2014). Most studies on these structural changes have aimed to understand ‘structure-property relationships’ – in particular, how structural changes control physical properties like viscosity and density (Wolf and McMillan 1995). For example, polymerised compositions display a reduction in viscosity with initial compression, followed by an increase in viscosity at higher pressures (Wolf and McMillan 1995; Kono 2018), and this phenomenon has been explained in terms of the structural changes (Wang et al. 2014). Understanding these phenomena is indeed very important for physical models of magmatic processes at high pressure (Stixrude et al. 2009). However, so far, there has been little attention to how these structural changes may affect trace element partitioning.

The potential importance of coordination changes in controlling partitioning was first pointed out by Keppler and Rubie (1993). These authors showed that Co and possibly Ni increased their coordination numbers with pressure in albite glasses, using crystal field spectroscopy. However, the albite composition is quite different to the mafic or ultramafic melts that would be relevant at depth in the Earth. Compositions better resembling natural melts were studied by Jones (2012) using X-ray absorption spectroscopy (XAS). Jones showed that $Ni^{2+}$ changed its coordination from predominantly four-fold to predominantly six-fold over the pressure range of 1–4 GPa. This coincides with a change in the pressure-dependence of its partition coefficient, suggesting that the partitioning may indeed be affected by the coordination changes. Over the same pressure range, no changes in coordination environments were observed for $Co^{2+}$, $W^{6+}$, $Fe^{2+}$ and $Fe^{3+}$, but the maximum pressure investigated was only 4 GPa (Jones 2012). More recently, de Grouchy et al. (2017) showed that Lu coordination changed abruptly from 6-fold to 8-fold at ~ 5 GPa in a model basaltic melt, using in-situ X-ray diffraction techniques. The mineral–melt partition coefficients of Lu for olivine, clinopyroxene and garnet also show a change in pressure-dependence at similar pressures to its coordination change (de Grouchy et al. 2017). Finally, Sanloup et al. (2018) found that the coordination of Nb changed at pressures between 5 and 9 GPa. Many more trace elements may undergo coordination changes, but only these few have been studied. Furthermore, it has been speculated that coordination changes of major elements (Si and Al) may affect trace element partitioning (Imai et al. 2012; Mann et al. 2012), but this has never been studied directly.

## 1.5 The approach taken in this thesis

Thus far I have described how (a) silicate melts are important in Earth evolution, (b) trace element partition coefficients are useful in modelling these processes, and (c) trace element partition coefficients may depend on structural changes in silicate melt with pressure. Therefore, the overall objective of this thesis is to explore pressure-induced changes in the structure of silicate melt that may affect trace element partitioning behaviour. I will now briefly review the experimental techniques that can be used to study coordination changes, and justify the approach taken in this thesis.

### *Element-specific techniques*

By far the most unambiguous method of determining coordination environments, at least for Si and Al, is NMR spectroscopy (Stebbins and Xue 2014). NMR is ideal because it is element-specific, and the 4-, 5- and 6-fold coordinated peaks are easily resolved in the spectra for Si and Al (Kanzaki et al. 1992; Yarger et al. 1995). $^{17}O$ NMR spectroscopy has also been used to infer different O environments as a function of pressure (e.g. Lee et al. 2004; Allwardt et al. 2005b). However, for some elements, using NMR to determine their environment is challenging because of low natural abundances of the NMR-active nucleus, and/or large quadrupolar broadening of the spectra, e.g. for $^{25}Mg$ and $^{43}Ca$ (Shimoda et al. 2008; Gambuzzi et al. 2015). A major limitation of NMR spectroscopy is that it is difficult to study trace elements, because long (and hence expensive) acquisition times are needed to obtain spectra with acceptable signal-to-noise ratios. Recording NMR spectra on samples at high temperatures and even high pressures can be done, but most studies investigate glasses at room temperature and pressure. This is because, at high temperature, the exchange between different species is more rapid than the timescale of the NMR experiment, and so a single peak is observed even when multiple environments are present (Farnan and Stebbins 1990; Stebbins and Farnan 1992; Kanehashi and Stebbins 2007; Le Losq et al. 2014). Recently, one laboratory developed a NMR probe that could sustain pressures up to 2.5 GPa (Edwards et al. 2014; Gaudio et al. 2015a), but this was very challenging because the components of the device had to be non-magnetic, and the sample volume needed to be large enough to retain sensitivity.

X-ray absorption spectroscopy (XAS) is another element-specific technique that has been widely used for determining cation coordination environments in glasses and melts (Henderson et al. 2014; Mastelaro and Zanotto 2018). XAS studies of elements heavier than phosphorous are routine (Penner-Hahn 1999), and even lighter elements such as Al, Si, Mg, Ca and even O can be studied (Li et al. 1995; Poe et al. 2001; Neuville et al. 2004; Henderson et al. 2014; e.g. Moulton et al. 2016). Unlike NMR spectra, X-ray absorption spectra reflect an average of all environments in a sample, and so the spectra are more difficult to interpret, and model compounds with known coordination environments are needed. However, the real strength of XAS, especially in comparison to NMR, lies in trace element work, because good spectra can be obtained of trace elements at concentrations as low as hundreds of ppm (Sutton et al. 2005; Newville 2014). XAS studies can also be done *in-situ* at high temperature in furnaces (e.g. Wilke et al. 2001; Berry et al. 2003b) and at high pressure in diamond anvil cells (Cormier et al. 2007; Sanloup et al. 2018) or large-volume presses (Pohlenz et al. 2018).

X-ray Raman scattering (XRS), also known as inelastic X-ray scattering, is a novel technique in which 'hard' X-rays can be used to obtain spectra from light elements. For light elements, this is a significant advantage, because the 'soft' x-rays that would be used for traditional XAS are easily attenuated in air. XRS has has been used to investigate changes in the local environment around O and Si with pressure (Lee et al. 2014), and may be a promising tool for future ultra-high pressure research (Petitgirard 2017).

### *Other techniques*

Raman spectroscopy has been used by many authors to investigate changes in the structure of compressed melts and glasses (Xue et al. 1991; e.g. Poe et al. 2001). However, as a vibrational spectroscopy, Raman spectra arise from many different vibrational modes of all species present in a sample, and so peak assignment can be difficult in a multicomponent glass. Some studies investigate simple systems containing few elements in order to get around this issue (e.g. Daniel et al. 1996). However, few studies have found any unambiguous evidence in Raman spectra alone for coordination changes (exceptions including Durben and Wolf 1991; and Muniz et al. 2016). A major advantage of Raman spectroscopy is that in-situ high-pressure experiments are routine (Durben and Wolf 1991; e.g. Deschamps et al. 2009; Kojitani et al. 2013) and do not require access to a synchrotron light source.

X-ray and neutron diffraction also provide valuable information about the structure of high-pressure glasses and melts (Salmon and Zeidler 2015). X-ray diffraction (XRD) has been used on glasses at room pressure (e.g. Tan and Arndt 1999), at high pressure but room temperature (e.g. Meade et al. 1992), and at high pressure and temperature (e.g. Funamori et al. 2004; Sanloup et al. 2013; de Grouchy et al. 2017). Diffraction suffers from similar limitations as Raman spectroscopy, in that it is not element-specific, and so interpreting the contributions to the integrated diffraction patterns in multicomponent systems can be challenging. For example, in order to estimate coordination numbers of Si using XRD on a basaltic melt, Sanloup et al. (2013) had to make large assumptions about the coordination number of Al. Recently, de Grouchy et al. (2017) used a novel approach to apply the method to a ‘trace’ element (Lu, present at 4 wt% in the melt). These authors collected data from Lu-bearing and Lu-free compositions in order to isolate the contribution of Lu. They found evidence for a coordination change of Lu using this strategy, however their fits were also based on assumed Al coordination environments from literature data. Nevertheless, this may be a promising approach for future work.

Finally, it should be noted that many studies have used molecular dynamic simulations to investigate coordination changes of major elements in silicate melts with pressure (Karki 2010). Studies have investigated both simple systems such as $GeO_2$ (e.g. Shanavas et al. 2006), multicomponent CMAS systems (e.g. Matsui 1996) and ‘natural’ systems (Guillot and Sator 2007). There is also promising work looking at trace element partitioning from this viewpoint (Wagner et al. 2017). Molecular dynamical studies can provide valuable information, often before the technical capabilities are available to verify the results experimentally. However, a detailed review of the findings of these studies is beyond the scope of this chapter.

### *Justification of the approach taken in this thesis*

In this thesis, I chose to use NMR spectroscopy and XAS on glasses quenched from high pressure and temperature. XAS was chosen because it is the best technique for investigating the local environment of trace elements, and NMR spectroscopy was chosen because it provides the least ambiguous data for major elements. For both techniques, studying glasses *ex situ*, rather than melts *in situ*, was easier – this enabled large datasets to be collected, so that the results could be shown to be reproducible, and the NMR spectra could be interpreted with less ambiguity.

However, there are structural differences between a glass and its corresponding melt at high pressure and temperature. When a melt is quenched, the structure continues to rearrange until it becomes so viscous that it 'falls out of equilibrium' with the rapidly dropping temperature. At this point, the melt structure is 'frozen in', and the temperature at which this occurs is known as the 'fictive temperature', $T_f$ (Stebbins 2016). The structure of a glass therefore does not represent the temperature at which it was melted; it represents $T_f$. For a perfectly isobarically quenched melt, the pressure recorded by the melt structure (the 'fictive pressure', $P_f$) should equal the pressure at which the sample was melted and quenched, but whether isobaric quenching is really possible in practice is questionable. These factors will be discussed in more detail in Chapter 2.

Trace element partitioning experiments were undertaken to complement the XAS and NMR data. The advantage of partitioning experiments is that the problems associated with quenching glasses are not an issue, because the distribution of trace elements is set during the experiment and chemical diffusion cannot occur on the fast timescale of the quench. I chose olivine–melt as the system to study for the partitioning experiments, rather than a metal-silicate system. This was because the composition of olivine should not vary much between experiments, so the effect of a change in the melt should be easier to interpret.

Two trace elements were chosen for study in this thesis: Ge and Ga. These elements were chosen for two reasons. Firstly, Ge and Ga are moderately siderophile elements that have been used in many models of core formation in the Earth (Schmitt et al. 1989; Walker et al. 1993; Hillgren et al. 1996; Jana and Walker 1997a; Jana and Walker 1997b; Capobianco et al. 1999; Holzheid et al. 2007; Righter et al. 2011; Siebert et al. 2011; Blanchard et al. 2015; Righter et al. 2017). The high-pressure partitioning behaviour of these elements is therefore of interest in these models. Secondly, Ge and Ga are expected to undergo coordination changes at experimentally accessible pressures. This is expected because Ge and Ga are geochemically similar to Si and Al, but have larger ionic radii. This means that germanate minerals undergo pressure-induced phase changes at lower pressures than silicate minerals (Ringwood 1970). In addition, the coordination number of Ge in $GeO_2$ glass increases at lower pressures than that of Si in $SiO_2$ glass (Itié et al. 1989; Ohtaka et al. 2001; Ohtaka et al. 2002; Majérus et al. 2004; Ohtaka et al. 2004; Vaccari et al. 2009; Baldini et al. 2010; Hong et al. 2014). It is reasonable to expect the same phenomenon to occur when Ge and Ga are dissolved in multicomponent melts as trace elements, but this has never been tested.

Finally, while the coordination of $Ge^{4+}$ was investigated in this work, some studies have suggested that $Ge^{2+}$ may be stable in silicate melts at low oxygen fugacity ($fO_2$). If so, this might have important consequences for both the study of $Ge^{4+}$ coordination undertaken here, and for Ge geochemistry in general. It has long been known that a given element in a different redox state can have a vastly different behaviour. The most well-known example of this is iron, which is the most abundant multivalent element in the upper mantle (Osborn 1959). $Fe^{2+}$ and $Fe^{3+}$ behave so differently that they are often treated as different elements (Berry et al. 2003a). Reactions involving $Fe^{2+}$ and $Fe^{3+}$ control the oxygen fugacity of the mantle (Frost 1991; Frost and McCammon 2008). The oxygen fugacity, in turn, controls the valence state of multivalent trace elements, such as V, Cr, Mn, Ti, and Eu. Understanding how the different oxidation states of these trace elements partition between minerals and melts can then provide a wealth of information, both in terms of recording the oxygen fugacities at which rocks formed (Mallmann and O'Neill 2009; Trail et al. 2012; e.g. Mallmann and O'Neill 2013) and identifying particular magmatic processes (e.g. Eu is often used to identify the crystallisation of plagioclase from a melt; Weill and Drake 1973). The existing data indicate that $Ge^{2+}$ may be stable at low $fO_2$, but precisely at what $fO_2$ is unclear, and there have been no studies of the silicate mineral–melt partitioning of this species. I chose to use XAS to investigate the speciation of Ge, because this technique has previously been used successfully to investigate redox states of Cr and Fe in glasses (Berry et al. 2003a; Berry and O'Neill 2004). I also conducted olivine–melt partitioning experiments to investigate how the behaviour of this species may differ from $Ge^{4+}$.

## 1.6 Research questions and thesis structure

The first research question addressed in this thesis is: do $Ge^{4+}$ and $Ga^{3+}$ undergo pressure-induced coordination changes when dissolved as trace cations in silicate melts? To answer this question, a series of Ge- and Ga-doped glasses were made at a range of pressures. The glasses were made using two approaches: either quenching melts from high temperature, or annealing the glass near the 'glass transition temperature' ($T_g$, the temperature at which a glass relaxes into a liquid). Ge- and Ga- K edge X-ray absorption near edge structure (XANES) spectra of these glasses were recorded. The XANES spectra show that both Ge and Ga increase their average coordination number with pressure, from around 1–2 GPa up to at least 10 GPa, and probably higher.

A surprising result was observed in the XANES spectra: in a particular set of samples, both Ge and Ga average coordination increased rapidly between 4 and 5 GPa. These two elements are not expected to behave in a similar way to one another, because Si and Al, increase their coordination numbers over very different ranges in pressure. For example, in natural compositions, Al begins to change its coordination upon initial compression, but Si does not show substantial changes until ~ 8 GPa (Guillot and Sator 2007). However, it is conceivable that the trace elements might both be affected by 'something' that is happening to the major elements between 4 and 5 GPa. That 'something' could be a coordination change of one or more of the major elements, or another kind of change in the local environment, such as changes in the number or type of neighbouring cations.

This hypothesis forms the second research question addressed in this thesis: do changes in the local environment of major elements affect the coordination of trace elements? To investigate this, a nuclear magnetic resonance (NMR) spectroscopic study was conducted of the same or similar samples for which Ge and Ga were investigated using XANES. NMR spectra of all major elements present in the glasses ($^{27}Al$, $^{29}Si$, $^{25}Mg$, $^{43}Ca$ and $^{17}O$) were recorded. $^{71}Ga$ NMR spectra were also recorded for comparison to the XANES results. The $^{27}Al$ NMR spectra show a rapid increase in average Al coordination number between 4 and 5 GPa, as was observed for Ge and Ga. In particular, there is a striking correlation between Ga and Al average coordination. These results suggest that coordination changes of Al may be influencing Ga coordination, and probably also Ge coordination.

How do such coordination changes affect trace element partitioning? This is the third research question addressed in this thesis. To address this, $Ge^{4+}$ partitioning between olivine and melt was studied. The olivine–melt system was chosen rather than metal–silicate, because the composition of olivine is relatively constant regardless of the pressure, temperature and melt composition. Thus, changes in the partitioning can be attributed more easily to changes occurring in the structure of the silicate melt. $Ge^{4+}$ is shown to become slightly more incompatible (having a preference for the melt) with pressure, whereas the opposite would be predicted in the absence of any coordination changes. However, quantitatively predicting how the coordination changes of $Al^{3+}$ and $Ge^{4+}$ in the silicate melt affect partitioning was unsuccessful. This highlights the need for a new form of an equation of state that incorporates coordination changes.

Finally, the fourth research question addressed in this thesis is: at what $fO_2$ does $Ge^{2+}$ become stable? To answer this, Ge valence state was determined using XAS in a series of glasses quenched from melts at a range of $fO_2$. The spectra show that that $Ge^{4+}$ transitions to $Ge^{2+}$ between ΔIW +2 and ΔIW -2, where IW is the $fO_2$ at the iron–wüstite buffer. Therefore, $Ge^{2+}$ was most likely to be the stable species at the time of core formation in the Earth. Preliminary experiments on the partitioning of $Ge^{2+}$ between olivine and melt indicate that this species is highly incompatible, in contrast to $Ge^{4+}$ which has a partition coefficient of close to one. Whether $Ge^{2+}$ undergoes pressure-induced coordination changes is unknown.

The overall objective of this thesis is to investigate pressure-induced changes in the structure of silicate melt, and how these affect trace element partitioning behaviour. The results show that $Ge^{4+}$ and $Ga^{3+}$ increase their coordination numbers with pressure; in the context of previous work on $Ni^{2+}$, $Co^{2+}$ and $Lu^{3+}$, this thesis strengthens the argument that many trace elements may undergo such changes. Furthermore, a possible influence of major element coordination changes on those of trace elements is suggested. More work is needed to unravel the influence of major and trace element coordination changes on the pressure dependence of trace element partitioning.

### *Structure of this thesis*

This thesis is organised into four main chapters, each addressing one of the research questions described above. The coordination environments of $Ge^{4+}$ and $Ga^{3+}$ in silicate melts are investigated in Chapter 2; a possible relationship between major and trace element coordination is assessed in Chapter 3; the effect of these coordination changes on $Ge^{4+}$ olivine–melt partitioning is investigated in Chapter 4; and the $fO_2$ at which $Ge^{2+}$ becomes stable is determined in Chapter 5. Each chapter is written in the form of a research paper. Methodology, results and discussion pertaining to each study are described within the chapters. A final summary of key findings, implications and directions for future work is provided in Chapter 6.

# Chapter 2: Coordination change of $Ge^{4+}$ and $Ga^{3+}$ in silicate melt with pressure

**Abstract**–The increase in the coordination numbers of Si and Al in silicate melts has been well studied, but few trace elements have been investigated to see if they do the same. In this work, the coordination of Ge and Ga in silicate glasses was studied using X-ray absorption spectroscopy. The glasses were prepared either by quenching melt or annealing glass at a range of pressures. Both Ge and Ga increase their coordination number with pressure from about 2 up to at least 10 GPa. The rate of the coordination change of Ge with pressure is higher in more depolymerized melts. This result is consistent with previous work on Al, therefore implying that these changes are highly relevant to natural melts. Furthermore, Ge and Ga show remarkably similar behaviour suggesting the possibility of a control on their coordination from the major elements.

## 2.1 Introduction

As discussed in Chapter 1, pressure-induced changes in the coordination number of Ge and Ga are expected in silicate melts for two reasons. Firstly, Ge and Ga are geochemically similar to Si and Al respectively, both of which increase their coordination number with increasing pressure (Wolf and McMillan 1995). Secondly, coordination changes have been observed in germanate and gallate glasses (Micoulaut et al. 2006; Cormier et al. 2007), as well as in chalcogenide glasses (e.g. Durandurdu and Drabold 2002; Yildirim et al. 2016). However, natural melts will contain Ge and Ga in trace quantities only. In this chapter I test the hypothesis that Ge and Ga will undergo pressure-induced coordination changes when dissolved as trace elements in multi-component melts.

X-ray absorption spectroscopy (XAS) is an ideal technique with which to test this hypothesis. XAS is element-specific, and the spectra are sensitive to the local environment of the element of interest. Spectra are plotted as the absorption of X-rays by the sample (or fluorescence of X-rays from the sample) as a function of X-ray energy. Absorption or fluorescence is at a maximum when the energy matches the binding energy of core electrons in the element of interest. Above this energy, the average local environment of the target element in the sample modulates the probability of absorption. Thus, changes in the shape of the spectra reflect changes in the local environment, including the coordination number. Quantitative information on coordination numbers and bond lengths can be obtained from the part of the spectrum well above the absorption edge, known as the extended X-ray absorption fine structure (EXAFS). On the other hand, the part of the spectrum close to the absorption edge, known as X-ray absorption near edge structure (XANES), is more sensitive to changes in local environment. XAS has been used in many previous studies to determine coordination changes of Ge in germanate glasses (Itié et al. 1989; Ohtaka et al. 2001; Ohtaka et al. 2002; Majérus et al. 2004; Ohtaka et al. 2004; Cormier et al. 2007; Vaccari et al. 2009; Baldini et al. 2010; Hong et al. 2014), and Ga in sodium gallosilicate and sodium gallogermante glasses (Cormier et al. 2007).

The samples synthesized for this study were glasses prepared in two different ways. The first set of glasses was prepared by quenching melt at a range of pressures. These samples are referred to as ‘quenched melts’ throughout this thesis. Glasses in the second set were prepared by taking a quenched melt prepared at 1 atm, and then annealing that glass at temperatures near the glass transition temperature ($T_g$), and a range of pressures. These samples are referred to as 'annealed glasses' throughout this thesis.

For quenched melts, it is well recognized that the structure of the glass is not the same as the structure of the actual melt at high temperature and pressure (Stebbins 2016). One difference is that the melt structure does not reflect the temperature of synthesis; it reflects the 'fictive temperature' ($T_f$). $T_f$ is the temperature at which the viscosity of the melt is too high to allow for structural rearrangement on the timescale of cooling, i.e. the temperature at which the melt structure is 'frozen in'. The other possible difference is that the melt structure may not reflect the pressure of synthesis, instead reflecting a lower 'fictive pressure' ($P_f$). This could result from localised pressure drops within the melt during the quench, because when the temperature drops, either the sample or the surrounding assembly may shrink, leading to pressure drops which cannot be instantaneously compensated for by the apparatus applying more pressure (Bista et al. 2015; Gaudio et al. 2015b).

Annealed glasses were synthesised in an effort to reduce the effect of a pressure drops during quenching. The rationale behind this is that because the experimental run temperature is lower, the temperature drop needed to 'freeze in' the structure (i.e. cross the glass transition) is smaller, and the time taken to reach the glass transition will also be shorter. These factors should reduce the likelihood that localised pressure drops in the sample will affect the $P_f$ recorded. Indeed, previous work has shown that annealed glasses record higher densities and Al coordination numbers than quenched melts made at the same pressure (Bista et al. 2015; Gaudio et al. 2015b). Gaudio et al. (2015b) suggested that the differences in density and Al coordination between quenched melts and annealed glasses of albite composition could be explained entirely by a higher $P_f$ in the annealed glasses.

For an annealed glass to preserve a $P_f$ similar to the run pressure, the sample needs to be held at a high enough temperature for a long enough time that it exhibits liquid-like behaviour. If this condition is met, the structure can relax under the pressure and temperature conditions of the experiment. However, the temperature must not be too high (or the timescale too long) otherwise (a) the metastable liquid may crystallise, and/or (b) localised pressure drops on the quench may reduce the

$P_f$, as for the quenched melt experiments. To estimate an appropriate temperature/timescale, $T_g$ analysis was used.

$T_g$ can be measured for a glass sample using a range of methods, including differential scanning calorimetry (Moynihan 1995). In this method, heat capacity ($C_p$) is measured while the glass is heated at a constant rate, typically 10 ºC/min, and the glass transition temperature is found as a maximum or a slope break in the $C_p$–T curve. $T_g$ depends on the heating rate (Moynihan et al. 1974), and so in this thesis, when $T_g$ is quoted as a number, this means $T_g$ measured at a heating rate of 10 °/min.

Once the $T_g$ of the composition used in this study was known, the annealed glass experiments were performed at temperatures close to $T_g$. The samples were held at these temperatures for (typically) two hours; a longer timescale than the timescale of heating for $T_g$ analysis, to ensure structural relaxation. However, some experiments were performed at lower temperatures, and because we have no precise constraints on how the glass transition varies with the timescale, it is unknown whether these samples were still behaving as liquids. If they were not behaving as liquids, a much lower $P_f$ would be expected, because the glass should not have the capability to relax fully at the pressure of the experiment. Indeed, this may well have occurred for some of the samples, as will be shown.

In this chapter XANES spectra are presented that show the coordinations of Ge and Ga are unaffected by composition at low pressure, but increase with pressure in both quenched melts and annealed glasses. The difference in results between quenched melts and annealed glasses is surprising, as is the similarity of the results for the two elements. These features raise questions that will be addressed using nuclear magnetic resonance spectroscopy in Chapter 3.

## 2.2 Methods

### *Sample synthesis*

The glasses in this study were synthesised from 13 different starting materials, which are listed in Table 2.1. Powdered oxide mixes of several compositions (AnDi, CAS, CMAS7 and L3) had been prepared for previous studies (O’Neill and Eggins 2002; O’Neill and Berry 2006). Oxide mixes for the other compositions, and additional material for the CMAS7G composition, were synthesised from reagent grade $SiO_2$, $Al_2O_3$, MgO, and $TiO_2$ (all dried at 1000 °C), $Na_2CO_3$, $K_2CO_3$ and $Ca_3(PO_4)_2$ (all dried at 200 °C), and $CaCO_3$, $Fe_2O_3$, and $Cr_2O_3$ (which were not dried). These reagents were mixed under acetone in an agate mortar, and the mix was then dried as a powder at 110 °C, pelletised and decarbonated by firing in air at 1050 °C. Approximately 3000 ppm reagent grade $GeO_2$ and/or $Ga_2O_3$ was then added to the starting materials, and mixed thoroughly under acetone.

Table 2.1. Nominal compositions of starting mixes (wt% oxide).

| | AnDi | CMAS7A | CMAS7F | CMAS7G | CAS1 | CAS4 | CAS5 |
|---|---|---|---|---|---|---|---|
| $SiO_2$ | 50.33 | 55.89 | 62.04 | 59.78 | 42 | 53.85 | 62.3 |
| $Al_2O_3$ | 15.39 | 15.91 | 6.09 | 12.61 | 20 | 12.31 | 14.8 |
| MgO | 10.79 | 12.49 | 13.99 | 2.38 | – | – | – |
| CaO | 23.49 | 15.71 | 17.88 | 25.23 | 38 | 33.84 | 22.9 |
| NBO/T [2] | 0.94 | 0.7 | 1.05 | 0.62 | 0.88 | 0.85 | 0.4 |
| $\Lambda_{th}$ [3] | 0.6 | 0.58 | 0.58 | 0.58 | 0.63 | 0.61 | 0.57 |

| | L3 | AvMORB [4] | CapeV. [4] | DB/3D | PAL/D | HiTiMB [4] | NHPG-1 |
|---|---|---|---|---|---|---|---|
| $SiO_2$ | 62.86 | 52.05 | 59.33 | 48.94 | 59.45 | 38.35 | 58.95 |
| $Al_2O_3$ | 17.92 | 16.12 | 11.85 | 15.04 | 13.07 | 8.38 | 14.98 |
| MgO | 9.41 | 8.21 | 12.95 | 11.33 | 4.17 | 10.5 | 6.99 |
| CaO | 9.81 | 12.31 | 6.13 | 8.39 | 8.87 | 10.29 | 8.59 |
| FeO* [1] | | 10.01 | 9.7 | 16.3 | 14.43 | 19.17 | – |
| $TiO_2$ | – | 1.3 | 0.05 | – | – | 12.72 | 3.99 |
| $Cr_2O_3$ | – | – | – | – | – | 0.61 | – |
| $Na_2O$ | – | – | – | – | – | – | 4 |
| $K_2O$ | – | – | – | – | – | – | 2 |
| $P_2O_5$ | – | – | – | – | – | – | 0.5 |
| NBO/T [2] | 0.33 | 0.42 | 0.5 | 0.49 | 0.22 | 0.67 | 0.4 |
| $\Lambda_{th}$ [3] | 0.55 | 0.56 | 0.55 | 0.56 | 0.53 | 0.57 | 0.56 |

[1] FeO* refers to total iron expressed as FeO. [2] NBO/T is the ratio of non-bridging oxygens to tetrahedrally coordinated cations. This was calculated following Appendix 1 in Mills (1993). The calculation requires knowing the $Fe^{3+}/Fe^{2+}$ ratio, because $Fe^{2+}$ is a network modifier whereas $Fe^{3+}$ may act as a network former. Equation 7 in Kress and Carmichael (1991) was used to find the $Fe_2O_3$/FeO ratio for each composition, assuming an $fO_2$ of air, pressure of 1 atm, and temperature of 1400 °C. This results in $2Fe_2O_3/(FeO+2Fe_2O_3)$ of approximately 0.6 for all the Fe-bearing compositions in this study. For the NBO/T calculation, all $Fe^{3+}$ is assumed to be a network former in tetrahedral coordination (Mysen and Richet, 2005). [3] $\Lambda_{th}$ refers to a theoretical optical basicity, which was calculated based on the stoichiometry of the composition following Equation 2 in Duffy and Ingram (1993) using optical basicities of oxides from Ottonello et al. (2001). [4] Composition name abbreviations are AvMORB = Average MORB, CapeV. = Cape Vogel, and HiTiMB = High-Ti Mare Basalt.

Most ambient-pressure samples were synthesised in vertical tube furnaces; some samples were synthesised in box furnaces. Ga-doped compositions were mixed with polyethylene oxide glue, loaded onto Pt/Rh wire loops, and hung in the furnace from a Pt wire chandelier. The Ge-doped samples were prepared in Pt capsules, which were welded shut at one end and crimped at the other end, because of the greater volatility of Ge. Larger batches of Ge- and Ga-doped glass were required to prepare the annealed glasses. Initially, these batches were made by melting the powdered oxide composition in graphite crucibles for about 15 min at 1300 °C. However, these samples retained very little Ge, despite the short run time. This is probably because the graphite crucible imposed a low $fO_2$ on the melt, increasing the volatility of Ge. To avoid this problem, subsequent samples were prepared in alumina crucibles. All ambient-pressure samples were prepared in air and quenched in water.

High-pressure experiments up to 6 GPa were conducted using end-loaded Boyd-England type piston cylinder apparatuses (200 T apparatuses were used up to 4 GPa, and 500 T from 4.5–6 GPa). For the quenched melt experiments, each sample was prepared by loading 50-60 mg of the oxide starting material into a 3.5 mm diameter Pt capsule, with ~5-6 mg of a Ru-$RuO_2$ oxygen buffer mix (80% $RuO_2$, 20% Ru) packed at each end of the capsule. The annealed glass experiments were prepared by loading powdered glass into 3.5 mm diameter Ag or Pt capsules with no oxygen buffer. Before welding the capsules shut, they were crimped loosely and dried at 110 °C overnight. Capsules in the quenched melt experiments were placed in an assembly composed of MgO, graphite, Pyrex and NaCl (see Figure 2.1); annealed glass experiments were run at low temperatures and so Pyrex was omitted from the assembly. This assembly was wrapped in Teflon foil and inserted into a 1/2” or 5/8” pressure vessel (the 5/8” assembly was only used for pressures up to 0.5 GPa). A Type B thermocouple, sheathed in mullite with a 5 mm alumina tip, was inserted through a bore in the top MgO spacer. The samples were equilibrated for 10 min to 24 h, at the temperatures and pressures listed in Table 2.2, Table 2.3, Table 2.4. The samples were quenched by cutting power to the graphite heater.

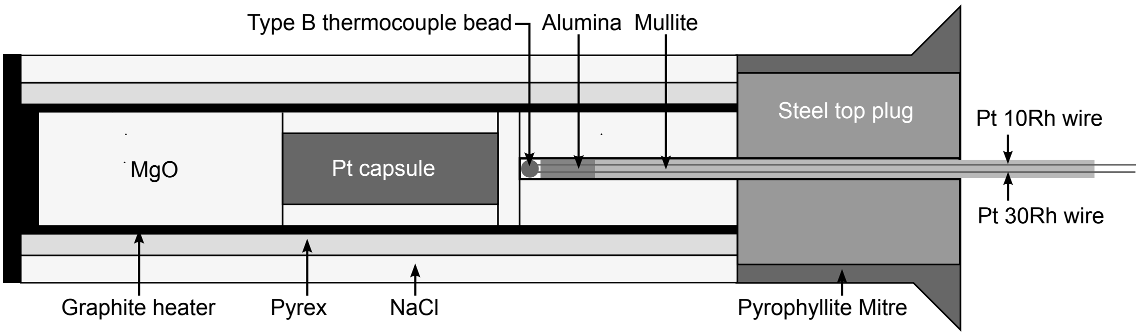

Figure 2.1. Cross section through a piston cylinder assembly.

Three annealed glass experiments were also conducted at higher pressures (8 and 10 GPa) in a 1200 T split sphere multi-anvil apparatus. For each experiment, the powdered glass starting material was packed into a 3.5 mm diameter Pt capsule, which was inserted into a Geophysical Lab 14/8 “G2” box assembly. This assembly consists of a box-shaped graphite heater surrounded by alumina and zirconia sleeves, inserted into an MgO octahedron (for a full description, refer to Leinenweber et al. 2012), and allows for a relatively large sample volume and reduced temperature gradients. A Type C thermocouple, sheathed in alumina, was used. The octahedron was placed in the centre of eight truncated cubes made of Toshiba F grade tungsten carbide, with pyrophyllite gaskets. Fibreglass sheets were used to insulate the outer faces of the cubes from the anvils, and copper electrodes on two of the cubes enabled power to flow through the heater. The experimental conditions are listed in Table 2.4. The pressure was ramped up over 6-20 h, and the sample was then heated at 100 °C/min to the desired temperature, held for 2 h, and then power was cut to quench the sample. Pressure was then slowly released over ~12 h.

Table 2.2. Ge- and Ga-doped quenched melt samples (composition series).

| Sample Name | Composition | Pressure | Temperature (°C) | Time (h) |
|---|---|---|---|---|
| | | Quenched melts doped with Ge | | |
| C4496 | AnDi | 0.5 GPa | 1500 | 20 |
| D1602 | CMAS7A | 0.5 GPa | 1500 | 22 |
| D1601 | CMAS7F | 0.5 GPa | 1500 | 22 |
| D1591 | CMAS7G | 0.5 GPa | 1500 | 20 |
| D1597 | CAS1 | 0.5 GPa | 1500 | 22 |
| D1598 | CAS4 | 0.5 GPa | 1500 | 22 |
| C4503 | L3 | 0.5 GPa | 1500 | 22 |
| D1605 | Av. MORB | 0.5 GPa | 1500 | 24 |
| D1611 | Cape V. | 0.5 GPa | 1500 | 20 |
| C4519 | Hi Ti M.B. | 0.5 GPa | 1500 | 24 |
| D1609 | DB/3D | 0.5 GPa | 1500 | 20 |
| D1608 | PAL/D | 0.5 GPa | 1500 | 20 |
| | | Quenched melts doped with Ga | | |
| E16/11/13A | Cape V. | 1 atm | 1400 | 13 |
| E16/11/13B | Av. MORB | 1 atm | 1400 | 13 |
| E16/11/13C | L3 | 1 atm | 1400 | 13 |
| E16/11/13D | CAS4 | 1 atm | 1400 | 13 |
| E16/11/13E | CAS5 | 1 atm | 1400 | 13 |
| E16/11/13F | CAS1 | 1 atm | 1400 | 13 |
| E19/11/13D | CMAS7A | 1 atm | 1394 | 16 |
| E19/11/13E | DB/3D | 1 atm | 1394 | 16 |
| E19/11/13F | CMAS7F | 1 atm | 1394 | 16 |
| E23/10/13A | CMAS7G | 1 atm | 1267 | 4 |

Table 2.3. Ge- and Ga-doped quenched melt samples (pressure series).

| Sample Name | Composition | Pressure | Temperature (°C) | Time (h) |
|---|---|---|---|---|
| **Quenched melts doped with Ge** | | | | |
| NHPG-1 pressure series | | | | |
| E13/11/13 | NHPG-1 | 1 atm | 1210 | 4 |
| D1637 | NHPG-1 | 1.0 GPa | 1500 | 6 |
| D1635 | NHPG-1 | 2.0 GPa | 1400 | 12 |
| D1638 | NHPG-1 | 3.0 GPa | 1500 | 16 |
| C4563 | NHPG-1 | 4.0 GPa | 1500 | 6 |
| uhppc253 | NHPG-1 | 6.0 GPa | 1650 | 6 |
| CMAS7A pressure series | | | | |
| E15/10/13 | CMAS7A | 1 atm | 1260 | 4 |
| D1602* | CMAS7A | 0.5 GPa | 1500 | 22 |
| D1588 | CMAS7A | 1.0 GPa | 1600 | 18 |
| C4491 | CMAS7A | 1.5 GPa | 1600 | 18 |
| D1589 | CMAS7A | 2.0 GPa | 1600 | 20 |
| C4493 | CMAS7A | 2.5 GPa | 1600 | 14 |
| D1590 | CMAS7A | 3.0 GPa | 1600 | 20 |
| D1592 | CMAS7A | 3.5 GPa | 1650 | 22 |
| C4506 | CMAS7A | 4.0 GPa | 1650 | 6 |
| CMAS7G pressure series | | | | |
| E23/10/13B | CMAS7G | 1 atm | 1267 | 4 |
| B1-080316 | CMAS7G | 1 atm | 1300 | 0.25 |
| C110416 | CMAS7G | 1 atm | 1300 | 0.25 |
| D05/04/16 | CMAS7G | 1 atm | 1300 | 0.25 |
| D1591 | CMAS7G | 0.5 GPa | 1500 | 20 |
| C4490* | CMAS7G | 1.0 GPa | 1650 | 16 |
| D1586 | CMAS7G | 1.5 GPa | 1650 | 5 |
| D1584 | CMAS7G | 2.0 GPa | 1650 | 14 |
| C4484 | CMAS7G | 2.5 GPa | 1650 | 13 |
| D1576 | CMAS7G | 2.5 GPa | 1650 | 4 |
| uhppc271 | CMAS7G | 2.5 GPa | 1650 | 2 |
| C4485 | CMAS7G | 3.0 GPa | 1650 | 5 |
| C4486 | CMAS7G | 3.5 GPa | 1650 | 5 |
| D1585 | CMAS7G | 4.0 GPa | 1650 | 5 |
| D1572 | CMAS7G | 4.0 GPa | 1650 | 5 |
| uhppc-251 | CMAS7G | 4.5 GPa | 1650 | 6 |
| uhppc-367 | CMAS7G | 4.5 GPa | 1650 | 5.5 |
| uhppc-369 | CMAS7G | 4.8 GPa | 1650 | 6 |
| uhppc-250 | CMAS7G | 5.0 GPa | 1650 | 6 |
| uhppc-258 | CMAS7G | 5.0 GPa | 1650 | 5 |
| uhppc-365 | CMAS7G | 5.0 GPa | 1650 | 4 |
| uhppc-370 | CMAS7G | 5.5 GPa | 1650 | 6 |

Table 2.3. (Continued).

| Sample Name | Composition | Pressure | Temperature (°C) | Time (h) |
|---|---|---|---|---|
| | | **Quenched melts doped with Ga** | | |
| | | CMAS7G pressure series | | |
| E23/10/13A* | CMAS7G | 1 atm | 1267 | 4 |
| B1-080316 | CMAS7G | 1 atm | 1300 | 0.25 |
| D1604 | CMAS7G | 0.4 GPa | 1650 | 24 |
| D1580 | CMAS7G | 1.0 GPa | 1650 | 4 |
| D1578 | CMAS7G | 2.0 GPa | 1650 | 5 |
| D1576 | CMAS7G | 2.5 GPa | 1650 | 4 |
| D1574 | CMAS7G | 3.0 GPa | 1650 | 4 |
| D1577 | CMAS7G | 3.5 GPa | 1650 | 14 |
| D1572 | CMAS7G | 4.0 GPa | 1650 | 5 |
| uhppc-367 | CMAS7G | 4.5 GPa | 1650 | 5.5 |
| uhppc-369 | CMAS7G | 4.8 GPa | 1650 | 6 |
| uhppc-258 | CMAS7G | 5.0 GPa | 1650 | 5 |
| uhppc-365 | CMAS7G | 5.0 GPa | 1650 | 4 |
| uhppc-370 | CMAS7G | 5.5 GPa | 1650 | 6 |

Table 2.4. Ge- and Ga-doped annealed glass samples.

| Sample Name | Pressure | Temperature (°C) | Time (h) | Starting material batch (Crucible material) |
|---|---|---|---|---|
| | | **Annealed glasses doped with Ge and Ga, unless specified** | | |
| D2210 | 1.0 GPa | 730 | 2 | B1-080316 ($Al_2O_3$) |
| D2212 | 1.5 GPa | 730 | 2 | B1-080316 ($Al_2O_3$) |
| D2208 | 2.0 GPa | 700 | 2 | D05/04/16 ($Al_2O_3$) |
| C5232 | 2.0 GPa | 600 | 1 | C11/04/16 ($Al_2O_3$) |
| D2209 | 2.5 GPa | 730 | 2 | D05/04/16 ($Al_2O_3$) |
| C5199 | 3.0 GPa | 780 | 2 | B1-080316 ($Al_2O_3$) |
| C5231 | 3.0 GPa | 600 | 1 | C11/04/16 ($Al_2O_3$) |
| D2125 | 3.5 GPa | 780 | 2 | B1-030216 (C) |
| D2189 | 3.5 GPa | 765 | 2 | B1-080316 ($Al_2O_3$) |
| D2213 | 3.5 GPa | 730 | 2 | B1-080316 ($Al_2O_3$) |
| D2173 | 4.0 GPa | 780 | 2 | B1-080316 ($Al_2O_3$) |
| D2207 | 4.0 GPa | 700 | 15 | D05/04/16 ($Al_2O_3$) |
| C5228 | 4.0 GPa | 600 | 1 | C11/04/16 ($Al_2O_3$) |
| uhppc357 (Ga only) | 5.0 GPa | 780 | 2 | B2-220216 (C) |
| uhppc358 (Ga only) | 6.0 GPa | 780 | 2 | B2-220216 (C) |
| uhppc372 | 6.0 GPa | 760 | 2 | B1-080316 ($Al_2O_3$) |
| MA-1117 | 8.0 GPa | 780 | 2 | B1-080316 ($Al_2O_3$) |
| MA-1121 | 8.0 GPa | 700 | 2 | B1-080316 ($Al_2O_3$) |
| MA-1118 | 10 GPa | 780 | 2 | B1-080316 ($Al_2O_3$) |

Along with the glass samples, model compounds that have Ge and Ga in known coordination environments were synthesized (these are listed in Table 2.5). Details of how each compound was prepared are given in the supplementary material (Section 7.1, pp. 195). The phase purity of the model compounds was verified by powder X-ray diffraction (XRD) using a STOE Transmission Powder Diffractometer System STADI P with a Co tube, operating at 40 kV and 30 mA.

Table 2.5. Model compounds with known Ge or Ga coordination environments.

| Name | Mineral analogue | Ga/Ge coordination number |
|---|---|---|
| | Ge-bearing | |
| qz-$GeO_2$ | Quartz | 4 |
| rt-$GeO_2$ | Rutile | 6 |
| ol-$Mg_2GeO_4$ | Olivine | 4 |
| spl-$Mg_2GeO_4$ | Spinel | 4 |
| wo-$CaGeO_3$ | Wollastonite | 4 |
| grt-$CaGeO_3$ | Garnet | 4 |
| en-$MgGeO_3$ | Enstatite | 4 |
| | Ga-bearing | |
| β-$Ga_2O_3$ | | 4 & 6 (50% of each) |
| spl-$ZnGa_2O_4$ | Spinel | 6 |
| ab-$NaGaSi_3O_8$ | Albite | 4 |
| crn-$Al_2O_3$ | Corundum, doped with ~3000 ppm Ga | 6 |
| an-$CaAl_2Si_2O_8$ | Anorthite, doped with ~3000 ppm Ga | 4 |

### *Sample characterisation*

Glass samples were mounted in epoxy, sectioned and polished. To confirm the major element concentrations of glasses matched those of the starting material and check for the presence of crystals, several glasses were analysed using a Hitachi S4300 SE/N Field Emission Scanning Electron Microscopy (FE-SEM), fitted with an Oxford X-Max EDS detector. Samples were analysed using a 15 kV accelerating voltage, 0.600 nA beam current and a working distance of 25 mm. Standards used for calibration were MgO for Mg, albite for Al and Na, sanidine for Si and K, diopside for Ca, $TiO_2$ for Ti, $Cr_2O_3$ for Cr, NaCl for Cl, $Fe_2O_3$ for Fe, and $PrP_5O_{14}$ for P.

The concentrations of Ge and Ga were determined in each sample by Laser Ablation Inductively Coupled Plasma Mass Spectrometry (LA-ICPMS), using an eximer laser system (wavelength 193 nm, 5 Hz pulse rate) coupled to an Agilent 7700 ICP-MS, with a HelEx ablation chamber, and He + Ar as the carrier gas. For each spot, 20 s of background was measured before ablating the sample for ~40 s. NIST 610 glass was used as the external standard, with Si as the internal standard;

no secondary standard was used, as high levels of accuracy were not necessary. The spot sizes used were either 37, 47 or 62 μm.

The $T_g$ of the CMAS7G composition glass was determined using differential scanning calorimetry (DSC) at the CNRS-Institut de Physique du Globe de Paris. A ~1 g batch of CMAS7G glass was melted at ambient pressure and quenched to form glass. The DSC analysis was repeated twice at a heating rate of 10°/min.

### *X-ray absorption spectroscopy*

Ge and Ga K-edge XANES and EXAFS spectra were recorded in fluorescence mode using the X-ray Absorption Spectroscopy (XAS) beamline of the Australian Synchrotron, over three days in December 2013 and three days in April 2016. A Si (111) crystal monochrometer (cooled by liquid nitrogen) was used to select the X-ray energy. The energy was calibrated by defining the first peak in the derivative spectrum of Au foil, recorded in transmission mode, to be at 11919.7 eV. The beamline energy resolution was 1.67 eV at the Ge K-edge and 1.56 eV at the Ga K-edge. The beam size was ~0.5 × 0.5 mm. Rh-coated mirrors were used for harmonic rejection. A 100-element Ge detector was used that has a nominally linear response to count rates. Due to the possibility of non-linearity between the incoming and outgoing count rates, intensity of the white line can vary systematically with count rate. To mitigate this effect, the distance between the detector and the sample was varied to maintain an approximately constant count rate of between 13,500 $s^{-1}$ and 16,700 $s^{-1}$ at the end of the scan in the 2013 experiment, and between 18,000 $s^{-1}$ and 25,000 $s^{-1}$ in the 2016 experiment. The energy ranges and step sizes used to acquire the spectra are detailed in Table 2.6. Count times were 1 s or 2 s per point so that the total scan time was ~30 min.

For each scan, the signals from all detector elements were averaged and divided by the incident photon flux using the programs Average or Sakura. Normalisation and background subtraction of spectra was performed using the program ATHENA (Ravel and Newville 2005). Linear combination fits were performed using MATLAB (The MathWorks Inc. 2015). Fitting of EXAFS spectra was done using ARTEMIS (Ravel and Newville 2005), with q-$GeO_2$ as the reference material. Four paths were used to fit the q-$GeO_2$ (R range 1.0–3.2 Å): single scattering from first-shell O, single scattering from second-shell Ge, single scattering from third-shell O and double scattering from first-shell O and second-shell Ge. These four paths contributed most to the spectrum and adding more paths did not improve the fit. To fit the glass samples, only one path was used (single scattering from first-shell O, R range 1.0–2.0 Å), and the $S_0^2$ parameter was constrained to be the same as the value obtained by fitting q-$GeO_2$.

Table 2.6. Energy ranges and step sizes used to acquire XANES and EXAFS spectra.

| | Pre-edge | Edge | Post-edge |
|---|---|---|---|
| | Energy ranges | | |
| Ge | 10903 – 11083 eV | 11083 – 11153 eV | 11153 – 11488 eV |
| Ga | 10167 – 10347 eV | 10347 – 10417 eV | 10417 – 10752 eV |
| | Step size | | |
| 2013 – XANES | 10 eV | 0.2 eV | 0.1$Å^{-1}$ to k=10 |
| 2016 – XANES | 8 eV | 0.25 eV | 0.1 $Å^{-1}$ to k=10 |
| 2013 – EXAFS | 10 eV | 0.4 eV | 0.05 $Å^{-1}$ to k=16 |

To check for systematic differences in spectra between beamtimes, four Ge spectra and three Ga spectra were recorded during both the 2013 and 2016 experiments. Comparing these spectra revealed a small systematic shift in the edge energy, and a small change in the intensity of the white line between the spectra recorded in different experiments. To account for this, the spectra recorded in 2016 were shifted by +0.37 eV. The intensity of the white line was not corrected for because the change was small (3 % at most).

In the data analysis, the linear combination fits provide the key results of this study. Where two spectra were acquired during different beamtimes for a single sample, both spectra were fit, and the resulting fit parameters were averaged. The error was taken as either the standard deviation of the fit parameters or the errors on the individual fits, whichever was larger.

## 2.3 Results

### *Sample characterization*

Average compositions of glasses made from different starting compositions, determined by FE-SEM, are listed in Table 2.7. For CMAS7A, CMAS7G and NHPG-1, compositions from multiple samples are averaged. Details of the individual samples are given in the supplementary material (section 7.2, p.197). Analytical totals in some samples were as low as 89% (C4506), but typically around

96–98%. These low totals likely result from dissolved volatiles in the melt (water or $CO_2$). The presence of volatiles is also indicated by the observation of large round vesicles in some of the samples. Samples containing vesicles are listed in the supplementary material (section 7.3, p.199).

Ge and Ga concentrations in all samples were determined using LA-ICPMS (see supplementary material, section 7.3, p.199). The average concentrations were 2162 ± 246 ppm Ga in Ga-doped samples, and 2663 ± 364 ppm Ge in Ge-doped samples. The standard deviation quoted is the standard deviation on the means of each sample, reflecting ~300 ppm variation in Ge and Ga content between samples. Standard deviations on multiple analyses within samples were typically ~10 – 100 ppm.

Table 2.7. Average compositions of glasses made with different starting compositions, determined using FE-SEM.

| | AnDi | CMAS7A | CMAS7F | CMAS7G | CAS1 | CAS4 | CAS5 |
|---|---|---|---|---|---|---|---|
| *n* | 3 | $15^{\dagger}$ | 3 | $37^{\dagger\dagger}$ | 2 | 3 | 3 |
| $SiO_2$ | 50.0 (3) | 51.9 (21) | 61.7 (3) | 58.2 (14) | 41.0 (1) | 49.7 (4) | 61.6 (1) |
| $Al_2O_3$ | 15.0 (2) | 14.4 (6) | 5.9 (1) | 12.2 (4) | 19.03 (3) | 11.24 (2) | 14.4 (1) |
| MgO | 10.5 (1) | 12.0 (16) | 14.1 (3) | 2.3 (1) | – | 1.63 (7) | |
| CaO | 22.5 (1) | 14.0 (58) | 17.63 (4) | 24.0 (5) | 35.50 (2) | 32.1 (2) | 21.7 (2) |
| Total | 98.0 (8) | 92.3 (30) | 99.3 (1) | 96.7 (21) | 95.5 (1) | 94.7 (4) | 97.7 (4) |

| | L3 | AvMORB | CapeV | DB/3D | PAL/D | HiTiMB | NHPG-1 |
|---|---|---|---|---|---|---|---|
| *n* | 3 | 3 | 3 | 3 | 3 | 2 | $9^{\dagger\dagger\dagger}$ |
| $SiO_2$ | 61.2 (3) | 51.1 (1) | 49.5 (3) | 47.8 (3) | 58.2 (2) | 37.18 (6) | 58.6 (5) |
| $Al_2O_3$ | 16.9 (2) | 15.5 (2) | 14.6 (2) | 14.38 (7) | 12.49 (8) | 8.09 (1) | 14.7 (2) |
| MgO | 8.94 (3) | 7.97 (8) | 21.7 (7) | 10.64 (3) | 3.85 (6) | 9.59 (4) | 6.70 (7) |
| CaO | 9.24 (2) | 11.7 (1) | 5.89 (5) | 7.91 (2) | 8.33 (5) | 9.8 (2) | 8.26 (7) |
| FeO* | – | 10.9 (2) | 4.65 (4) | 16.69 (1) | 15.3 (1) | 19.4 (2) | |
| $TiO_2$ | – | 1.27 (8) | – | – | – | 11.6 (2) | 3.8 (1) |
| $Cr_2O_3$ | – | – | – | – | – | 0.50 (6) | |
| $Na_2O$ | – | 0.22 (3) | 0.49 (2) | – | – | – | 3.8 (3) |
| $K_2O$ | – | – | – | – | – | – | 1.87 (8) |
| $P_2O_5$ | – | – | – | – | – | – | 0.43 (3) |
| $RuO_2$ | – | – | – | – | – | 0.85 (6) | |
| Total | 96.35 (3) | 98.7 (1) | 96.8 (5) | 97.4 (5) | 98.2 (2) | 97.0 (3) | 98.1 (5) |

*n* is the number of analyses. FeO* refers to total iron expressed as FeO. $^{\dagger}$The 15 analyses of CMAS7A are from five different samples. $^{\dagger\dagger}$The 37 analyses of CMAS7G are from ten different samples, including quenched melts and annealed glasses. $^{\dagger\dagger\dagger}$The 9 analyses of NHPG-1 are from six different samples. The larger standard deviations on CMAS7A and CMAS7G result from small deviations in the composition between different batches of the starting material used in different experiments. Other compositions are all measured on the run products of 0.5 GPa experiments (‘Quenched melts doped with Ge’ in Table 2.2), with the exception of the CAS5 composition which was prepared at 1 atm (sample E16/11/13E).

Crystals were observed in only two of the quenched melt samples: D1609, and C4519. In D1609, the crystals were < 1 μm in size. In C4519, the crystals were < 1 μm wide but up to 10 μm long. Due to their small size, these crystals were not identified.

Crystals of corundum ($Al_2O_3$) were observed in most of the annealed glasses. The largest and most abundant crystals were observed in the highest-pressure sample, MA1118 (Figure 2.2). In this sample, corundum crystals are up to ~ 70 μm in size. If these essentially pure $Al_2O_3$ crystals were the product of devitrification of the glass, it would be expected that the immediately adjacent glass should be strongly depleted in Al. However, no evidence for this was observed by EDS analysis. Instead, these crystals are more likely to be fragments of the alumina crucible used to melt the starting material. The alumina crucible was broken in order to extract the glass, and pieces of glass were picked to make the starting material for the annealed glasses. Although care was taken to pick out only glass, fragments of alumina ~100 μm in size would have been difficult to spot if they had adhered to the glass chips.

As well as corundum, unidentified 'mottled patches' were observed in BSE in the three highest-pressure experiments. These patches have well-defined boundaries (Figure 2.2A,B), and contain a mottled texture in BSE reflecting a heterogeneous composition (Figure 2.2C), however their bulk composition is the same as that of the surrounding glass. Within the mottled texture, dark parts contain ~ 6 wt% more $SiO_2$ and ~ 6 wt% less CaO than the surrounding glass; the converse was observed in the light parts. These mottled features probably represent the onset of crystallisation. It is not expected that the presence of these corundum crystals and 'mottled features' will contribute significantly to the XANES or EXAFS spectra, because they make up a small fraction of the sample.

All quenched melt samples were buffered using a mixture of Ru and $RuO_2$. The experimental products were checked to see that both phases were present. Most samples contained either both phases or $RuO_2$ only, so the $fO_2$ must have been either at or above the Ru–$RuO_2$ buffer. Phases present in sample D1592 could not be checked because no buffer was exposed at the surface. The only sample that certainly reduced during the run was D1572, which contained Ru metal only.

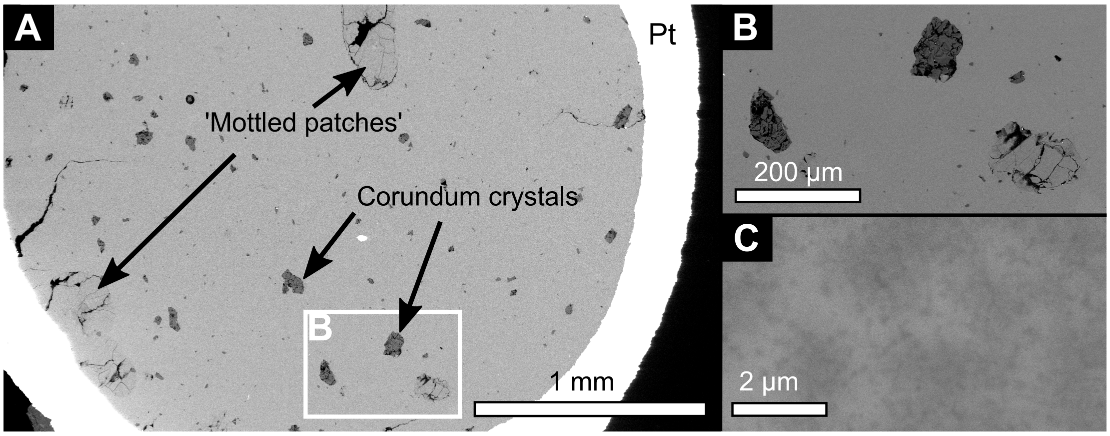

Figure 2.2. (A) BSE image of MA1118, showing corundum crystals and unidentified 'mottled patches'. (B) Close up of corundum crystals and one ‘mottled patch’. (C) Close up of the interior of the ‘mottled patch’ shown in (B).

DSC analysis indicated that the $T_g$ of a glass of CMAS7G composition (quenched at ambient pressure) was 777 ± 0.5 °C.

### *X-ray absorption spectroscopy*

The full Ge- and Ga XANES spectra for a quenched melt prepared at 1 atm are shown in

Figure 2.3 to demonstrate that spectra are well normalised. In subsequent figures, only the near-edge part of the spectra will be shown.

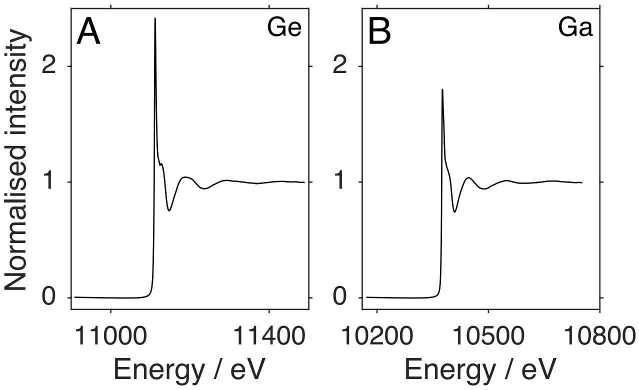

Figure 2.3. (A) Ge and (B) Ga K-edge XANES spectra of sample B1-080316.

To determine the differences in XANES spectra between 4- and 6-fold coordinated Ge and Ga, spectra of model compounds were acquired Figure 2.4. In the $^{[6]}$Ge- and $^{[6]}$Ga-bearing samples, the absorption edge is at higher energy, the intensity of the white line is greater and wider, and the intensity of the first minimum lower than in samples containing $^{[4]}$Ge- and $^{[4]}$Ga. Therefore, these are the types of spectral changes expected if a coordination change is preserved in the glass samples.

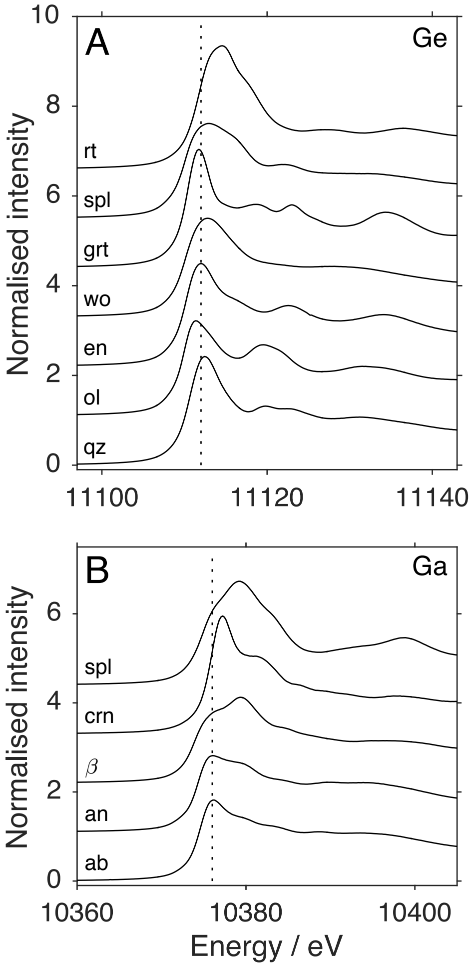

Figure 2.4. (A) Ge K-edge XANES spectra of model compounds: qz-$Ge^{[4]}O_2$, ol-$Mg_2{}^{[4]}GeO_4$, en-$Mg^{[4]}GeO_3$, wo-$Ca^{[4]}GeO_3$, grt-$Ca^{[4]}GeO_3$, spl-$Mg_2{}^{[4]}GeO_4$, and rt-${}^{[6]}GeO_2$. (B) Ga K-edge XANES spectra of model compounds: ab-$Na^{[4]}GaSi_3O_8$, Ga doped an-$CaAl_2Si_2O_8$, β-$Ga_2O_3$, Ga doped crn-$Al_2O_3$, and spl-$ZnGa_2O_4$. Spectra are offset for clarity, and dotted lines are a guide to the eye.

The spectra of glasses show very little change with composition, but significant changes with pressure. Figure 2.5 shows spectra of quenched melts of different compositions made at the same pressure; these spectra show no shift in the edge energy and only subtle variations in shape. However, Figure 2.6 shows that the differences in spectra between the lowest- and highest-pressure glass samples reflect the changes seen between 4-fold and 6-fold coordination model compounds. This indicates that the coordination numbers of Ge and Ga are unaffected by composition (at least, at ambient pressure), but increase with pressure.

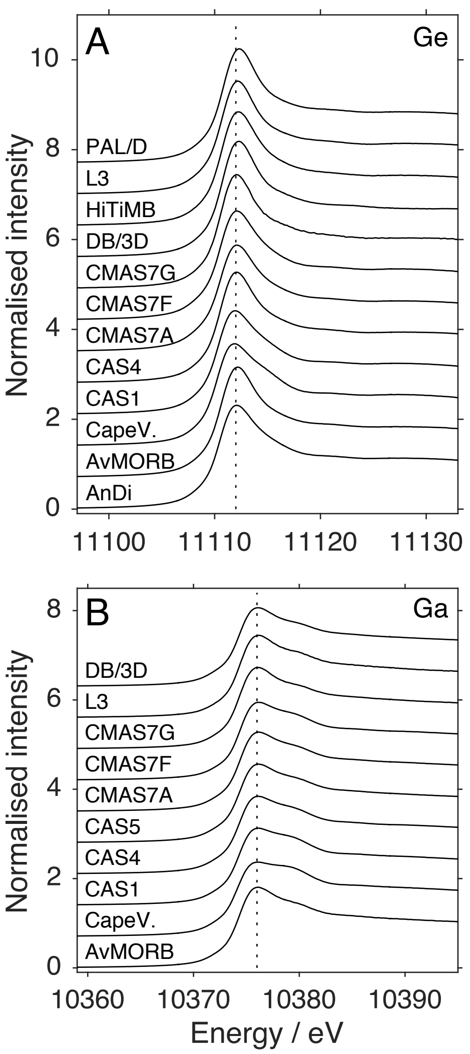

Figure 2.5. (A) Ge and (B) Ga K-edge XANES spectra of glasses of various compositions. Ge-bearing glasses were prepared at 0.5 GPa; Ga-bearing glasses were prepared at 1 atm. Spectra are offset for clarity, and dotted lines are a guide to the eye.

In Figure 2.6 the Ge XANES spectrum of the 10 GPa annealed glass exhibits a shoulder at ~11109 eV, which is not seen in the spectra of model compounds. This feature is seen in the spectra of all the annealed glasses (and is more pronounced at lower pressures), but only in one of the quenched melts – sample D1572 (4 GPa). The shoulder is at the same energy as the white line of $Ge^{2+}$ in silicate glass (see Chapter 5), suggesting that Ge has been partially reduced. The annealed glass samples were unbuffered, so while the reduction of $Ge^{4+}$ to $Ge^{2+}$ is unexpected, it is possible. The quenched melts were buffered with Ru-$RuO_2$, but the $RuO_2$ in sample D1572 was consumed, allowing the $fO_2$ of the sample to decrease. I therefore interpret this shoulder as a $Ge^{2+}$ component in the samples. For a more detailed justification of this interpretation, please see the supplementary material (section 7.4, p.202).

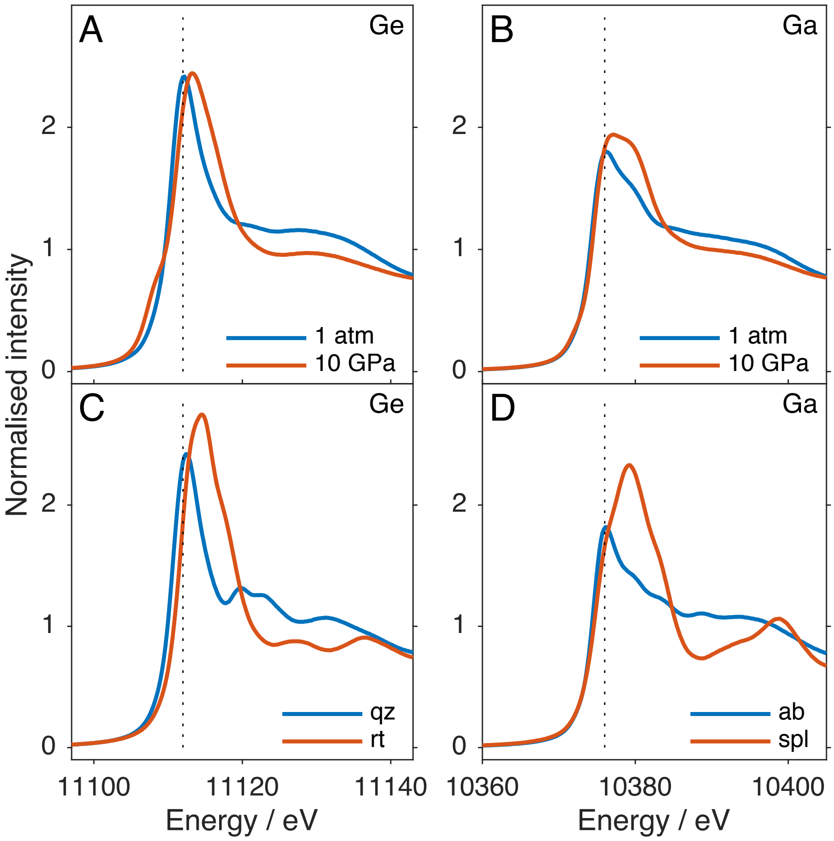

Figure 2.6. (A, B) Ge and Ga K-edge XANES spectra for samples prepared at 1 atm (B1-080316) and 10 GPa (MA1118). (C) the spectra of qz-[4]$GeO_2$ and rt-[6]$GeO_2$. (D) the spectra of ab-Na[4]$GaSi_3O_8$ and spl-Zn[6]$Ga_2O_4$. Dotted lines are a guide to the eye.

For the purposes of determining the coordination of $Ge^{4+}$, the $Ge^{2+}$ component needed to be removed from the spectra. This was achieved by linear combination fitting each spectrum using three end-members: the spectrum of a $Ge^{2+}$-bearing glass (sample D12/04/16, see Chapter 4), the spectrum of a quenched melt containing $Ge^{4+}$ prepared at ambient pressure (B1-080316), and the spectrum of rt-[6]$GeO_2$. The spectra of these three end-members are shown in Figure 2.7A. The linear combination of the end-members is given by:

$$y = A \cdot s_1 + B \cdot s_2 + (1 - A - B) \cdot s_3$$

Equation 2.1

where $y$ is the linear combination fit, $s_1$, $s_2$, and $s_3$ are the end-member spectra, and $A$ and $B$ are the fit parameters. Each mixed spectrum was fit to Equation 2.1 using a least-squares method. Fits were better for the low-pressure samples than for the higher-pressure samples (Figure 2.7B, C), where the [6]Ge component is more important, because the spectrum of a crystalline compound is not an ideal analogue for the spectrum of $^{[6]}$Ge in a glass. However, the fits are assumed to be sufficient to allow the proportion of the Ge$^{2+}$ component in each spectrum to be estimated (given as fit parameter *A* in Table 2.8). This component was then removed by subtraction of the appropriate proportion of the Ge$^{2+}$ spectrum from each mixed spectrum; the resulting 'difference spectrum' was then renormalized.

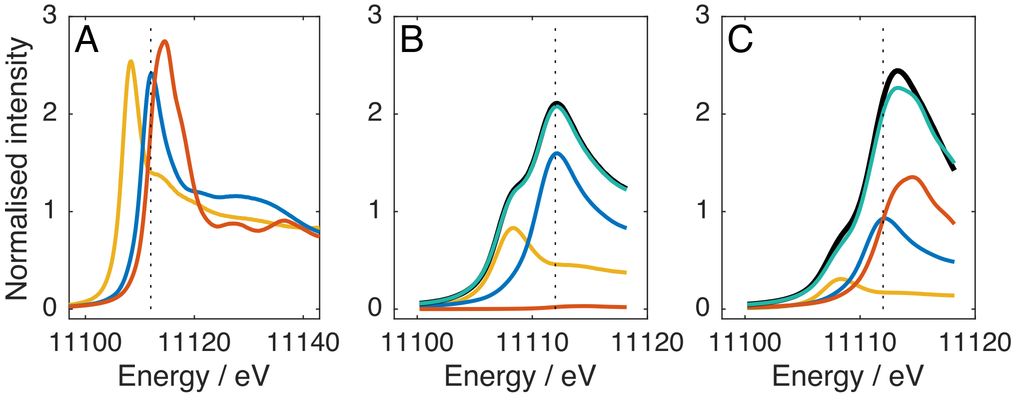

Figure 2.7. (A) Ge XANES spectra of a Ge$^{2+}$-bearing glass (D12/04/16, yellow), a $^{[4]}$Ge$^{4+}$-bearing glass (B1-080316, blue) and rt-$^{[6]}$Ge$^{4+}$O$_2$ (red). (B) A linear combination fit (green) to the spectrum of D2210 (black). (C) A linear combination fit (green) to the spectrum of MA1118 (black). In panels B and C, the yellow, blue and red curves are the components of the fit, which correspond to the end-members shown in panel A. Dotted lines are a guide to the eye.

Table 2.8. Fit parameters from Equation 2.1 used to determine the $Ge^{2+}$ component in the annealed glasses.

| Sample | Pressure (GPa) | $A$ – $Ge^{2+}$ | $B$ – $^{[4]}Ge^{4+}$ | $(1-A-B)$ – $^{[6]}Ge^{4+}$ |
|---|---|---|---|---|
| D2210 | 1 | 0.327 (4) | 0.661 (9) | 0.01 (1) |
| D2212 | 1.5 | 0.300 (5) | 0.683 (10) | 0.02 (1) |
| C5232 | 2 | 0.101 (6) | 0.885 (12) | 0.01 (1) |
| D2208 | 2 | 0.298 (5) | 0.665 (11) | 0.04 (1) |
| D2209 | 2.5 | 0.280 (5) | 0.666 (11) | 0.05 (1) |
| C5199 | 3 | 0.220 (7) | 0.686 (16) | 0.09 (2) |
| C5231 | 3 | 0.090 (7) | 0.870 (14) | 0.04 (2) |
| D2125 | 3.5 | 0.671 (4) | 0.282 (8) | 0.05 (1) |
| D2189 | 3.5 | 0.156 (7) | 0.706 (15) | 0.14 (2) |
| D2213 | 3.5 | 0.254 (7) | 0.622 (14) | 0.12 (2) |
| C5228 | 4 | 0.101 (5) | 0.847 (11) | 0.05 (1) |
| D1572* | 4 | 0.087 (10) | 0.882 (21) | 0.03 (2) |
| D2173 | 4 | 0.255 (8) | 0.618 (16) | 0.13 (2) |
| D2207 | 4 | 0.257 (7) | 0.604 (14) | 0.14 (2) |
| uhppc372 | 6 | 0.185 (12) | 0.528 (24) | 0.29 (3) |
| MA1117 | 8 | 0.058 (18) | 0.425 (38) | 0.52 (4) |
| MA1121 | 8 | 0.107 (17) | 0.468 (35) | 0.42 (4) |
| MA1118 | 10 | 0.122 (19) | 0.386 (41) | 0.49 (5) |

*Sample D1572 is a quenched melt sample; all others are annealed glasses. Numbers in parentheses give the 95% confidence interval on the last digit of the fit parameter.

The progressive changes in the Ge and Ga spectra with pressure, corresponding to an increase in coordination, are shown in Figure 2.8. The $Ge^{2+}$ component has been removed from the annealed glass spectra (marked with an asterisk) in Figure 2.8A. While each pressure series shows a similar trend, the magnitude of the changes vary, so the relative extent of the coordination change in each sample was quantified using linear combination fitting.

The linear combination fits were made using a low- and a high-pressure end-member. The low-pressure end-member was the quenched melt of appropriate composition made at ambient pressure. The high-pressure end-member was the spectrum of MA1118 (an annealed glass prepared at 10 GPa). Each spectrum was fit using the equation

$$y = A \cdot s_1 + (1 - A) \cdot s_2$$

Equation 2.2

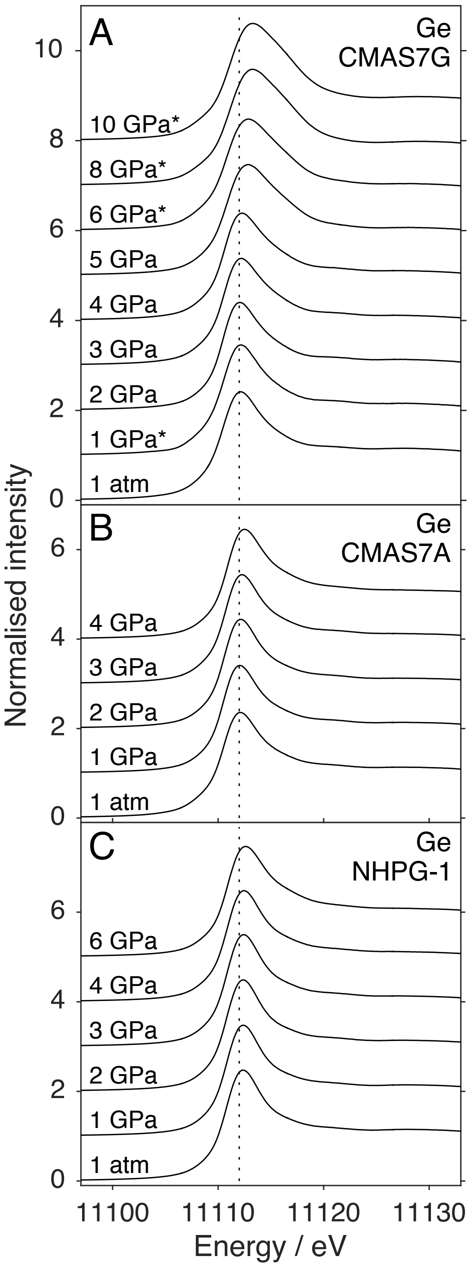

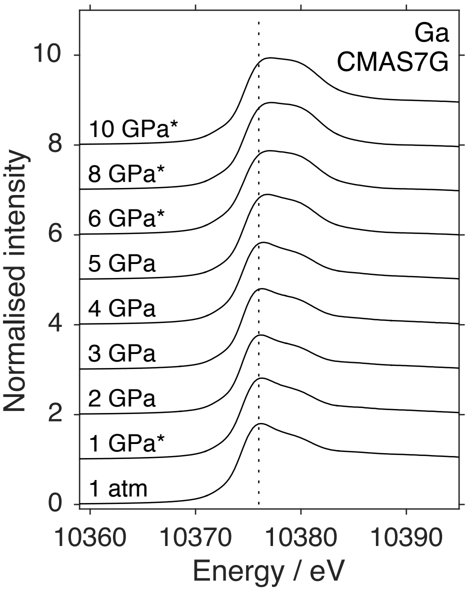

Figure 2.8. (Left) Selected, representative Ge K-edge XANES spectra of samples synthesised at the pressures indicated for the compositions (A) CMAS7G, (B) CMAS7A and (C) NHPG-1. *Asterisks indicate spectra of annealed glass samples; other spectra are for quenched melt samples. Annealed glass spectra have had the $Ge^{2+}$ component removed as described in the text and illustrated in Figure 2.7. (Right) Selected, representative Ga K-edge XANES spectra of samples synthesised at the pressures indicated. *Asterisks indicate spectra of annealed glass samples; other spectra are for quenched melt samples. Dotted lines are a guide to the eye.

where $y$ is the linear combination fit, $s_1$, and $s_2$ are the end-member spectra, and $A$ is the fit parameter (i.e. the fraction of the low-pressure end-member). Examples of these fits for each composition are shown in Figure 2.9.

The relative changes in the average coordination number with pressure for Ge and Ga are shown in Figure 2.10 and Figure 2.11. In these figures, the fraction of the high-pressure end-member (i.e. $(1-A)$ in Equation 2.2) is plotted against pressure. The vertical axis can be interpreted as proportional to the average coordination number, although the proportionality is unknown, and is probably different between Ge and Ga.

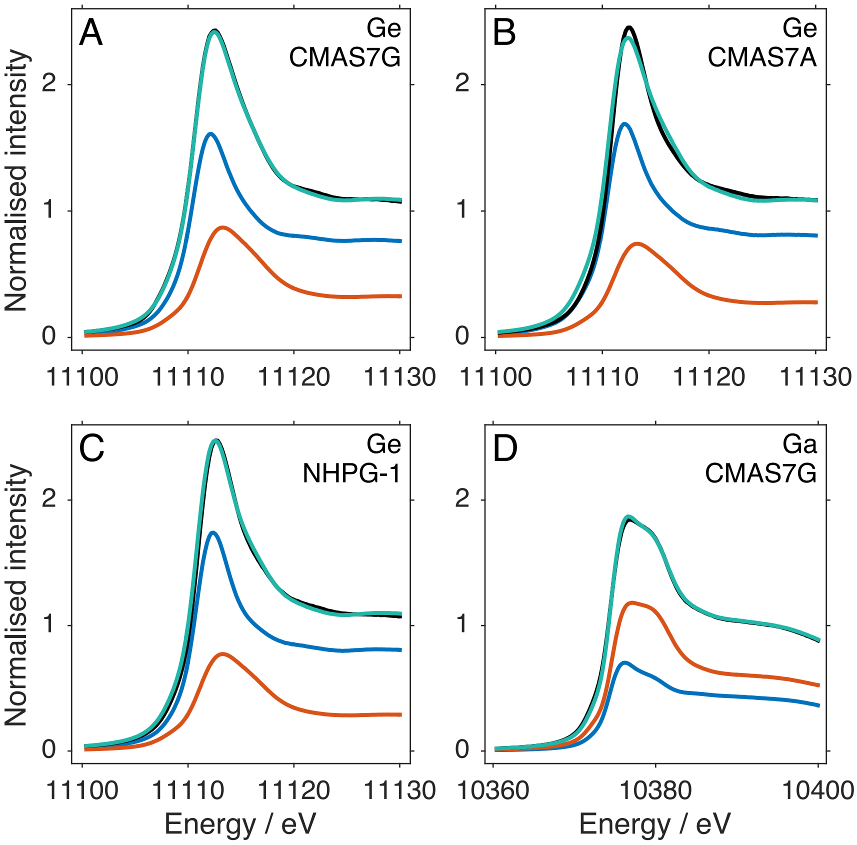

Figure 2.9. Linear combination fits of Ge and Ga XANES spectra. (A) Ge spectrum of D2207 (4 GPa, CMAS7G). (B) Ge spectrum of C4506 (4 GPa, CMAS7A). (C) Ge spectrum of uhppc253 (6 GPa, NHPG-1). (D) Ga spectrum of uhppc258 (6 GPa, CMAS7G). In each panel, the black curve is the spectrum, the green curve is the fit, and the blue and red curves are the low- and high-pressure components of the fit respectively.

For all compositions, a gradual increase in coordination number is seen with pressure, but the rate and extent of this increase varies. For the quenched melts of composition CMAS7G and CMAS7A, there is a rapid increase in Ge coordination from about 3 GPa. This change is less rapid for the composition NHPG-1. In particular, the quenched melts of composition CMAS7G show a remarkable increase in Ge coordination between 4 and 4.5 GPa.

On the other hand, the coordination change of Ge in annealed glasses appears to begin at lower pressures (1.5 GPa), but increases steadily up to 10 GPa. The annealed glasses were made at a range of temperatures, and the rate at which the coordination changes with pressure is lower in the samples prepared at 600 °C than in the samples made at 700 °C or higher. The 8 GPa samples also show a substantial difference in the Ge coordination between the sample made at 700 °C and the one made at 780 °C. Fits to the Ga spectra also show a substantial increase in coordination between 4 and 4.5 GPa in the quenched melts, and a steadier increase in coordination with pressure in the annealed glasses.

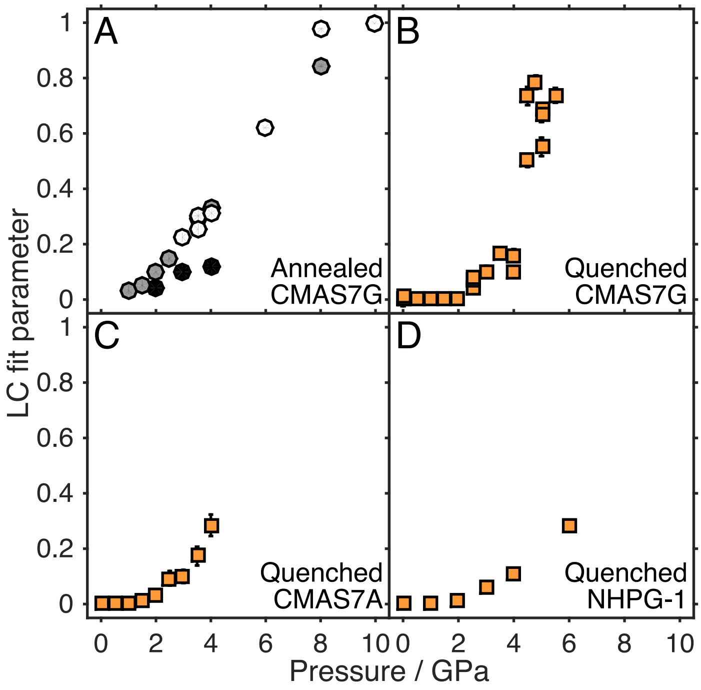

Figure 2.10. The fraction of the high-pressure component derived from linear combination fitting of each Ge K-edge XANES spectrum, plotted against the pressure of synthesis. (A) Fits to spectra of annealed glasses (circles) of composition CMAS7G, which were annealed at different temperatures: black = 600 °C, grey = 700-730 °C, white = 765-780 °C. (B, C, D) Fits to spectra of quenched melts (orange squares) of compositions CMAS7G, CMAS7A and NHPG-1.

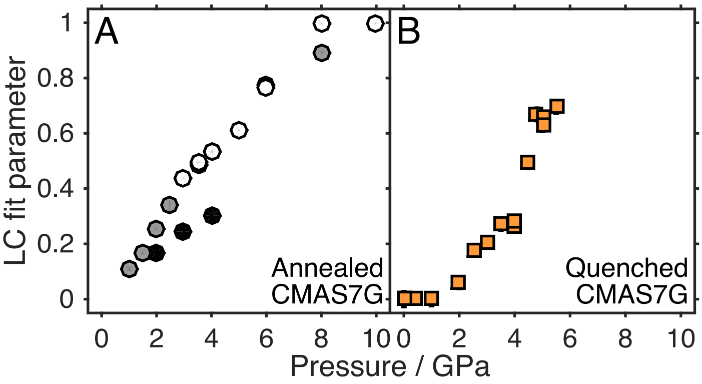

Figure 2.11. The fraction of the high-pressure component derived from linear combination fitting of each Ga K-edge XANES spectrum, plotted against pressure of synthesis. (A) Fits to spectra of annealed glasses (circles) of composition CMAS7G, which were annealed at different temperatures: black = 600 °C, grey = 700-730 °C, white = 760-780 °C. (B) Fits to spectra of quenched melts (orange squares) of composition CMAS7G.

EXAFS spectra have the potential to provide quantitative information on the local environment of Ge. Germanium EXAFS spectra for the qz-Ge$^{[4]}$O$_2$, and the 1, 4 and 6 GPa samples of NHGP-1 composition are shown in Figure 2.12 (black curves). If the coordination changed from tetrahedral to octahedral, the Ge-O bond length should increase (e.g., the bond length in qz-[4]$GeO_2$ is 1.74 Å, whereas that in rt-[6]$GeO_2$ is 1.87 Å). If this were the case, the first peak in the Fourier transform of the EXAFS should shift to greater radial distance. Such a shift is not apparent in Figure 2.12B. Fits to the spectra (shown in red in Figure 2.12) yield bond lengths and coordination numbers that are within error of each other for all samples, suggesting that EXAFS is not sensitive enough to resolve the changes that are apparent in the XANES spectra for these samples.

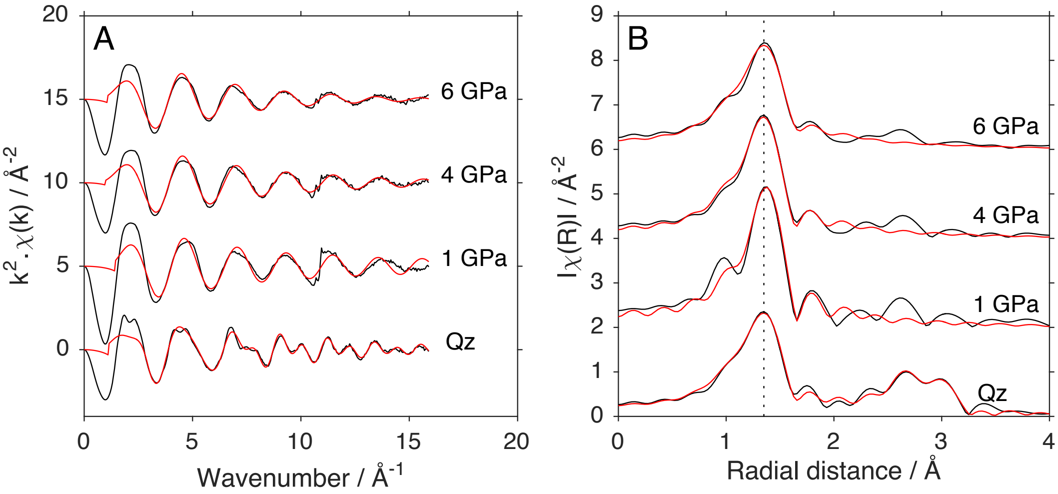

Figure 2.12. Ge K-edge EXAFS spectra (black curves) of samples of NHPG-1 composition plotted in (A) k-space and (B) R-space. Dotted line is a guide to the eye. Red curves are fits to the spectra; refer to text for details.

## 2.4 Discussion

### *Evidence for and extent of coordination changes*

The key finding in this study is that Ge and Ga do undergo pressure-induced coordination changes when dissolved as trace elements in silicate melt. The shape of Ge and Ga XANES spectra are change little with composition at low pressure, but change substantially with increasing pressure. These changes are similar to those observed in model compounds containing known coordination environments. The changes seen in the spectra are also comparable to those in many previous studies of amorphous $GeO_2$ under pressure (Itié et al. 1989; Ohtaka et al. 2001;

Ohtaka et al. 2002; Majérus et al. 2004; Ohtaka et al. 2004; Cormier et al. 2007; Vaccari et al. 2009; Baldini et al. 2010; Hong et al. 2014).

The extent of the coordination change in the samples is unknown, but is probably not complete. From 0 to 2 GPa, little change in the extent of coordination is seen, which suggests that only four fold coordinate environments are present at these pressures. The spectra begin to change from about 3 GPa, indicating the beginning of a coordination change. If the spectra were to stop changing with pressure, this might indicate that the coordination was predominantly 6-fold and therefore no longer changing with pressure. However, the results do not convincingly show this. Furthermore, studies of $GeO_2$ glass, and Ga in germanate and silicate glasses indicate the coordination in these samples extends over a wide range of pressure. Early studies of Ge suggested a rapid change between ~6 and 13 GPa, (Itié et al. 1989; Ohtaka et al. 2001; Ohtaka et al. 2002; Ohtaka et al. 2004), whereas more recent studies show that a completely octahedral state is not reached until about 20-30 GPa, if at all (Majérus et al. 2004; Cormier et al. 2007; Vaccari et al. 2009; Baldini et al. 2010; Hong et al. 2014). The coordination of Ga in jadeite glass changes over a pressure range from 0 to 15 GPa (Cormier et al. 2007). Since all these literature studies suggest a wide pressure range of transformation, and there is limited data at high pressure, the coordination change is most likely incomplete in the samples, but cannot be quantified.

### *Factors that might affect preserved coordination environments*

Even if the extent of coordination change in the glasses could be quantified, it would be likely to differ from the coordination in the melt at the conditions of the experiments. As described in section 2.1 (Introduction), the $T_f$ and $P_f$ recorded in the structure of a glass may differ from the pressure and temperature of synthesis. The results would be straightforward to interpret if the $T_f$ of all samples were similar and the $P_f$ of samples were equal to that of the run pressure – or if not equal, at least increased in proportion to increasing run pressure. However, these two conditions may not be met.

### **Dissolved water in the quenched melts**

One key issue affecting the glasses is the presence of dissolved water. The very low totals from the chemical analyses of the quenched melts (92.3 ± 3.0, 96.7 ± 2.1 and

98.1 ± 0.5 from CMAS7A, CMAS7G and NHPG-1 respectively) indicate that there are dissolved volatiles (probably water) in the glasses. This interpretation is also supported by the observation of large round vesicles in many of the samples. The presence of water could result from the starting material not being fully dried prior to the experiment. Capsules were left at 110 °C overnight before welding them shut, but the oxide mixtures were kept at room temperature and therefore may have absorbed moisture from the air over time, which was not driven off when the capsules were dried.

However, the amount of water dissolved in the annealed glasses should be negligible, because these samples were synthesised by first melting the starting composition at 1300 °C in air. Some water could have been introduced to the powdered glass during grinding under acetone, but this should have dried off when the capsules were left at 110 °C overnight before they were sealed. The powdered glass used for the annealed glass experiments is unlikely to be as hygroscopic as the powdered oxide mixtures used as the starting materials for quenched melts.

The effect of water on melt structure in general—polymerisation in particular—has been well studied (Manning 2018), but the specific effect on cation coordination is not well known. Malfait et al. (2012) found that in rhyolites, increased water content caused a decrease in the proportion of higher-coordinate Al, but in andesite the effect was the opposite. Xue and Kanzaki (2008) found that hydrous glasses prepared at 2 kbar contained more higher-coordinate Al than anhydrous glasses prepared at 1 atm, and postulate that water leads to an increase in average Al coordination; but since we know for sure that pressure increases average Al coordination, it is hard to compare the two sample sets directly. The compositions used in this study have NBO/T similar to andesites, so we could hypothesise that dissolved water in the melts would lead to a higher average Al coordination environment, and perhaps the same would hold true for Ge and Ga. However, this is very speculative with such little data. Another effect of water is to decrease the viscosity of the liquid, thereby possibly altering $T_f$, which will be discussed in the next section.

### Changes in fictive temperature in quenched melts

The two key factors affecting the $T_f$ of a quenched melt are the cooling rate and the viscosity of the melt. The cooling rate is unlikely to vary between samples, because all were quenched in the same way – by cutting power to the assembly (at least up to 6 GPa where the assemblies used were the same; multi-anvil experiments might have slightly different quench rates). Therefore, if the viscosity were equal between the samples, $T_f$ would not vary regardless of the run temperature. For example, Figure 2.13 illustrates the run conditions of three experiments (*a*, *b*, and *c*) performed at different temperatures. When these experiments are quenched, all three samples cross the glass transition at point *d*, and so all have the same $T_f$. However, the viscosity of the melt, and hence the position of the glass transition curve in Figure 2.13, may vary between samples.

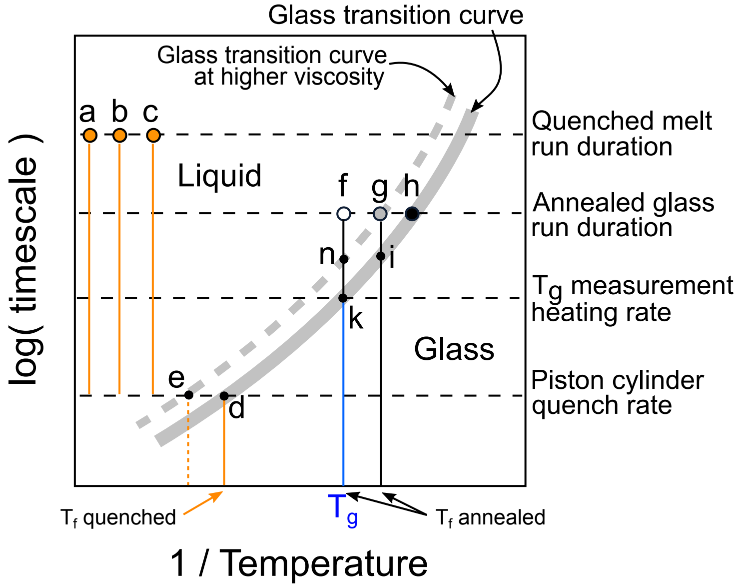

Figure 2.13. Conceptual illustration of how the $T_f$ of samples may vary depending on what temperature they cross the glass transition. The orange symbols (a, b and c) represent the run conditions of three quenched melt experiments. The white, grey and black symbols (f, g and h) represent the run conditions of three annealed glass experiments. See text for more details. Note that this is a conceptual illustration only, for the purpose of aiding discussion, and axes are not to scale.

There are three main ways that the viscosity of the melt may vary between samples. Firstly, the effects of pressure were investigated for three different compositions in this study, with NBO/T of 0.70, 0.62 and 0.40 for CMAS7A, CMAS7G and NHPG-1 respectively. If we use NBO/T as a proxy for viscosity, then all else equal, the greater viscosity of CMAS7A should mean that on quenching it would cross the glass transition at a higher temperature (e.g. point *e* in Figure 2.13). Therefore, $T_f$ preserved in CMAS7A should be higher than CMAS7G, which should in turn be higher than NHPG-1.

Secondly, dissolved water has a strong influence on viscosity. Adding water interrupts the polymerisation of the network (Burnham 1975) and causes a large decrease in $T_g$ (Deubener et al. 2003). In quenched melts, the result would be that hydrous melts would have a lower $T_f$ compared with dry melts. If some samples contained more water than others, they would therefore have different $T_f$. Furthermore, if pressure either promoted or inhibited the dissolution of water into the melt, this would also lead to differences in $T_f$ between samples as a function of pressure. Without knowing the water contents of the samples, it is impossible to quantify this discussion with any certainty. As a proxy for water content, I have plotted the analytical total against pressure in the supplementary material, Figure 7.1 (section 7.2, p.197). There is no correlation between analytical total and pressure apart from in the CMAS7A pressure series, which does show lower totals at higher pressure. Future work will be needed to quantify the water contents of all samples investigated.

Thirdly, the effect of pressure itself might influence viscosity regardless of the presence or absence of volatiles. Previous work has shown that in compositions relevant to those studied here (i.e. $NBO/T < 1$), viscosity typically decreases with pressure up to ~4 GPa, but then increases with pressure higher than ~3–5 GPa (Funakoshi et al. 2002; Suzuki et al. 2005; Sakamaki et al. 2013; Kono 2018). This is probably because initial compression is accommodated by increasing the bond angles between neighbouring tetrahedral units, which will lead to the breaking of some bridging oxygen bonds and therefore depolymerisation of the network (Sakamaki et al. 2013; Wang et al. 2014). Beyond this pressure, coordination changes become a more important compression mechanism (Sakamaki et al. 2013; Wang et al. 2014). If the same occurs in the melts studied here, then we expect that as viscosity decreases up to ~3-5 GPa, $T_f$ should decrease. Above this pressure, $T_f$ should increase again.

Unfortunately, it is very difficult to estimate how much of an effect $T_f$ is likely to have on coordination changes of Ge and Ga in these samples. Previous work on the temperature-dependence of cation coordination has mainly involved synthesising glasses with different fictive temperatures and using NMR spectra to determine coordination. For Si and Al, coordination numbers tend to increase with increasing temperature in compositions that contain appreciable non-bridging oxygens (Stebbins 1991; Allwardt et al. 2005a; Stebbins et al. 2008), although in Brich aluminoborosilicates and borates, both Al and B coordination decreases with temperature (Stebbins and Ellsworth 1996; Wu and Stebbins 2010; Morin and Stebbins 2016). Al coordination is also found to behave differently in highly polymerised systems. For example, Allwardt et al. (2005a) found that the NBO-poor $NaAlSi_3O_8$ glasses exhibit a decrease in Al coordination with temperature, and Mailfait et al. (2012) found no measurable change in Al coordination with temperature in rhyolite glasses (NBO/T = 0.03). This result contradicts the results of Stebbins et al. (2008), who reported an increase in Al coordination number with temperature in calcium aluminosilicate glasses with NBO/T ranging from 0 to 0.8. However, most of these studies rely on only two data points for each composition investigated, because of the difficulty in synthesising glasses with different fictive temperatures.

Based on the previous work, the best guess that we can make for the samples in this thesis (NBO/T range from 0.4 to 0.7) is that increasing $T_f$ might cause a small increase in the Ge and Ga coordination numbers preserved in the glass. Any attempts to quantify this will be meaningless given the sparse data available.

### Changes in fictive pressure in quenched melts

The fictive pressure of a quenched melt should in principle be the same as the run pressure unless there are pressure drops during the quench. Unfortunately, there almost certainly *are* pressure drops during the quench. For one thing, the quenching process was not isobaric in these experiments. When power was cut to the furnace, the pressure gauge showed a drop of several kbar before the temperature read by the thermocouple dropped below 800 °C. This effect was smaller at lower pressures. In the 200 T piston cylinder presses, no attempt was made to quench isobarically by manually maintaining hydraulic pressure. In contrast, the 500 T press (used for pressures of 4.5–6.0 GPa) and the 1200 T multi-anvil apparatus (used for pressures > 6 GPa) had automated systems that compensated for the pressure drop on quenching by applying more load. However, it is unlikely that these systems could respond quickly enough to avoid any drop in pressure as the sample quenched. We can expect the $P_f$ of all quenched melt samples to be lower than that of the run pressure.

An added complication is that if $T_f$ was higher, there would be less time for a drop in pressure on the quench before the glass transition was crossed. So if $T_f$ increased with pressure, $P_f$ might also increase with pressure.

**Changes in fictive temperature in the annealed glasses**

The issues surrounding $T_f$ that applied to the quenched melt samples are slightly different when it comes to annealed glasses. Firstly, in contrast to the quenched melt samples, dissolved water is not expected in the annealed glasses, as discussed above. Therefore, the possibility that dissolved water affects the viscosity of the liquid and hence, the glass transition temperature, can be discounted.

Furthermore, the effect of pressure on viscosity is not likely to affect $T_f$ even if it still affects $T_g$. This concept is illustrated in Figure 2.13. The $T_g$ measurement was performed at a given heating rate (point *k*), which is on a shorter timescale than the duration of the annealing experiments. Therefore, when an annealed glass is equilibrated at a temperature close to that measured for $T_g$, it will plot at position *f* in Figure 2.13 (same temperature, but longer timescale, so therefore above the glass transition curve and in the liquid regime). When this experiment is quenched, the glass transition will be crossed at point *k*, and so $T_f$ will equal the measured $T_g$. If the viscosity increases, for example due to higher pressure, the glass transition (dashed curve) will still be crossed at the same temperature (e.g. for experiment *f*, it will cross the glass transition at point *n* and $T_f$ will still equal $T_g$).

However, unlike the quenched melts, the run temperature will alter $T_f$. If a lower run temperature is used (point *g* in Figure 2.13), the glass transition will be crossed at point *i* and $T_f$ will be lower than $T_g$. For example, the difference in result between samples MA1117 and MA1121 could be explained by the difference in $T_f$ between the two samples. If that were the case it would indicate that increasing temperature promotes an increase in average coordination number of Ge and Ga.

All of the above holds true provided that the run conditions of the annealing experiments are at lower temperature than point *d*, the fictive temperature obtained from a piston cylinder quench rate. If the run temperature of the annealing experiment is higher than point *d*, the behaviour will be the same as that of the quenched melts.

## Changes in fictive pressure in the annealed glasses

In annealed glasses, $P_f$ is expected to be closer to that of the run pressure due to a smaller temperature drop on the quench. While we cannot say for certain that $P_f$ is the same as run pressure, it is likely to at least be higher than the $P_f$ of the quenched melts. However, this statement is only valid if, at the run pressure and temperature, the glass structure fully relaxed and entered the metastable liquid regime (in other words, if the run temperature was above the glass transition temperature at that pressure).

As discussed above, the effect of pressure on the viscosity of the sample, and therefore on the glass transition is uncertain. However, setting aside this unknown, we can expect that the samples made at 780 °C are most likely to have been above the glass transition temperature. The $T_g$ of the CMAS7G composition was found to be 777 °C at a heating rate of 10 °C/min. $T_g$ was reached after heating for under 1.5 h in the measurements, whereas in the annealed glass experiments, samples were held at pressure and temperature for 2 h. The longer timescale of the experiments compared to the $T_g$ measurement implies that the samples should be in the liquid regime (e.g. at point *f* in Figure 2.13), *unless* there is a severe effect of pressure on the glass transition temperature.

The samples made at 700-730 °C show very similar results to the samples made at 780 °C (Figure 2.10 and Figure 2.11). This could be taken as evidence that even at 700 °C (80 ° below the measured $T_g$) the samples were still exhibiting liquid-like behaviour. The exception to this is the sample MA1121, made at 700 °C and 8 GPa, which shows a smaller change compared with MA1117, which was made at 780 °C and the same pressure. This might indicate that pressure causes an increase in the glass transition temperature and that at 8 GPa, 700 °C and two hours was not hot/long enough for the glass to fully relax (whereas it was hot/long enough at 4 GPa). However, MA1121 contained 'mottled patches' interpreted to represent the onset of crystallisation, which would not occur below the glass transition temperature. Instead, as discussed in the last section, the difference could result from different $T_f$ preserved in these samples.

The samples made at 600 °C all record lower coordination numbers than the samples made at 700–780 °C. This can be interpreted to mean that at 600 °C, two hours was not long enough for the samples to fully relax. However, all three samples record higher coordination numbers for both Ge and Ga than melts quenched at ambient pressure (and that the coordination increases systematically with pressure), so the samples must have partially relaxed. The glass transition temperature is not a single temperature but typically a range of several tens of degrees (Stebbins 2016). On a two-hour timescale, 600 °C might be within the glass transition, allowing only a partial relaxation of the glass (e.g. at point *h* in Figure 2.13).

To summarise, the results indicate that the annealed glasses made at temperatures above 700 °C were in the liquid regime during the experiment, and therefore the $P_f$ they record is expected to be systematically higher than that of the quenched melts at the same pressure. On the other hand, the annealed glasses made at 600 °C are most likely incompletely relaxed.

### *Differences in coordination change between quenched melts and annealed glasses*

With all of the above considerations about fictive pressure and temperature in mind, we can make some observations about the results. As expected, the annealed glasses mostly show higher average coordination environments than the quenched melts at most pressures (with the exception of the samples annealed at 600 °C, which is explained by their incomplete relaxation). However, it is clear that for both Ge and Ga, a rapid increase in coordination is apparent between 4 and 5 GPa in the quenched melts, whereas the annealed glasses increase their coordination much more steadily. This phenomenon was unexpected, but it is important to attempt to explain it, to interpret which behaviour would be expected in the melt at high pressure and temperature: a gradual change, or a rapid increase at some critical pressure?

One could argue that the quench rates change in the quenched melt samples between the 0–4 GPa and the 4.5+ GPa samples, since they were made in a different apparatus. A different quench rate would lead the glass transition to occur at a different temperature; the T and P ‘frozen in’ would therefore differ. However, the assembly used was the same, so this seems unlikely. The only other difference is that the apparatus used for the 4.5+ GPa experiments had an automatic system controlling pressure which attempted to retain run pressure during quenching. If the system could respond quickly enough, the 4.5+ GPa experiments might show a less severe pressure drop on the quench, and hence record a relatively higher $P_f$. However, this does not seem likely because pressure drops were observed on the quench despite the automated system, and it is probable that the pressure drops occurring on a local scale within the sample could not be compensated for by the apparatus.

Another possibility is that the glass transition temperature might increase as a function of pressure. This would mean that in the quenched melts, increasing pressure would cause an increase in $T_f$ and $P_f$ (as discussed above). This could conceivably lead to the steepening of the slope seen in the quenched melts. The result would be different for annealed glasses, because $T_f$ would not vary with pressure. Assessing this possibility is not easy because the effects of pressure on $T_g$ are not well known.

Another, speculative possibility is that there are five-coordinate environments that are more readily created or preserved in either the annealed glasses or quenched melts. Since XANES can only give an average coordination environment, no model compounds containing $^{[5]}$Ge or $^{[5]}$Ga were obtained, this possibility cannot be assessed with the present data. However NMR can give quantitative proportions of four-, five- and six-fold coordinated Al, which might shed some light on the issue.

Finally, our understanding of how silicate melts respond to pressure predicts a slow initial increase in coordination, followed by a more rapid change when coordination changes become the dominant compression mechanism (Sakamaki et al. 2013; Wang et al. 2014). Furthermore, this changeover point does appear to occur at around 4–6 GPa in some of the compositions studied (Sakamaki et al. 2013; Wang et al. 2014). However, if this phenomenon explains the rapid increase in Ge and Ga at 4–5 GPa in the quenched melts, it does not explain why a similar change is not observed in the annealed glasses. To summarise, the cause of the differences between the quenched melts and annealed glasses is unclear, but this will be discussed further in Chapter 3.

### *Similarity between Ge and Ga*

A second unexpected observation is that Ge and Ga show similar trends in coordination with pressure. Both Ge and Ga increase their coordination rapidly between 4 and 5 GPa in the quenched melts of CMAS7G composition, and show more steady increases with pressure in the annealed glasses. Since the extents of the coordination changes cannot be quantified, Ge and Ga cannot be directly compared, however the observed similarity is surprising considering that Al and Si change their coordination over very different pressure ranges. Al changes its coordination between ~1–10 GPa in these samples; but Si typically remains in predominantly tetrahedral coordination until about 8 GPa (Guillot and Sator 2007). While Ge and Ga were expected to change their coordination at pressures lower than Si and Al, there is no evidence that Ga has become substantially more highly coordinated than Ge in the samples, and there is no reason to expect that both elements should undergo the rapid increase between 4 and 5 GPa. This raises the question of whether Ge and Ga might be influenced by some change in the major element coordination or the network structure of the glass at this pressure. This possibility will be assessed using NMR spectroscopy in Chapter 3.

### *Effect of composition*

A third observation of note is the change in the pressure-dependence of Ge coordination with composition. The coordination change appears to occur at different rates with pressure in different compositions. The Ge coordination in NHPG-1 composition seems to increase the least with pressure; the fraction of the high-pressure component is ~0.3 at 6 GPa, whereas the CMAS7G and CMAS7A compositions reach the same fraction at around 4.2 and 4 GPa respectively. These differences could be due to the difference in polymerization of the three compositions: NHPG-1 is the most polymerized with NBO/T of 0.4, CMAS7G has an NBO/T of 0.62 and CMAS7A is the least polymerized with NBO/T of 0.7.

It is important to keep in mind that the difference between the compositions could result from a different fictive temperature between the three datasets due to their different viscosities. If this were the reason, then it would indicate that higher temperatures favour lower coordination environments (because the most polymerised composition, NHPG-1, which would have the highest $T_f$, shows the least change with pressure). However, this would be the opposite effect to that predicted based on the literature, as discussed earlier.

Furthermore, there is some evidence from the literature that Al and Si change their coordination at lower pressures in less polymerized compositions, because of the different mechanisms for forming the higher coordinate units (Stebbins 2016). Mechanisms involving non-bridging oxygens, which are abundant in depolymerised compositions, are energetically favourable compared with mechanisms involving bridging-oxygens, which are abundant in polymerised compositions (Wolf and McMillan 1995). The results for Ge and Ga are consistent with this interpretation. This is important because more mafic, depolymerized melts are more relevant to natural melts, suggesting that the coordination changes of not only major elements but also trace elements could be occur in melts in the Earth's upper mantle.

## 2.5 Conclusions

In this work I have demonstrated that trace elements Ge and Ga both undergo coordination changes in silicate melts with increasing pressure. While coordination changes of these cations have been observed in glasses by XAS before, this is the first time their behaviour has been studied as trace elements. The key results are that there is a striking and surprising difference between the quenched melts and annealed glasses, and a surprising similarity in the behaviour of Ge and Ga. Considering that Al and Si behave very differently, this raises the question of whether the major element coordination changes could be influencing the coordination of both trace elements. These features will be investigated further using NMR spectroscopy in the next chapter. The increased coordination change in more mafic systems suggests that these changes are important in the Earth, and therefore coordination changes of Ge and Ga are expected in natural melts, which will affect their partitioning, as will be discussed in Chapter 4.

# Chapter 3: Relationship between trace and major element coordination changes in silicate melts: insights from nuclear magnetic resonance spectroscopy

**Abstract—**Changes in the structure of silicate melt with pressure include the coordination of major elements and network connectivity. I test the hypothesis that these changes may influence the coordination numbers of trace cations $Ge^{4+}$ and $Ga^{3+}$, whose coordination was shown to change with pressure in Chapter 2. Nuclear Magnetic Resonance (NMR) spectra are acquired for all major elements, and Ga, in the same (or similar) samples studied in Chapter 2. The most striking result is a strong correlation between $Al^{3+}$ coordination and $Ga^{3+}$ coordination, and a weaker correlation between $Al^{3+}$ and $Ge^{4+}$ coordination. These correlations suggest that changes in Al coordination number may influence the coordination of both trace elements. This is the first evidence that trace element coordination may be affected by that of major elements, and further work is needed to see if this phenomenon extends to other trace elements, particularly those that are network modifiers rather than network formers.

## 3.1 Introduction

Pressure-induced changes in the structure of silicate melts can have important consequences for their physical and chemical properties. Coordination changes of Si and Al were first proposed to potentially affect physical properties of melts by Waff (1975), and this has been confirmed by numerous studies since then (see Wolf and McMillan 1995). More recently, it has been recognized that coordination changes of trace elements in silicate melts could affect their partitioning behaviour, and coordination changes of $Ni^{2+}$, $Co^{2+}$ and $Lu^{3+}$ have been observed (Keppler and Rubie 1993; Jones 2012; de Grouchy et al. 2017). In this thesis I have shown that Ge and Ga also undergo pressure-induced coordination changes (Chapter 2).

A possible relationship between major element and trace element coordination changes has never previously been investigated, but the work presented in Chapter 2 suggests that this is a possibility. $Ge^{4+}$ and $Ga^{3+}$ both show a dramatic increase in their average coordination number between 4 and 5 GPa in glasses quenched from high-pressure melts. This behaviour was unexpected, because geochemically similar cations $Si^{4+}$ and $Al^{3+}$ change their coordination over very different pressure ranges. Could it be, then, that a change in the major element coordination or some other structural change in the melt was driving an increase in both $Ge^{4+}$ and $Ga^{3+}$ coordination?

As a thought experiment, consider $Ge^{4+}$ substituting in trace quantities for $Si^{4+}$ in a forsterite crystal. The $Ge^{4+}$ substitutes on the $Si^{4+}$ site and therefore takes tetrahedral coordination. If the forsterite ($Mg_2SiO_4$) is subjected to lower mantle pressures, it will undergo phase transitions to form perovskite ($MgSiO_3$) and periclase (MgO). In perovskite, the $Si^{4+}$ is octahedrally coordinated, and the $Ge^{4+}$, which should still substitute for $Si^{4+}$, will also be octahedrally coordinated. In minerals, therefore, the trace element coordination number is completely controlled by the major element coordination number.

Does major element coordination control trace element coordination in melts, as well? In highly polymerized systems, there is evidence that it does. Majérus et al. (2004) studied binary $GeO_2$–$SiO_2$ glasses and found that coordination of $Ge^{4+}$ changed at different pressures depending on which cation was more abundant. In a 70% $GeO_2$ glass, the coordination change took place over ~7 to 20 GPa, whereas in a 20% $GeO_2$ glass, the coordination change started at around 10 GPa and was incomplete at 26 GPa. Considering that end-member $GeO_2$ and $SiO_2$ glasses are known to change coordination numbers over different pressure ranges, Majérus et al. argued that the coordination changes in these glass were driven by the dominant cation. Simply extrapolating these results would indicate that if $Ge^{4+}$ were present only in trace quantities, its coordination should be fully controlled by $Si^{4+}$, as would be the case in a mineral.

However, the glasses studied by Majérus et al. (2004) are very different to natural magmas. Unlike the fully polymerized $GeO_2$–$SiO_2$ system, natural magmas contain network-modifying cations such as $Ca^{2+}$ and $Mg^{2+}$, which introduce a lot more flexibility into the melt structure. Indeed, in the CMAS glasses studied in Chapter 2, a coordination change of $Ge^{4+}$ is observed at far lower pressures than would be expected for Si. In complex melts there are no defined "sites" on which trace elements must substitute, potentially allowing trace elements to change their coordination independently of the major elements.

Nevertheless, this does not preclude some control on trace element coordination by the melt structure, even if it is not in such a direct way as in minerals and fully polymerised glasses. The observation that both $Ge^{4+}$ and $Ga^{3+}$ rapidly increase their coordination number at the same pressure is unexpected if they are behaving entirely independently. While this could be coincidence, it could also result from a change of some kind in the melt structure that influences both Ge and Ga.

To investigate this, nuclear magnetic resonance (NMR) spectroscopy was used to study the local environments of all the major elements (Al, Si, Mg, Ca and O) in the same or similar samples that were studied in Chapter 2. Ga coordination was also investigated using NMR, to check that the variations in Ga XANES spectra with pressure were correctly interpreted as coordination changes.

In quenched melt samples, a rapid increase in $Al^{3+}$ average coordination number is found between 4 and 5 GPa, as was seen for $Ge^{4+}$ and $Ga^{3+}$. There is a striking correlation between $Ga^{3+}$ and $Al^{3+}$ coordination number, but the correlation between $Al^{3+}$ and $Ge^{4+}$ coordination is not as strong. This suggests that coordination changes of $Al^{3+}$ may be influencing those of the trace cations, and that the influence may be stronger on $Ga^{3+}$. This observation may have important consequences for trace element partition coefficients, if the phenomenon extends to other trace cations in addition to $Ge^{4+}$ and $Ga^{3+}$.

## 3.2 Methods

### *Sample synthesis*

Most of the annealed glass samples investigated in this study were the same samples synthesized for XANES in Chapter 2. Only two additional annealed glasses were made (for experimental details, refer to Chapter 2). These were MA1125 (10 GPa), which was made because the 10 GPa sample made in Chapter 2 did not yield enough material for NMR as well as XANES spectroscopy; and D2173 (4 GPa), which was made to test the effect of grinding the glass to a powder. This sample was extracted from the capsule, lightly ground in an agate mortar to form a powder, and then half of this powder was heavily ground for several more minutes. $^{27}Al$ spectra of the two batches were recorded to check for any differences.

New quenched melt samples were synthesized for this study, because the samples used for XANES spectroscopy had been previously embedded into epoxy. The CMAS7G composition was used, and most samples were doped with 3000 ppm $Ga_2O_3$. For the purpose of $^{71}Ga$ NMR, some samples were made with a higher concentration of Ga. One sample, C4798, was made by adding 3.4 wt % $Ga_2O_3$ to the CMAS7G mixture. Two further samples, B1-101215 and uhppc-342-333, were made using a CMAS7G composition in which half the moles of Al were replaced by Ga. This was done because Ga should have the same network-forming role as Al in the melt, and so by replacing Al with Ga, it was hoped that the polymerization of the melt would be unaffected. Starting mixes were made using reagent grade $SiO_2$, $Al_2O_3$, MgO, $CaCO_3$ and $Ga_2O_3$, which were mixed thoroughly under acetone and then fired as a pellet at 1050 °C in air to decarbonate. Nominal compositions in both weight and mole percent are given in Table 3.1.

Table 3.1. Nominal major element compositions of starting materials.

| | CMAS7G | | CMAS7G (3.4 wt % $Ga_2O_3$) | | CMAS7G (11 wt % $Ga_2O_3$) | |
|---|---|---|---|---|---|---|
| | wt % | mol % | wt % | mol % | wt % | mol % |
| $SiO_2$ | 59.60 | 61.07 | 57.78 | 60.44 | 56.79 | 61.15 |
| $Al_2O_3$ | 12.57 | 7.59 | 12.19 | 7.51 | 5.99 | 3.80 |
| MgO | 2.38 | 3.63 | 2.30 | 3.59 | 2.25 | 3.61 |
| CaO | 25.15 | 27.61 | 24.38 | 27.33 | 23.96 | 27.64 |
| $Ga_2O_3$ | 0.30 | 0.10 | 3.35 | 1.12 | 11.01 | 3.80 |
| NBO/T* | | 0.616 | | 0.574 | | 0.620 |

* NBO/T was calculated using the method described in Appendix 1 of Mills (1993). $Ga_2O_3$ was treated in the same way as $Al_2O_3$ for the calculation.

Two samples, D1679 and uhppc-269, were made enriched in $^{17}O$. To do this, a CMAS7G composition mix was made using 75% $^{17}O$-enriched $SiO_2$, $Mg(OH)_2$ and $Ca(OH)_2$, and natural abundance $Al_2O_3$. The $Mg(OH)_2$ and $Ca(OH)_2$ were assumed to be hydrated, and the mix was calculated by assuming $MgO+1.1H_2O$ and $CaO+1.1H_2O$. The mix was ground under acetone for 30 minutes, pressed into a pellet and fired in Ar at 1100°C for 1 h.

Ambient-pressure glasses were made by melting the starting material in graphite crucibles using a box furnace. High-pressure glasses were made in a piston cylinder apparatus. The starting material was packed into Pt capsules; no oxygen buffer was included in the capsules except for C4794, which had ~30 mg of a Ru–$RuO_2$ mixture (20% Ru, 80% $RuO_2$ by weight) at each end. For pressures 2.5 GPa and below, a 5 mm capsule was used in a standard 5/8" assembly composed of MgO, Pyrex, graphite and NaCl, all wrapped in Teflon foil. The 5/8" pressure vessels could not accommodate pressures > 2.5 GPa, so for higher pressures, a 3.5 mm capsule in a ½" assembly was used. To obtain sufficient material for NMR, two experiments were run at each pressure above 2.5 GPa and the resulting samples were combined. Of the two 5 GPa experiments were carried out, the first one (uhppc-269) was made using the $^{17}O$ enriched composition. After the $^{17}O$ spectra were recorded, this sample was then combined with the second 5 GPa sample, uhppc-314, which was not enriched in $^{17}O$. Sample uhppc-314 quenched after ten minutes due to a failure in the apparatus, but at 1650 °C this time should be sufficient to have equilibrated the high-pressure melt structure. A small glass chip was reserved from most samples and mounted in epoxy; the remaining sample was crushed to a powder for NMR.

Table 3.2. List of samples and their experimental conditions.

| Sample | P (GPa) | T (°C) | Time (h) | Composition |
|---|---|---|---|---|
| | | **Quenched melts** | | |
| B3-180615 | 1 atm | 1300 | 15 min | CMAS7G |
| B3-301915 | 1 atm | 1300 | 25 min | CMAS7G |
| C4901 | 0.6 | 1500 | 1 h | CMAS7G |
| C4799 | 1.0 | 1600 | 1 h | CMAS7G |
| D1679 | 1.0 | 1650 | 1 h | $^{17}$O-enriched CMAS7G |
| C4794 | 1.05 | 1600 | 30 min | CMAS7G |
| C4900 | 2.0 | 1600 | 1 h | CMAS7G |
| C4896 | 2.5 | 1600 | 1 h | CMAS7G |
| C4904-C4905 | 3.0 | 1600 | 1 h | CMAS7G |
| D1840-D1842 | 3.5 | 1650 | 30 min | CMAS7G |
| C4878-C4879 | 4.0 | 1650 | 30 min | CMAS7G |
| C4892-C4942 | 4.5 | 1650 | 30 min | CMAS7G |
| uhppc-269 | 5.0 | 1650 | 6 h | $^{17}$O-enriched CMAS7G |
| uhppc-269-314 | 5.0 | 1650 | 6 h / 10 min* | CMAS7G |
| | | **Ga-enriched quenched melts** | | |
| C4798 | 1.0 | 1600 | 1 h | CMAS7G (3.4 wt% $Ga_2O_3$) |
| B1-101215 | 1 atm | 1300 | 20 min | CMAS7G (11 wt% $Ga_2O_3$) |
| uhppc-342-333 | 5.0 | 1650 | 1 h | CMAS7G (11 wt% $Ga_2O_3$) |
| | | **Annealed glasses** | | |
| C5232 † | 2.0 | 600 | 1 h | CMAS7G |
| C5231 † | 3.0 | 600 | 1 h | CMAS7G |
| C5228 † | 4.0 | 600 | 1 h | CMAS7G |
| D2210 † | 1.0 | 730 | 2 h | CMAS7G |
| D2212 † | 1.5 | 730 | 2 h | CMAS7G |
| D2208 † | 2.0 | 700 | 2 h | CMAS7G |
| D2209 † | 2.5 | 730 | 2 h | CMAS7G |
| C5199 † | 3.0 | 780 | 2 h | CMAS7G |
| D2125 † | 3.5 | 780 | 2 h | CMAS7G |
| D2213 † | 3.5 | 730 | 2 h | CMAS7G |
| D2189 † | 3.5 | 765 | 2 h | CMAS7G |
| D2207 † | 4.0 | 700 | 15 h | CMAS7G |
| D2173** | 4.0 | 780 | 2 h | CMAS7G |
| MA1125 | 10.0 | 780 | 2 h | CMAS7G |

† Samples prepared for an earlier study (Chapter 2). *The two times listed reflect the different run durations of two experiments that were combined to make this uhppc-269-314. **Sample D2173 was divided into two portions; one of which was heavily ground and the other was lightly ground.

### *$^{17}$O enrichment*

Four of the quenched melt samples (B3-300915, C4798, C4900, C4904-C4905) were enriched in $^{17}$O after they were synthesized, following an approach that has been previously used for $^{17}$O enrichment of ceramic materials (Fernandes et al.

2018). Samples were placed into a glass vial, which was evacuated and cooled in liquid nitrogen. 70% $^{17}$O-enriched $O_2$ gas was introduced into the vial, and, due to the cold temperature, condensed inside the vial. The vial was then sealed, allowed to come to room temperature, and then placed in a horizontal furnace. The temperature was ramped at 5 °C/min to a dwell temperature of 700 °C. Samples were held at 700 °C for 48 h before cooling at 5 °C/min. In the heating processes, the $^{17}$O that had condensed in the vial exchanged with the O atoms in the sample, leading to $^{17}$O enrichment.

### *Sample characterization*

Many of the annealed glass samples contained a small fraction of crystals, which were observed optically and shown by EDS to be corundum ($Al_2O_3$), as described in Chapter 2. Most of the quenched melt samples synthesized in this study were checked for the presence of crystals in two ways: (1) by inspecting the backscattered electron (BSE) image of reserved glass chips on a Hitachi S-4300 SE/N Field Emission Scanning Electron Microscope (FE-SEM), and (2) by collecting X-ray diffraction patterns of the powdered glasses using a STOE Transmission Powder Diffractometer System STADI P with a Co tube, operating at 40 kV and 30 mA. No evidence for crystals was found in these samples.

Compositions of several of the CMAS7G glass chips were analysed using the FE-SEM with an Oxford X-Max EDS detector, to confirm that the compositions was similar to that of the starting material. The compositions of the glasses made with 11 wt% $Ga_2O_3$ were also measured, however, no glass chip was reserved from the 2.5 wt% $Ga_2O_3$ glass. The beam conditions used for EDS analysis were 15 kV accelerating voltage, 0.600 nA and the working distance was 25 mm. A PAP matrix correction was used. Standards used to calibrate element concentrations were albite for Na and Al, MgO for Mg, sanidine for Si, diopside for Ca and gallium arsenide for Ga. 3

### *NMR spectroscopy*

NMR spectroscopy experiments were performed on Bruker Avance III spectrometers equipped with widebore superconducting magnets at the University of St Andrews, UK (9.4 T and 14.1 T) or the UK 850 MHz Solid State NMR facility, Warwick UK (20.0 T). Powdered glass samples were packed into $ZrO_2$ rotors and rotated at the magic angle.

$^{27}$Al MAS NMR spectra for quenched melt samples were acquired at 9.4 and 14.1 T (at Larmor frequencies of 104.26 and 156.41 MHz, respectively) by rotating samples at rates of 12 or 20 kHz in 4 mm or 3.2 mm rotors, respectively. Spectra for annealed glass samples were acquired by spinning samples at a rate of 40 kHz in a 1.9 mm rotor. A short flip angle (~18°) was used with a relaxation interval of at least 2 s. A longer relaxation interval of 5 s was used for most of the annealed glass samples due to the presence of a crystalline component in some samples. Obtaining quantitative proportions of different coordination environments is not possible if relaxation intervals are not long enough (Edén 2015). Two-dimensional $^{27}$Al MQMAS spectra were acquired using a triple-quantum z-filtered pulse sequence and a relaxation interval of 1 s. Spectra were referenced to aluminium acetylacetonate ($\delta_{iso} = 0.0$ ppm, $C_Q = 3.0$ MHz, $\eta_Q = 0.15$) as a secondary reference relative to 1.0 M aqueous solution of $Al(NO_3)_3$ ($\delta_{iso} = 0$ ppm). The triple-quantum excitation and conversion were performed under high power; single quantum coherence was produced with a low power pulse. The $F_1$ spectral width was matched to the spinning speed. The two-dimensional spectra are presented as sheared spectra, plotted as contours with 32 levels at an increment of 1.2.

$^{29}$Si MAS NMR spectra were acquired at 9.4 T (at a Larmor frequency of 79.49 MHz) by rotating samples at a rate of 14 kHz in 4 mm rotors using a conventional HFXY probe. Spectra were acquired using a flip angle of 45° and 120 s relaxation interval. Initial spectra acquired using a HX probe showed signal resulting from probe background. The background signal on the HFXY probe was investigated by acquiring a spectrum with a rotor filled with NaCl (s) rotating at a rate of 14 kHz. No signal was observed after the averaging of 496 transients, so spectra of all samples were acquired again using the HFXY probe. Three spectra were also acquired at 14.1 T (at a Larmor frequency of 119.24 MHz) by rotating samples in 4 mm rotors in a HXY probe. A 90° flip angle was used with a relaxation interval of 120–240 s. Experimental shifts are reported relative to tetramethyl silane (TMS ) ($\delta_{iso} = 0$ ppm) using Octakis(trimethylsiloxy)silsesquioxane, (Q8M8) ($\delta_{iso} = 11.4$ ppm) as a secondary reference.

$^{27}$Al–$^{29}$Si correlation spectra were acquired at 14.1 T (at Larmor frequencies of 156.40 MHz for $^{27}$Al and 119.25 MHz for $^{29}$Si) using a D-HMQC correlation experiment (Gan 2007; Tricot et al. 2011; Tricot et al. 2014) and pulse lengths of 1.5 μs and 4 μs or 3 μs for $^{27}$Al and $^{29}$Si, respectively, 6.8 ms $SR4_1^2$ dipolar recoupling scheme prior to $t_1$, 28 $t_1$ increments, a rotor synchronised $t_1$ increment delay of 35.7 μs and a relaxation interval of 1 s. Samples were rotated at 14 or 28 kHz in a 4 mm or 1.9 mm rotor in HXY probes. Spectra were referenced as described above.

$^{25}$Mg MAS NMR spectra were acquired at 9.4, 14.1 and 20.0 T (at Larmor frequencies of 24.48, 36.75 and 52.04 MHz, respectively). Initial spectra acquired at 14.1 T in a 4 mm low-γ probe overlapped almost completely with a significant probe background, observed by acquiring a spectrum with a rotor packed with NaCl (s), so spectra were acquired again at 9.4 and 20.0 T using a 4 mm HX low-γ probe with samples rotated at a rate of 14 kHz. Spectra were acquired using a CPMG pulse sequence (Meiboom and Gill 1958) for signal enhancement. The number of echoes acquired and spikelet spacing differed between spectra and is listed in the figure captions. Spectra were referenced to MgO ($\delta_{iso}$ = 25 ppm, $C_Q$ = 0 MHz) as a secondary reference with respect to 1 M $MgCl_2$ ($\delta_{iso}$ = 0 ppm).

$^{43}$Ca MAS NMR spectra were acquired at 20.0 T (at a Larmor frequency of 57.22 MHz) by rotating the sample at 14 kHz in a 4 mm HX low-γ probe. A double frequency sweep (DFS) enhancement was added before the CT selective 90° pulse and a relaxation interval of 1 s was used between each transient. Spectra were referenced to a $CaCl_2$ saturated solution ($\delta_{iso}$ = 0 ppm).

$^{71}$Ga MAS NMR spectra were acquired at 14.1 T and 20.0 T (at Larmor frequencies of 183.05 and 259.36 MHz, respectively) by rotating the sample at a rate of 60 kHz in a 1.3 mm HX probe. Spectra were acquired using a CPMG pulse sequence, with a hyperbolic secant (HS) pulse added before the echo train to further improve the signal-to-noise ratio. Number of echoes acquired and spikelet spacing is listed in the figure captions. Relaxation intervals used were 3 s at 20.0 T and 2 s at 14.1 T. Spectra were referenced to $GaPO_4$ ($\delta_{iso}$ = 111 ppm, $C_Q$ = 8.8 MHz, $\eta_Q$ = 0.5) as a secondary reference with respect to $Ga(NO_3)_3$ ($\delta_{iso}$ = 0 ppm).

$^{17}$O MAS NMR spectra were acquired at 14.1 T and 9.4 T (at Larmor frequencies of 81.34 MHz and 54.24 MHz, respectively) using 3.2 mm or 4 mm HX probes by rotating samples at rates of 20 kHz or 14 kHz. A relaxation interval of 5 s was used at both fields and spectra were acquired with either CT selective 90° or short flip angle single pulse or spin echo pulse sequence (CT selective 90° and 180°). A HS pulse was added prior to the spin echo pulse sequence for signal enhancement of gas-enriched samples. Spectra were referenced with respect to (natural abundance) distilled water ($\delta_{iso}$ = 0 ppm). $^{17}$O multiple MQMAS experiments were performed using a z-filtered pulse sequence. As for $^{27}$Al, the triple-quantum excitation and conversion were performed under high power, single quantum coherence was produced with a low power pulse, and the $F_1$ spectral width was matched to the spinning speed. Spectra presented in figures are sheared.

$^{27}$Al, $^{25}$Mg and $^{71}$Ga lineshapes were fitted using the software DMFIT (Massiot et al. 2002) using the 'CzSimple' fitting function, which is based on the Czjzek distribution function (Czjzek et al. 1981). For the $^{25}$Al spectra, MQMAS spectra were fit initially to obtain $C_Q$ (the quadrupolar coupling constant) and dCSA (chemical shift anisotropy) parameters. These parameters were then used to fit the 1D spectra, by adjusting the relative intensities of the peaks, with only minor adjustments to $C_Q$ and dCSA to get a good fit. This procedure was necessary to obtain quantitative proportions of the different coordination environments.

$^{29}$Si spectra were fitted using a program written in Julia (Bezanson et al. 2017), which performed a fit to all spectra simultaneously using three Gaussian peaks.

## 3.3 Results

### *Sample characterisation*

The average composition of the high-pressure CMAS7G quenched melt samples is given in Table 3.3, along with the composition of Ga-enriched samples B1-101215 and uhppc-342-333. Compositions deviated slightly from the nominal composition of the starting material; NBO/T values have been calculated for the actual compositions. The low analytical totals in the CMAS7G samples may indicate the presence of dissolved volatiles.

B1-101215 only retained ~6 wt% $Ga_2O_3$ from a nominal starting composition of 11 wt %. This is probably due to Ga loss during synthesis, since the sample was made in a graphite crucible; the graphite could locally impose a low $fO_2$ on the sample, increasing the volatility of Ga.

Table 3.3. Compositions of glass samples from EDS analysis.

| | Average CMAS7G | | B1-101215 | | uhppc-342-333 | |
|---|---|---|---|---|---|---|
| | wt % (*n*=9) | mol % | wt % (*n*=2) | mol % | wt % (*n*=4) | mol % |
| $SiO_2$ | 57.68 (63) | 62.36 (68) | 60.15 (65) | 63.77 (69) | 59.81 (25) | 63.18 (26) |
| $Al_2O_3$ | 11.78 (10) | 7.51 (6) | 6.49 (9) | 4.06 (6) | 6.50 (17) | 4.05 (11) |
| MgO | 2.29 (18) | 3.70 (29) | 2.16 (5) | 3.41 (8) | 2.26 (7) | 3.55 (12) |
| CaO | 22.82 (58) | 26.43 (67) | 23.33 (3) | 26.50 (3) | 22.66 (20) | 25.64 (23) |
| $Ga_2O_3$ | n.d. | – | 6.67 (34) | 2.27 (11) | 10.56 (34) | 3.57 (12) |
| Total | 94.6 (11) | – | 98.8 (4) | – | 101.8 (7) | – |
| NBO/T* | | 0.585 (20) | | 0.617 (7) | | 0.550 (8) |

* NBO/T was calculated using the method described in Appendix 1 of Mills (1993). $Ga_2O_3$ was treated in the same way as $Al_2O_3$ for the calculation. Numbers in parentheses are one standard deviation on the last digit, and *n* refers to the number of analyses.

### *Aluminium-27*

$^{27}$Al NMR has been used extensively in the literature to determine proportions of four-, five- and six-fold coordinated Al environments in glasses quenched from high-pressure melts (Yarger et al. 1995; Allwardt et al. 2005c; Allwardt et al. 2007; Kelsey et al. 2009; Bista et al. 2015; Morizet et al. 2015). Each coordination environment gives rise to a distinct peak in the spectrum with an isotropic chemical shift of approximately 60, 25 and 0 ppm for $^{[4]}$Al, $^{[5]}$Al and $^{[6]}$Al respectively. Note that for quadrupolar nuclei the resonance position is the sum of the isotropic chemical shift and a quadrupolar shift and $\delta_{iso}$ cannot necessarily be determined from the MAS lineshape alone. However, spectral acquisition at multiple fields or the acquisition of two-dimensional MQMAS spectra can provide accurate measurement of $\delta_{iso}$.

The spectra obtained for samples in this study show three resolved peaks which can attributed to $^{[4]}$Al, $^{[5]}$Al and $^{[6]}$Al in order of decreasing shift, with the proportions varying as a function of pressure. Figure 3.1A shows the $^{27}$Al NMR spectrum of selected samples of different pressures. The ambient pressure sample contains only $^{[4]}$Al, but the higher pressure samples also show peaks corresponding to $^{[5]}$Al and $^{[6]}$Al. The three peaks corresponding to $^{[4]}$Al, $^{[5]}$Al and $^{[6]}$Al can also be clearly resolved in two-dimensional MQMAS NMR spectra, and spectra of three samples of low, medium and high pressures are shown in Figure 3.1B.

Spectra of the two batches (lightly ground and heavily ground) of D2173 look very similar (Figure 3.2) apart from a slight narrowing of the [5]Al peak in the heavily ground sample. This indicates that grinding the samples to a fine powder did not cause any substantial relaxation of the high-pressure structure.

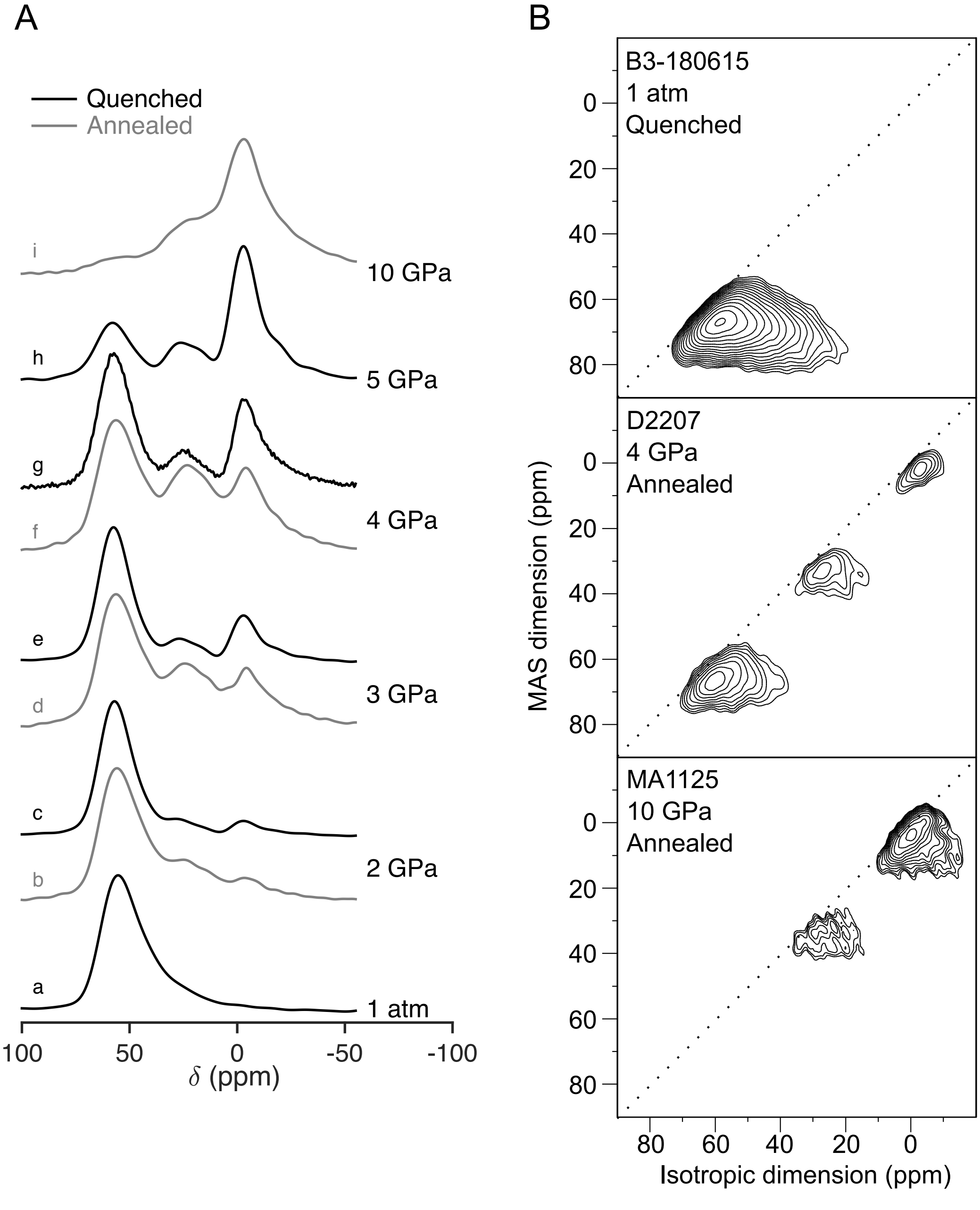

Figure 3.1. (A) $^{27}$Al MAS NMR spectra (14.1 T) of selected samples: (a) B3-180615, (b) D2208, (c) C4900, (d) C5199, (e) C4904-C4905, (f) D2207, (g) C4878-C4879, (h) uhppc269-314, (i) MA1125. All spectra have been normalised to the same maximum height. (B) $^{27}$Al MQMAS NMR spectra (14.1 T) of selected glass samples.

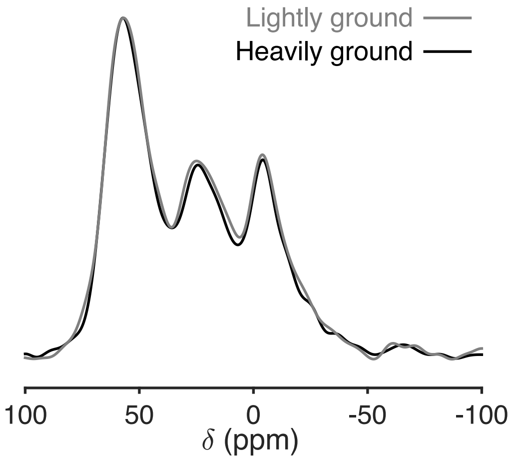

Figure 3.2. $^{27}$Al MAS NMR spectra of D2173 (14.1 T). The two spectra are for two batches of this sample, which were lightly and heavily ground. Spectra are normalised to the same maximum height.

The spectra of some of the annealed glass samples also contained a sharp peak at around 10–20 ppm. In the MAS spectra, this sharp peak overlaps with the $^{[5]}$Al peak (Figure 3.3A), but it can be resolved completely in the corresponding MQMAS spectra (Figure 3.3B). This sharp peak likely represents the small amount of corundum ($Al_2O_3$) that was observed in many of the annealed glass samples. The isotropic chemical shift of corundum reported in the literature is $16.0 \pm 0.2$ (Jakobsen et al. 1989). A similar sharp peak overlapping partly with the $^{[5]}$Al peak was observed in synthetic basaltic glasses by Morizet et al. (2015), who also attributed this peak to corundum. A $^{29}$Si–$^{27}$Al correlation experiment revealed no correlation between the $^{29}$Si spectrum and the sharp peak in the $^{27}$Al spectrum, indicating that the sharp peak represents an alumina phase.

$^{27}$Al spectra of Ga-enriched samples (B1-101215 and uhppc-342-333) were also acquired for comparison to the samples with trace levels of Ga. At ambient pressure, the spectrum of B1-101215 (Ga-enriched) looks the same as that of B3-180615 (0.3 wt % $Ga_2O_3$), containing only $^{[4]}$Al. However, at higher pressures, the Ga-enriched sample contains less $^{[5,6]}$Al than the 0.3 wt% $Ga_2O_3$ sample, as shown in Figure 3.4. The presence of only $^{[4]}$Al in the 1 atm sample, but all three coordination environments in the high-pressure sample is confirmed by MQMAS spectra (Figure 3.5).

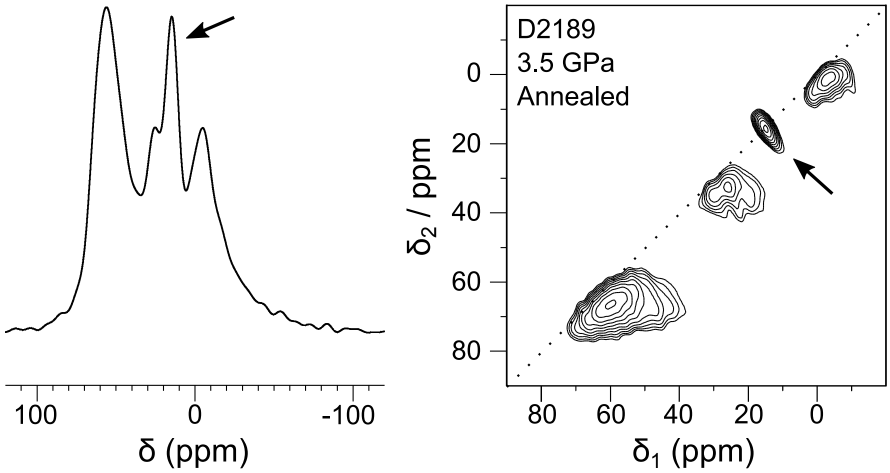

Figure 3.3. $^{27}$Al MAS and MQMAS NMR spectra (14.1 T) for a sample containing a sharp peak with no quadrupolar coupling.

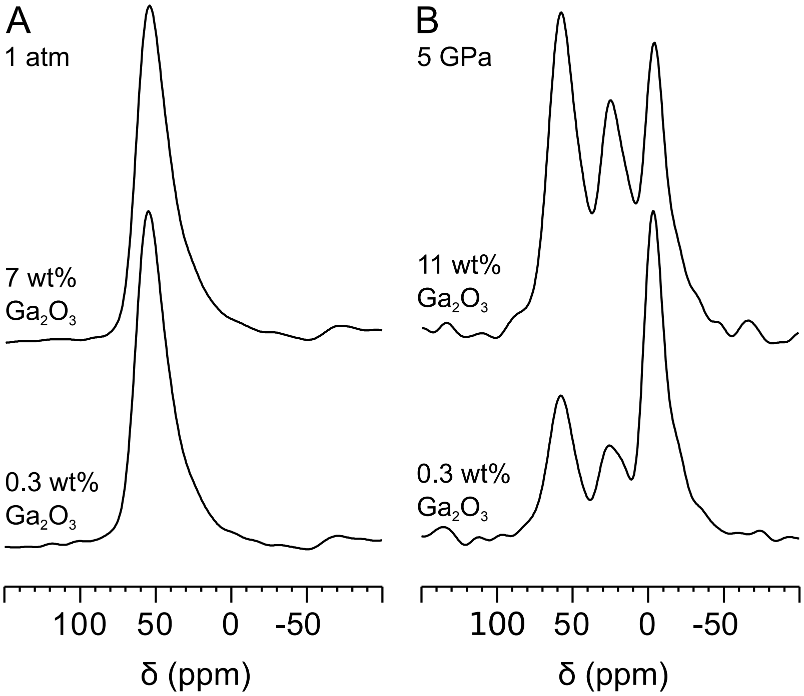

Figure 3.4. $^{27}$Al MAS NMR spectra (14.1 T) of glasses containing different Ga concentrations, made at (A) 1 atm pressure, B3-180615 (0.3 wt% $Ga_2O_3$) and B1-101215 (7 wt% $Ga_2O_3$), and (B) 5 GPa, uhppc269-314 (0.3 wt% $Ga_2O_3$) and uhppc342-333 (11 wt% $Ga_2O_3$).

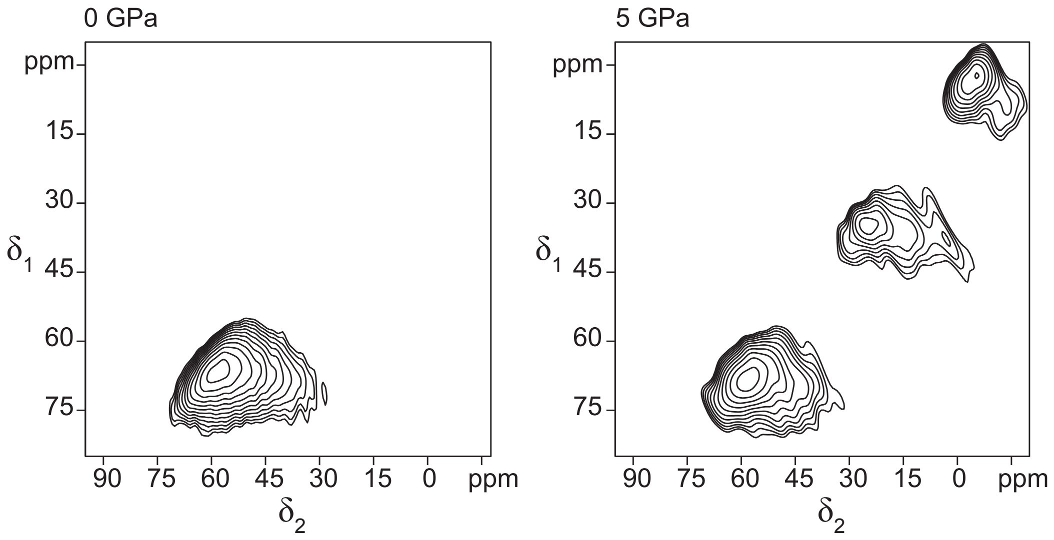

Figure 3.5. $^{27}$Al MQMAS NMR spectra (14.1 T) of samples with 11 wt% Ga: (left) B1-101215, 1 GPa and (right) uhppc-342-333, 5 GPa.

All spectra were fit using a Czjzeck distribution to model the quadrupolar parameters (and a Gaussian distribution of isotropic chemical shift) to determine proportions of four-, five- and six-fold coordinated Al sites. The sharp peak from corundum was also included in the fit so that it would not interfere with the results from the glassy environments. An example of a fitted spectrum is given in Figure 3.6.

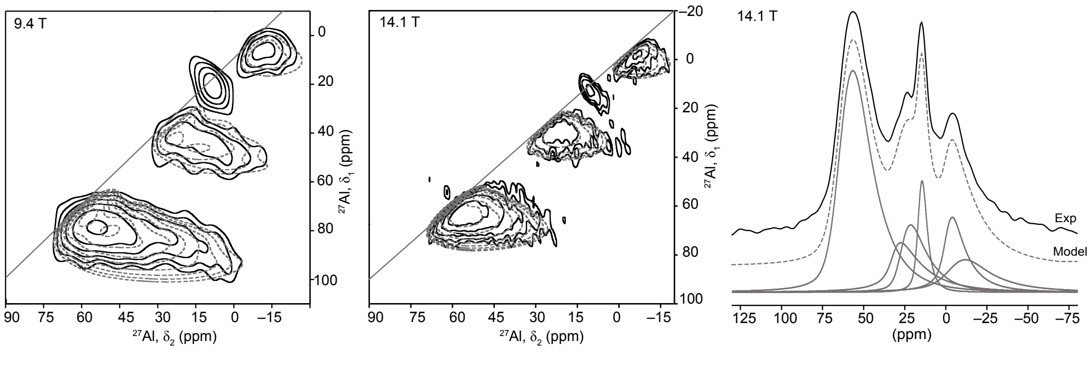

Figure 3.6. Fits to the spectrum of D2213 (glass annealed at 3.5 GPa). (Left, middle panels): MQMAS spectra (solid lines) at two fields (9.4 T and 14.1 T), with fits to the spectra shown as dashed lines. (Right panel): 1D MAS spectrum recorded at 14.1 T (solid black line), with fit (dashed line) and fit components (solid grey lines).

Fits were performed for both MAS and MQMAS spectra, and for two fields when the data was available. Multiple lines were used in fitting some of the $^{[5]}$Al and $^{[6]}$Al peaks in the spectra, in order to produce a good fit. What these multiple contributions represent physically is uncertain (see Discussion). Table 3.4 shows the results of several fits to C4900 and MA1125. Fits to C4900 were performed using three lines and both 9.4 and 14.1 T, and an additional fit using five lines at 14.1 T. Three lines were used to fit to MA1125 at both fields. The results are similar between all fits; the largest difference is 7% between the $AlO_5$ contributions obtained in the fits to MA1125. The largest difference in the average coordination number obtained is 0.09 between the fits to C4900 at two fields. The most accurate results should come from the spectra collected using 14.1 T, and as many lines as were needed to obtain a good fit; the results from these fits are given in Table 3.5 for each sample. Full fit parameters are listed in the supplementary material (section 7.5, p.207).

Table 3.4. Results of the fits to 1D MAS spectra at different magnetic field strengths.

| Sample / Field | % $AlO_4$ | % $AlO_5$ | % $AlO_6$ | Average CN |
|---|---|---|---|---|
| C4900 / 9.4 T (3 lines) | 83.4 | 4.3 | 12.4 | 4.30 |
| C4900 / 14.1 T (3 lines) | 86.4 | 6.3 | 7.3 | 4.21 |
| C4900 / 14.1 T (5 lines) | 87.4 | 6.0 | 7.0 | 4.22 |
| MA1125 / 9.4 T (3 lines) | 3.6 | 67.7 | 28.7 | 5.25 |
| MA1125 / 14.1 T (3 lines) | 7.0 | 60.9 | 32.1 | 5.25 |

The relative proportions of the four-, five- and six-fold coordinated Al environments vary with pressure, as shown in Figure 3.7. The proportion of $^{[4]}$Al decreases, while those for the $^{[5]}$Al and $^{[6]}$Al sites systematically increase with pressure. The annealed glasses for the most part contain more $^{[5]}$Al, but less $^{[4]}$Al and $^{[6]}$Al, than the quenched melts, such that the average Al coordination number for both annealed glasses and quenched melts are similar. The average coordination number increases with pressure differently for quenched melts and annealed glasses, as shown in Figure 3.8.

The errors on the data points plotted in Figure 3.7 and Figure 3.8 cannot be quantified. However, an estimate can be made from the differences in results between fits to spectra collected at different fields (Table 3.4). As described earlier, the largest difference in the percentage of an $AlO_x$ species was 7%, and for the average coordination number, a difference of 0.09. Therefore, one could imagine error bars of ± 5% on each data point in Figure 3.7, and 0.1 on each data point in Figure 3.8 (error bars are not plotted because the true errors may be larger or smaller than these estimates). However, the trends observed in these data are so strong that adding these error bars would not affect the interpretations of this study.

Table 3.5. Al coordination numbers derived from fits to the spectra collected at 14.1 T.

| Sample | P (GPa) | T (ºC) | % $AlO_4$ | % $AlO_5$ | % $AlO_6$ | Average |
|---|---|---|---|---|---|---|
| | | | **Quenched melts** | | | |
| B3-180615 | 1 atm | 1300 | 100 | 0 | 0 | 4.00 |
| C4794 | 1.0 | 1650 | 93 | 3 | 4 | 4.11 |
| C4900 | 2.0 | 1600 | 87 | 6 | 7 | 4.22 |
| C4896 | 2.5 | 1600 | 78 | 12 | 10 | 4.32 |
| C4904-C4905 | 3.0 | 1600 | 69 | 10 | 21 | 4.51 |
| D1840-D1842 | 3.5 | 1650 | 62 | 12 | 26 | 4.63 |
| C4878-C4879 | 4.0 | 1650 | 56 | 19 | 25 | 4.69 |
| C4892-C4924 | 4.5 | 1650 | 42 | 15 | 43 | 5.01 |
| uhppc-269-341 | 5.0 | 1650 | 27 | 16 | 57 | 5.31 |
| | | | **Annealed glasses** | | | |
| C5232 | 2.0 | 600 | 81 | 11 | 7 | 4.26 |
| C5231 | 3.0 | 600 | 72 | 18 | 10 | 4.38 |
| C5228 | 4.0 | 600 | 68 | 21 | 11 | 4.44 |
| D2210 | 1.0 | 730 | 89 | 8 | 3 | 4.14 |
| D2212 | 1.5 | 730 | 84 | 13 | 4 | 4.20 |
| D2208 | 2.0 | 700 | 76 | 16 | 8 | 4.32 |
| D2209 | 2.5 | 730 | 71 | 18 | 11 | 4.40 |
| C5199 | 3.0 | 780 | 58 | 23 | 19 | 4.61 |
| D2125 | 3.5 | 780 | 49 | 29 | 22 | 4.72 |
| D2213 | 3.5 | 730 | 52 | 25 | 23 | 4.71 |
| D2189 | 3.5 | 765 | 48 | 25 | 27 | 4.79 |
| D2207 | 4.0 | 700 | 44 | 38 | 19 | 4.75 |
| D2173 | 4.0 | 780 | 52 | 33 | 15 | 4.62 |
| MA1125 | 10 | 780 | 7 | 61 | 32 | 5.25 |

For annealed glasses that contained a corundum peak, the percentages of each site were renormalised so that they added to 100%.

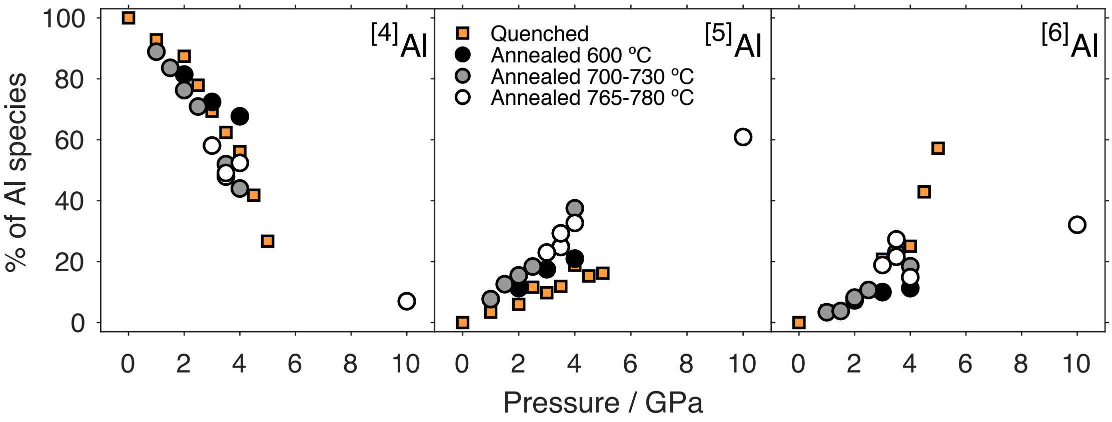

Figure 3.7. Plots showing how the percentage of each Al species varies with pressure.

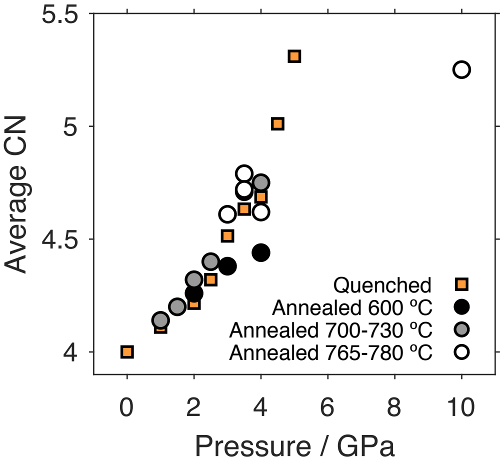

Figure 3.8. Average Al coordination number (CN) as a function of pressure.

The average coordination number of Al is the best form for comparison to the Ge and Ga XANES data, because XANES spectra reflect an average of all coordination environments in the samples. The average coordination numbers of Ge, Ga and Al all increase quite rapidly in the quenched melt samples between 4 and 5 GPa. To assess whether Al coordination changes might be affecting those of the trace elements Ge and Ga, the results from XANES for Ge and Ga are plotted for comparison with the Al coordination number in Figure 3.9. The trends observed with pressure are quite similar for the three elements. To assess how similar, the coordination of Ge vs. Al and Ga vs. Al is plotted in Figure 3.10. A strong correlation is observed between Ga and Al, whereas the correlation between Ge and Al is not as good.

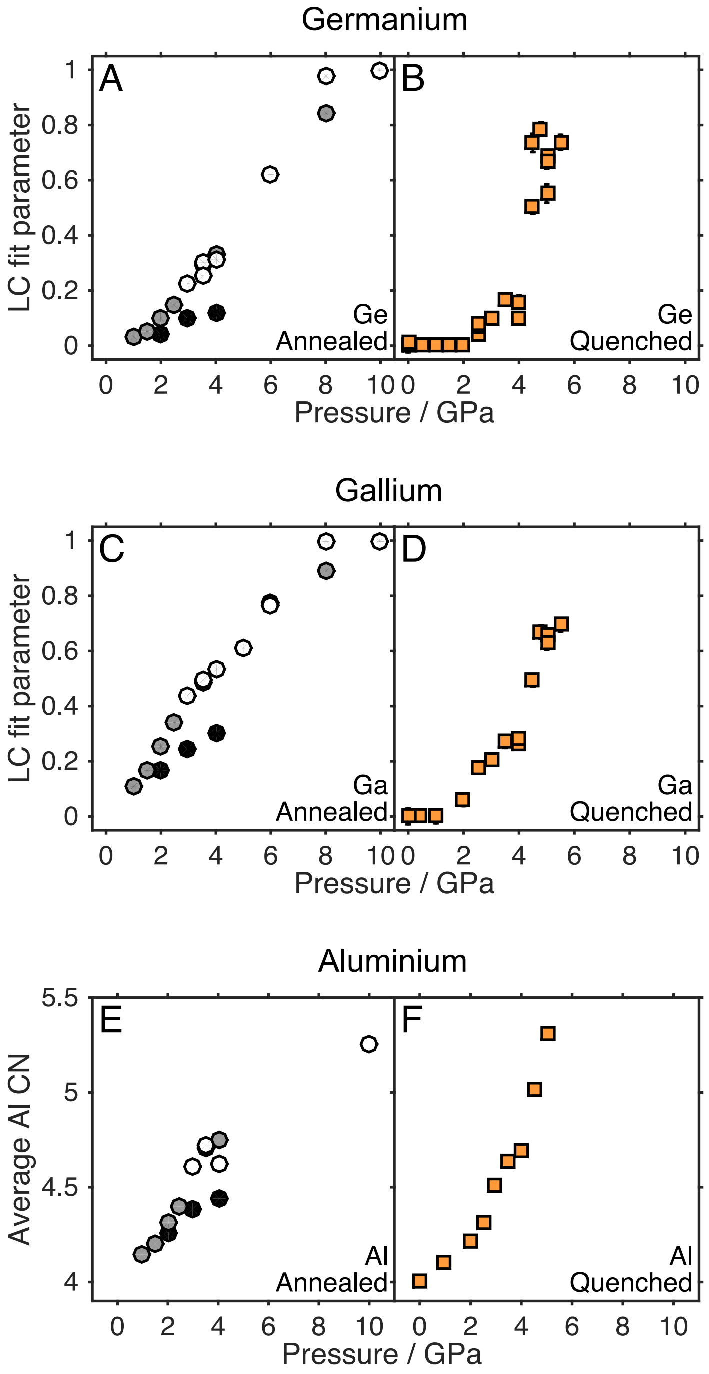

Figure 3.9. Comparison of Ge, Ga and Al coordination changes as a function of pressure in the composition CMAS7G. Symbols are the same as in Figure 3.7.

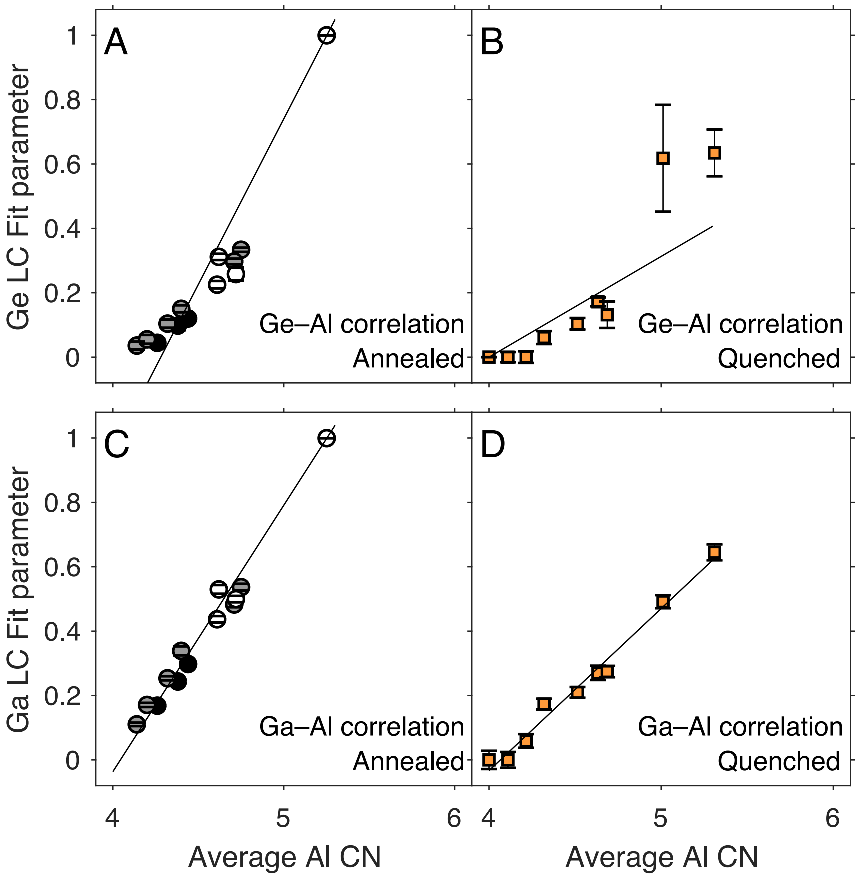

Figure 3.10. Relationship between Ge (A and B) and Ga (C and D) and Al coordination changes. Ge and Ga linear combination (LC) fit parameters are plotted on the vertical axis; these values are from LC fits between the lowest and highest pressure Ge or Ga spectra (see Chapter 2). The values on the vertical axis are relative only; they cannot be directly tied to a particular average coordination number (i.e., the maximum value of 1 reflects the average coordination number of the highest-pressure sample, which is probably different for Ge and Ga, and cannot be quantified). The average Al coordination number, which is quantified, is on the horizontal axis.

### *Silicon-29*

$^{29}$Si spectra collected at 9.4 T are presented in Figure 3.11A. A single broad peak is observed at all pressures investigated. The shape of the peak and the presence or absence of shoulders varies, but these variations are not systematic with pressure. The 4.5 and 5 GPa samples appear to be shifted by a few ppm to higher chemical shift compared with the lower-pressure samples.

Four spectra collected at 14.1 T are presented in Figure 3.11B. The spectrum of the 10 GPa sample, MA1125, is a projection of a $^{27}$Al–$^{29}$Si D-HMQC correlation spectrum. This spectrum is significantly narrower and centred at less negative chemical shift. However, because it is from a correlation spectrum, it shows only Si near Al, so it cannot be directly compared. A MAS NMR spectrum of this sample has not been acquired.

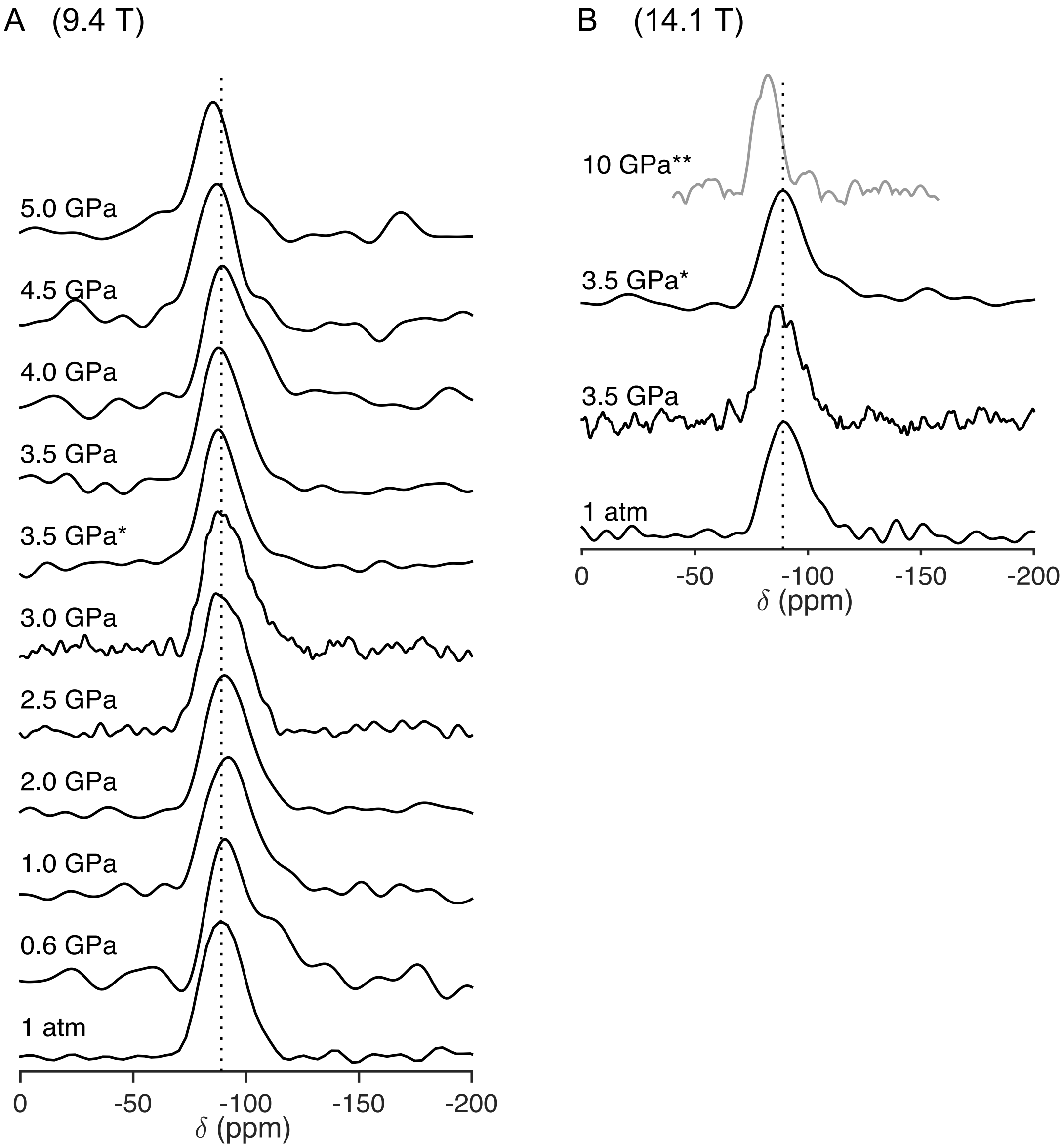

Figure 3.11. $^{29}$Si MAS NMR spectra recorded at (A) 9.4 T and (B) 14.1 T of samples made at pressures indicated. *3.5 GPa sample marked with * is an annealed glass sample (D2125). **10 GPa sample plotted in grey (MA1125) is a projection of a $^{27}$Al-$^{29}$Si D-HMQC correlation experiment. The dotted line plotted at –89 ppm is a guide to the eye.

To better assess whether the spectral features correlate with pressure, three parameters were determined: the position of the peak maximum, the position of the centroid, and the half width at half maximum. These are tabulated in Table 3.6 and plotted against pressure in Figure 3.12. All correlate to some extent with pressure, but with some scatter.

Fitting the $^{29}$Si data was challenging because of the low signal-to-noise ratio in the spectra and the lack of clear, systematic shoulders on the peaks. A principle component analysis indicated that three components would describe 95% of the variation in the set of eleven spectra (collected at 9.4 T), and so three Gaussian peaks were used in fitting. All eleven spectra were fit at once in an effort to identify common components in the spectra.

Table 3.6. Positions, centroids and half widths of $^{29}$Si peaks.

| Sample | P (GPa) | Field | Position | Centroid | Half width |
|---|---|---|---|---|---|
| B3-180615 | 1 atm | 9.4 T | -89.1 | -90.0 | 11.4 |
| | | 14.1 T | -89.2 | -90.9 | 10.6 |
| C4901 | 0.6 | 9.4 T | -90.7 | -94.7 | 12.8 |
| C4799 | 1 | 9.4 T | -92.1 | -93.6 | 12.7 |
| C4900 | 2 | 9.4 T | -90.5 | -92.7 | 12.0 |
| C4896 | 2.5 | 9.4 T | -86.7 | -90.4 | 12.0 |
| C4904-C4905 | 3 | 9.4 T | -87.5 | -91.9 | 11.7 |
| D2125 | 3.5 | 9.4 T | -87.7 | -89.7 | 9.8 |
| | | 14.1 T | -89.0 | -92.6 | 10.9 |
| D1840-D1842 | 3.5 | 9.4 T | -87.9 | -89.1 | 11.1 |
| | | 14.1 T | -86.7 | -87.6 | 9.8 |
| C4878-C4879 | 4 | 9.4 T | -89.5 | -93.2 | 13.0 |
| C4892-C4924 | 4.5 | 9.4 T | -87.1 | -86.6 | 10.7 |
| uhppc-269-314 | 5 | 9.4 T | -85.5 | -84.2 | 9.9 |

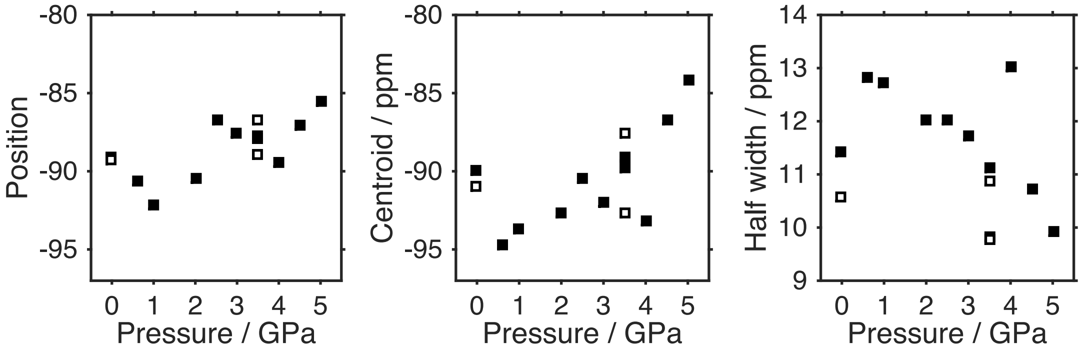

Figure 3.12. Features of the Si NMR peak (position, centroid and half width) plotted against pressure. Closed symbols are for spectra collected at 9.4 T, open symbols are for spectra collected at 14.1 T.

A least-squares fitting algorithm was used that allowed constraints on the fit parameters, which were width, height and position of the three peaks. The width of each peak was constrained to be the same for all samples. The starting ‘guess’ for the width was 10 ppm, and this was allowed to vary, but a penalty was imposed on the model if it varied more than ± 3 ppm. Initial guesses for the positions of the three peaks were –80, –91 and –109 ppm, based on literature values for approximate chemical shifts of $Q^2$, $Q^3$ and $Q^4$ species (Smith et al. 1983), although the peaks may not in fact represent these species, as will be discussed. Pressure could affect the chemical shifts of the peaks due to changing bond angles, and therefore the position of each peak was not constrained to be the same between samples. A penalty was imposed on the model if the positions varied by more than ± 5 ppm for Peak 1 and Peak 2 and ± 3 ppm for Peak 3. When that penalty was removed and the initial guess was changed, the model still converged on peaks at approximately the same positions. The height of each peak was constrained only to be non-negative.

To assess the error on the fitted parameters, a bootstrap method was used. This involved randomly resampling the data and repeating the least-squares fit 1000 times. A mean value and standard deviation could then be determined for each fit parameter; these are reported in Table 3.7. Standard deviations on the fit parameters are very small relative to the true error on the fits from the noise in the spectra, which has not been quantified. Fit parameters are plotted against pressure in Figure 3.13, and fits and their components are plotted in Figure 3.14.

Table 3.7. Mean fit parameters for fits to $^{29}$Si spectra recorded at 9.4 T.

| Sample (P, GPa) | Chemical shift (ppm) | | | Height | | |
|---|---|---|---|---|---|---|
| | Peak 1 | Peak 2 | Peak 3 | Peak 1 | Peak 2 | Peak 3 |
| B3-180615 (1 atm) | -80 | -90 | -109 | 0.04 | 1.03 | 0.08 |
| C4901 (0.6) | -80 | -91 | -110 | 0.00 | 0.93 | 0.37 |
| C4799 (1.0) | -80 | -92 | -109 | 0.11 | 0.95 | 0.26 |
| C4900 (2.0) | -80 | -91 | -109 | 0.01 | 1.02 | 0.18 |
| C4896 (2.5) | -80 | -90 | -109 | 0.01 | 1.04 | 0.11 |
| C4904-C4905 (3.0) | -80 | -90 | -109 | 0.00 | 1.01 | 0.18 |
| D2125 (ann) (3.5) | -80 | -88 | -109 | 0.00 | 0.98 | 0.11 |
| D1840-D1842 (3.5) | -80 | -89 | -109 | 0.00 | 1.02 | 0.09 |
| C4878-C4879 (4.0) | -80 | -90 | -109 | 0.00 | 0.98 | 0.30 |
| C4892-C4924 (4.5) | -80 | -87 | -109 | 0.16 | 0.89 | 0.05 |
| uhppc269-314 (5.0) | -79 | -87 | -109 | 0.25 | 0.77 | 0.09 |

Widths of peaks are 10.8 (1), 9.83 (6) and 9.55 (6) for Peak 1, Peak 2 and Peak 3 respectively. The largest standard deviations on the fit parameters obtained using the bootstrap method are 0.1 ppm for peak positions (chemical shift) and 0.01 for peak heights. Since true errors are likely to be much larger due to the signal-to-noise ratio of the spectra, only two significant figures have been reported.

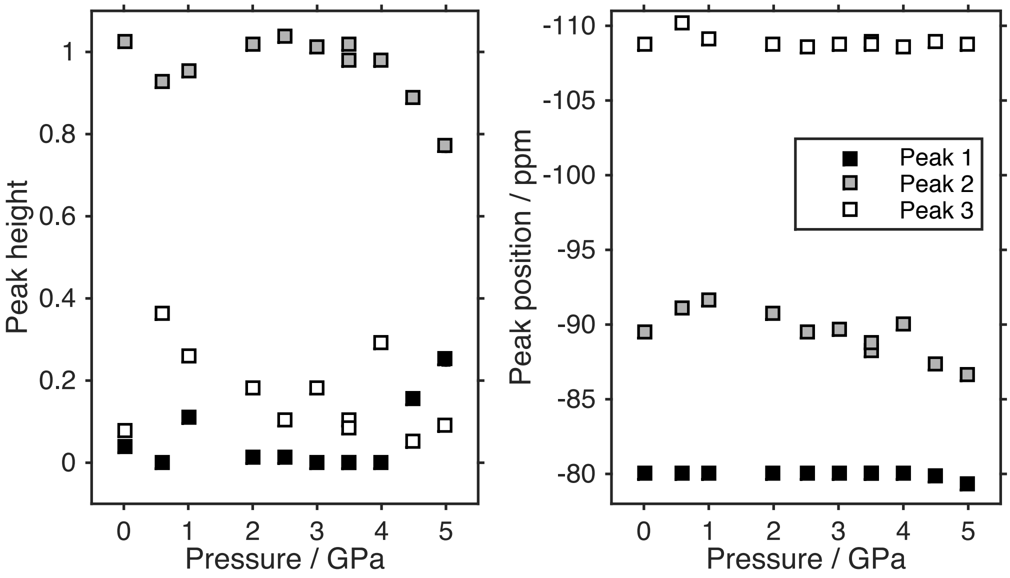

Figure 3.13. Peak heights and positions as a function of pressure for the fits to $^{29}$Si spectra. Errors on the fit parameters, obtained using a bootstrap method, are smaller than the size of the symbols, but the true error is probably much larger given the signal-to-noise ratio of the spectra.

### *Aluminium–silicon correlation*

$^{27}$Al–$^{29}$Si D-HMQC correlation spectra were acquired for several samples (Figure 3.15). The spectra indicate that Al in all four-, five- and six-fold environments is correlated with the single Si peak. Spectra for B3-180615 and D1840-D1842 have the best signal-to-noise ratio due to larger sample volumes. In these spectra, it can be seen that the cross peak corresponding to $^{[4]}$Al has a maximum at ~ –89 ppm in the $^{29}$Si dimension, whereas the $^{[6]}$Al cross peak occurs at ~ –86 ppm in the $^{29}$Si dimension. This indicates that the $^{[6]}$Al species correlates more strongly with a component in the $^{29}$Si spectrum that is located at less negative chemical shift. The spectra for samples D2125 and D2213 have lower sensitivity, but are consistent with this observation. The spectrum of MA1125 shows a cross peak for $^{[6]}$Al, which is the dominant Al species, at even higher chemical shift: ~–82 ppm in the $^{29}$Si dimension. In this spectrum, the projection in the $^{29}$Si dimension is also at higher chemical shift and narrower than in other samples (as also shown in Figure 3.11)

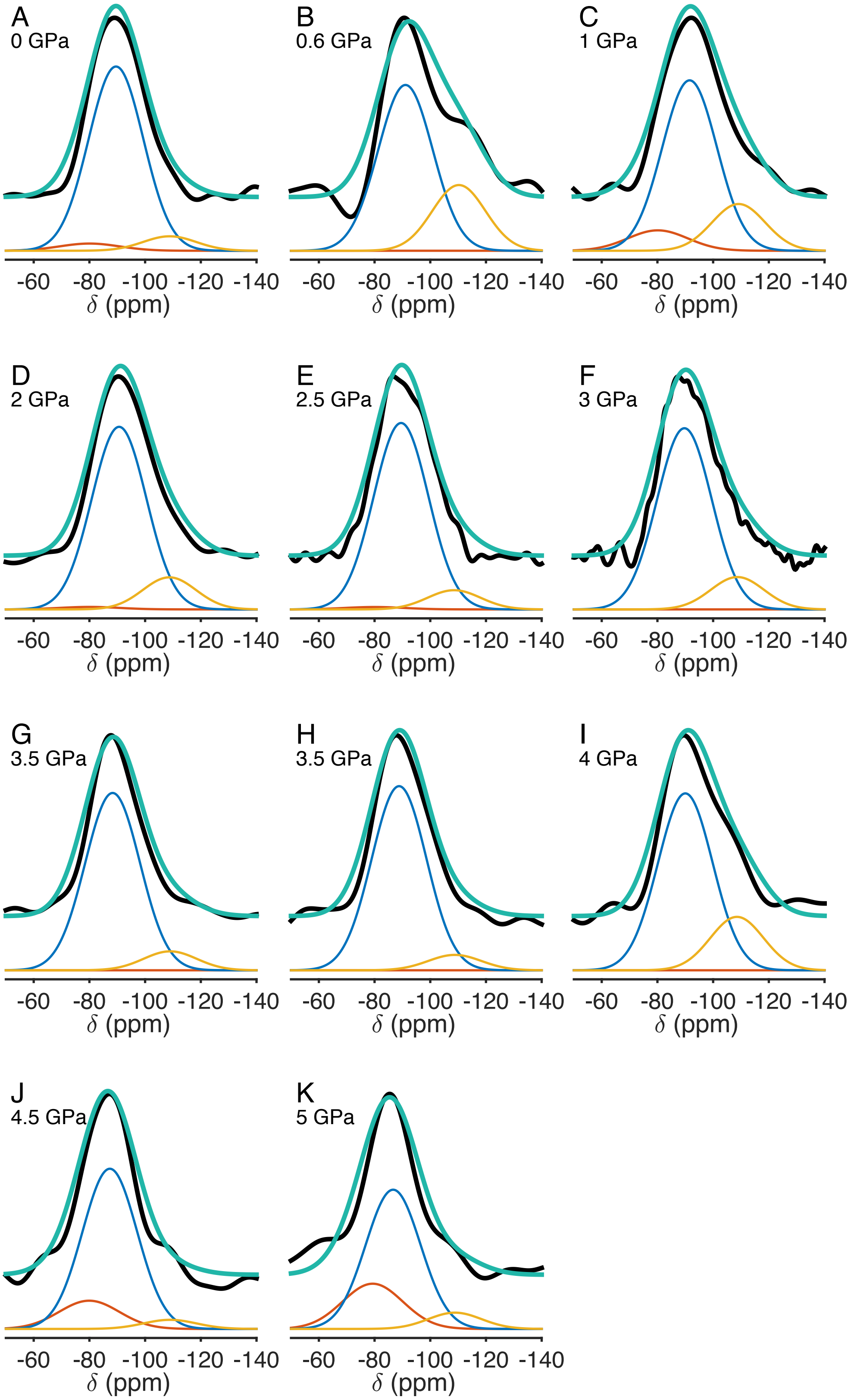

Figure 3.14. Fits (green) to the $^{29}$Si spectra collected at 9.4 T (black). Individual components are shown as thin coloured lines, offset below the spectra for clarity. Peak 1 = red, Peak 2 = blue, Peak 3 = yellow.

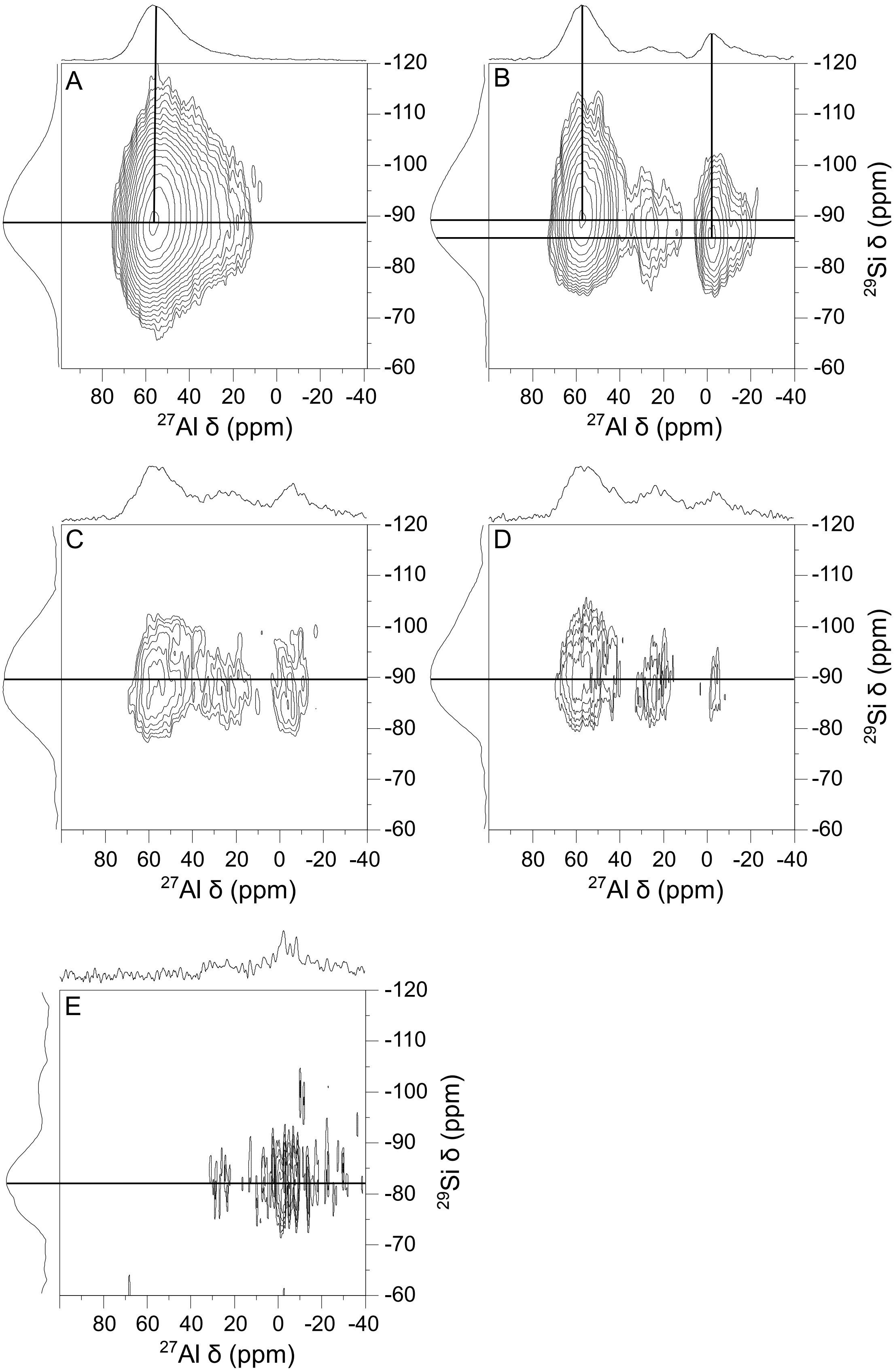

Figure 3.15. $^{27}$Al-$^{29}$Si D-HMQC correlation spectra. (A) B3-180615, 1 atm, (B) D1840-D1842, 3.5 GPa, (C) D2125, 3.5 GPa, (D) D2213, 3.5 GPa, (E) MA1125, 10 GPa. The latter three spectra are very noisy due to the small sample volume.

*Magnesium-25*

$^{25}$Mg spectra took a long time to acquire (~1-2 days for each spectrum) due to the low concentration of Mg in the samples (~3.6 mol% MgO) and the experimental challenges of studying quadrupolar nuclei with low γ. Thus, even using a CMPG pulse sequence, the signal-to-noise ratio is low. Spectra display a broad peak with an isotropic chemical shift of ~45 ppm (see Figure 3.16). Fits to spectra of B3-180615 acquired at 9.4 T and 20.0 T are shown in Figure 3.17.

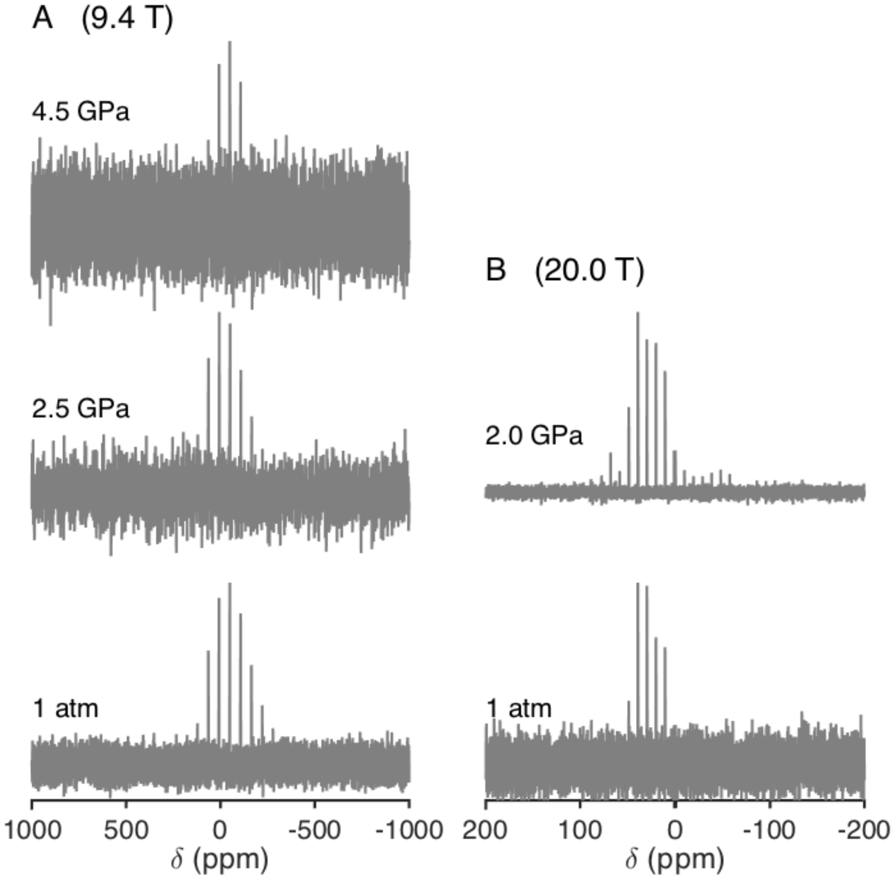

Figure 3.16. $^{25}$Mg MAS NMR spectra collected at (A) 9.4 T and (B) 20.0 T, for samples B3-180615 (1 atm), C4900 (2.0 GPa), C4896 (2.5 GPa), and C4892-C4924 (4.5 GPa). Spectra have been normalised to constant height. Spikelet spacing is 1400 Hz in (A) and 500 Hz in (B). The number of echoes acquired was 150 in all spectra except for C4896, for which only 50 echoes were acquired.

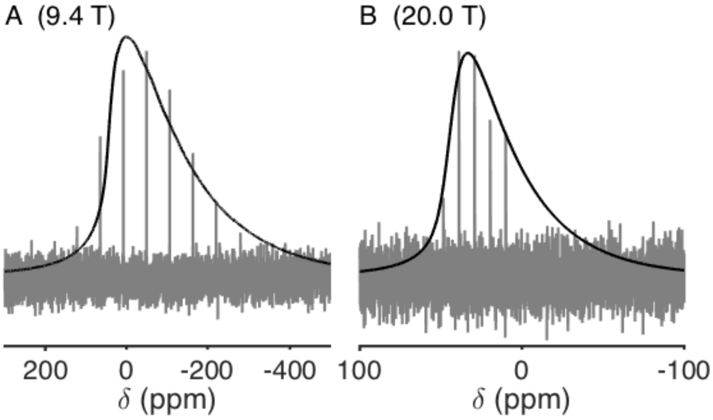

Figure 3.17. Fits to $^{25}$Mg spectra of B3-180615 at two fields. Fit parameters at both fields are $\delta_{iso}$ = 45 ppm, dCSA (distribution of isotropic chemical shift) = 10, CQ = 3.5 MHz.

## *Calcium-43*

A single $^{43}$Ca spectrum was acquired for the ambient-pressure glass sample (B3-180615) at 20.0 T. The spectrum has very poor sensitivity, but shows a peak centred at around ~0 ppm (Figure 3.18). A spectrum was also attempted for a high-pressure sample, but due to the small sample volume, a signal was not seen in the time available.

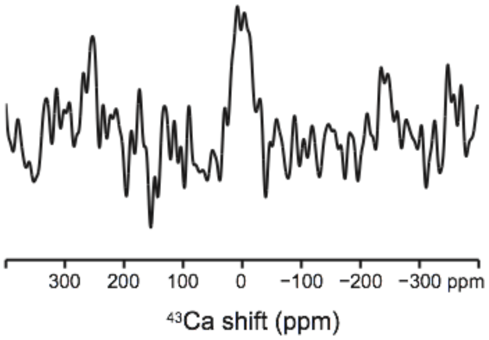

Figure 3.18. $^{43}$Ca MAS NMR spectrum of B3-180615.

## *Oxygen-17*

$^{17}$O spectra obtained from two $^{17}$O-enriched samples (prepared at 1 atm and 5 GPa) are presented in Figure 3.19 and Figure 3.20 along with corresponding fits. Two peaks are observed in the ambient pressure sample, corresponding to bridging oxygens (BO, at ~ −40 ppm) and non-bridging oxygens (NBO, ~ −100 ppm). In the high-pressure sample, additional intensity is observed between the BO and NBO peaks, in both 1D and 2D, which could represent an additional contribution to the spectrum. This would be consistent with previous $^{17}$O work on high-pressure glasses (Lee et al. 2004; Allwardt et al. 2005b; Lee et al. 2012). As such, in Figure 3.20, a third small peak was used in fitting the spectrum. However, as shown in Figure 3.21, it is not possible to say that the third peak results in a better fit to the data, due to the noise in the spectrum.

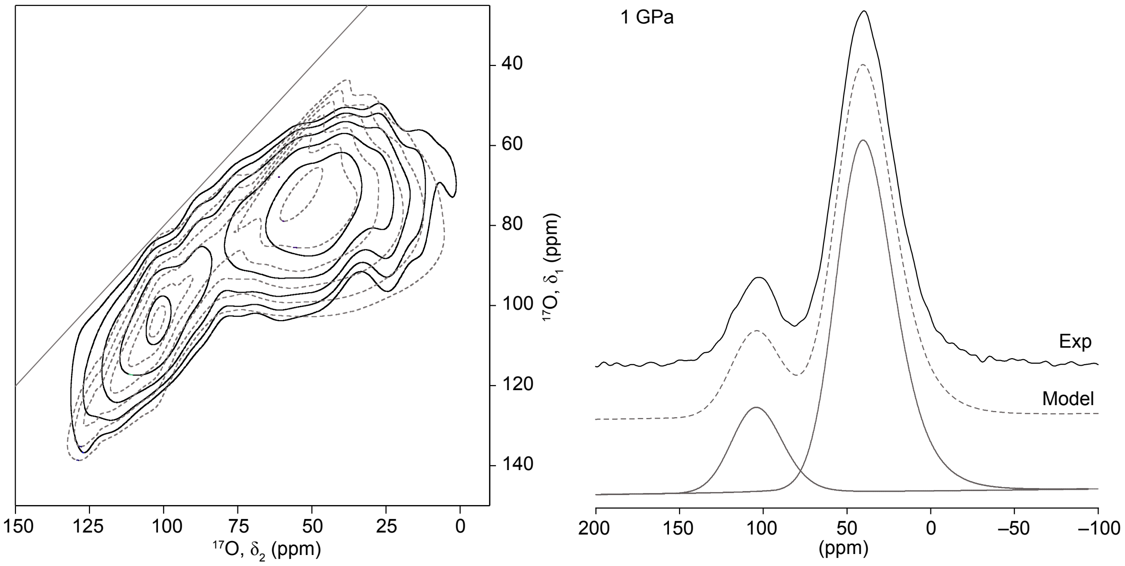

Figure 3.19. $^{17}$O NMR spectra of D1679 (1 GPa) collected at 14.1 T.

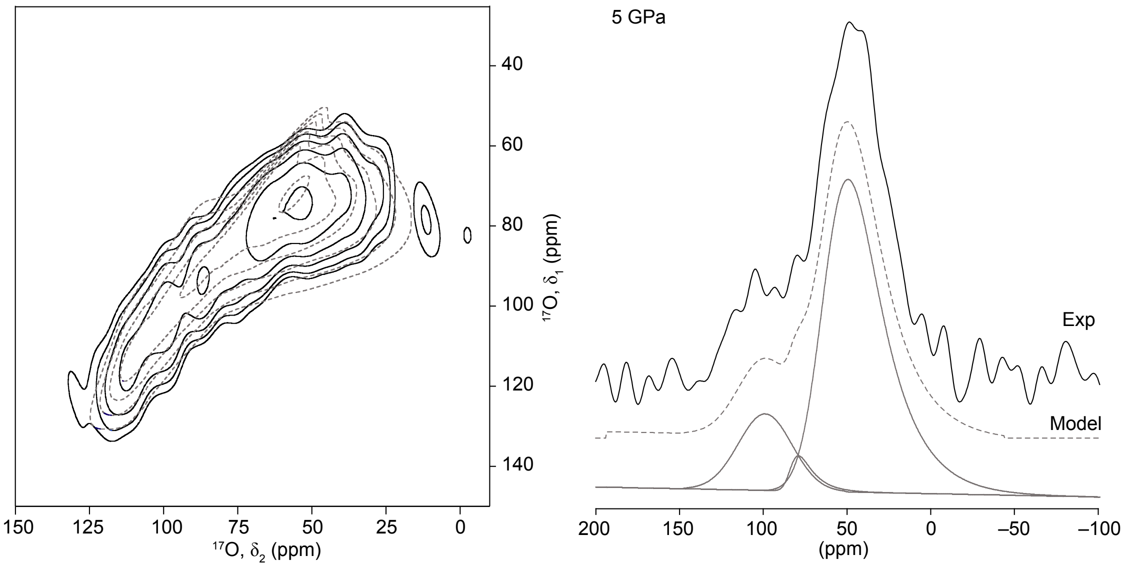

Figure 3.20. $^{17}$O NMR spectra of uhppc-269 (5 GPa) collected at 14.1 T.

Spectra of samples that were enriched in $^{17}$O using post-synthetic gas-exchange are shown in Figure 3.22. All spectra show the two peaks for NBO and BO, but no evidence of additional intensity between those peaks.

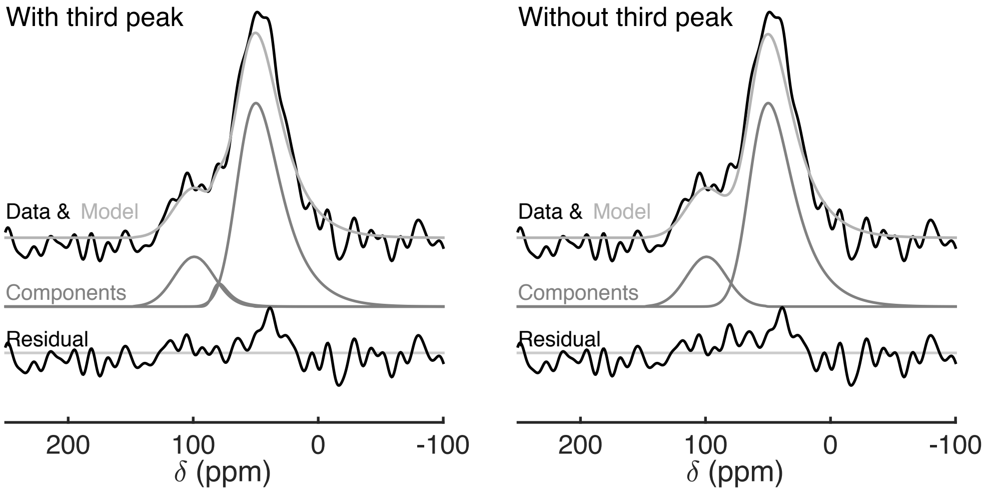

Figure 3.21. $^{17}$O NMR spectrum of uhppc-269 (5 GPa), and model with three peaks (left) and two peaks (right). Residuals are shown as the lower black curves, with a grey horizontal line as a guide to the eye.

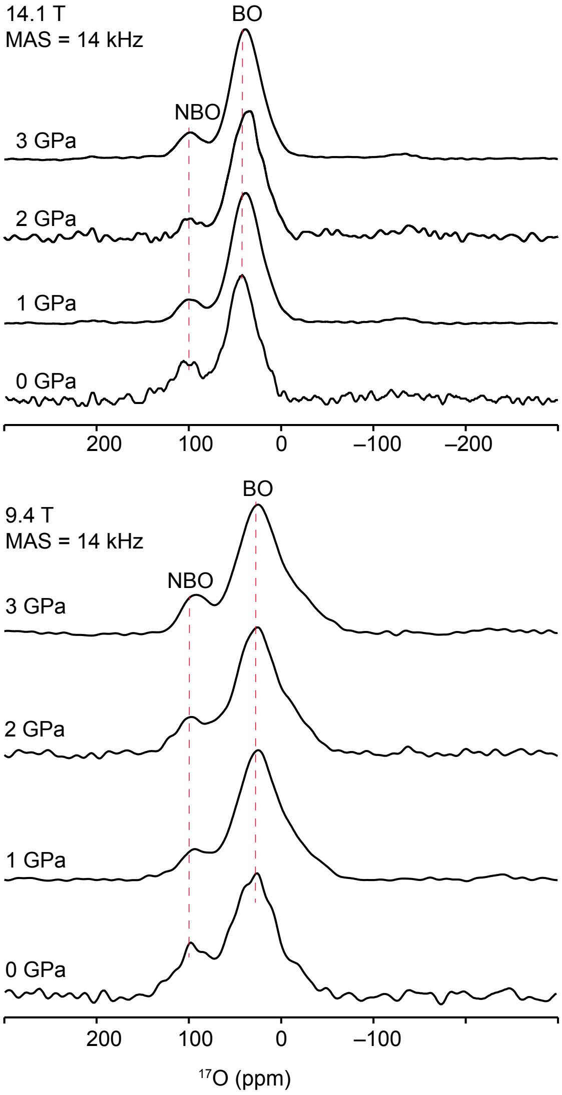

Figure 3.22. $^{17}$O NMR spectra of samples B3-300915 (0 GPa), C4798 (1 GPa), C4900 (2 GPa) and C4904-C4905 (3 GPa) after $^{17}$O enrichment via the gas-exchange method.

## *Gallium-71*

$^{71}$Ga spectra of the Ga-enriched samples at two fields are shown in Figure 3.23. At 14.1 T, the spectra overlap with spinning sidebands; at 20.0 T the quadrupolar broadening is reduced, the spectral lineshapes are narrower and the overlap is less noticeable, but the signal-to-noise ratio is lower. The spectra are shown expanded in Figure 3.24. The lineshape for the 1 atm sample (B1-101215) can be fitted well with a single peak that has $\delta_{iso}$ ~ 160 ppm (fit parameters are given in Table 3.8). However, the same fit parameters cannot be used for the spectra collected at both 14.1 T and 20.0 T, as shown in Figure 3.24 (dashed curve). The sample made at 5GPa (uhppc-333) clearly contains more intensity at more negative chemical shift. This additional intensity reflects at least one, and probably two, other environments. However, robust fitting of these additional peaks is not possible due to their significant overlap and low signal-to-noise ratio.

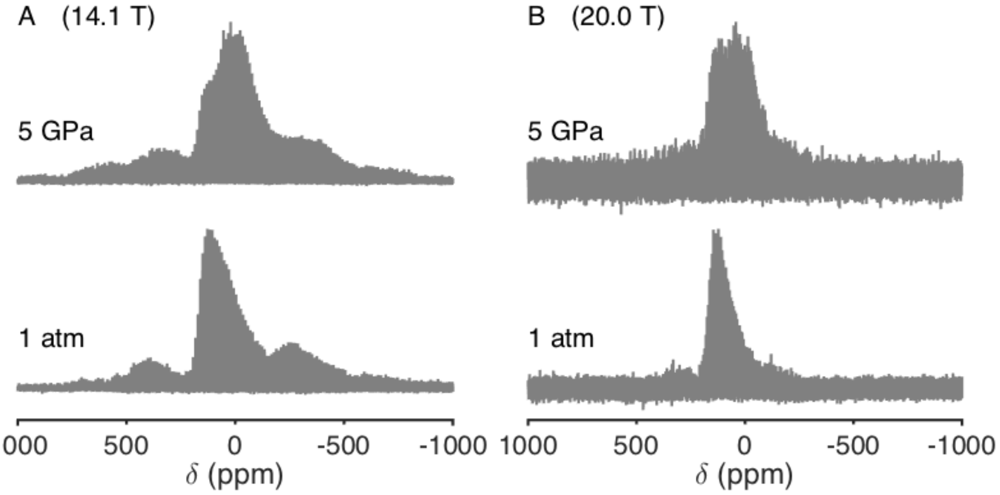

Figure 3.23. $^{71}$Ga MAS NMR spectra of samples B1-101215 (1 atm) and uhppc-342-333 (5 GPa) at two fields. (A) Spectra collected at 14.1 T, using 300 and 100 echoes for samples B1-101215 and uhppc-342-333 respectively, with a spikelet spacing of 2000 Hz. (B) Spectra collected at 20.0 T, using 400 echoes. Spikelet spacing is 1500 Hz for B1-101215 and 1200 Hz for uhppc-342-333.

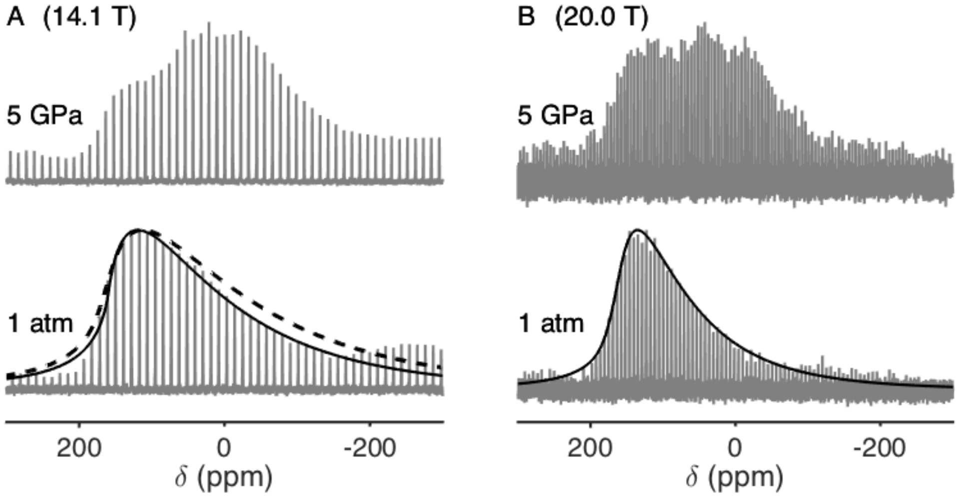

Figure 3.24. Close up of the same $^{71}$Ga spectra shown in Figure 3.23, along with fitted curves. In (A), dashed curve is a fit using the same parameters as the fit to the 20.0 T spectrum. Solid curve is a better fit to the data with lower dCSA and $C_Q$ (see Table 3.8).

Spectra of the samples with lower Ga concentration (Figure 3.25) have much lower signal-to-noise ratios. However, the spectra of the low-pressure (1 atm and 1 GPa) samples can be fitted reasonably well using the parameters listed in Table 3.8, whereas the spectrum of uhppc-269-314 (0.3 wt% $Ga_2O_3$, 5 GPa) is centred at lower chemical shift. This agrees qualitatively with the results obtained for the 11 wt% $Ga_2O_3$ samples.

Table 3.8. $^{71}$Ga fit parameters for sample B1-101215 at different fields.

| Field | $\delta_{iso}$ (ppm) | dCSA (ppm) | $C_Q$ (MHz) |
|---|---|---|---|
| 14.1 T | 159.6 | 0 | 12.4 |
| 20.0 T | 163.6 | 25 | 13.6 |

dCSA is the chemical shift anisotropy; $C_Q$ is the quadrupolar coupling constant.

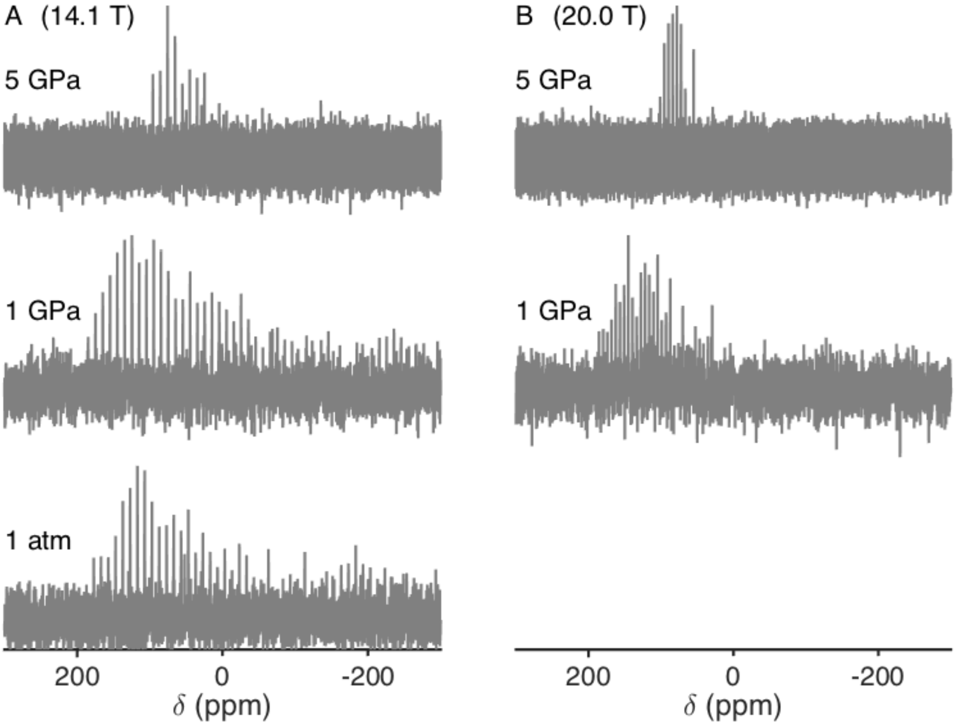

Figure 3.25. $^{71}$Ga spectra recorded at (A) 14.1 T and (B) 20.0 T of samples containing lower Ga concentrations. The spectra are for samples B3-180615 (1 atm, 0.3 wt% Ga), C4794 (1 GPa, 2.5 wt% Ga) and uhppc-269-314 (5 GPa, 0.3 wt% Ga). 400 echoes were used in acquisition of all spectra except for the spectrum of C4974 at 20.0 T, for which 100 echoes was used. Spikelet spacing in (A) is 1833 Hz for B3-180615 and C4794, and 1857 Hz for uhppc-269-314; spikelet spacing in (B) is 1500 Hz for both spectra.

## 3.4 Discussion

### *Aluminium-27*

#### **Al environments in the samples**

The $^{27}$Al spectra indicate that the high-pressure samples contain Al in four-, five- and six-fold coordination environments, and, in some samples, a corundum environment. In many samples, multiple types of $^{[5]}$Al and $^{[6]}$Al sites appear to be present. In some samples, two peaks were used in fitting both $^{[5]}$Al and $^{[6]}$Al sites (excluding the corundum peak). Only one peak was needed to fit the $^{[4]}$Al site. A clear example of this can be seen in Figure 3.1, in the 5 GPa spectrum. This is a quenched melt sample, so no corundum is present; there are two contributions to the $^{[5]}$Al peak, and probably two contributions to the $^{[6]}$Al peak as well. The multiple sites are also observed in the $^{27}$Al–$^{29}$Si correlation spectra.

What do these multiple five- and six-fold Al environments represent, physically? They could represent pentahedral or octahedral units with different distortions. Alternatively, by analogy with Si Q-species, perhaps they represent higher-coordinated Al sites with different numbers of non-bridging oxygens. Since they are observed in the $^{27}$Al–$^{29}$Si correlation spectra, they may also represent Al species next to different types of Si $Q^n$ species.

### Differences between quenched melts and annealed glasses

The differences between quenched melts and annealed glasses are very interesting. At a given pressure, the annealed glasses systematically contain more $^{[5]}$Al and less $^{[4]}$Al than the quenched melt samples.

The reason that annealed glasses contain more $^{[5]}$Al is uncertain. It could be that more $^{[5]}$Al is preserved in these samples, whereas it more readily converts to $^{[4]}$Al on quenching in the quenched melts. Alternatively, it is possible that more $^{[5]}$Al is created in the annealed glasses compared to the quenched melts. However, this does not agree with previous work showing that higher fictive temperatures favour more $^{[5]}$Al (Stebbins et al. 2008; Morin and Stebbins 2016). The $T_f$ of the annealed glasses is probably close to $T_g$, whereas the $T_f$ of quenched melts cannot be quantified but could be higher than $T_g$. Thus it would be expected that more $^{[5]}$Al would be created in the quenched melts than the annealed glasses, whereas the opposite is observed. Therefore, better preservation of $^{[5]}$Al in annealed glasses is the preferred interpretation.

However, this does not necessarily mean that annealed glasses simply record a higher fictive pressure, as proposed by Gaudio et al. (2015a) for albite glass. These authors showed that quenched melts recorded a lower fictive pressure than annealed glasses, and accordingly had a lower density and a lower Al coordination number. When this was corrected for, the two types of samples showed a consistent trend with pressure. However, the data presented in this thesis show a rapid increase in average Al, Ge and Ga coordination between 4 and 5 GPa in quenched melt samples, whereas annealed glasses do not show such a rapid increase at any pressure. If the only difference between these sample sets was fictive pressure, then a similar pressure-dependence of coordination should be seen, just shifted to different pressures. Even if the difference in fictive pressure was greater at higher pressures, this should cause exaggeration of the trend seen in the quenched melts.

However, no such trend is seen in the annealed glasses. The reason for this is unclear.

Glasses annealed at 600 ºC show lower average Al coordination numbers, as well as lower Ga and Ge coordination numbers, than glasses annealed at higher temperatures. The difference between samples annealed at 600 ºC and at ≥700 ºC increases at higher pressures. This is likely to be because the 600 ºC samples did not fully equilibrate to the high-pressure structure during the timescale of the experiment. Østergaard et al. (2015) studied sodium borosilicate glass at 1 GPa, and showed that when the glass was compressed at temperatures more than 0.7 $T_g$, at least some permanent densification occurred, with the amount of densification becoming constant above $T_g$. The samples annealed at 600 ºC, (0.77 $T_g$) would therefore be expected to be incompletely densified compared to samples annealed above 700 ºC (0.90 $T_g$) or at 780 ºC (~ $T_g$), in agreement with the observations.

### Effect of high Ga content

Another interesting phenomenon is how the Al coordination changes depend on the Ga content of the melt. At 5 GPa, the sample that was enriched in Ga contains less higher-coordinate Al than the sample containing only 3000 ppm Ga. This could be because Ga increases its coordination more readily than Al, and so in the Ga-enriched sample, more of the compression is accommodated by Ga coordination changes before Al begins to change its coordination.

### Comparison to literature data

Figure 3.26 and Figure 3.27 show the Al coordination numbers obtained in this study plotted along with data obtained in by $^{27}$Al MAS NMR in previous work on similar compositions (CAS and basaltic compositions). The effect of pressure on Al coordination in these literature studies is generally similar to that presented in this study, however, there are some notable differences. Firstly, the amount of $^{[6]}$Al in the quenched melts at 5 GPa is almost double than what has been seen before in the literature, and this increase is reflected in the larger average coordination (Figure 3.27). Secondly, the average Al coordination number of the 10 GPa annealed glass sample is identical to that in a glass quenched from 10 GPa in the study of Allwardt et al. (2005c), but the contributions to that average from individual coordination environments are quite different. The sample in the present study contains less $^{[4]}$Al and less $^{[6]}$Al but far more $^{[5]}$Al. Thirdly, the difference between average coordination numbers in quenched melts and annealed glasses obtained in this study is not as large as the difference observed by Bista et al. (2015).

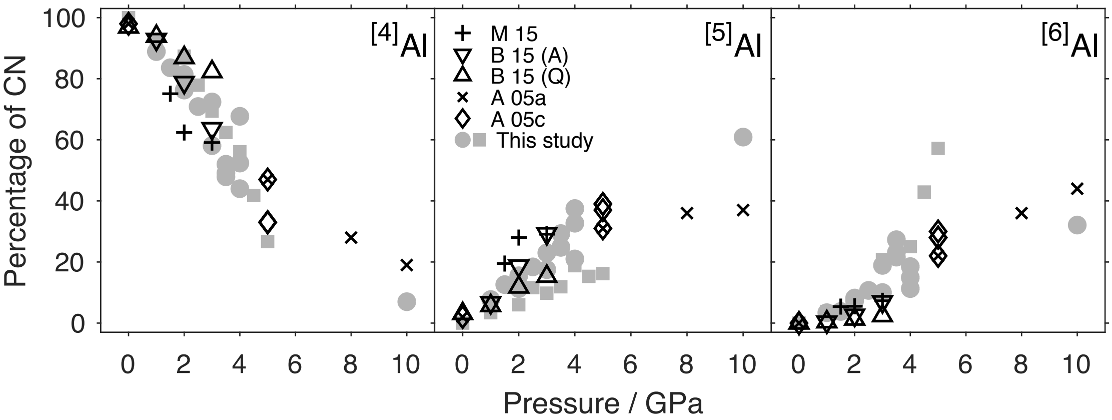

Figure 3.26. Comparison of Al coordination environments in the literature to those determined in this study. M 15 = (Morizet et al. 2015), B 15 (Bista et al. 2015), where A refers to annealed and Q refers to quenched, A 05a (Allwardt et al. 2005c), A 05c (Allwardt et al. 2005b). Grey symbols are data from this study; squares are quenched melts and circles are annealed glasses, as plotted earlier in Figure 3.7.

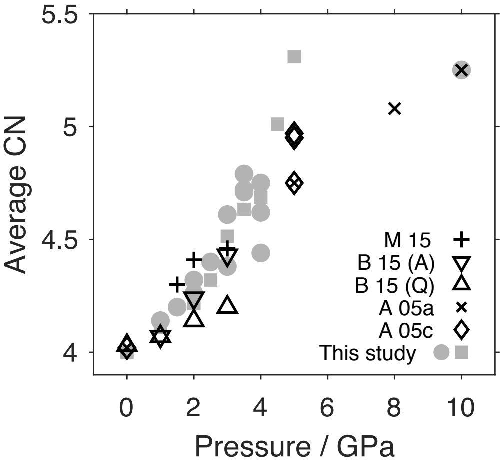

Figure 3.27. Comparison of average Al coordination number as a function of pressure in this study to similar compositions in the literature.

It is possible that some of these difference result from different flip angles and relaxation intervals used in previous work. Spectra presented in this study were acquired with an 18° flip angle and at least 2 s relaxation interval, whereas spectra obtained by Allwardt et al. (2005c; 2005b) and Bista et al. (2015) were acquired using a longer flip angle of 30° and shorter relaxation interval (0.1–0.2 s). The spectra of Morizet et al. (2015), were acquired with 13.8° flip angle and 1 s relaxation interval, so are more likely to be quantitative. Considering the difficulty in obtaining quantitative spectra from quadrupolar nuclei, the results presented in this thesis are reasonably consistent with previous work.

One final point to note regarding the Al data is that the average coordination recorded in the 10 GPa annealed glass is a little less than that recorded in the 5 GPa quenched melt sample. This could be because of the difference in decompression rates. The 10 GPa sample is the only data point for Al made in a multi-anvil apparatus, and it was temperature-quenched isobarically but then decompressed at room temperature overnight. Allwardt et al. (2005c; 2005b) showed that there was a difference between Al coordination in samples which were decompressed either rapidly (over ~ 1s) or slowly, over ~ 14 h. The rapidly-decompressed samples had a higher average coordination number of Al than the slowly-decompressed samples, indicating that some structural relaxation occurred during slow decompression. The 10 GPa sample made in this study was decompressed slowly, so it is possible that this sample reflects lower average coordination numbers than it otherwise would.

### *Silicon-29 and the aluminium–silicon correlation spectra*

The $^{27}$Al–$^{29}$Si correlation spectra provide a critical piece of information for interpreting the 1D $^{29}$Si spectra. As shown in Figure 3.15, the $^{[4]}$Al peak correlates with a component in the Si spectrum at around –90 ppm, but the $^{[6]}$Al peak correlates with a component in the Si spectrum at higher chemical shift (~–86 to –82 ppm). This is expected because the longer bonds associated with $^{[5,6]}$Al units will cause deshielding of the Si species to which they are bonded. This deshielding has been shown previously for $^{29}$Si NMR spectra of minerals and high-pressure glasses where the presence of $^{[5,6]}$Si cause the $^{[4]}$Si signal to move to higher chemical shift (Stebbins and Kanzaki 1991; Xue et al. 1991).

Figure 3.12 shows that in the $^{29}$Si spectra, the centroid moves to higher chemical shift with pressure and the width of the peak decreases. The shift in the centroid most likely reflects an increase in the number of higher-coordinate Al environments bonding with Si, which, as discussed, produce a signal at higher chemical shift. The narrowing of the peak is more difficult to explain but may indicate that a $^{[4]}$Si–$^{[5,6]}$Al species produces a narrower signal. Alternatively, it may indicate a decrease in the distribution of $Q^n$ species.

Fits of $^{29}$Si the spectral lineshapes indicate two dominant components for samples prepared at pressures at and below 4 GPa, with a third component (Peak 1) becoming important at higher pressures. Peak 1 is at ~ 80 ppm and probably reflects Si bonded to higher-coordinate Al, as discussed above. The positions of Peak 2 and Peak 3 are consistent with $Q^3$ and $Q^4$ species (Smith et al. 1983; Magi et al. 1984), which is reasonable given that these two species are expected to be dominant in a composition with NBO/T ~ 0.6.

However, these peak assignments should be treated with great caution, because there may be many overlapping peaks within the signals. $Q^3$ may disproportionate to form $Q^4 + Q^2$ (Stebbins 1987), and the chemical shift of $Q^2$ is similar to that of Peak 1. Furthermore, each $Q^n$ species may have different numbers of Al neighbours which also affects its chemical shift (by about 5 ppm for each additional Al neighbour) (Smith et al. 1983; Magi et al. 1984), meaning that the overall $Q^4$ and $Q^3$ signals may not be Gaussian. The fits therefore do not provide any reliable information on their own, but they are consistent with the other observations that indicate that the changes in the Si can spectra can be mainly attributed to Al coordination changes.

### *Magnesium-25*

Fits to the $^{25}$Mg spectra give $\delta_{iso}$ ~ 45 ppm, which is consistent with Mg in four-fold coordination. Spectra of minerals containing $^{[4]}$Mg give isotropic chemical shifts of 47–61 ppm, whereas $^{[6]}$Mg environments typically have shifts of ~ –3 to 14 ppm (MacKenzie and Meinhold 1994; Dupree et al. 1997; Kroeker and Stebbins 2000; Shimoda et al. 2007).

Mg is a network modifier (and/or charge compensator) in these glasses and does not form part of the tetrahedral network, yet it still seems to occupy tetrahedral coordination. This is consistent with results of O'Neill and Berry (2006), who suggested that $Mg^{2+}$ (along with $Mn^{2+}$, $Fe^{2+}$, $Ni^{2+}$, $Co^{2+}$) occupies a tetrahedral coordination environment in a suite of 31 CMAS, CAS and MAS compositions, (including CMAS7G), on the basis of constant activity coefficient ratios between the cations.

The data presented in this work show no change in the $^{25}$Mg spectra with pressure up to 4.5 GPa. It should be noted, however, that it is possible that the signal from a

[6]Mg in these glasses might be unobservable due to a large quadrupolar broadening. There is no evidence to support or contradict this possibility. As pointed out by Shimoda (2007), primitive magmas in the mantle are Mg-rich, so if Mg does undergo pressure induced coordination changes, this could have important consequences for the properties of the melt.

### *Calcium-43*

A very weak signal was obtained in a $^{43}$Ca NMR spectrum of B3-180615, centred at around ~0 ppm. Previous $^{43}$Ca NMR studies on silicate glasses have shown that the position of the peak shifts depending on the role calcium plays as either a network modifier, charge compensator, or a mixture of both (Angeli et al. 2007; Gambuzzi et al. 2015). A peak centred at around 0 ppm was shown for the glass in which calcium was both network former and charge compensator, and using a combination of MQMAS NMR and molecular dynamic modelling, Gambuzzi et al. (2015) showed that a distribution of [5]Ca, [6]Ca and [7]Ca sites with a minor contribution (2%) from [4]Ca sites were present. A distribution of Ca coordination numbers is therefore expected in the ambient-pressure glass studied here. This distribution might shift with pressure, but no data has been obtained for higher-pressure samples.

### *Oxygen-17*

$^{17}$O spectra contained two peaks, which were assigned as NBO and BO by comparison to previous work (e.g. Allwardt et al. 2005b; Stebbins et al. 2008). The BO peak is larger than the NBO peak, consistent with what is expected of the composition which has NBO/T ~ 0.6, so each tetrahedral unit has, on average, 3.4 BO and 0.6 NBO (i.e. 85% BO). This agrees reasonably well with fits to the spectra indicating 79% BO (see supplementary material, section 7.6, p. 209).

Additional intensity may be present between the BO and NBO peaks in the spectrum of the 5 GPa sample (uhppc-269). Such intensity has been observed in previous work in both MAS and MQMAS $^{17}$O spectra, and attributed to oxygen bonding between [4]Si and [5,6]Al (Lee et al. 2004; Allwardt et al. 2005c; Lee et al. 2012). However, as shown in Figure 3.21, whether this peak exists in the data presented here is not clear. Further work would be needed to get spectra with higher signal-to-noise ratios in order to resolve this.

No additional intensity was observed between the BO and NBO peaks at 1, 2 or 3 GPa in samples that were enriched in $^{17}O$ by a gas-exchange method. However, the enrichment method required the glass to be annealed at 700 °C for 48 h, and this may have caused the high-pressure structures in the glass to relax. Samples annealed at high pressures at 700 °C preserve the high-coordinate Al environments after annealing for just 2 h, so it is reasonable to assume that the during ambient-pressure annealing the high-pressure structures in the glass would relax. Unfortunately, $^{17}O$ enrichment was not successful when the samples were annealed at lower temperatures.

### *Gallium-71*

$^{71}Ga$ NMR spectra have not previously been recorded in silicate glasses, however the positions of the peaks corresponding to different coordination environments are known from spectra of gallium oxide (Massiot et al. 1995), gallosilicate zeolite minerals (Timken and Oldfield 1987; Bayense et al. 1992), and glasses in the $Na_2O$-$Ga_2O_3$-$P_2O_5$ system (Belkebir et al. 2000; Caron et al. 2014; Ren and Eckert 2014).

Spectra of the ambient-pressure sample B1-101215 were collected at two fields and fits were made for both fields; however, the same parameters could not be used for both fits. I am not sure why this is, but I can speculate. If there are small contributions of $^{[5]}Ga$ and maybe even $^{[6]}Ga$ in the ambient-pressure sample, these peaks might cause a broadening of the line shape. This could also explain why the $C_Q$ obtained from these fits is quite high, especially compared to some literature data which suggest $C_Q$ around 6–8 for $^{[4]}Ga$, $^{[5]}Ga$ and $^{[6]}Ga$ in sodium gallate glasses (Ren and Eckert 2014).

However, it is still reasonable to assume that in the B1-101215 the dominant contribution is from $^{[4]}Ga$, because the $\delta_{iso}$ values obtained from fitting (~160 ppm) agree broadly with literature values of 120 ppm in glass (Ren and Eckert 2014) and 200 ppm in β-$Ga_2O_3$ (Massiot et al. 1995). In the high-pressure sample (uhppc-342-333), the highest intensity in the $^{71}Ga$ spectra is at lower chemical shift to the low-pressure samples, probably indicating a contribution of higher coordination environments. In Figure 3.24B, the additional intensity appears to display two peaks, one centred at around 45 ppm and the other at around –10 ppm. These peaks overlap significantly, which makes resolving the two peaks difficult.

However, their positions are reasonably consistent with the chemical shifts observed in the literature for $^{[5]}$Ga (20-43 ppm) and $^{[6]}$Ga (–24 to –70 ppm) in $Na_2O$-$Ga_2O_3$-$P_2O_5$ glasses (Belkebir et al. 2000; Caron et al. 2014; Ren and Eckert 2014). Therefore, the $^{71}$Ga spectra acquired in this study indicate that Ga is predominantly four-fold coordinated at low pressure, but contains four, five and six-fold coordinated species at 5 GPa, consistent with the results from XANES spectroscopy.

### *Relationships between Al and trace elements*

Similarities are seen in the pressure-dependence of coordination number for Al, Ga and Ge. In quenched melts, all three elements show a rapid increase in average coordination between 4 and 5 GPa, whereas the coordination increases more steadily with pressure in annealed glasses. In particular, the correlation between Al and Ga coordination is striking (Figure 3.10C, D), and considering that the correlation is seen in both annealed glasses and quenched melts, it is unlikely to be simply a coincidence. However, what this correlation represents is ambiguous.

One possibility is that Ga is 'forced' to change its coordination at exactly the same pressures as Al does, analogous to how trace Ga substituting into an aluminous mineral would take the coordination of the Al site. With the information available, this cannot be ruled out. Certainly the same cannot be said for Ge and Si, since Ge coordination changes were observed at pressures well below where Si would be expected to change its coordination. Since Ge changes its coordination at much lower pressures than Si, it would be reasonable to expect that the Ga changes its coordination at lower pressures than Al. Even if Ga coordination is influenced by Al coordination changes, it is probably not constrained to behave in exactly the same way.

An alternative explanation is that since Ga plays a similar role in the melt structure to Al, its coordination changes in a similar way to Al (albeit, perhaps, at lower pressures). In this scenario, trace elements behave completely independently of the major elements in the melt, and the correlation between Al and Ga results simply from their similarity. However, this scenario cannot explain the observation of a rapid coordination change of Ge at the same pressures as Al and Ga (in quenched melts at 4–5 GPa), unless it was simply coincidence.

The preferred interpretation of these data is that Al coordination changes do have some influence on, but not complete control over, Ge and Ga coordination. Whether this extends to other trace elements—particularly elements that are network modifiers rather than network formers—would be an interesting area for future work.

## 3.5 Conclusion

A study of the local environments of all major elements in CMAS7G composition glasses compressed to 10 GPa has been undertaken. Aluminium changes its coordination from predominantly four-fold at 1 atm to predominantly five- and six-fold at 10 GPa. Silicon spectra show no evidence for coordination changes, but the $^{[4]}$Si signal shifted to higher chemical shift and became narrower with pressure, most likely related to the formation of higher-coordinate Al. Magnesium spectra are consistent with four-fold coordination and no changes were seen with pressure up to 4.5 GPa. A single $^{43}$Ca spectrum is consistent with a distribution of coordination environments. Ga is predominantly tetrahedrally coordinated at ambient pressure and contains four, five and six-fold coordination environments at 5 GPa.

Changes in the Al coordination number with pressure correlate well with Ga coordination, and also to some degree with Ge coordination, which indicates that Al may influence the coordination number of these trace elements. Further work is needed to assess whether this influence would extend to other trace elements.

If a trace element undergoes a coordination change, this should affect its partition coefficient, because of the reduction in partial molar volume of the melt species. If the major elements in the melt, such as Al, undergo coordination changes, this may also affect trace element partitioning by changing the activity coefficient of the trace element in the melt. If a model could be developed to predict how coordination changes of trace and major elements might affect trace element partitioning, this would be a very useful tool in geochemistry. This is discussed in the next chapter.

## 3.6 Acknowledgements

While I have already acknowledged the colleagues who have contributed to this thesis in the main Acknowledgements section, I would like to reiterate here the

contribution that Nasima Kanwal has made to this chapter. Nasima assisted me during my time at the University of St Andrews to record NMR spectra of all of my samples, and has recorded just as many spectra since I left. Nasima also generated some of the figures in this chapter (Figures 3.5, 3.6, 3.17, 3.18, 3.19 and 3.20), and performed all of the fits to the $^{27}$Al MAS and MQMAS spectra, which is a significant amount of time and effort. I am very grateful for her assistance and expertise.

# Chapter 4: Pressure effect on partitioning of $Ge^{4+}$ between olivine and silicate melt

**Abstract—**I test the hypothesis that the olivine–melt partitioning of $Ge^{4+}$ is affected by the coordination changes of $Ge^{4+}$ and/or $Al^{3+}$ in silicate melts with pressure. Olivine–melt partitioning experiments were conducted over a pressure range from 0.5 to 4.5 GPa. The experiments were buffered at high oxygen fugacity to ensure only $Ge^{4+}$ (and not $Ge^{2+}$) was present. From 0.5 to 4.5 GPa, the Ge–Si distribution coefficient decreases by about two log units. The decrease with pressure is not as steep as previous studies have suggested. However, the oxygen fugacity in these previous experiments was not buffered, and therefore the data may reflect a mixture of $Ge^{4+}$ and $Ge^{2+}$. A thermodynamic treatment of the effect of pressure on the partitioning of $Ge^{4+}$ indicates that the Ge–Si distribution coefficient is expected to increase with pressure, whereas the data show the opposite. To model how the coordination changes of $Ge^{4+}$ and/or $Al^{3+}$ affect the partition coefficients will require a new form of an equation of state. Such a model has great potential for understanding how pressure affects trace element partitioning in general.

## 4.1 Introduction

In Chapter 2, it was shown that $Ge^{4+}$ changes its coordination with pressure in silicate melts. In this chapter, I determine the partitioning behaviour of $Ge^{4+}$ as a function of pressure, to investigate how the partitioning is influenced by the changing coordination of Ge, and possibly Al, with pressure.

I chose to investigate olivine–melt partitioning, because olivine has a well-defined structure, with a well-defined thermal expansion and compressibility. Therefore, changes in olivine–melt partitioning can be more easily interpreted in terms of their relationship to structural changes in the melt phase.

The olivine–melt partitioning behaviour of $Ge^{4+}$ was first studied by Capobianco and Watson (1982). These authors showed that $Ge^{4+}$ partitioning at ambient pressure had a weak dependence on temperature and $SiO_2$ content of the silicate melt. They also report the results of one experiment at 2 GPa, which had a lower partition coefficient than the ambient pressure experiments.

The change in partitioning with pressure can, in principle, be predicted from thermodynamic data for components in the exchange reaction:

$$\mathrm{Mg_2SiO_4}^{\mathrm{Fo}} + \mathrm{GeO_2}^{\mathrm{melt}} \leftrightharpoons \mathrm{Mg_2GeO_4}^{\mathrm{Fo}} + \mathrm{SiO_2}^{\mathrm{melt}}$$

Equation 4.1

where the superscripts indicate the phase (Fo = forsterite). The distribution coefficient for this reaction is the ratio of Ge and Si partition coefficients:

$$K_{D}{}^{ol-melt}_{Ge-Si} = \frac{D_{Ge}^{ol-melt}}{D_{Si}^{ol-melt}} = \frac{X_{Ge}^{ol}/X_{Ge}^{melt}}{X_{Si}^{ol}/X_{Si}^{melt}}$$

Equation 4.2

where *D* is the partition coefficient, $K_D$ is the distribution coefficient, and *X* indicates mole fraction. When $K_D$ is related to the equilibrium constant for the reaction, $K_{eq}$, the change of $K_D$ with pressure at constant temperature depends only on the volume change of the reaction ($\Delta_r V$), if it is assumed that the volumes of each component, as well as activity coefficients are independent of pressure. The change of $K_D$ with pressure can then be defined as:

$$\ln K_{D\,P2} = \ln K_{D\,P1} - \frac{1}{RT} \Delta_r V_{T,1bar}(P_2 - P_1)$$

Equation 4.3

where T is temperature, P is pressure and R is the ideal gas constant.

Capobianco and Watson (1982) collated data for molar volumes of the components in the exchange reaction, from which it can be shown that $\Delta_r V$ is negative; the volume term in Equation 4.3 is therefore positive and $\ln K_D$ should increase with pressure. However, Capobianco and Watson neglected the negative in front of the volume term, leading them to erroneously state that the observed decrease in $K_D$ was consistent with what was predicted from the volume change of reaction. In fact, the predicted change is opposite to the change they observed.

There have been no systematic studies of Ge partitioning with pressure. Besides Capobianco and Watson, only four other studies have reported olivine–melt partition coefficients for Ge at high pressures, and many of these data points have large error bars (Adam and Green 2006; Imai et al. 2012; Davis et al. 2013; Le Roux et al. 2015). However, these data all show a decrease with higher pressures and temperatures, consistent with the single data point from Capobianco and Watson at 2 GPa.

All of these experiments were conducted in graphite capsules. The experiments are therefore at relatively low, and unbuffered $fO_2$ conditions, leading to the possibility of $Ge^{2+}$ forming. As shown in Chapter 5, $Ge^{2+}$ is highly incompatible.

In this chapter, I conduct a systematic study of $Ge^{4+}$ partitioning between olivine and melt at a range of pressures (0.5–4.5 GPa) and temperatures (1320–1650 °C). The experiments are done in piston-cylinder apparatuses in platinum capsules, buffered at high oxygen fugacity to ensure only $Ge^{4+}$ is present. I will also present a more detailed attempt at predicting the change in partitioning with pressure based on the volume change of the reaction. The fact that this cannot reproduce the observed data indicates that (a) Ge is likely to be undergoing a coordination change in the silicate melt, and (b) any predictive model for partition coefficients with pressure needs to account for structural changes in the melt phase.

## 4.2 Methods

### *Sample synthesis*

Samples were prepared from three starting compositions, named ‘CMAS40’, ‘W98’ and ‘W98+Fo’. W98 is loosely based on a melt composition from Walter (1998). Nominal compositions of the starting materials are listed in Table 4.1. These starting materials were synthesised from reagent grade $SiO_2$, $Al_2O_3$, MgO, and $TiO_2$ (all dried at 1000 °C), $Na_2CO_3$, $K_2CO_3$ and $Ca_3(PO_4)_2$ (all dried at 200 °C), and $CaCO_3$, $Fe_2O_3$, (which were not dried prior to weighing). Trace elements Ge, Ni, Co, Mn, V, Sc, Y and Cr were added as oxides. These reagents were mixed under acetone under an agate mortar, and dried as a powder at 110°C. The mix was then pelletised and decarbonated by firing in air at 1050 °C.

Table 4.1. Nominal starting compositions.

| | CMAS40** | W98 | W98+Fo |
|---|---|---|---|
| | | Major elements (wt%) | |
| $SiO_2$ | 47.79 | 40.21 | 40.34 |
| $Al_2O_3$ | 6.59 | 6.20 | 5.64 |
| MgO | 40.81 | 20.49 | 23.31 |
| CaO | 3.15 | 8.00 | 7.28 |
| FeO* | | 11.59 | 11.13 |
| $TiO_2$ | | 4.50 | 4.09 |
| $Na_2O$ | | 3.50 | 3.19 |
| $K_2O$ | | 3.50 | 3.19 |
| $P_2O_5$ | | 0.90 | 0.82 |
| | | Trace elements (ppm) | |
| $GeO_2$ | 4617 | 5160 | 4697 |
| NiO | | 1020 | 928 |
| CoO | | 989 | 901 |
| MnO | | 1060 | 965 |
| $V_2O_5$* | 1238 | 520 | 473 |
| $Sc_2O_3$ | 295 | 240 | 218 |
| $Y_2O_3$ | 10511 | 1080 | 983 |
| $Cr_2O_3$ | | 940 | 856 |

*Of the CMAS40 samples, only C4444, D2413, D2374 and C5299 contained $V_2O_5$.

To reduce the iron in W98 compositions, the pellet was fired again at 1000 °C in a vertical gas-mixing furnace, in an atmosphere of 20% CO, 80% $CO_2$. W98+Fo was prepared by adding 10 wt% of a mix of forsterite ($Fo_{90}$) composition to a batch of the W98 composition. The forsterite mix was prepared from MgO, $SiO_2$ and $Fe_2O_3$ powdered oxides, mixed under acetone and dried at 110 °C; iron in this mix was not reduced prior to adding it to the W98 composition.

The W98 composition was re-fired at 20% CO and 80% $CO_2$ twice during the several years of the project. The initial batch of W98 is labelled W98.1, with the last digit increasing each time the powder was fired again. This was done because the powder may have absorbed some $CO_2$ from the atmosphere over time.

One batch of CMAS40 composition, which was used for just one sample in this study (D2413), was prepared differently to the rest. The major elements were mixed together as powdered oxides and carbonates as described above, along with $TiO_2$, $HfO_2$ and $SrCO_3$. However, the trace elements Y, Sc, V, Mn, Ba, Zn and Zr were added as stock solutions (all dissolved in 2% or 10% $HNO_3$, except for Zn which was dissolved in 2% HCl). The powders and solutions were mixed together thoroughly in an agate mortar and left to dry. The resulting powder was then denitrified by heating it in a Pt crucible over a Bunsen burner, and then decarbonated by firing as a pellet at 1050 ºC overnight. Finally, powdered $GeO_2$ was mixed in under acetone; this final composition was then dried at 110 ºC. Trace element concentrations in this sample (D2413) are listed in Table 4.2, as they are somewhat different to the other samples of CMAS40 composition.

Table 4.2. Trace element concentration in sample D2413.

| | Concentration (ppm) |
|---|---|
| $GeO_2$ | 2728 |
| $TiO_2$ | 5164 |
| $HfO_2$ | 1656 |
| SrO | 1368 |
| $Y_2O_3$ | 5023 |
| $Sc_2O_3$ | 601 |
| $V_2O_5$ | 1774 |
| $MnO_2$ | 308 |
| BaO | 5450 |
| ZnO | 242 |
| $ZrO_2$ | 1329 |

Experiments were conducted using 200 T end-loaded Boyd-England type piston cylinder apparatuses. Each sample was prepared by loading ~20 mg of the oxide starting material into a 2.3 mm diameter Pt capsule, with ~2 mg of a Ru-$RuO_2$

oxygen buffer mix (80% $RuO_2$, 20% Ru) packed at each end of the capsule. The Ru-$RuO_2$ buffer is highly oxidising ($fO_2$ similar to that of air; e.g. log$fO_2$ = -0.7 at 1400 ºC). Before welding the capsules shut, they were crimped loosely and dried at 110 °C overnight. Capsules were placed in an assembly composed of MgO, graphite, Pyrex and NaCl (see Chapter 2). This assembly was wrapped in Teflon foil and inserted into a 1/2" pressure vessel. A Type B thermocouple, sheathed in mullite with a 5 mm alumina tip, was inserted through a bore in the top MgO spacer. The samples were equilibrated for 4–48 h, at the temperatures and pressures listed in Table 4.3. The samples were quenched by cutting power to the graphite heater.

Some attempts were made at preparing samples at ambient pressure in vertical gas-mixing furnaces, however the crystals grown in these samples were not large enough for LA-ICPMS.

Table 4.3. Experimental conditions.

| Sample Name | Pressure (GPa) | Temperature (ºC) | Time (h) | Composition |
|---|---|---|---|---|
| D1515 | 0.5 | 1450 | 24 | CMAS40 |
| C4444 | 1 | 1500 | 24 | CMAS40 |
| D2413 | 1 | 1500 | 24 | CMAS40 |
| C4396(3) | 1.5 | 1550 | 6 | CMAS40 |
| D2374 | 2 | 1575 | 24 | CMAS40 |
| D1517 | 2.5 | 1600 | 6 | CMAS40 |
| C5299 | 3.3 | 1650 | 5.5 | CMAS40 |
| C4396(4) | 3.5 | 1650 | 4 | CMAS40 |
| D2411 | 1 | 1320 | 42 | W98.3 |
| D2427 | 1.74 | 1355 | 42 | W98.3 |
| C4451 | 3 | 1500 | 24 | W98.1 |
| C4735 | 3.5 | 1470 | 24 | W98.2 |
| D1715 | 3.5 | 1450 | 24 | W98.2 |
| D1703 | 4 | 1500 | 24 | W98.2 |
| D2472 | 4 | 1490 | 24 | W98.3 |
| C4650 | 2 | 1400 | 23 | W98.2+Fo |
| D1718 | 3.5 | 1500 | 24 | W98.2+Fo |
| D1758 | 4 | 1550 | 24 | W98.2+Fo |
| C4757 | 4.5 | 1550 | 15 | W98.2+Fo |
| C4521 | 4.5 | 1500 | 20 | W98.3+Fo |

### *Major and trace element analysis*

After the experimental runs, charges were mounted in epoxy, sectioned and polished. The major element compositions of olivine and melt in each sample were determined using a Hitachi S-4300 SE/N Field Emission Scanning Electron Microscope (FE-SEM) fitted with an Oxford X-Max EDS detector. The accelerating voltage used was 15 kV, the beam current was 0.600 nA and the working distance was 25 mm. Standards used to calibrate element concentrations were as follows: Albite (Na, Al), MgO (Mg), Sanidine (Si), Diopside (Ca), $TiO_2$ (Ti), $Fe_2O_3$ (Fe), $YP_5O_{14}$ (Y), NaCl (Cl). A PAP matrix correction was used. Point analyses were used for olivine crystals, but since an average composition for the quenched melt was needed, large (up to 200 x 200 μm) area analyses were used on the melt phase. Areas chosen for analysis were typically in the regions of fewer or smaller quench crystals, and cracks in the sample were avoided.

Trace element abundances in olivine and melt in each sample were determined using Laser Ablation Inductively Coupled Plasma Mass Spectrometry (LA-ICPMS). The laser ablation system consists of an eximer laser (Lambda Physik Complex 110, wavelength 193 nm) with a HelEx ablation chamber (designed at ANU) coupled to an Agilent 7700 ICP-MS. The carrier gas used was He. For each spot, 20 s of background was measured before ablating the sample for ~40 s, at a laser pulse rate of 5 Hz. Spot sizes of 22 – 62 μm were used; the smallest spot sizes were used when crystals were very small.

The external standard used was NIST 610 glass; this was analysed at the beginning of each analytical session and then after every ~10 spots. $SiO_2$ was chosen as the internal standard; this was determined by FE-SEM. A secondary standard was also analysed at regular intervals; the standard used was either NIST-612 (Jochum, 2011) or BCR-2G (Wilson, 1997). An in-house Excel spread sheet was used to reduce data from LA-ICPMS.

## 4.3 Results

Backscattered electron (BSE) images of typical run products are shown in Figure 4.1. Melt in samples made <2 GPa quenched to a nice glass (e.g. Figure 4.1A, D2427), but in samples made at higher pressures, the melt phase contains variably sized quench phases – skeletal olivines with long rod-like shapes that in some samples are up to 1 mm long (as shown in Figure 4.1C, D2374).

Analytical totals for FE-SEM analyses were typically 99–101 wt% for olivine crystals, but ranged from 91–98 wt% for the melt phases. This may be due to the presence of some water dissolved in the melt, and/or due to the slightly rough surface resulting from the quench crystals present in many samples. In C4444 and C4396(3), many small vesicles were observed in the melt residue between quench crystals, as shown in Figure 4.1D.

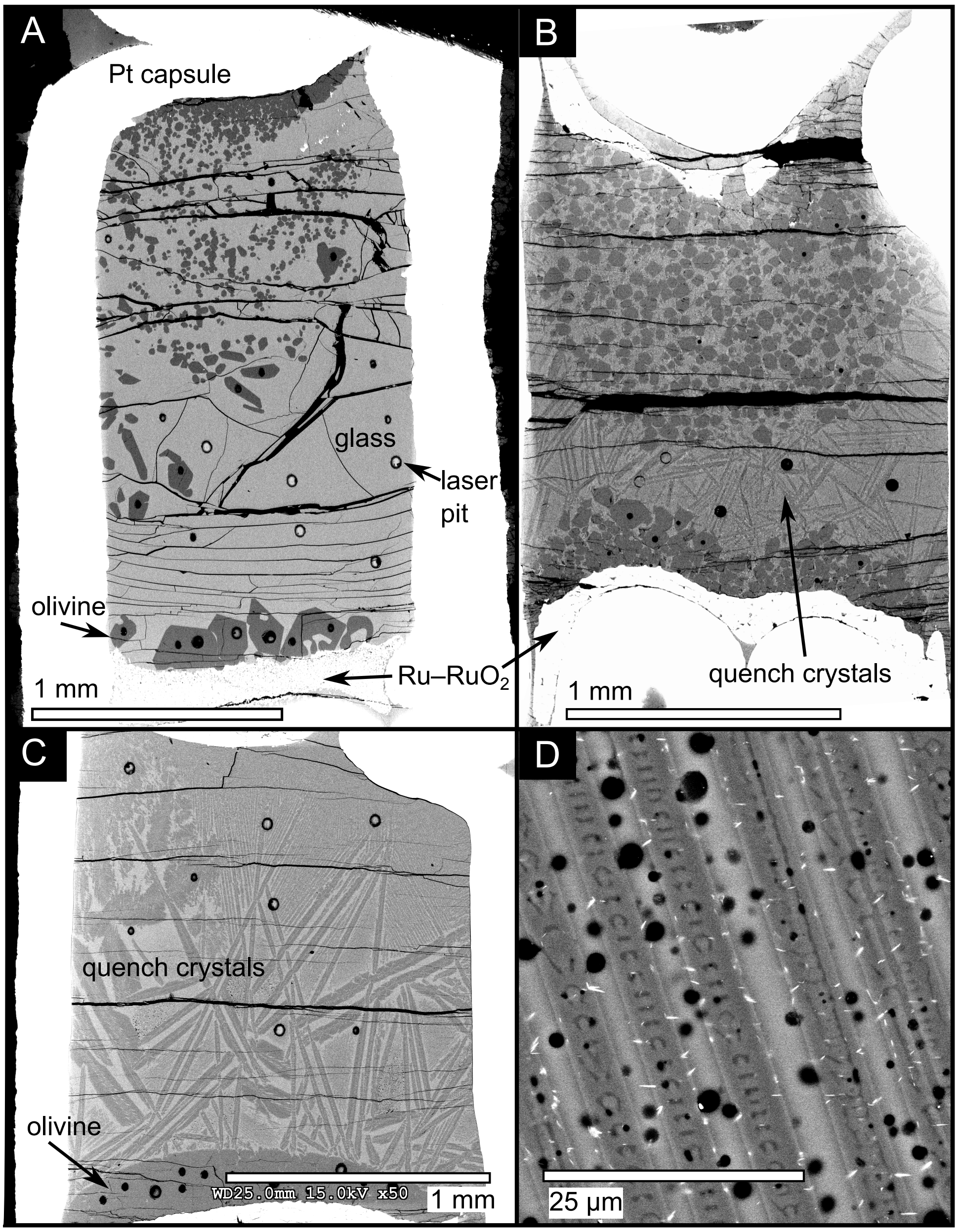

Figure 4.1. Backscattered electron (BSE) images of (A) D2427, (B) C5299, (C) D2374, and (D) a close-up of the melt phase in C4444 showing quench crystals and vesicles.

Major and trace element compositions of run products are given in the supplementary material, Section 7.6, p.209. Calculated partition and distribution coefficients are given in Table 4.4.

Table 4.4. Olivine–melt partition and distribution coefficients

| Sample | P (GPa) | T (ºC) | $D_{Si}$ | sd | $D_{Ge}$ | sd | $K_{D\ Ge\text{–}Si}$ | sd | $K_{D\ Ge\text{–}Si}$ | sd |
|---|---|---|---|---|---|---|---|---|---|---|
| D1515 | 0.5 | 1450 | 0.84 | 0.01 | 0.61 | 0.02 | 0.72 | 0.02 | -0.33 | 0.03 |
| C4444 | 1 | 1500 | 0.91 | 0.01 | 0.57 | 0.01 | 0.63 | 0.01 | -0.47 | 0.02 |
| D2413 | 1 | 1500 | 0.89 | 0.02 | 0.59 | 0.02 | 0.66 | 0.02 | -0.41 | 0.03 |
| C4396(3) | 1.5 | 1550 | 0.87 | 0.00 | 0.56 | 0.01 | 0.64 | 0.01 | -0.44 | 0.02 |
| D2374 | 2 | 1575 | 0.87 | 0.02 | 0.53 | 0.03 | 0.61 | 0.03 | -0.49 | 0.05 |
| D1517 | 2.5 | 1600 | 0.88 | 0.01 | 0.51 | 0.01 | 0.58 | 0.01 | -0.55 | 0.02 |
| C5299 | 3.3 | 1650 | 0.85 | 0.01 | 0.48 | 0.02 | 0.56 | 0.02 | -0.57 | 0.04 |
| C4396(4) | 3.5 | 1650 | 0.85 | 0.01 | 0.49 | 0.02 | 0.57 | 0.02 | -0.56 | 0.04 |
| D2411 | 1 | 1320 | 1.05 | 0.01 | 0.73 | 0.03 | 0.70 | 0.03 | -0.36 | 0.04 |
| D2427 | 1.74 | 1355 | 1.06 | 0.01 | 0.69 | 0.03 | 0.66 | 0.03 | -0.42 | 0.04 |
| C4451 | 3 | 1500 | 1.07 | 0.02 | 0.68 | 0.02 | 0.63 | 0.02 | -0.46 | 0.04 |
| C4735 | 3.5 | 1470 | 1.05 | 0.01 | 0.66 | 0.03 | 0.63 | 0.03 | -0.47 | 0.04 |
| D1715 | 3.5 | 1450 | 1.08 | 0.01 | 0.62 | 0.02 | 0.57 | 0.02 | -0.57 | 0.03 |
| D1703 | 4 | 1500 | 1.06 | 0.01 | 0.65 | 0.01 | 0.61 | 0.01 | -0.49 | 0.02 |
| D2472 | 4 | 1490 | 1.07 | 0.01 | 0.61 | 0.01 | 0.57 | 0.01 | -0.56 | 0.02 |
| C4650 | 2 | 1400 | 1.07 | 0.01 | 0.69 | 0.01 | 0.64 | 0.01 | -0.44 | 0.02 |
| D1718 | 3.5 | 1500 | 1.10 | 0.02 | 0.58 | 0.02 | 0.53 | 0.02 | -0.64 | 0.03 |
| D1758 | 4 | 1550 | 1.09 | 0.01 | 0.59 | 0.02 | 0.55 | 0.02 | -0.60 | 0.03 |
| C4757 | 4.5 | 1550 | 1.06 | 0.01 | 0.60 | 0.01 | 0.57 | 0.01 | -0.57 | 0.02 |
| C4521 | 4.5 | 1500 | 1.14 | 0.02 | 0.65 | 0.04 | 0.56 | 0.03 | -0.57 | 0.06 |

The combined effects of pressure and temperature on ln$K_D$ can be seen in Figure 4.2. Pressure and temperature are highly correlated, because the conditions of the experiments followed the liquidus up in pressure and temperature. It is clear that ln$K_D$ decreases with increasing pressure and/or temperature.

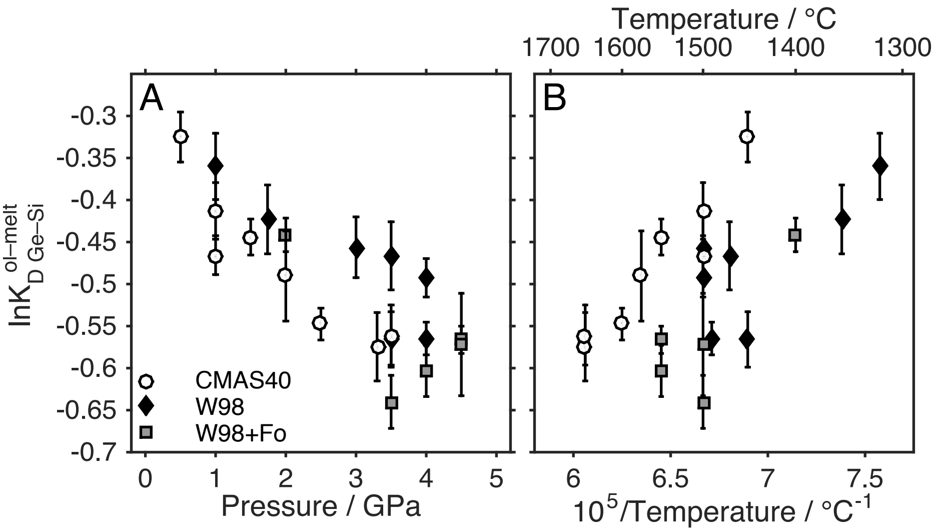

Figure 4.2. ln$K_D$ plotted against pressure (A) and inverse temperature (B).

To isolate the pressure effect from the temperature effect, values of ln$K_D$ were fit to an equation of the form

$$\ln K_D = a + \frac{b}{T} + \frac{c * P}{T}$$

Equation 4.4

where $a$, $b$ and $c$ are the fit parameters, proportional to the enthalpy, entropy and volume changes of the reaction respectively. Fit parameters derived using a least squares fitting method in MATLAB (The MathWorks Inc. 2015) are $a = -0.98 \pm 0.43$, $b = (8.8 \pm 6.2) \times 10^2$ and $c = -61 \pm 24$. The fit can be seen in Figure 4.3, along with the 95% confidence interval on the predicted values. This confidence interval gives a better indication of how well the fit reproduces the data than the errors on individual fit parameters, which are highly correlated.

To illustrate how the data is scattered around the fitted plane, the data has been projected onto a single temperature in Figure 4.3A, and a single pressure in Figure 4.3B. To achieve this projection, the deviation of the data points from the predicted value at their original pressure and temperature was calculated. The data were then plotted with the same deviation from the predicted values at 1500 °C or 3 GPa.

From these results, it can be seen that pressure has a greater effect than temperature on the partition coefficients. This is evident because of the steeper negative slope of the pressure effect compared to the temperature effect. However, more data would be needed to really constrain these competing effects. In addition, the parameterisation does not consider the effect of composition.

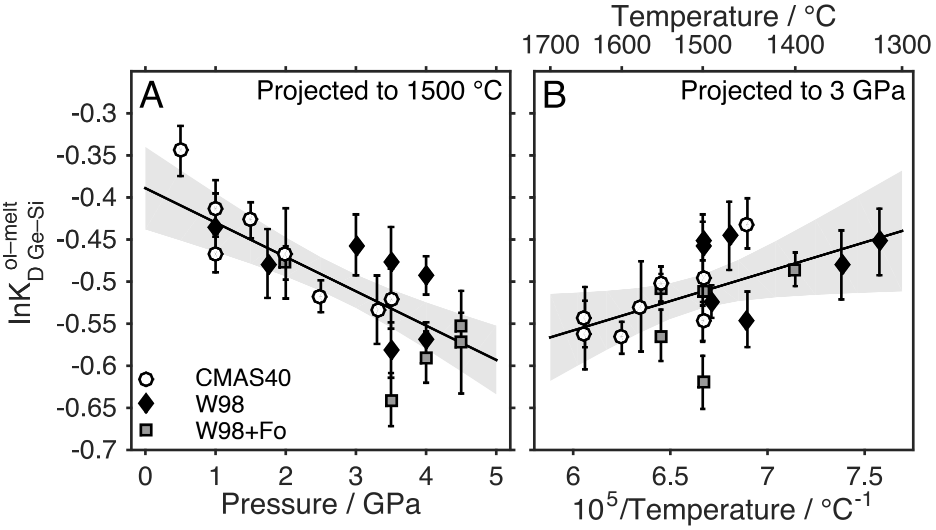

Figure 4.3. The fit to ln$K_D$ data using Equation 4.4, shown as the black line with 95% confidence intervals indicated by the grey regions. In (A), the fit is shown for a single temperature (1500 ºC) as a function of pressure; in (B) the fit is shown and at a single pressure (3 GPa) as a function of inverse temperature. To 'project' the data points onto 1500 ºC (in A) or 3 GPa (in B), the points are offset from the fit by their deviations from the predicted value at their original pressure and temperature. This is done to illustrate the scatter in the data around the fit.

## 4.4 Discussion

### *Are the samples in equilibrium?*

Our interpretations of the Ge partitioning results rely on the samples being in equilibrium. If the diffusion of Ge is too slow through the mineral or melt phases, the partition coefficients may not represent a true equilibrium value.

Diffusion of Ge through silicate melt has been measured in only two studies: Mungall et al. (1999) and Hahn et al. (2005). Both studies showed that Ge diffusion in rhyolitic melts was comparable to the diffusion of network formers predicted by the Eyring equation, which relates diffusivity to viscosity of the melt. Thus, Ge diffusion through more basaltic compositions, relevant to this study, can be reasonably estimated from the diffusion of Si. For example, Lesher et al. (1996) measured Si diffusion through a basaltic melt at 1400 ºC and 2 GPa and determined a diffusion coefficient of $2.9 \times 10^{11}$ m$^2$/s. Based on the simple approximation $x^2 = Dt$, where $x$ is distance, $D$ is the diffusion coefficient and $t$ is time, Si would be expected to diffuse 1.6 mm in 24 h through the melt. This diffusion length should be sufficient to avoid any significant heterogeneity in Ge concentration in the melt phase.

However, diffusion through the crystal will be much slower. Germanium diffusion has not been measured in olivine, but probably behaves comparably to Si. Recent measurements of relatively fast Si diffusion through olivine by Fei et al. (2012) give diffusion coefficients on the order of $10^{-19}$ $m^2/s$ at ~1500 °C. The $x^2 = Dt$ approximation indicates that Si would diffuse through olivine only 0.2 um in 24 h.

Thus, it is expected that Ge will not diffuse at all through the crystals but will probably diffuse fast enough to maintain equilibrium in the melt. As olivine crystals grow from small crystal nuclei, they will incorporate some Ge into the structure. The amount of Ge incorporated would be determined by its partition coefficient, which is less than one. As such, as a crystal grows, Ge will become slightly enriched in the melt surrounding the growing crystal. The quenched melt should not show this heterogeneity because diffusion should be fast enough to equilibrate the Ge concentration on the time scale of the experiment. Therefore, diffusion of Ge through the crystal is not necessary to maintain an equilibrium partition coefficient. Thus it is reasonable to expect that the data reflect true equilibrium partition coefficients.

### *Comparison to previous work*

Olivine–melt partition coefficients for Ge have been measured by several previous studies, at pressures from 1 atm to 10 GPa. The data from these studies are summarised in Table 4.5.

Table 4.5. Compilation of literature data for olivine–melt partitioning of Ge (expressed as ln$K_D$ where $K_D$ is the Ge–Si distribution coefficient between olivine and melt).

| Study | Sample | T (°C) | Pressure | Capsule | ln$K_D$ | s.d. |
|---|---|---|---|---|---|---|
| C&W 82 | 2h1.5 | 1400 | 1 atm | Pt95Au5 | −0.36 | 0.04 |
| C&W 82 | 2h.5 | 1400 | 1 atm | Pt95Au5 | −0.35 | 0.09 |
| C&W 82 | 3b | 1400 | 1 atm | Pt95Au5 | −0.31 | 0.10 |
| C&W 82 | 3c | 1400 | 1 atm | Pt95Au5 | −0.32 | 0.11 |
| C&W 82 | 3e | 1400 | 1 atm | Pt95Au5 | −0.43 | 0.21 |
| C&W 82 | 3g | 1400 | 1 atm | Pt95Au5 | −0.24 | 0.20 |
| C&W 82 | 3f | 1400 | 1 atm | Pt95Au5 | −0.36 | 0.17 |
| C&W 82 | 4e | 1450 | 1 atm | Pt95Au5 | −0.31 | 0.06 |
| C&W 82 | 7e | 1350 | 1 atm | Pt95Au5 | −0.25 | 0.17 |
| C&W 82 | 7g | 1350 | 1 atm | Pt95Au5 | −0.24 | 0.13 |
| C&W 82 | 7f | 1350 | 1 atm | Pt95Au5 | −0.14 | 0.10 |
| C&W 82 | 8g | 1300 | 1 atm | Pt95Au5 | −0.13 | 0.09 |
| C&W 82 | 8f | 1300 | 1 atm | Pt95Au5 | −0.19 | 0.10 |
| M&D 87 | 32.1B | 1300 | 1 atm | Pt | −0.29 | 0.19 [#] |
| M&D 87 | 32CD | 1300 | 1 atm | Pt | −0.31 | 0.12 [#] |
| M&D 87 | 35AB | 1300 | 1 atm | Pt | −0.36 | 0.25 [#] |
| M&D 87 | 35C | 1300 | 1 atm | Pt | −0.30 | 0.03 [#] |
| K 93 | PO 49 | 1525 | 1 atm | None; $fO_2$ fixed at IW −0.5 | −2.08 | 0.41 |
| C&W 82 | HP | 1500 | 2 GPa | C | −0.45 | 0.07 |
| M 94 | D1 | 2080 | 10 GPa | Re | −1.20 | † |
| A&G 06 | R77 | 1100 | 2 GPa | C in Pt | −0.57 | 0.03 |
| A&G 06 | R79 | 1075 | 1 GPa | C in Pt | 0.02 | 0.04 |
| I 12 | P777 | 1700 | 2 GPa | C in Pt | −0.53 | 0.22 |
| I 12 | S1606 | 1850 | 5 GPa | C | −1.26 | 0.40 |
| I 12 | S1615 | 1850 | 5 GPa | C | −1.61 | 0.18 |
| I 12 | S1605 | 2150 | 10 GPa | C | −1.45 | 0.41 |
| I 12 | S1614 | 2150 | 10 GPa | C | −1.31 | 0.25 |
| D 13 | Average of 11 experiments* | ~1465 | 3 GPa | C in Pt | −0.82 | 0.17 |
| LeR 15 | G81 | 1450 | 2 GPa | C | −0.36 | 0.12 |
| LeR 15 | G84 | 1500 | 2 GPa | C | −0.43 | 0.14 |
| LeR 15 | G107 | 1325 | 1.5 GPa | C | −0.18 | 0.12 |
| LeR 15 | G109 | 1300 | 1.5 GPa | C | −0.06 | 0.12 |

* Davis et al. 2013 reports Ge partitioning data for 11 experiments, all conducted at the same pressure (3 GPa) and at similar temperatures (1460–1475 °C). Since there were no obvious correlations of ln$K_D$ with any compositional variable, the data have been averaged. The standard deviation reported here is the standard deviation of all ln$K_D$ values, which ranged from −0.48 ± 0.03 to −1.05 ± 0.22. The abbreviations for studies used in this table and in subsequent figures are: C&W 82 (Capobianco and Watson 1982), M 94 (McFarlane 1994), M&D 87 (Malvin and Drake 1987), K 93 (Kennedy et al. 1993), LeR 15 (Le Roux et al. 2015), D 13 (Davis et al. 2013), A&G 06 (Adam and Green 2006) and I 12 (Imai et al. 2012). [#] Malvin and Drake (1987) do not report an error on the Si analyses of each phase, so the standard deviation reported here is based only off the error they report on the Ge partition coefficient. † No error was reported on the data point from McFarlane (1994). In the figures below and in fits to the literature data, a 20% error is assumed.

The temperature-dependence of partitioning obtained in this study is compared to previous work at ambient pressure in Figure 4.4. In this figure, data from this study are projected onto a pressure of 1 atm using Equation 4.4. Literature data from the ambient-pressure experiments of Capobianco and Watson (1982) and Malvin and Drake (1987) are plotted for comparison. The data from the literature have such large error bars that they cannot define a clear trend as a function of temperature; however the literature data are perfectly consistent with the trend defined by the data from this work (shown as the black line and grey limits of error).

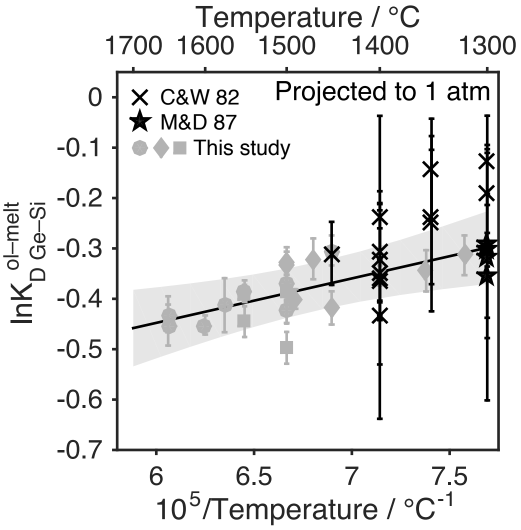

Figure 4.4. Temperature dependence of $\ln K_D$ at ambient pressure. Data from this study is projected to 1 atm pressure for comparison to ambient-pressure data from the literature (Capobianco and Watson 1982; Malvin and Drake 1987).

However, the ambient-pressure partition coefficient measured by Kennedy (1993) of -2.08 is not plotted because it is significantly lower than all the other data. The value is probably not reliable for two reasons. Firstly, the author does not report a capsule material, so the experiment was most likely conducted on a loop exposed to the furnace; this means Ge could have escaped from the sample during the run, due to its moderate volatility. Secondly, the $fO_2$ of the experiment was IW -0.5. At this $fO_2$, it is expected that a substantial fraction (~64%) of the Ge will have a 2+ valence, and $Ge^{2+}$ is highly incompatible (see Chapter 5). Thus, the low partition coefficient obtained by Kennedy (1993) is unlikely to be an equilibrium partition coefficient for $Ge^{4+}$.

Figure 4.5 shows the high-pressure literature data compared to the data collected in this study. In this figure, the data are not projected onto any pressure or temperature. Error bars on most of the literature data are much larger than the errors on data from this study, but the literature data still appear to show a fairly well defined trend with pressure, which is a lot steeper than the trend obtained by this study.

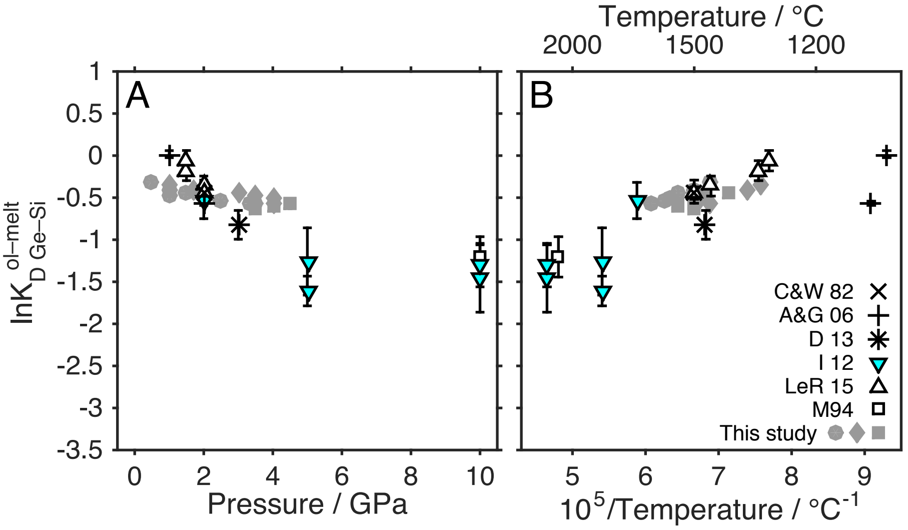

Figure 4.5. Comparison of the data presented in this study to literature data at high pressure. In this figure, neither my data nor the literature data have been projected onto a temperature or pressure, so the trends observed could reflect either or both variables in each plot.

When the literature data are fit to Equation 4, the trend as a function of pressure becomes even steeper, and the trend as a function of temperature reverses in direction. Fit parameters derived using a least-squares fitting algorithm in MATLAB are $a = 0.045 \pm 0.88$, $b = 302 \pm 869$ and $c = -462 \pm 170$. Figure 4.6 shows these literature data projected onto constant temperature (in A) and constant pressure (in B) using the fit described above. The literature data can then be compared to the data from this study, which are plotted as grey symbols with the fit shown as a black line with grey margins of error. The trend seen in the literature data is quite different to the trend of data in this study.

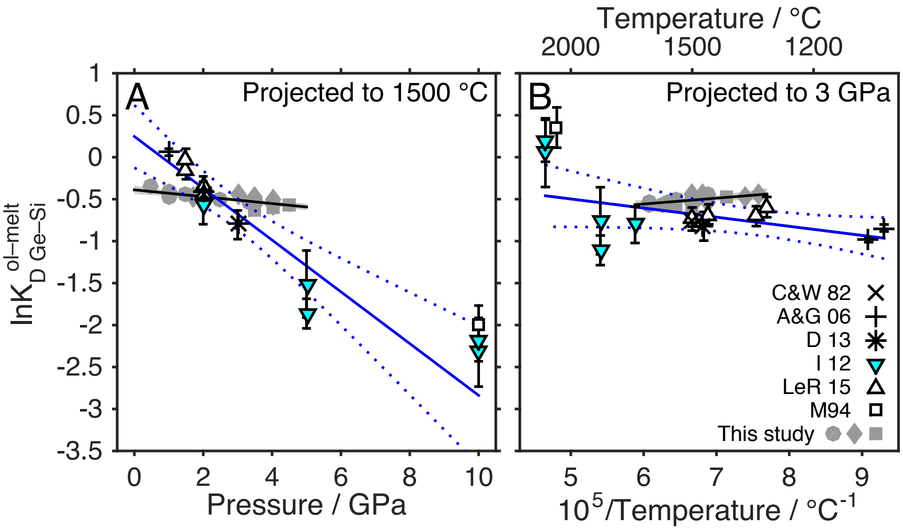

Figure 4.6. Comparison of the data presented in this study to literature data at high pressure. In this figure, I have corrected the data using two fits. My data has been projected to 1500 C or 3 GPa using the fit described in the text; literature data has been fit separately to the same equation. The fit to the literature data is given by the blue line and the dotted curves are the 95% confidence intervals on predicted values for this fit.

The reason that literature data show a different pressure-dependence than the data from this study may be a component of $Ge^{2+}$ in the experiments, because all but one of the experiments reported so far in the literature were done in graphite capsules (some with a Pt outer capsule). The only exception is the data point of McFarlane (1994), which was an experiment in a Re capsule, but no error was reported for this partition coefficient (a 20% error was assumed for the plots and the fit to the literature data). The $fO_2$ was not buffered in any of these experiments, but in the experiments done in graphite capsules, $fO_2$ must be below the C-CO oxygen buffer (Médard et al. 2008).

The only study that attempted to determine $fO_2$ was Davis et al. (2013). Davis et al. calculated log$fO_2$ to be -6.4 and -5.9 (at 1470 °C and 3 GPa, equivalent to ΔIW +1.7 and +2.2) in two of their experiments, but not the same experiments for which Ge partition coefficients were measured. However, the experiments of Davis et al., as well as experiments of Adam and Green (2006) and Imai et al. (2012) report vanadium partition coefficients, which can be used to calculate $fO_2$ using Equation 15 in Mallmann and O'Neill (2009). Using V partitioning, the average $fO_2$ calculated from all data of the three studies is ΔIW -1.0, with a standard deviation of 0.3, and the average error on each calculated $fO_2$ is 0.4.

Based on the data presented in Chapter 5, the $Ge^{4+}$–$Ge^{2+}$ transition occurs over the range IW +2 to IW -2. Since the calculated $fO_2$ of experiments from literature studies, based on V partitioning, is within that range, it seems likely that a component of $Ge^{2+}$ would be present in many of these experiments. The fraction of $Ge^{2+}$ would be likely to vary somewhat between experiments (we have no constraints on how $Ge^{2+}$ responds to temperature, pressure or composition). Thus, I would argue that all existing high-pressure Ge partitioning data in the literature are unreliable, due to the likelihood of a mixture of 4+ and 2+ valence states.

Finally, one other factor that might affect the samples is the possible presence of dissolved water, which may affect partitioning to an unknown extent. If water concentration did differ substantially with pressure, our interpretation of the pressure effect on partitioning might be incorrect. However, there is no evidence that the water content does differ substantially with pressure, as all experiments were synthesised via the same methodology. Future work to analyse water concentrations and to repeat the partitioning experiments under dry conditions would be valuable to constrain these effects.

### *A thermodynamic evaluation of the effect of pressure on partitioning*

As described in the Introduction to this chapter, the simplest way to predict a change in $\ln K_D$ with pressure is to relate it to the $\Delta_r V$ (volume change of the exchange reaction) using Equation 4.3.

Capobianco and Watson (1982) calculated $\Delta_r V$ by taking the molar or partial molar volumes of each component in the reaction from the literature, and determined that $\Delta_r V$ was negative. A negative $\Delta_r V$ would imply an increase in $\ln K_D$ with pressure, but the data clearly indicate the opposite. Capobianco and Watson did not consider errors on the volumes of each component. To see if the observed data could be within error of the calculation, molar volumes from various literature sources, along with their errors (when reported) are compiled in Table 4.6. A ‘preferred’ $\Delta_r V$ is calculated based on the most up-to-date or appropriate molar volumes. In this context, ‘appropriate’ means values for partial molar volumes of $GeO_2$ and $SiO_2$ in multicomponent melts, rather than values for molar volumes of pure $GeO_2$ or $SiO_2$ liquids. A minimum and maximum $\Delta_r V$ is also calculated by taking the extreme values and their errors.

The preferred $\Delta_r V$, as well as the minimum and maximum values for $\Delta_r V$ are all negative, though there is a substantial range in their values. The predicted change in $\ln K_D$ can be then calculated using Equation 4.3, where the value for $\ln K_{D\,PI}$ at 1500 °C (P1 = 1 atm) is fixed as -0.37 (determined using the fit to the data). The result of this calculation is shown in Figure 4.4.4, in comparison with the data projected onto a temperature of 1500°C. The predicted and observed values show the opposite trends, even when the maximum $\Delta_r V$ is considered.

Table 4.6. Literature data for molar volumes of components in Equation 4.1.

| Component | Molar volume at 1500 °C ($cm^3$ $mol^{-1}$) | Reference |
|---|---|---|
| $Mg_2SiO_4$ olivine | 46.28 ± 0.03 * | Holland and Powell (1998); Robie and Hemmingway (1995) |
| | 46.12 ± 0.06 | Extrapolated using a 2nd order polynomial fit to the V/V0 data from Table 1 of Bouhifd et al. (1996) (error is taken from 1530 °C data point). |
| $Mg_2GeO_4$ olivine | 47.80 ± 0.11 * | Extrapolated from equation in Table 4 of Fiquet et al. (1992); relative error is assumed to be 0.23%; this is the same as on the highest temperature data point at 1400 °C |
| $SiO_2$ liquid | 26.88 ± 0.02 * | Partial molar volume of $SiO_2$ in an iron-free melt at 1500 °C from Table 6 of Lange and Carmichael (1987) |
| | 26.43 | Pure silica liquid; Holland and Powell (1998) |
| | 27.3 | Pure silica liquid; Holland and Powell (2011) |
| | 27.47 | Pure silica liquid; Mao et al. (2001) |
| $GeO_2$ liquid | 29.9 ± 0.34 | Pure $GeO_2$ liquid; Dingwell et al. (1993) |
| | 29.7 ± 0.24 * | Partial molar volume at infinite dilution of $GeO_2$ in AnDi liquids at 1527 ºC from Holzapfel et al. (2001). It is not possible to extrapolate this to 1500 °C. However the reported volumes from 1127 to 1527 °C are all within error. |
| | 30.3 | Pure $GeO_2$ liquid at 1400 ºC, extrapolated from measurements of binary oxides by Riebling (1963) |
| $\Delta_r V_{1500\,C,1bar}$ minimum | −2.36 ± 0.02 | |
| $\Delta_r V_{1500\,C,1bar}$ maximum | −0.55 ± 0.8 | |
| $\Delta_r V_{1500\,C,1bar}$ preferred | −1.14 ± 0.8 | |

*'Preferred' volumes are marked with an asterisk.

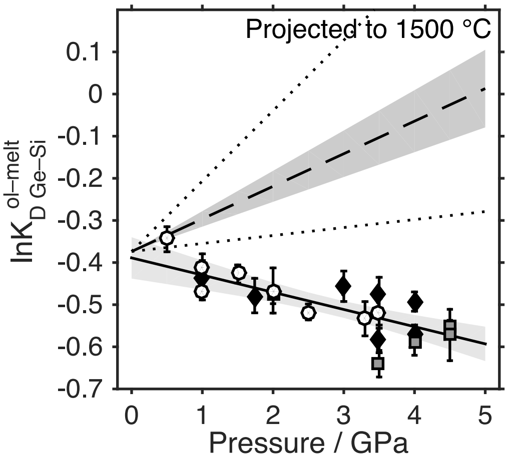

Figure 4.7. A comparison of my data, projected to 1500 C, to the predicted change in ln$K_D$ with pressure at 1500 C based on the volume change of Equation 4.1. Dashed line is the prediction from the preferred value of ∆V, grey region is the limits of error associated with this, and dotted lines are the predicted lnKd if the absolute minimum or maximum values of ∆V are taken. In all cases, the predicted lnKd increases with pressure, whereas the experimental data decrease.

The discrepancy between observed and predicted changes in ln$K_D$ with pressure could simply result from the molar volume of a component being incorrect. However, since a range of values for volumes of each component have been considered, and they are all fairly consistent with one another, this seems unlikely. Assuming the volumes are reasonable leaves us with two other options to explain the discrepancy: (i) the compressibility of the components; or (ii) a structural change occurring in the melt, such as a coordination change.

The simplification that volume is independent of pressure in Equation 4.3 can be removed if the pressure-dependence of volume is known. Then, the $\Delta_r V$ term is replaced with an integral of volume as a function pressure:

$$\ln K_{D\,P2} = \ln K_{D\,P1} - \frac{1}{RT}\,\Delta_r\left[\int_{P1}^{P2} V(P)_T\,dP\right]$$

Equation 4.5.

where $V(P)_T$ represents an expression for volume as a function of pressure at a given temperature; namely, an equation of state (EOS). There are many equations of state, but for this calculation the Murnaghan EOS was chosen due to its simplicity and tractability. The Murnaghan EOS is:

$$P = \frac{\kappa_T}{\kappa'_T}\left[\left(\frac{V_{1\ bar,T}}{V}\right)^{\kappa'_T} - 1\right]$$

Equation 4.6

where V is volume, $V_{1\ bar,\ T}$ is the ambient pressure molar volume, $\kappa_T$ is the bulk modulus and $\kappa'_T$ is the pressure derivative of the bulk modulus, all at the temperature of interest (indicated by the subscript T).

The value of $\kappa'_T$ for most crystalline geological materials is close to 4, so this approximation was used in the thermodynamic dataset of Holland and Powell (1998). The value of $\kappa'_T$ for melt components is not well known. Ghiorso (2004) suggested that it may be substantially higher, ~10–12. However, Rigden (1988) calculated κ' = 4.85 from the results of their shock compression experiments on anorthite-diopside melt performed. Regardless of the most appropriate value, κ' is a third order effect, and whether 4 or 12 is chosen will make little difference to the result at the fairly low pressures of interest here. Setting $\kappa'_T = 4$, the Murnaghan EOS can be rearranged and integrated:

$$\int_{1\ bar}^{P} V dP = \frac{V_{1\ bar,T}}{3}\left[\left(1 + \frac{4P}{\kappa_T}\right)^{3/4} - 1\right]$$

Equation 4.7

With this approach, all that is needed to adjust the previous calculation to incorporate the effect of pressure on volume is the value for $\kappa_T$ of each component. The $\kappa_T$ can be calculated from $\kappa_{298}$ (the bulk modulus at 298 K) using the following equation (Holland and Powell 1998):

$$\kappa_T = \kappa_{298}\left(1 - 1.5\times10^{-4}(T - 298)\right)$$

Equation 4.8

The mineral components, which are fairly incompressible, have large values of bulk modulus. Both the Si-forsterite and Ge-forsterite have $\kappa_{298}$ = 125 GPa (Liebermann 1975; Holland and Powell 1998), which equates to $\kappa_T$ = 97 GPa at 1500 °C using equation 8. The liquid components, on the other hand, are expected to be more compressible, but their bulk moduli are less well constrained. The bulk modulus for pure silica liquid is 58 GPa at 1500 °C (Holland and Powell 1998), whereas a value of 14 GPa was determined for $SiO_2$ in multicomponent silicate melts at 1400 °C (Kress and Carmichael 1991). The latter value is similar to values of bulk moduli ranging from 18–22 GPa for enstatite, wollastonite, diopside, anorthite and forsterite liquids determined by molecular dynamics simulations (Matsui 1996). Thus, as a generous assumption for bulk modulus, $\kappa_T = 14$ GPa is used for both $GeO_2$ and $SiO_2$ melt components.

The result of the calculation is shown in Figure 4.8. As shown, incorporating the pressure-dependence of volume introduces a curvature to the predicted values of $\ln K_D$ – the slope flattens out at higher pressures. However, this is still insufficient to explain the difference between the observed and predicted values.

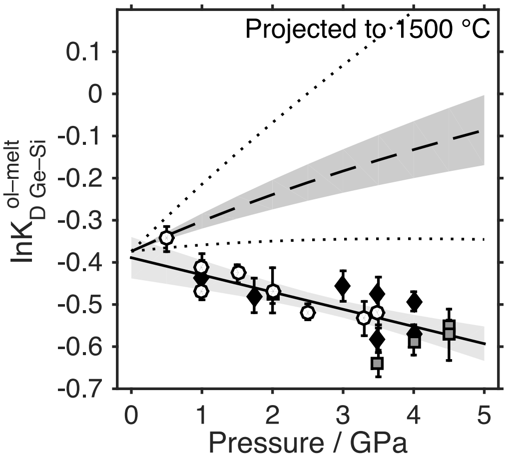

Figure 4.8. Same as Figure 4.7, but predicted change in $\ln K_D$ includes compressibility via the Murnaghan EOS.

The remaining possibility is that structural changes in the melt are affecting the partitioning behaviour. There are several ways in which this could occur.

Firstly, a change in the Ge coordination number in the melt, which was shown to begin from about 2 GPa in silicate melts (Chapter 2), will change the molar volume of the $GeO_2$ melt component. Although this coordination change is expected to proceed slowly over a range of pressures up to at least 10 GPa, a coordination change should have a significant effect on Ge partitioning. As an example, the molar volume of the rutile form of $GeO_2$ (14.4 $cm^3\ mol^{-1}$) is about half that of the quartz form (28.2 $cm^3$ $mol^{-1}$), calculated from the lattice parameters determined by Smith and Isaacs (1964) and Haines et al. (2000). If the predicted change in ln$K_D$ is calculated using the molar volume of r-$^{[6]}$$GeO_2$ as the molar volume for $GeO_2$ in the melt, the ln$K_D$ is predicted to decrease very steeply with pressure (i.e. Ge becomes rapidly more incompatible with pressure; at 5 GPa, predicted ln$K_D$ is −5). Thus, changes in volume associated with a coordination change of a liquid component will have a large effect on the partitioning behaviour.

However, any predictive model needs to consider more factors than just the volume change. If Ge is present in the melt in multiple coordination environments, which is expected at this range of pressures, then there will be an enthalpy and configuration entropy term that needs to be added to the calculation. Another complication is the potential effect of other structural changes in the silicate melt on the partitioning of Ge. For example, there are substantial changes in Al coordination over this pressure range. The Al coordination change, since it is a major element, could affect the activity coefficients of Ge and Si, and an activity term would also be needed.

The best predictive model developed so far for trace element partitioning is the lattice strain model (Wood and Blundy 2014). Mineral–melt partition coefficients for elements of the same charge, plotted against ionic radius, fall on a parabola with parameters $r_0$ (the 'ideal' ionic radius for the crystallographic site), $D_0$ (the partition coefficient of a fictional cation with the ideal radius), and $E_0$ (the Young's modulus for the site). These parameters define the position, height and width of the parabola respectively. While this model has been very successful, it is not well equipped to deal with changes occurring as a function of pressure, especially if there are changes in the melt structure, since the model considers only factors of the crystallographic site and does not explicitly account for melt structure. A few studies have investigated the pressure effect on the parabolic curves, and show that the parameters change systematically with pressure, but differently for different minerals and different cation charges (e.g. Suzuki et al. 2012 and references within) However, attempts to explain this based on the hypothetical 'site' occupied by the cations in the melt are so far very preliminary (Imai et al. 2012). The lattice strain model, as it does not explicitly consider the structure of the coexisting melt, is therefore not well suited to explaining how partition coefficients vary with pressure and the effect of melt structural changes on the partition coefficients.

## 4.5 Conclusion

As I have shown, the change in olivine–melt partitioning of Ge with pressure cannot be explained by existing thermodynamic data and equations of state for the volumes of components in silicate melts. I argue that this is due to structural changes occurring in the silicate melt which cannot, at present, be incorporated into these calculations. These structural changes include coordination changes of the trace elements of interest (i.e. Ge) as well as coordination changes of the major element Al. This range of factors requires additional terms to be added to the equation – to incorporate configurational entropy, enthalpy, and activity coefficients that are all functions of pressure. There are no existing equations that can provide a framework for modelling these effects, but this would be a very important tool to aid our understanding of trace element partitioning in magmatic systems at high pressures.

# Chapter 5: Divalent germanium: stable at low $fO_2$ and highly incompatible in olivine

**Abstract—**In the Earth's upper mantle and crust, Ge is almost exclusively tetravalent. Divalent germanium can be synthesised, but has only once been observed in nature. However, it has been inferred that $Ge^{2+}$ may be stable in silicate melts under reducing conditions, based on metal–silicate partitioning experiments. Whether this species was stable at conditions relevant to Earth's core formation (i.e. ~ΔIW -2) has been unclear due to conflicting data from different studies. In this work, I present X-ray absorption spectra of a series of silicate glasses quenched from melts. The spectra show that the $Ge^{4+}$–$Ge^{2+}$ transition is completed over the range ΔIW +2 to ΔIW -2 and that the $Ge^{2+}$–O bond length is 1.89 ± 0.03 Å. Four exploratory olivine–melt partitioning experiments were also conducted, which show that $Ge^{2+}$ is highly incompatible. The speciation of Ge must therefore be taken into account when modelling magmatic processes in reduced environments, such as Earth's core formation and the generation of basalts on the moon and other planetary bodies. In particular, the highly incompatible nature of $Ge^{2+}$ can provide a simple explanation for the anomalous enrichment of Ge in KREEP basalts, which was previously ascribed to lunar mantle metasomatism.

## 5.1 Introduction

The work presented in the preceding chapters has shown that the coordination number of $Ge^{4+}$ increases with pressure in silicate melts, perhaps causing important changes in its partitioning behaviour between silicate melt and other phases, such as silicate minerals or metal. Although Ge is not widely used as a petrogenetic indicator, its mineral–melt partition coefficients have been used to investigate mantle heterogeneity (de Argollo and Schilling 1978) and possible metasomatism of the lunar mantle (Dickinson et al. 1989). Ge metal–silicate partitioning has been more widely applied to models of the process of core formation in the Earth (Schmitt et al. 1989; Walker et al. 1993; Hillgren et al. 1996; Jana and Walker 1997a; Jana and Walker 1997b; Capobianco et al. 1999; Holzheid et al. 2007; Righter et al. 2011; Siebert et al. 2011; Righter et al. 2017) and in the Moon (Steenstra et al. 2016).

While investigating Ge metal–silicate partitioning, Schmitt et al. (1989) noticed that the slope of the logD–log$fO_2$ curve (where D is the partition coefficient) indicated a 2+ valence state for Ge. These authors suggested that $Ge^{2+}O$ was the stable species in the melt at oxygen fugacities below the iron-wüstite buffer, IW. This was a surprising result, because $Ge^{2+}$ had not been observed in nature until Bonnet (2017) identified a $Ge^{2+}$–bearing sphalerite using X-ray absorption spectroscopy (XAS), but this occurrence is for Ge bonded with sulfur, not oxygen. Even in chalcogenide glasses, Ge remains in a 4+ valence state (Zhou et al. 1991; Sen et al. 2005), and synthetic compounds containing $Ge^{2+}$–O bonds are rare; only three such compounds ($GeCl(H_2PO_2)$, $Na[Ge_4(PO_4)_3]$, and $Ge_2(H_2PO_2)_6$) are listed in the ICSD database (Cempírek and Groat 2013).

Capobianco et al. (1999), sceptical of the 2+ valence state reported by Schmitt et al. (1989), conducted a series of metal–silicate partitioning experiments and determined the valence state to be 4+. However, most of their experiments were at an $fO_2$ close to or above IW, whereas the experiments of Schmitt et al. (1989) were all below IW, as pointed out by Kegler and Holzheid (2011). Further experiments conducted by Kegler and Holzheid agreed very well with the data of Schmitt et al. (1989), predicting a 2+ valence. Recently, experiments conducted at similar $fO_2$ by Siebert et al. (2011) predicted a nominal valence of 2.7, suggesting a mixture of 2+

and 4+ valences. A summary of the ranges in $fO_2$ investigated by each study is presented in Figure 5.1.

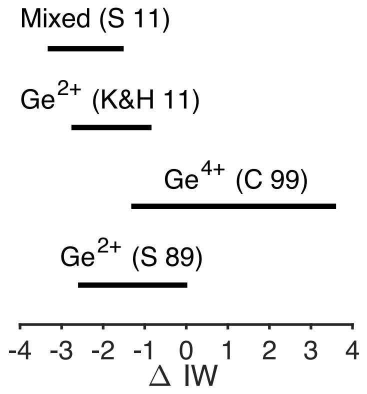

Figure 5.1. The $fO_2$ ranges investigated, and Ge valence states determined by four previous studies: 'S 89' = Schmitt et al. (1989), 'C 99' = Capobianco et al. (1999), 'K&H 11' = Kegler and Holzheid (2011) and 'S 11' = Siebert et al. (2011).

These four studies (Schmitt et al. 1989; Capobianco et al. 1999; Kegler and Holzheid 2011; Siebert et al. 2011) indicate that $Ge^{2+}$ becomes stable below IW, but precisely where that transition occurs is not clear. The experiments in all studies were carried out at different conditions (temperature, pressure, and composition), and none of the individual studies span a range in $fO_2$ from well above to well below IW. The $fO_2$ at the time of core formation in the Earth is estimated to have been ~ΔIW -2 (Wood et al. 2006), and so it is still unclear whether $Ge^{2+}$ would have been the dominant species in the Earth at that time.

Determining at what $fO_2$ $Ge^{2+}$ becomes stable is important for two reasons. First, if $Ge^{4+}$ were stable in the reduced environment of the early Earth, then pressure-induced coordination changes (described in Chapter 2) could have a profound effect on Ge metal–silicate partitioning in a deep magma ocean. However, if $Ge^{2+}$ were the stable species, the coordination changes of $Ge^{4+}$ will not be relevant, and whether $Ge^{2+}$ undergoes similar changes is unknown. Second, the $fO_2$ of the lunar mantle is thought to be at or below IW (Wieczorek et al. 2006); perhaps $Ge^{2+}$ is the stable species on the moon? Ge is highly depleted in lunar rocks, but Ge is enriched by up to 300 fold in KREEP basalts (Dickinson et al. 1989). Using knowledge of $Ge^{4+}$ mineral–melt partition coefficients, which are typically close to unity, Dickinson et al. (1989) proposed a model involving lunar mantle metasomatism to explain the anomalous Ge enrichments. However, while metal–silicate partition coefficients for $Ge^{2+}$ have been determined, nothing is known about the silicate mineral–melt partitioning of this species.

In this study, I aim to determine at what $fO_2$ $Ge^{2+}$ becomes stable in silicate melts, by conducting experiments at a range of $fO_2$, from air (ΔIW +10) to ΔIW -3. Rather than using metal–silicate partitioning experiments, the speciation is studied directly using X-ray absorption spectroscopy (XAS). XAS is an element-specific technique that is ideal for determining trace element speciation, because the absorption edge typically shifts systematically to higher energy with increasing valence state, e.g. for V, Cr and Fe (Wong et al. 1984; Berry et al. 2003a; Berry and O'Neill 2004). XAS has also previously been used to distinguish $Ge^{2+}$ from $Ge^{4+}$ and $Ge^0$ in sulfides (Pugsley et al. 2011; Cook et al. 2015; Belissont et al. 2016; Bonnet et al. 2017), but never before in oxides. I also conducted four preliminary partitioning experiments at low $fO_2$ to investigate the olivine–melt partitioning of $Ge^{2+}$.

I will show that the $Ge^{4+}$ to $Ge^{2+}$ transition occurs between ΔIW+2 and ΔIW-2, and that $Ge^{2+}$ is highly incompatible in olivine. These results suggest that $Ge^{2+}$ was indeed stable in the reducing conditions of the early Earth, and probably also on the Moon and other planetary bodies.

## 5.2 Methods

### *Sample synthesis*

#### **Starting materials**

Three different silicate compositions within the CMAS system were used in this study. The compositions are named CMAS7G, AnDi and CMAS40 (see Table 5.1). CMAS7G was used for ambient-pressure glass synthesis, because it is a good-glass former (low MgO) and has a low liquidus temperature (high $SiO_2$). AnDi was used for high-pressure glass synthesis, because it better approximates a basaltic melt than CMAS7G. Finally, the MgO-rich CMAS40 composition was used for olivine–melt partitioning experiments.

Table 5.1. Nominal major element compositions of starting materials (wt%).

| | CMAS7G | AnDi | CMAS40 |
|---|---|---|---|
| $SiO_2$ | 58.78 | 50.33 | 48.60 |
| $Al2O_3$ | 12.61 | 15.91 | 6.70 |
| MgO | 2.38 | 12.49 | 41.50 |
| CaO | 25.23 | 15.71 | 3.20 |

Starting materials were made from a powdered oxide mixture, prepared using reagent grade $SiO_2$, $Al_2O_3$, MgO and $CaCO_3$. These oxides were mixed under acetone and fired at 1050 °C to remove the carbonate. The CMAS40 composition was additionally doped with trace elements. Two exploratory samples, D2270 and C4444, were doped only with $GeO_2$ (0.46 wt%), $Sc_2O_3$ (0.03 wt%), $V_2O_3$ (0.12 wt%) and $Y_2O_3$ (1.05 wt%). The trace elements in this sample were added as oxides. In order to investigate partitioning with reference to a lattice strain model, subsequent samples were doped with $GeO_2$ (0.27 wt%), $Sc_2O_3$ (0.06 wt%), $V_2O_3$ (0.18 wt%), $Y_2O_3$ (0.50 wt%), $TiO_2$ (0.52 wt%) $HfO_2$, (0.16 wt%), SrO (0.14 wt%), $MnO_2$ (0.03 wt%) BaO (0.54 wt%), ZnO (0.02 wt%) and $ZrO_2$ (0.13 wt%). $TiO_2$, $HfO_2$ and $SrCO_3$ were added to the mixture as powders, but the trace elements Y, Sc, V, Mn, B, Zn and Zr were added as stock solutions, dissolved in 2% or 10% $HNO_3$ (except for Zn which was dissolved in 2% HCl). The powders and solutions were mixed together thoroughly in an agate mortar and left to dry. The resulting powder was then denitrified by firing as a pellet at 1050 °C overnight. Finally, powdered $GeO_2$ was mixed in under acetone and this mixture was then dried at 110 °C.

### Ambient-pressure experiments

Preparing silicate melts doped with Ge as a function of $fO_2$ at atmospheric pressure is made difficult by its volatility, which increases with decreasing $fO_2$ (e.g. Norris and Wood 2017), resulting in almost complete loss of Ge from samples in a matter of minutes using the traditional approach of synthesising samples in a gas-mixing furnace with the wire-loop method, as used in studies of non-volatile elements such as Fe or Cr (e.g. Berry et al. 2003a; Berry and O'Neill 2004). To get around this problem, a new experimental setup was designed (Figure 5.2), which turns the volatility of Ge from a disadvantage into an advantage.

Powdered samples of the CMAS7G composition were hung on a Re ribbon loops with the aid of polyethylene oxide as a glue, subsequently removed by heating after drying. The mix was not doped with Ge; instead, Ge was added to the sample during the experiment by bathing the sample in Ge-containing vapour. To achieve this, the loop was hung in the top of a ~20 cm long silica tube, which was sealed at the bottom, but open at the top. Approximately 0.5 to 1.2 g of $GeO_2$ powder was placed in the bottom of the tube. When the tube was hung in the furnace, the sample was located in the furnace hot spot (1200 °C) while the temperature at the bottom of the tube was ~ 900 °C. This enabled the $GeO_2$ powder in the bottom to gradually evaporate (but not melt). The vapour, the dominant species in which is GeO (Barton and Heil 1970), percolates up through the tube and flow past the sample. In some experiments, ceramic wool was placed in the middle of the silica tube (and, in one experiment, D28/01/16, at the top), to help slow the rate of GeO vapour transfer. Since the tube was open at the top, the sample could equilibrate with the $fO_2$ in the furnace set by the CO-$CO_2$ gas mixture. The $fO_2$ was varied between ΔIW +2 to ΔIW -3. Samples and their run conditions are listed in Table 5.2.

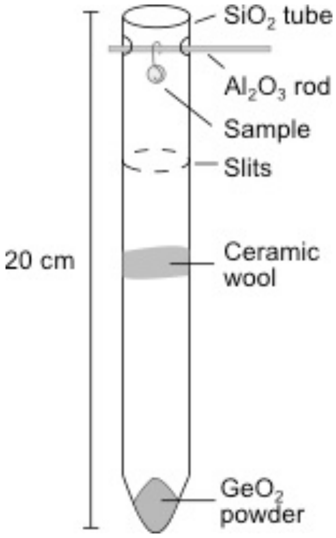

Figure 5.2. Experimental assembly that was suspended in a furnace by the $Al_2O_3$ rod for ambient-pressure, low-$fO_2$ experiments.

Quenching the sample to glass in this setup was not entirely straightforward. In all experiments, the tube was dropped into a bucket of water, but gas bubbles in the tube would often prevent the sample from coming into immediate contact with the water. When this occurred, the samples would contain small, unidentified quench crystals. In some experiments, slits were cut in the sides of the tube, which encouraged the tube to break when it hit the bottom of the bucket. Even with the slits, the tube did not always break. When it did break, the samples quenched to give a glass with few or no crystals.

Table 5.2. Experimental conditions of ambient-pressure, low-$fO_2$ experiments.

| Sample | ΔIW | Time (h) | Ge concentration (wt%) | | | |
|---|---|---|---|---|---|---|
| | | | Average | Max | Min | *n** |
| D21/01/16 | +2.0 | 6.8 | 1.2 (3) | 1.5 | 0.8 | 7 |
| D17/12/15 | +1.0 | 8 | 0.7 (1) | 0.9 | 0.6 | 10 |
| D30/11/15 | 0.0 | 14 | 0.3 (1) | 0.4 | 0.1 | 11 |
| D19/12/15 | +0.5 | 8 | 0.34 (5) | 0.41 | 0.28 | 5 |
| D18/12/15 | -0.5 | 7.5 | 0.22 (2) | 0.23 | 0.18 | 10 |
| D15/12/15 | -1.0 | 7.5 | 0.15 (2) | 0.19 | 0.10 | 10 |
| D14/04/16 | -1.0 | 5 | 0.07 (4) | 0.12 | 0.03 | 6 |
| D25/01/16 | -1.5 | 7.5 | 0.053 (6) | 0.058 | 0.047 | 3 |
| D16/04/16 | -1.5 | 5 | 0.041 (8) | 0.048 | 0.027 | 6 |
| D28/01/16 | -1.75 | 6 | 0.041 (9) | 0.051 | 0.025 | 6 |
| D17/04/16 | -2.5 | 4.2 | 0.050 (9) | 0.058 | 0.035 | 6 |
| D12/04/16 | -3.0 | 4.75 | 0.065 (8) | 0.077 | 0.055 | 6 |

*n = number of analyses. Numbers in parentheses are one standard deviation on the last digit. Temperature in the furnace hot spot was 1200 ºC in all experiments. Concentrations of Ge in the glasses were determined by LA-ICPMS.

### High-pressure experiments

Four additional glass samples were prepared at 1500ºC and 1 GPa using a 200 T end-loaded Boyd-England type piston cylinder apparatus, and six olivine–melt partitioning experiments were conducted using the same method. Samples are listed in Table 5.3.

Table 5.3. List of high-pressure experiments.

| Sample | Time (h) | Ge concentration (ppm) | | | |
|---|---|---|---|---|---|
| | | Average | Max | Min | *n** |
| *Glass samples* | | | | | |
| C5201 | 24 | 0.18 (2) | 0.20 | 0.16 | 5 |
| C5204 | 24 | 0.66 (1) | 0.67 | 0.64 | 6 |
| C5206 | 24 | 4.04 (3) | 4.07 | 4.01 | 6 |
| C5234 | 10.5 | 3.3 (2) | 3.6 | 3.0 | 5 |
| *Partitioning experiments* | | | | | |
| D2270 | < 24* | *Ge concentrations of olivines and melt in the partitioning experiments are given in Table 5.11 and Table 5.12.* | | | |
| D2357 | 24 | | | | |
| D2368-i | 48 | | | | |
| D2368-ii | 48 | | | | |
| C4444 | 24 | | | | |
| D2413 | 24 | | | | |

All samples were equilibrated at 1500 ºC and 1 GPa for the times indicated. *Sample D2270 quenched before 24 h due to a failure with the apparatus.

Most of these experiments were conducted in graphite capsules containing two layers. A mixture of Ge and either Co or Ni metal powders (1:1 ratio by weight) was packed at the bottom of each capsule. The powdered oxide mixture (AnDi for the glasses or CMAS40 for the partitioning experiments) was placed on top of the metal mixture. The metal mixtures served to both add Ge to the charge, and to enable the calculation of $fO_2$ retrospectively using the Co–CoO or Ni–NiO equilibria. In some capsules a small amount of Si metal was also added to further reduce the $fO_2$. The amounts of each component added to the capsules are detailed in Table 5.4.

Table 5.4. Components used in graphite capsules for high-pressure experiments.

| | Partitioning experiments | | | | Glass synthesis experiments | | | |
|---|---|---|---|---|---|---|---|---|
| | D2270 | D2357 | D2368-a | D2368-b | C5201 | C5204 | C5206 | C5234 |
| Si metal (mg) | 1.1 | 0.3 | 0.1 | – | 0.9 | 0.6 | – | 0.3 |
| Ge-M* 1:1 mix (mg) | 3.3 | 2.6 | 0.7 | 1.5 | 10.9 | 10.3 | 11.7 | 9.6 |
| Silicate mix** (mg) | 12.1 | 12.1 | 5.5 | 8.0 | 33.4 | 35.5 | 34.3 | 32.5 |
| Ge-M* wt % | 20 | 17 | 11 | 16 | 24 | 22 | 25 | 23 |
| Si wt % | 6.7 | 2 | 0.8 | 0 | 2 | 1.3 | 0 | 0.7 |

* M denotes metal, referring to Ni for C5201 or Co for all other samples. **Silicate mix used was CMAS40 for the partitioning experiments (D2270, D2357, D2368-a, and D2368-b). For the other experiments, the silicate mix used was AnDi.

Two of the partitioning experiments (prepared for Chapter 4) were carried out at high $fO_2$ by using Pt capsules and a Ru-$RuO_2$ oxygen buffer mix (80% $RuO_2$, 20% Ru). The Ru-$RuO_2$ buffer is highly oxidising, with a $\log fO_2$ of -0.2 at 1500 °C (O'Neill and Nell 1997), which is similar to that of air ($\log fO_2 = -0.7$). These samples was prepared by loading ~20 mg of the CMAS40 starting material into a 2.3 mm diameter Pt capsule, with ~2 mg of the Ru-$RuO_2$ mixture packed at each end of the capsule. Before welding the capsules shut, they were crimped loosely and dried at 110 °C overnight.

The capsules were placed in an assembly composed of MgO spacers, a graphite heater in a Pyrex sleeve, and NaCl as a pressure medium. This assembly was wrapped in Teflon foil and inserted into a pressure vessel with a bore size of either a 1/2” (C4444 and D2413) or 5/8” (all other experiments). A Type B thermocouple, sheathed in mullite with a 5-mm alumina tip, was inserted through a bore in the top MgO spacer. The samples were equilibrated for 10–48 h (see Table 5.3), at 1500 °C and 1 GPa, before quenching by cutting power to the graphite heater. Sample C4444 was run at 1500 °C and 1 GPa for 24 h twice, because on the first run, an error in programming the temperature control meant that the experiment was not rapidly quenched. The capsule was recovered and the experiment repeated with the correct quenching procedure. Note that capsules D2368-a and D2368-b were run together in one experiment, and it was not possible to determine which capsule was which after the experiment (suffixes ‘i’ and ‘ii’ were arbitrarily assigned).

### Standards for XAS

Ideally, samples containing Ge in known valence states are desirable for comparison with the samples described above, but as $Ge^{2+}$ does not readily form oxide compounds, none were available. Compounds containing $Ge^{2+}$ bonded to other ligands, such as S, Se or I, do not make good standards because the XANES spectra vary greatly with the ligand (Pugsley et al. 2011). There is no difficulty obtaining well-characterized standards for $Ge^{4+}$ and $Ge^{0}$ (metal) and several standards with these valence states were examined (Table 5.5).

Five $Ge^{4+}$ standards were prepared: $Ge^{4+}O_2$ in the quartz form (q-$GeO_2$), and four Ge-doped glasses quenched from melts that were synthesized in air, at which high $fO_2$, all Ge should be $Ge^{4+}$. The q-$GeO_2$ sample was prepared by firing $GeO_2$ powder at 1060 °C for 24 h in air. The glass samples were made using the CMAS7G composition, doped with different concentrations of $GeO_2$ (~300 ppm, ~3000 ppm and 3 wt%). These mixes were loaded into Pt capsules. The capsules were welded shut at one end, but only crimped at the other end, and suspended in a furnace. The 300-ppm and 3-wt% samples were heated in the furnace together at 1284 °C, and the 3000-ppm sample was heated in a separate experiment at 1330 °C. All samples were heated for four hours before quenching in water. An additional sample was prepared by heating a batch of CMAS7G, doped with ~3000 ppm $GeO_2$, in an alumina crucible at 1300 °C for 15 minutes (in air) before quenching into water. These samples are listed in Table 5.5.

Two $Ge^{0}$ standards were used, prepared by Ridgway et al. (2004). One sample was prepared by implanting Ge atoms into 2-μm thick amorphous silica. These Ge atoms should be dispersed throughout the silica at a concentration of $3 \times 10^{17}$ atoms $cm^{-2}$. A second sample was prepared by annealing the Ge-implanted silica at 1100 °C, which led to the formation of crystalline Ge nanoparticles 5–10 nm in size. These two standards were used rather than a pure crystalline Ge metal, because they should better represent how $Ge^0$ might be present in the silicate melt: either as dissolved $Ge^0$ or as Ge metal nuggets.

Table 5.5. List of standards used for comparison to glasses made at low $fO_2$.

| Sample | Expected speciation | Details | Synthesis |
|---|---|---|---|
| q-$GeO_2$ | $Ge^{4+}$ | $GeO_2$ in quartz form | 1 atm, 1060 °C, 24 h, prepared for Chapter 2 |
| B1-080316 | $Ge^{4+}$ | ~3000 ppm $GeO_2$ | 1 atm, 1300 °C, 15 min, $Al_2O_3$ crucible, prepared for Chapter 2 |
| E02/12/13A | $Ge^{4+}$ | ~300 ppm $GeO_2$ | 1 atm, 1287 °C, 4 h, Pt capsule |
| E02/12/13B | $Ge^{4+}$ | ~3 wt% $GeO_2$ | 1 atm, 1287 °C, 4 h, Pt capsule |
| E04/11/13* | $Ge^{4+}$ | ~3000 ppm $GeO_2$ | 1 atm, 1330 °C, 4 h, Pt capsule |
| Ge (imp) | $Ge^0$ | Ge in $SiO_2$, implanted | (Ridgway et al. 2004) |
| Ge (ann) | $Ge^0$ | Ge in $SiO_2$, annealed | (Ridgway et al. 2004) |

*The sample E04/11/13 was only used for EXAFS.

### *Sample characterisation*

Quenched samples were mounted in epoxy, sectioned and polished. The glass samples were checked using an optical microscope for the presence of quench crystals. Glass samples were also examined under Type A immersion oil (refractive index, n, =1.515) using a Nikon Eclipse LV100POL microscope fitted with a Plan Apo 100× objective (numerical aperture = 1.4, ∞/0) to check for the presence of micro-nuggets. Nuggets were observed in all of the ambient-pressure glass samples.

Major element concentrations were determined for several ambient-pressure glasses to confirm that the compositions were similar to that of the starting material. Major element concentrations were also determined for olivine and melt phases in all partitioning experiments. Samples were analysed using a Hitachi S4300 SE/N Field Emission Scanning Electron Microscope (FE-SEM) fitted with an Oxford X-Max EDS detector. The operating conditions were 15 kV accelerating voltage, 0.600 nA beam current, and a working distance of 25 mm. Standards were MgO for Mg, albite for Al, sanidine for Si, diopside for Ca, $TiO_2$ for Ti, Co metal for Co, and $La_8Sr_2Ge_6O_{26}$ for Ge. Point analyses were used for crystals, but in most cases area analyses were used for the melt phase of the partitioning experiments to include quench crystals in the composition. For the ambient-pressure glass samples, point analyses were used to avoid the metal nuggets. The composition of the metal nuggets was also determined using EDS.

Trace element concentrations in all samples were determined by Laser-Ablation Inductively Coupled Plasma Mass Spectrometry (LA-ICPMS). An excimer laser with a wavelength of 193 nm and a pulse rate of 5 Hz was used. This system was coupled to an Agilent 7700 ICP-MS using He+Ar as the carrier gas. Samples were ablated for ~40 s with ~20 s of background measured for each spot. The external standard was NIST 610 glass; Si was used as the internal standard, determined by SEM. The spot size used was between 37–47 μm for glass samples. For samples containing olivine and melt, a 28 μm spot size was typically used, however a 22 μm spot was used for sample D2270 which contained smaller olivines than the other samples. To improve the detection limit, some analyses of large olivines in D2357 were made with a 47 μm diameter spot. An in-house Excel spread sheet was used to reduce the data.

Compositions of Ge-Co metal alloys in the partitioning experiments were obtained using an electron probe microanalyser (EPMA). A CAMECA SX 100 was used in WDS mode, with operating conditions of 20 kV and 20 nA. A 20–50 μm diameter beam was used to get an average composition over the fine quench textures of the metal alloy. Ge and Si were measured on a TAP crystal at the L-α and K-α lines respectively. Ni and Co was measured on a LLIF crystal at the K-α line. Ge, Si and Co metals were used as standards.

### *X-ray absorption spectroscopy*

Ge K-edge XANES and EXAFS spectra were recorded at the X-ray Absorption Spectroscopy (XAS) beamline of the Australian Synchrotron. The x-ray energy was selected using a liquid nitrogen cooled Si (111) crystal; high-energy harmonics were rejected by Rh coated mirrors. To calibrate the energy, a spectrum of Au foil was recorded in transmission mode, and the first peak in the derivative spectrum was defined to be 11919.7 eV. The beam size was ~ 0.5 × 0.5 mm, and the beamline energy resolution was 1.67 eV at the Ge K-edge.

XANES spectra were recorded in fluorescence mode using a 100-element Ge detector. To avoid any systematic variations of white line intensity with count rate, the distance between the detector and the sample was varied to maintain count rates between 18,000 $s^{-1}$ and 25,000 $s^{-1}$ for XANES spectra. EXAFS spectra were recorded at 10 K using a cryostat with a count rate at the end of the scan of 75,000 $s^{-1}$ for all spectra. Energy ranges and step sizes are given in Table 5.6.

Table 5.6. Energy ranges and step sizes used to acquire XANES and EXAFS spectra.

| | Pre-edge | Edge | Post-edge |
|---|---|---|---|
| Energy ranges | 10903 – 11083 eV | 11083 – 11153 eV | 11153 – 11488 eV |
| Step sizes – XANES | 8 eV | 0.25 eV | 0.1 $Å^{-1}$ to k=10 |
| Step sizes – EXAFS | 8 eV | 0.5 eV | 0.035 $Å^{-1}$ to k=16 |

The spectrum of Ge in $SiO_2$ (implanted) was recorded in a previous experiment (described in Chapter 2). This spectrum was shifted in energy -0.37 eV to account for systematic differences between spectra recorded in the two experiments (2013 and 2016, as described in Chapter 2).

For each scan, the signals from all detector elements were averaged and divided by the incident photon flux using the programs Average or Sakura. Normalisation and background subtraction of spectra, as well as linear combination fitting and fitting of EXAFS spectra were performed using the programs ATHENA and ARTEMIS (Ravel and Newville, 2005).

## 5.3 Results

### *Experimental products (ambient-pressure glasses)*

Sub-micron metal nuggets were present in all of the ambient-pressure experiments, but EDS analysis showed that these were Re, not Ge. This is supported by LA-ICPMS data – down-hole ablation profiles of Re show large spikes indicating the presence of nuggets, but spikes are not seen in the down-hole ablation profiles of Ge. In high-pressure experiments (both glasses and low-$fO_2$ partitioning experiments), clusters of metal nuggets are seen near the edges of the capsule or near grain boundaries, but these were easily avoided during analysis.

The product of an ambient-pressure experiment is shown in Figure 5.3. Although not all of the melts quenched perfectly to glass beads, the fraction of quench crystals was small in most cases.

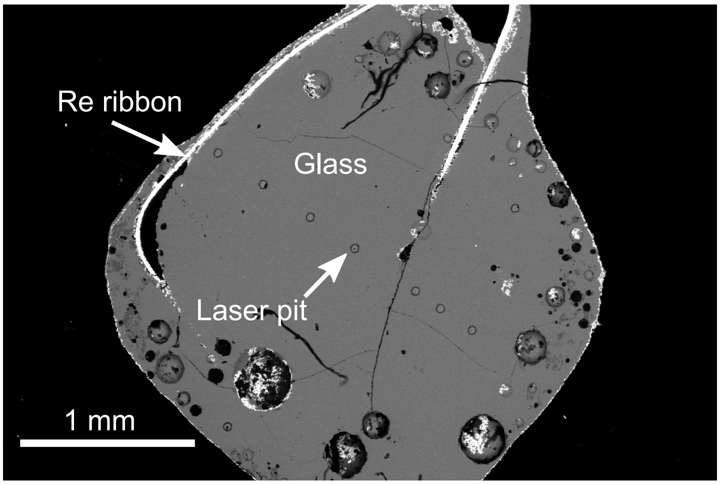

Figure 5.3. Backscattered electron image of sample D30/11/15.

The ambient-pressure glass samples were all made using the same starting material, so their compositions are not expected to differ. The composition of several samples were determined using EDS and shown to be very close to that of the nominal starting composition (see Table 5.7). However, the Ge concentration differs greatly between samples. In general, more reduced samples contain less Ge dissolved in the melt, probably due to its greater volatility, and/or lower solubility, at lower $fO_2$. Ge concentrations were also quite heterogeneous within the samples. The standard deviations on average concentrations were typically around 20%, but up to 57% in D14/04/16. In general, the concentration of Ge was lower near the edges of the sample than in the middle. The concentrations of Ge in each sample are listed in Table 5.2.

Table 5.7. Major element compositions for selected samples.

| | D17/12/15 | sd | D19/12/15 | sd | D21/01/16 | sd | D30/11/15 | |
|---|---|---|---|---|---|---|---|---|
| *n* | 3 | | 3 | | 3 | | 2 | |
| MgO | 2.41 | 0.14 | 2.43 | 0.02 | 2.53 | 0.16 | 2.40 | 0.08 |
| $Al_2O_3$ | 12.29 | 0.68 | 11.73 | 0.31 | 12.42 | 0.36 | 12.17 | 0.09 |
| $SiO_2$ | 58.67 | 1.09 | 58.50 | 0.63 | 57.95 | 0.67 | 58.57 | 0.95 |
| $P_2O_5$ | 0.08 | 0.14 | 0.63 | 0.56 | 0.00 | 0.00 | 0.38 | 0.13 |
| CaO | 24.27 | 0.83 | 24.55 | 0.27 | 24.64 | 0.56 | 24.75 | 0.62 |
| $GeO_2$ | 0.98 | 0.19 | 0.45 | 0.04 | 1.97 | 0.12 | 0.48 | 0.09 |
| Total | 98.70 | 0.61 | 98.28 | 0.24 | 99.51 | 0.16 | 98.75 | 0.11 |

The high-pressure samples contain a large blob of metal alloy at one end of the capsule, and many samples also contain several smaller blobs of metal. The compositions of the smaller blobs were typically within <1 mol% of the larger mass, and all analyses were averaged for calculating $fO_2$. The Ge concentrations of the glasses in the high-pressure samples are given in Table 5.3.

### *$fO_2$ of high-pressure samples*

The $fO_2$ of the high-pressure samples was calculated using the Co-CoO (or Ni-NiO) equilibrium following the approach described by Kegler and Holzheid (2011) for the Fe-FeO equilibrium. This approach results in the equation:

$$\Delta[\mathrm{M{-}MO}] = 2 \cdot \log \frac{X_{\mathrm{MO}} \cdot \gamma_{\mathrm{MO}}}{X_{\mathrm{M}} \cdot \gamma_{\mathrm{M}}}$$

Equation 5.1

where M is the metal used in the experiment (Co or Ni), Δ[M–MO] is the log$fO_2$ relative to the buffer (Co–CoO or Ni–NiO), $X$ is the mole fraction and $\gamma$ is the activity coefficient (with subscripts indicating the species).

The activity coefficients of CoO and NiO in silicate melts are 1.51 ± 0.28 and 2.70 ± 0.52 respectively. These values were determined from a wide range of compositions by Holzheid et al. (1997). Activity coefficients of Ni or Co in the metal phase were obtained from thermodynamic studies of the binary Ge–Co or Ge–Ni liquid alloys (Ishida and Nishizawa, 1991; Nash and Nash, 1987). These activity coefficients were reported as a function of composition in the alloys, in increments of 10 mol%. In order to estimate the activity at the specific concentration measured in our samples, the reported data was resampled at a fine scale using a spline interpolation method. Some of the alloys in the experiments also contain Si (see Table 5.8), which I assume has negligible effect on the activity coefficients of Co or Ni.

Once values for Δ[Co–CoO] or Δ[Ni–NiO] were determined, they were converted to values of ΔIW. The IW buffer is 2.37 log units below the Co–CoO buffer, and 3.83 log units below the Ni–NiO buffer at 1500 °C and 1 bar (O’Neill and Pownceby, 1993). The effect of pressure on the $fO_2$ of the buffers is similar for all the buffers used in this study at 1 GPa (Frost, 1993), so the ΔIW values were calculated by adding 2.37 or 3.83 log units to the values of Δ[Co–CoO] or Δ[Ni–NiO] respectively.

Table 5.8. Compositions of metal alloys in high-pressure experiments, CoO or NiO concentration in the melt, and calculated $fO_2$ relative to IW.

| | Ge in alloy (mol%) | Co (or Ni*) in alloy (mol%) | Si in alloy (mol%) | CoO (or NiO*) in melt (mol%) | ΔIW |
|---|---|---|---|---|---|
| *Glass experiments* | | | | | |
| C5201* | 36.6 (9) | 63.4 (8)* | n.d. | 0.025 (1) * | -1.3 (2) |
| C5204 | 41.1 (2) | 58.7 (2) | 0.11 (2) | 0.41 (2) | -0.9 (2) |
| C5206 | 38.2 (2) | 61.7 (3) | 0.10 (1) | 2.05 (1) | 0.4 (2) |
| C5234 | 38.5 (3) | 61.3 (3) | 0.10 (2) | 1.86 (5) | 0.3 (2) |
| *Partitioning experiments* | | | | | |
| D2270 | 30.2 (17) | 41.1 (21) | 28.8 (24) | $7 (1) \times 10^{-6}$ | -9.5 (2) |
| D2357 | 36.0 (15) | 51.2 (5) | 12.7 (13) | $2.0 (5) \times 10^{-5}$ | -7.2 (3) |
| D2368-i | 44.1 (6) | 55.7 (6) | 0.12 (4) | 0.44 (1) | -0.7 (2) |
| D2368-ii | 45.2 (4) | 54.7 (5) | 0.15 (4) | 0.39 (2) | -0.7 (2) |

*C5201 contains Ni, whereas all other samples contain Co.

### *X-ray absorption spectroscopy*

Representative XANES spectra are shown in Figure 5.4 for samples D12/04/16, made at ΔIW -3.0, and B1-080316, made in air. The spectra are well normalised to the pre- and post-edge regions. Even at this scale, there are large differences between the spectra.

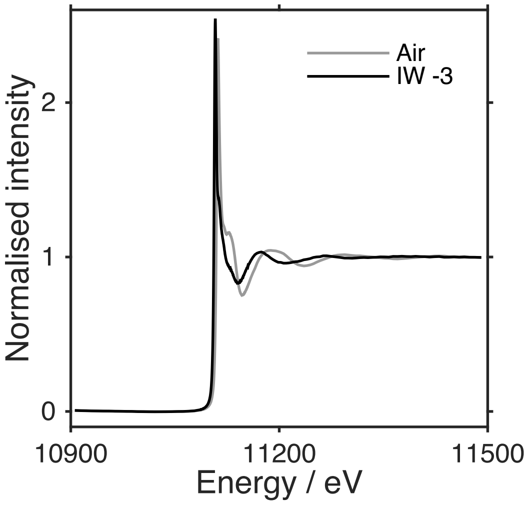

Figure 5.4. Normalised XANES spectra of samples B1-080316 (air) and D12/04/16 (ΔIW -3.0).

Figure 5.5 shows spectra of samples prepared at a range of $fO_2$, along with the spectra of q-$GeO_2$ and two forms of Ge metal. The spectra of the three glasses prepared in air are similar to the spectrum of q-$GeO_2$, indicating that $Ge^{4+}$ is the only species stable in the sample made in air (spectrum ‘t’ is an anomaly that will be discussed in the next section). In the glass prepared at the lowest $fO_2$ (IW -3.0, spectrum labelled ‘c’), the speciation or local environment of Ge must be different to that of the high-$fO_2$ glasses, because the absorption edge is shifted to lower energy. This shift in the spectrum is not likely to indicate the presence of $Ge^0$ in the low-$fO_2$ glass, because the spectra of reference $Ge^0$ samples ('a' and 'b') have a different shape and their absorption edge occurs at even lower energy. Therefore, I assign the spectrum of the lowest $fO_2$ glass sample to be representative of $Ge^{2+}$. In spectra of glass samples made at intermediate $fO_2$ conditions, I interpret the two peaks to reflect the presence of both $Ge^{2+}$ and $Ge^{4+}$ in the samples.

**Beam damage**

Previous studies have found that the energy imparted to the sample by the X-ray beam can cause multivalent elements to change their valence state. For example, Alessi et al. (2013) report oxidation of U, Wilke et al. (2008) report reduction of S, and Ferreira et al. (2013) report reduction of Fe. It was therefore necessary to investigate whether the valence state of Ge was affected by the X-ray beam.

To assess whether any beam damage occurred, two spectra were recorded consecutively at the same spot on samples D12/04/16 and D17/04/16 (prepared at IW-3 and IW-2.5 respectively). The spectra are very similar; the only change is a slight (~2%) decrease in the intensity of the white line in the second spectrum from each sample. This does not rule out the possibility of beam damage in the first few minutes of the first scan, but there was no way to test whether this occurred at the XAS beamline. Monitoring intensity at a single energy as a function of time was not possible because the detector had a slow response time to significant changes in count rate. The fact that a $Ge^{2+}$ spectrum is observed consistently, even after two scans at the same spot, indicates that the $Ge^{2+}$ species is stable under the X-ray beam.

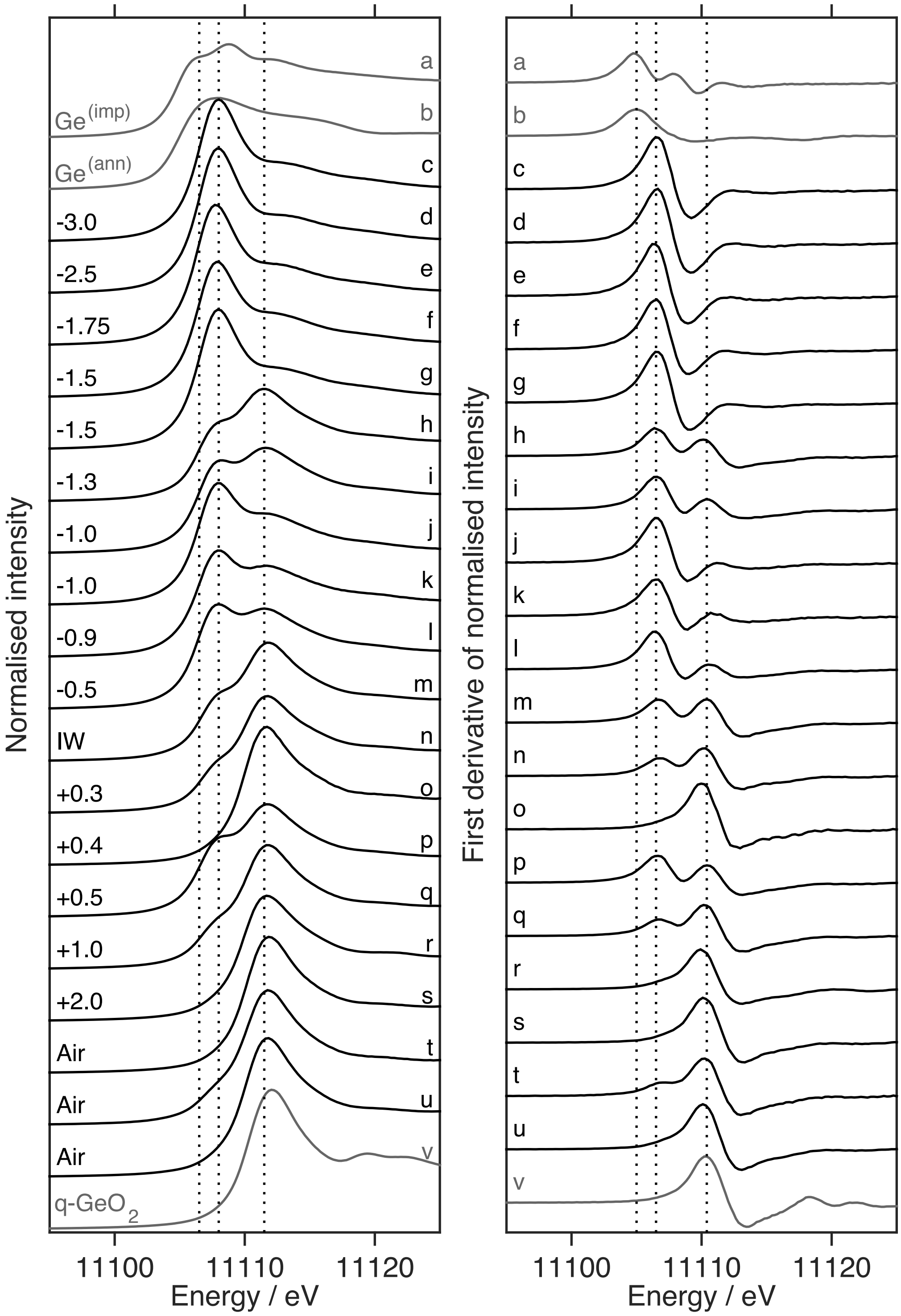

Figure 5.5. Ge K-edge XANES spectra plotted as normalised intensity (left panel) and the first derivative of normalised intensity (right panel). Spectra are plotted in order of increasing oxygen fugacity from the top down. Black curves are glass samples, grey curves are model compounds. In the left panel, numerical labels are the oxygen fugacity relative to IW; 'Air' indicates the sample was prepared in air. Vertical dashed lines are plotted at 11105.0 eV, 11106.5 eV and 11110.4 eV as guides to the eye. The letter labels indicate the specific samples, listed in Table 5.9.

Table 5.9. List of samples corresponding to spectra shown in Figure 5.5.

| Label | ΔIW | Sample | Scan no. |
|---|---|---|---|
| a | – | Ge (imp) | 7203 |
| b | – | Ge (ann) | 6432 |
| c | -3 | D12/04/16 | 6384 |
| d | -2.5 | D17/04/16 | 6380 |
| e | -1.75 | D28/01/16 | 6488 |
| f | -1.5 | D25/01/16 | 6413 |
| g | -1.5 | D16/04/16 | 6385 |
| h | -1.3 | C5201 | 6490 |
| i | -1 | D15/12/15 | 6410 |
| j | -1 | D14/04/16 | 6388 |
| k | -0.86 | C5204 | 6623 |
| l | -0.5 | D18/12/15 | 6487 |
| m | 0 | D30/11/15 | 6386 |
| n | +0.34 | C5234 | 6615 |
| o | +0.41 | C5206 | 6622 |
| p | +0.5 | D19/12/15 | 6389 |
| q | +1 | D17/12/15 | 6390 |
| r | +2 | D21/01/16 | 6387 |
| s | Air | E021213B | 6611 |
| t | Air | E021213A | 6617 |
| u | Air | B1-080316 | 6323 |
| v | – | Sd-Quartz | 7155 |

However, I did not repeat the test for samples that only contained $Ge^{4+}$. As will be discussed in the next section, there is a possibility that a small amount of $Ge^{4+}$ was reduced by beam damage to $Ge^{2+}$ in samples prepared at high $fO_2$.

**Effect of concentration**

Since the concentrations of Ge in the ambient-pressure, low-$fO_2$ samples varied widely (hundreds of ppm at the lowest $fO_2$ to ~2 wt% at ΔIW +2.0), it was important to see if there was any effect of Ge concentration on the spectra. The spectra of a series of samples prepared in air are shown in Figure 5.6. It can be seen that the spectrum of the 300-ppm sample is somewhat different to the spectra of the samples containing 3000 ppm and 3 wt% Ge. The spectrum of the sample with the lowest concentration of Ge exhibits a small shoulder on the low-energy side of the absorption edge. This shoulder may be a feature of the $Ge^{4+}$ spectrum that is only visible at low concentrations. However, it is at the same energy as the absorption edge of the $Ge^{2+}$ spectrum, suggesting the possibility of a component of $Ge^{2+}$ in the sample.

If this shoulder does represent $Ge^{2+}$, it is unlikely that the $Ge^{2+}$ was stable during the experiment, which was conducted in air. The shoulder is more likely to be a product of beam damage. For example, if a fixed amount (e.g. 30 ppm) of $Ge^{4+}$ was reduced to $Ge^{2+}$ by the X-ray beam, this would be clearly visible in the spectrum of the 300-ppm sample but not in the spectra of the 3000-ppm or 3-wt% samples. Linear combination fitting will be used to determine how much $Ge^{2+}$ this sample may contain.

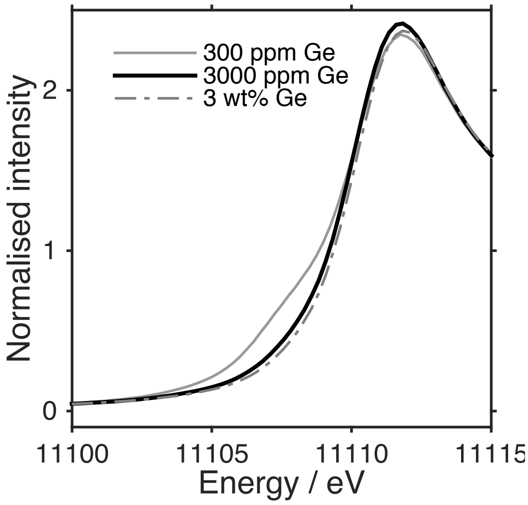

Figure 5.6. Ge K-edge XANES spectra of glasses containing different concentrations of Ge (E021213A, 300 ppm; B1-080316, 3000 ppm; E021213B; 3 wt%).

### Linear combination fitting

Linear combination fitting was used to quantify the Ge speciation in each glass sample, by assuming that the low- and high-$fO_2$ end-member spectra (D12/04/16 and B1-080316) represent the pure species $Ge^{2+}$ and $Ge^{4+}$ respectively. This assumption is justified by the observation that the greatest changes in spectral shape, reflecting changes in speciation, occur for samples made between ΔIW +2.0 and ΔIW -2.0. Beyond these limits, the spectra remain constant, indicating a constant speciation of either $Ge^{2+}$ or $Ge^{4+}$ within the resolution of the spectroscopy. Therefore, these end-member $Ge^{2+}$ and $Ge^{4+}$ spectra were combined to reproduce the intermediate $fO_2$ spectra. An example of a fit is shown in Figure 5.7.

As described earlier, E02/12/13A deviates from this trend. If this shoulder on the absorption edge is assumed to represent $Ge^{2+}$, possibly formed by beam damage, linear combination fitting can be used to estimate the proportion of $Ge^{2+}$ in the sample. As shown in Figure 5.8A, a combination of 10.6 % of the $Ge^{2+}$ end-member (D12/04/16) and 89.4 % of the $Ge^{4+}$ end-member (B1-080316, 3000 ppm Ge) produces a good fit to the spectrum of E02/12/13A. If the 3-wt% Ge sample is used as the $Ge^{4+}$ end-member, the proportions are 13.1 % $Ge^{2+}$ and 86.9 % $Ge^{4+}$, but the fit is not as good (Figure 5.8B).

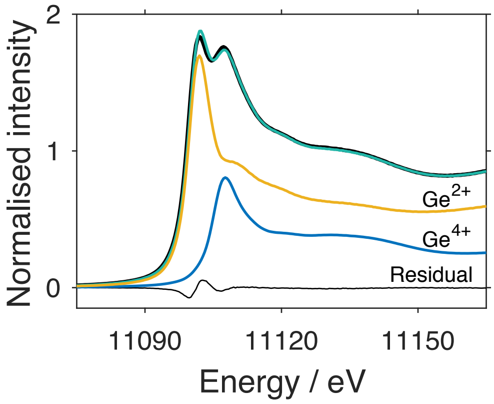

Figure 5.7. Example of the linear combination fit (green) to the spectrum of sample D18/12/15 (black). The yellow and blue curves show the 2+ (D12/04/16) and 4+ (B1-080316) components of the fit, which are weighted at 66.7 % and 33.3 % respectively.

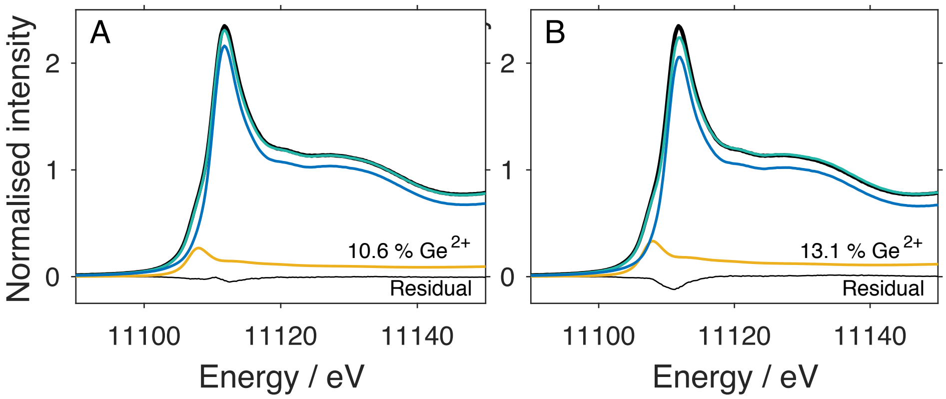

Figure 5.8. Linear combination fits (green) to the spectrum of sample E02/12/13A (black). (A) and (B) use different end-member spectra for the $Ge^{4+}$ component: B1-080316 (3000 ppm Ge) is used in (A), and E02/12/13B (3 wt% Ge) is used in (B). The $Ge^{2+}$ end-member used is D12/04/16 in both cases.

The results of the linear combination fits for all samples are plotted in Figure 5.9. As expected, a sigmoidal shape defines the transition from $Ge^{2+}$ to $Ge^{4+}$. The slope of the sigmoid shown in Figure 5.9 can be defined thermodynamically by considering the reaction describing reduction of $Ge^{4+}$ to $Ge^{2+}$:

$$\mathrm{Ge^{4+}O_2} \rightleftharpoons \mathrm{Ge^{2+}O}+\tfrac{1}{2}\mathrm{O_2}$$

Equation 5.2

The equilibrium coefficient, $K_{eq}$, for Equation 5.2 is:

$$K_{eq} = \frac{X_{\mathrm{Ge^{2+}O}} \cdot \gamma_{\mathrm{Ge^{2+}O}} \cdot (fO_2)^{1/2}}{X_{\mathrm{Ge^{4+}O_2}} \cdot \gamma_{\mathrm{Ge^{4+}O_2}}}$$

Equation 5.3

where $X$ is the mole fraction, and $\gamma$ is the activity coefficient. By taking the logarithm, Equation 5.3 can be rewritten as

$$\log \frac{X_{\mathrm{Ge^{2+}O}}}{X_{\mathrm{Ge^{4+}O_2}}} = -\frac{1}{2} \log fO_2 + \log K_{eq} - \log \frac{\gamma_{\mathrm{Ge^{2+}O}}}{\gamma_{\mathrm{Ge^{4+}O_2}}}$$

Equation 5.4

The activity coefficient term can be incorporated into the equilibrium constant term if it is assumed that activity coefficients for GeO and $GeO_2$ in a given melt composition are constant (Henry's Law). This is valid if the concentrations of Ge are low, although for the higher-$fO_2$ samples, Ge concentrations could be a few wt%. Making the assumption that Henry's Law holds, we define

$$\log K'_{eq} = \log K_{eq} - \log \frac{\gamma_{\mathrm{Ge^{2+}O}}}{\gamma_{\mathrm{Ge^{4+}O_2}}}$$

Equation 5.5

where $K'_{eq}$ is the equilibrium constant for a given melt composition. By rearranging Equation 5.5, we can then write

$$\frac{\mathrm{Ge^{4+}}}{\Sigma\mathrm{Ge}} = \frac{1}{1 + 10^{-\frac{1}{2} \cdot \log fO_2 + \log K'_{eq}}}$$

Equation 5.6

where $\sum\mathrm{Ge} = \mathrm{Ge^{4+}} + \mathrm{Ge^{2+}}$. Equation 5.6 describes oxidation state as a sigmoidal function of $\log fO_2$ for a two-electron transition. Fitting the ambient-pressure data to this equation gives $\log K'_{eq} = -6.0 \pm 0.2$. Fitting the high-pressure data to this equation gives $\log K'_{eq} = -4.9 \pm 0.7$.

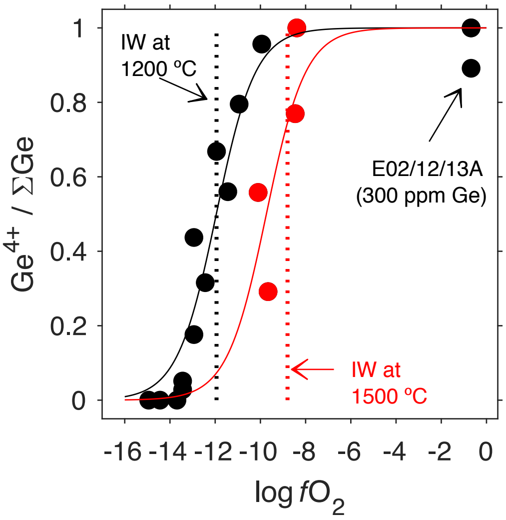

Figure 5.9. Linear combination fitting results for glass samples. End-members used in the fits were B1-080316 (3000 ppm Ge) and D12/04/16 for $Ge^{4+}$ and $Ge^{2+}$ respectively. Errors on the fit parameters are smaller than the size of the symbols. Black circles indicate ambient-pressure experiments and red circles indicate high-pressure experiments. The solid black and red curves are fits to the data using the Equation 5.6.

To compare these two values, the difference in the $fO_2$ of the IW buffer at 1200 °C and 1500 °C (3.14 log units, as shown in Figure 5.9) must be taken into account. In Equation 5.6, $\log fO_2$ is multiplied by 0.5, so to compare $\log K'_{eq}$ values we simply add or subtract 0.5 × 3.14 log units. Therefore the value of $\log K'_{eq}$ for the high-pressure, 1500 °C data (-4.9 ± 0.7) is equivalent to -6.5 ± 0.7 at 1200 °C, which is within error of the value obtained for the ambient-pressure, 1200 °C data (-6.0 ± 0.2).

The choice of the $Ge^{4+}$ end-member spectrum used in the linear combination fitting has only a small effect on the results. In Figure 5.9, the $Ge^{4+}$ end-member spectrum used was B1-080316 (3000 ppm Ge), but the fit results are very similar if the spectrum of E02/12/13B (3 wt% Ge) is used. The results are different if E02/12/13A (300 ppm Ge) is used as the end-member, because of the shoulder that resembles a $Ge^{2+}$ component in the spectrum (Figure 5.6). The fit results therefore predict a smaller amount of $Ge^{2+}$ in each of the spectra around the transition. Nevertheless, the resulting sigmoidal curve is within error of that shown in Figure 5.9, and the choice of end-member used in the fitting therefore has no bearing on the conclusions of this study.

## EXAFS

The EXAFS spectrum of $Ge^{2+}$ is very different to that of $Ge^{4+}$. Figure 5.10 shows the EXAFS and Fourier transforms for a glass sample containing $Ge^{2+}$ (D12/04/16), one containing $Ge^{4+}$ (E04/11/13), and q-$Ge^{4+}O_2$.The EXAFS are highly damped in the $Ge^{2+}$ spectrum, and the Fourier transform indicates that the Ge–O bond length is longer than in $Ge^{4+}$.

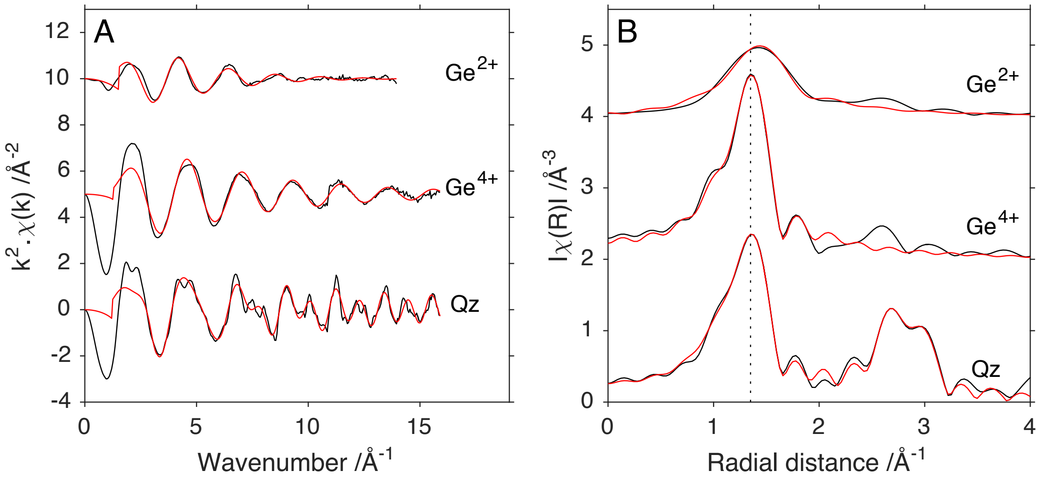

Figure 5.10. (A) Ge K-edge EXAFS spectra and (B) the Fourier transforms of the EXAFS spectra of D12/14/16 ($Ge^{2+}$), E04/11/13 ($Ge^{4+}$), and q-$GeO_2$ (Qz). Black curves are the spectra and red curves are fits to the spectra. Dashed line in (B) is a guide to the eye.

The EXAFS spectra were fit using the ARTEMIS software, after merging and de-glitching the spectra using ATHENA. Four paths were used to fit the reference material, q-$GeO_2$: single scattering from first-shell O, single scattering from second-shell Ge, single scattering from third-shell O and double scattering from first-shell O and second-shell Ge. The data was fit in R space, over the range 1.0–3.2 Å, and a k-range of 3–14. These four paths contributed most to the spectrum and adding more paths did not improve the fit.

To fit the glass samples, only one path was used – single scattering from first-shell O. In all cases the spectra were fit in R-space over the range 1.0–2.0 Å. E04/11/13 was fit over a k-range 3–14, whereas the range was only 3–10 for D12/04/16 due to the damped data. The EXAFS fit parameters for each spectrum are listed in Table 5.10. Fits are plotted along with the spectra in Figure 5.10.

For the $Ge^{4+}$–bearing glass, E04/11/13, the coordination number (N) was fixed at 4 and the other parameters were allowed to vary in the fit. For the $Ge^{2+}$–bearing glass, D12/04/16, three fits were performed. In the fit listed in Table 5.10 and plotted in Figure 5.10, the coordination number was allowed to vary, while $S_0^2$ was fixed at the value obtained in the fit to the $Ge^{4+}$–bearing glass. Two further fits, in which the coordination number was fixed to 4, produced very similar results.

For the glass containing $Ge^{4+}$ (E04/11/13, synthesised in air), the bond length is $1.750 \pm 0.005$ Å assuming a coordination of 4; hence the ionic radius of $Ge^{4+}$ is 0.37 Å, taking the ionic radius of $O^{2-}$ in tetrahedral coordination as 1.38 Å from Shannon (1976). This value compares quite well with the ionic radius of $Ge^{4+}$ in tetrahedral coordination ($r_{tet}$) of 0.39 Å listed by Shannon (1976), and with the value of 0.38 Å for $Ge^{4+}$ in the tetrahedral sites of oxide spinels of O'Neill and Navrotsky (O'Neill and Navrotsky 1983).

In contrast, the bond length for $Ge^{2+}$–O from the glass D12/04/16 synthesised at IW-3.0 is $1.89 \pm 0.03$ Å, giving $r_{tet}$ of $0.51 \pm 0.03$ Å. This is in good agreement with $Ge^{2+}$–O bond lengths in the only structurally characterized oxide compounds with $Ge^{2+}$ coordinated to $O^{2-}$, namely $GeCl(H_2PO_2)$, $NaGe_4(PO_4)_3$, and $Ge_2(H_2PO_2)_6$, which range from 1.86 to 1.95 Å (Cempírek and Groat 2013). The $Ge^{2+}$ in these compounds has the distorted tetrahedral coordination of a triangular pyramid, with a "stereochemically active lone pair of electrons oriented opposite to the triangle of anions" (Cempírek and Groat 2013), suggesting that tetrahedral coordination may be important in stabilizing $Ge^{2+}$ in minerals and melts. The coordination number obtained by EXAFS fitting is $3.4 \pm 1.0$, which is also consistent with this conclusion.

Shannon (1976) does not list a value for the ionic radius of $Ge^{2+}$ in this coordination, but gives 0.73 Å for $Ge^{2+}$ in octahedral coordination ($r_{oct}$); this comes from Ahrens (1952), who proposed an heuristic method for estimating the ionic radii of poorly known cations based on ionization potentials. Nevertheless, taking this estimate at face value, we can make an estimate for $r_{tet}$ for $Ge^{2+}$ as follows. The ratio $r_{tet}/r_{oct}$ of divalent cations with similar $r_{oct}$, namely Co, Fe, Mg, Mn, Ni and Zn, as given by Shannon (1976), is $0.80 \pm 0.01$, suggesting $r_{tet}$ for $Ge^{2+}$ should be $0.582 \pm 0.09$ Å, somewhat larger than our measurement of $0.51 \pm 0.03$ Å. If the latter is correct, it would mean that $r_{tet}$ for $Ge^{2+}$ was smaller than that for any other divalent cation except $Be^{2+}$, for which $r_{tet}$ is much smaller at 0.27 Å. For comparison, $r_{tet}$ for $Mg^{2+}$ is 0.57 Å (Shannon 1976).

Table 5.10. EXAFS fit parameters for spectra of $Ge^{4+}$ standards, q-$GeO_2$ and E04/11/13, and the $Ge^{2+}$-bearing glass, D12/04/16.

| | q-$GeO_2$ ($Ge^{4+}$) | | | | E04/11/13 ($Ge^{4+}$) | D12/04/16 ($Ge^{2+}$) |
|---|---|---|---|---|---|---|
| Path | [Ge]–O.1 | [Ge]–Ge.1 | [Ge]–O.2–Ge.1 | [Ge]–O.3 | [Ge]–O.1 | [Ge]–O.1 |
| N | 4 | 4 | 8 | 4 | 4 | 3.4 (10) |
| $S_0^2$ | 0.95 (6) | 0.953 | 0.953 | 0.953 | 0.87 (5) | 0.87 |
| $\sigma^2$ ($Å^2$) | 0.0034 (7) | 0.0021 (6) | 0.008 (12) | -0.001 (2)* | 0.0017 (6) | 0.008 (5) |
| $E_0$ (eV) | 5.7 (8) | 5.7 | 5.7 | 5.7 | 6.0 (9) | 9 (4) |
| $\Delta r$ (Å) | 0.018 (5) | 0.012 (10) | 0.02 (8) | -0.05 (2) | 0.011 (5) | 0.15 (3) |
| Reference path length (Å) * | 1.739 | 3.153 | 3.316 | 3.406 | 1.739 | 1.739 |
| Path length in sample (Å) ** | 1.757 (5) | 3.165 (10) | 3.34 (8) | 3.35 (2) | 1.750 (5) | 1.89 (3) |

N is the degeneracy (for first-shell oxygens, this equals the coordination number), $S_0^2$ is the amplitude reduction factor, $\sigma^2$ is the mean square relative displacement, $E_0$ is the difference in reference energy compared to the standard, $\Delta r$ is the change in half-path length compared to the 'reference path length'. *The 'reference path length' is calculated from lattice parameters of $GeO_2$ (Smith and Isaacs, 1964). ** The 'path length in sample' is calculated by adding $\Delta r$ to the 'reference path length'. Paths are from the central atom [Ge] to one or more surrounding atoms. For example, [Ge]–O.1 refers to scattering from first-shell oxygen atoms. Errors on the last digit are provided in parentheses; values without errors quoted were constrained in the fit. *The negative value of $\sigma^2$ obtained for the [Ge]–O.3 path of q-$GeO_2$ does not make physical sense, but it is within error of zero.

## *Partitioning experiments*

### Experimental olivine–melt partitioning results

A typical run product from a partitioning experiment is shown in Figure 5.11. Concentrations of major and trace elements in olivine and melt are listed in Table 5.11 and Table 5.12, respectively. Olivine–melt partition coefficients are given in Table 5.13.

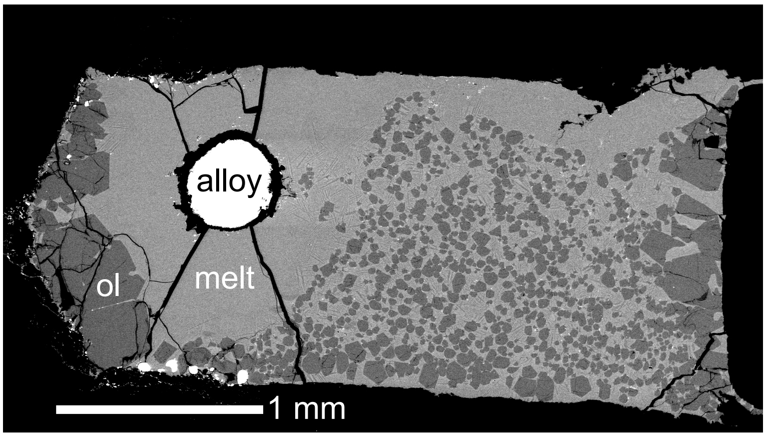

Figure 5.11. Backscattered electron image of sample D2357.

Table 5.11. Major and trace element analyses of experimental olivines.

| | D2270 | D2357 | D2368-i | D2368-ii | C4444 | D2413 |
|---|---|---|---|---|---|---|
| | | | Major elements by FE-SEM (wt%) | | | |
| *n* | 4 | 5 | 3 | 5 | 6 | 9 |
| MgO | 57.7 (3) | 57.5 (3) | 56.5 (3) | 56.7 (2) | 57.2 (4) | 57 (9) |
| $Al_2O_3$ | 0.16 (1) | 0.14 (2) | 0.15 (3) | 0.18 (4) | – | – |
| $SiO_2$ | 43.0 (2) | 42.8 (2) | 42.5 (2) | 42.5 (2) | 42.7 (2) | 42.9 (6) |
| CaO | 0.13 (2) | 0.07 (6) | 0.12 (4) | 0.11 (2) | – | – |
| CoO | – | – | 0.79 (1) | 0.7 (2) | – | – |
| Total | 101.0 (4) | 100.5 (5) | 100.1 (4) | 100.3 (5) | 99.9 (5) | 100 (1) |
| | | | Trace elements by LA-ICPMS (ppm, unless specified) | | | |
| *n* | 5 | 3 | 8 | 6 | 7 | 10 |
| Na | – | – | – | – | 1.3 (2) | bdl |
| $Al_2O_3$ (wt%) | 0.062 (5) | 0.074 (6) | 0.106 (1) | 0.105 (1) | 0.017 (1) | 0.0214 (7) |
| CaO (wt%) | 0.08 (2) | 0.074 (4) | 0.11 (1) | 0.10 (2) | 0.044 (2) | 0.06 (1) |
| P | – | – | – | – | 42 (2) | 53 (6) |
| K | – | – | – | – | bdl | bdl |
| Sc | 26 (1) | 40 (2) | 46.5 (5) | 46.8 (6) | 26.0 (5) | 42 (1) |
| Ti | – | 220 (14) | 63.4 (8) | 65 (2) | 3.0 (2) | 23 (2) |
| V | 149 (18) | 31 (2) | 252 (3) | 257 (6) | 4 (1) | 2.2 (1) |
| Cr | – | – | – | – | 2.6 (2) | 1.2 (2) |
| Mn | – | 220 (2) | 779 (4) | 759 (8) | 8.9 (4) | 634 (11) |
| Fe | – | – | – | – | 74 (7) | 49 (5) |
| Co | 0.15 (3) *n*=4 | 1.79 *n*=1 | 0.66 (3) wt% | 0.59 (3) wt% | 22.6 (2) | 3.53 (9) |
| Ni | – | – | – | – | 359 (5) | 45 (3) |
| Zn | – | 7.8 (3) *n*=2 | 250 (3) | 255 (3) | 17 (1) | 254 (5) |
| Ge | < 0.27* | < 0.068* | 1409 (53) | 1146 (50) | 1759 (36) | 1275 (32) |
| Sr | – | 0.092 *n*=1 | 0.2 (1) | 0.14 (2) | 0.02 (3) | 0.3 (3) |
| Y | 52 (3) | 16.7 (3) *n*=2 | 21.7 (3) | 21.0 (2) | 50 (1) | 17.6 (7) |
| Zr | – | 1.2 *n*=1 | 1.3 (1) | 1.34 (7) | 0.14 (3) | 1.03 (9) |
| Ba | – | bdl | – | – | bdl | 0.5 (5) |
| Hf | – | 2.25 *n*=1 | – | – | 0.009 (3) | 2.3 (2) |

*Maximum values reported for Ge in D2270 and D2357 are the lowest detection limit for Ge obtained from LA-ICPMS for the respective samples. *n* = number of analyses. bdl = below detection limit. Numbers in parentheses are one standard deviation on the last digit.

The $fO_2$ of these partitioning experiments has been calculated using the Co-CoO equilibrium (see Table 5.8). However, it was also possible to calculate $fO_2$ using the partitioning of V between olivine and silicate melt. Equation 5 from Mallmann and O'Neill (2013) was used for this purpose. This equation is only calibrated for an $fO_2$ range of between four log units above and below the quartz-fayalite-magnetite (QFM) oxygen buffer and so it is appropriate to use for samples D2368-i and -ii only. For these two samples, the $\log fO_2$ ΔIW values calculated are 2.47 ± 0.05 for D2368-i, and 2.26 ± 0.10 for D2368-ii. These values are around three log units higher than the values calculated using the Co–CoO equilibrium, which gave ΔIW -0.7 ± 0.2 for both samples (see Table 5.8).

Mallmann and O'Neill (2013) also describe a geothermometer based on the partition coefficients of Y and Sc. This is applied to the samples in this chapter as a check that the nominal temperature of the experiment (1500 °C) was in fact the temperature at which the samples equilibrated. Equation 3 in Mallmann and O'Neill (2013) was used and the calculated temperatures are listed in Table 5.13. Calculated temperatures are all within one standard deviation of 1500 ºC except for sample C4444. This sample was made using a capsule that had been previously used in an experiment that did not quench correctly, so it is possible that this has influenced the Y and Sc distribution in the sample.

Table 5.12. Major and trace element analyses of experimental melt.

| | D2270 | D2357 | D2368-i | D2368-ii | C4444 | D2413 |
|---|---|---|---|---|---|---|
| Major elements by FE-SEM (wt%) | | | | | | |
| *n* | 9 | 6 | 4 | 5 | 8 | 8 |
| MgO | 27 (2) | 29.9 (2) | 27.8 (5) | 28 (3) | 36.6 (5) | 30.5 (4) |
| $Al_2O_3$ | 10.8 (9) | 10.2 (1) | 11.7 (6) | 11 (1) | 7.4 (3) | 9.9 (3) |
| $SiO_2$ | 55.8 (6) | 53.5 (2) | 50.0 (3) | 50.9 (8) | 47.1 (3) | 48.4 (7) |
| CaO | 6.0 (5) | 4.56 (5) | 6.1 (1) | 5.1 (6) | 3.37 (8) | 4.4 (1) |
| $TiO_2$ | – | 0.48 (2) | 0.95 (6) | 0.91 (8) | – | – |
| CoO | – | – | 0.715 (6) | 0.59 (3) | – | – |
| $GeO_2$ | – | – | 1.124 (8) | 1.24 (7) | – | – |
| $Y_2O_5$ | – | – | – | – | 1.09 (3) | 0.1 (2) |
| BaO | – | 0.98 (7) | 1.00 (4) | 1.0 (1) | – | 1.39 (6) |
| Total | 99.3 (3) | 99.5 (4) | 99.4 (6) | 99.11 (8) | 95.6 (5) | 95 (1) |
| Trace elements by LA-ICPMS (ppm, unless specified) | | | | | | |
| *n* | 2 | 9 | 7 | 5 | 8 | 9 |
| Na | – | – | – | – | 359 (7) | 466 (15) |
| $Al_2O_3$ (wt%) | 9.3 (2) | 9.2 (1) | 10.1 (3) | 9.74 (6) | 1.75 (6) | 2.33 (5) |
| CaO (wt%) | 5.07 (5) | 4.48 (8) | 5.5 (2) | 4.51 (7) | 2.24 (7) | 2.86 (9) |
| P | – | – | – | – | 64.4 (7) | 181 (6) |
| K | – | – | – | – | 191 (5) | 320 (21) |
| Sc | 212 (2) | 324 (3) | 349 (14) | 336 (4) | 170 (2) | 304 (10) |
| Ti (wt%) | – | 0.244 (5) | 0.43 (1) | 0.409 (5) | 0.0052 (2) | 0.322 (5) |
| V | 32.69 (8) | 11 (2) | 781 (13) | 741 (10) | 919 (22) | 765 (19) |
| Cr | – | – | – | – | 12.2 (3) | 3.0 (5) |
| Mn | – | 371 (3) | 1421 (30) | 1394 (23) | 25.4 (0.7) | 1321 (39) |
| Fe | – | – | – | – | 636 (24) | 383 (10) |
| Co | 0.09 (1) | 2.1 (5) | 0.46 (1) wt% | 0.41 (2) wt% | 22.2 (3) | 2.72 (5) |
| Ni | – | – | – | – | 175 (6) | 16 (3) |
| Zn | – | 11.9 (3) | 352 (7) | 343 (6) | 33.6 (4) | 336 (17) |
| Ge (wt%) | 0.0011 (1) | 0.0015 (3) | 0.91 (1) | 0.88 (2) | 0.309 (3) | 0.218 (2) |
| Sr (wt%) | – | 0.169 (1) | 0.189 (5) | 0.178 (2) | 0.00130 (4) | 0.159 (4) |
| Y (wt%) | 0.931 (3) | 0.281 (3) | 0.31 (1) | 0.294 (3) | 0.72 (2) | 0.263 (9) |
| Zr (wt%) | – | 0.141 (1) | 0.160 (5) | 0.153 (2) | 0.0159 (3) | 0.134 (3) |
| Ba (wt%) | – | 0.79 (1) | – | – | 0.00128 (4) | 0.73 (2) |
| Hf (wt%) | – | 0.195 (2) | – | – | 0.00037 (1) | 0.179 (4) |

*n* = number of analyses. Numbers in parentheses are one standard deviation on the last digit.

Table 5.13. Olivine–melt partition coefficients, D, for the elements indicated.

| | D2270 | D2357 | D2368-i | D2368-ii | C4444 | D2413 |
|---|---|---|---|---|---|---|
| Al | 7.3 (6) × $10^{-3}$ | 8.0 (6) × $10^{-3}$ | 1.05 (4) × $10^{-2}$ | 1.08 (1) × $10^{-2}$ | 9.4 (7) × $10^{-3}$ | 0.0092 (4) |
| Ca | 0.018 (5) | 0.0164 (9) | 0.021 (2) | 0.022 (3) | 0.020 (1) | 0.020 (4) |
| P | – | – | – | – | 0.66 (3) | 0.29 (4) |
| Sc | 0.136 (7) | 0.123 (5) | 0.134 (5) | 0.140 (3) | 0.153 (4) | 0.139 (7) |
| Ti | – | 9.0 (6) × $10^{-2}$ | 1.48 (5) × $10^{-2}$ | 1.59 (6) × $10^{-2}$ | 4 (5) × $10^{-3}$ | 7.1 (6) × $10^{-3}$ |
| V | 5.0 (6) | 2.8 (5) | 0.323 (7) | 0.347 (9) | 4 (1) × $10^{-3}$ | 2.9 (2) × $10^{-3}$ |
| Cr | – | – | – | – | 0.22 (2) | 0.41 (9) |
| Mn | – | 0.592 (8) | 0.55 (1) | 0.54 (1) | 0.35 (2) | 0.48 (2) |
| Fe | – | – | – | – | 0.12 (1) | 0.13 (1) |
| Co | 1.9 (5) | 0.9 (2) | 1.44 (6) | 1.5 (1) | 1.01 (2) | 1.30 (4) |
| Ni | – | – | – | – | 2.05 (8) | 2.8 (6) |
| Zn | – | 0.66 (3) | 0.71 (2) | 0.74 (1) | 0.52 (3) | 0.76 (4) |
| Ge | < 0.03* | < 0.005* | 0.155 (6) | 0.131 (6) | 0.57 (1) | 0.59 (2) |
| Sr | – | 5.44 (5) × $10^{-5}$ | 1.2 (7) × $10^{-4}$ | 8 (1) × $10^{-5}$ | 2 (2) × $10^{-3}$ | 2 (2) × $10^{-4}$ |
| Y | 6.1 (4) × $10^{-3}$ | 6.0 (1) × $10^{-3}$ | 7.0 (3) × $10^{-3}$ | 7.2 (1) × $10^{-3}$ | 6.9 (2) × $10^{-3}$ | 6.7 (4) × $10^{-3}$ |
| Zr | – | 8.52 (7) × $10^{-4}$ | 8.1 (5) × $10^{-4}$ | 8.7 (5) × $10^{-4}$ | 9 (2) × $10^{-4}$ | 7.7 (7) × $10^{-4}$ |
| Hf | – | 1.16 (1) × $10^{-3}$ | – | - | 2.5 (9) × $10^{-3}$ | 1.3 (1) × $10^{-3}$ |
| T** | 1466 (53) | 1491 (30) | 1496 (37) | 1500 (16) | 1468 (24) | 1484 (49) |

*Maximum values reported for Ge in D2270 and D2357 are based on lowest detection limit for Ge in olivine in these samples (Table 5.11). **Temperature (ºC) calculated using the Sc/Y geothermometer of Mallmann and O'Neill (2013).

Figure 11 shows the Ge partition coefficient plotted against $fO_2$. In the two most reduced samples, Ge was not detected in the olivines by LA-ICPMS. The Ge detection limit for D2357 was much better than for D2270, because the crystals were larger in D2357, allowing a larger spot size to be used. Sample D2357 therefore provides the best estimate of the maximum partition coefficient for $Ge^{2+}$ as 0.005, indicating that $Ge^{2+}$ is highly incompatible. This is very different to $Ge^{4+}$, which has olivine-melt partition coefficients of 0.58 ± 0.01 (Table 5.13).

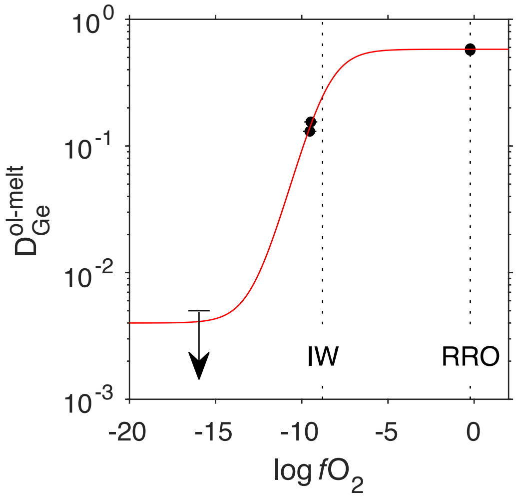

Figure 5.12. Partition coefficients of C4444, D2413, D2368-i, and D2368-ii. Values of log$fO_2$ for each sample were calculated from the Co–CoO equilibrium. The maximum partition coefficient for D2357 is shown as a downward arrow, and the horizontal bar is the error on the $fO_2$ calculated. IW and RRO indicate the iron–wüstite and Ru-RuO$_2$ buffers respectively. The red curve is a fit to the data using Equation 5.7.

These data can be fit to a sigmoidal equation (see Equation 19 in Mallmann and O'Neill 2009):

$$D_{Ge\ (bulk)}^{ol-melt} = \frac{D_{Ge2+}^{ol-melt} \cdot K'_{eq} \cdot (fO_2)^{-0.5} + D_{Ge4+}^{ol-melt}}{K'_{eq} \cdot (fO_2)^{-0.5} + 1}$$

Equation 5.7

where $K'_{eq}$ is the equilibrium constant for a given melt composition, as defined in Equation 5.6. Note that Equation 5.7 is slightly different to Equation 19 of Mallmann and O'Neill (2009) in that the latter contains $(K'_{hom})^{-1}$ instead of $K'_{eq}$. However, $K'_{eq}$ as defined in Equation 5.6 is in fact the inverse of $K'_{hom}$ in Mallmann and O'Neill (2009), because of the way Equation 5.2 is written (Mallmann and O'Neill derive $K'_{hom}$ from the inverse of Equation 5.2). To maintain consistency within this chapter, I retain the definition as given in Equation 5.6 and therefore do not include the negative power in Equation 5.7.

From the partitioning data, $D_{Ge4+}^{ol-melt}$ is constrained to be 0.58 ± 0.01. $D_{Ge2+}^{ol-melt}$ is unknown, but based on the data, it should be $<0.005$. In order to fit $K'_{eq}$, $D_{Ge2+}^{ol-melt}$ was set at 0.004. This value is arbitrary and has negligible effect on the fitted value of $K'_{eq}$, because $K'_{eq}$ controls only the position of the sigmoid in log$fO_2$ space (and the slope is fixed by the number of electrons involved in the reaction). The fit, shown as the red curve in Figure 5.12, predicts $K'_{eq} = 5.5\ (\pm 0.3) \times 10^{-5}$ and log$K'_{eq}$ = -4.3 ± 0.2. This is within error of the result obtained by fitting the XANES data from high-pressure experiments, which gave a log$K'_{eq}$ = -4.9 ± 0.7. When this value is converted to a log$K'_{eq}$ at 1200 °C, we obtain -5.9 ± 0.2 at 1200 °C, which is within error of the value obtained for the ambient-pressure data (-6.0 ± 0.2).

However, if the $fO_2$ of D2368-i and D2368-ii were taken from the V partitioning data, the log$K'_{eq}$ obtained is -2.94 ± 0.03. If this is converted to a 1200 °C value we obtain -4.51 ± 0.03. This is not within error of any of the previous results.

**Systematics of olivine–melt trace element partition coefficients**

Partition coefficients for a number of trace elements are plotted against their ionic radii in Figure 5.13. If partitioning between phases was at equilibrium then the values for elements of the same charge that occupy the same crystallographic site should fall on a parabola, with the form (Brice 1975; Blundy and Wood 1994):

$$D_i = D_o * exp\left(\frac{-4\pi E_S N_A \left(\frac{r_o}{2}(r_o - r_i)^2 + \frac{1}{3}(r_o - r_i)^3\right)}{RT}\right)$$

Equation 5.8

where $D_i$ is the partition coefficient as a function of ionic radius $r_i$, $N_A$ is Avogadro's number, $R$ is the ideal gas constant, $T$ is temperature in K, $D_0$ is the partition coefficient of a fictional cation with the 'ideal' radius $r_0$, and $E_S$ is the Young's modulus for the crystallographic site.

Figure 5.13 shows the partition coefficients from two partitioning experiments, D2413 and D2357. Equation 5.8 was fit to most of the 2+ cations: Mg, Zn, Mn, Ca and Sr. The partitioning of Co is not described by a simple lattice-strain model because of crystal field effects (Wood and Blundy 2014) and so this cation was not included in the fits. The multivalent element Mn is included, because at the conditions of these experiments, it is expected to be predominantly in the 2+ valence state, based on unpublished XANES spectra of synthetic MORB equilibrated at a range of $fO_2$ values (Berry, A.J., pers. comm.). Partition coefficients for Be were also calculated using Equation 1 in Burnham and O'Neill (2016) in order to better constrain the fit, however the samples in this study contained no Be.

Equation 5.8 can only be fit to elements that have the same charge and occupy the same site, and at least three elements are required in order to constrain a parabola. It was therefore not possible to fit lattice strain models to the 3+ cations, because $Al^{3+}$ substitutes on both tetrahedral and octahedral sites, leaving only $Sc^{3+}$ and $Y^{3+}$. Likewise, no fit was made for the 4+ cations. $Si^{4+}$ and $Ge^{4+}$ occupy the tetrahedral site, but $Hf^{4+}$ and $Zr^{4+}$ are too large for this site (Jollands et al. 2014), and $Ti^{4+}$ may substitute via Ti-clinohumite-like defects at high pressure and/or if water is present (Hermann et al. 2005; Berry et al. 2007).

The lattice strain models for 2+ cations indicate that $Ge^{2+}$ does not occupy the octahedral site in olivine, because it has a much lower partition coefficient compared to other 2+ cations of similar radii. Instead, $Ge^{2+}$ probably substitutes onto the tetrahedral site, causing distortion of this site due to its large tetrahedral ionic radius (0.51 Å).

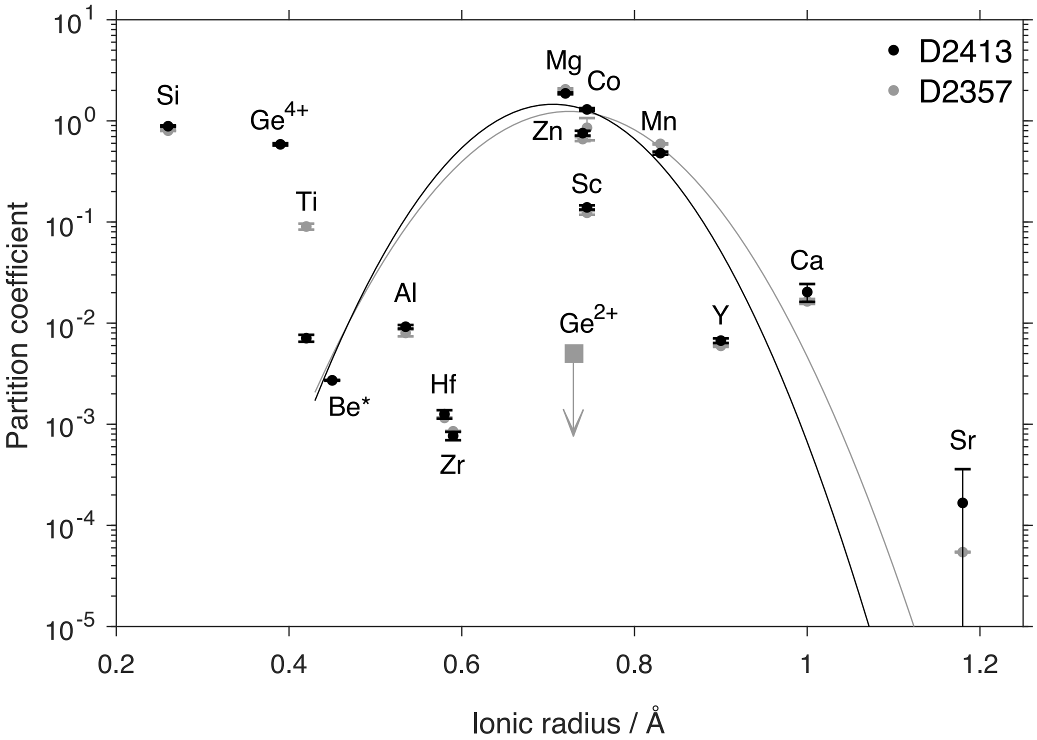

Figure 5.13. Partition coefficients of elements in D2413 (black) and D2357 (grey) plotted against their ionic radii. The black and grey curves show fits to Equation 5.8 for the 2+ cations in the two samples (see text for details of cations included in fits). Fit parameters are as follows: for D2413, $D_0 = 1.5 \pm 1.0$, $E_s = 1.7 (\pm 1.4) \times 10^2$, $r_0 = 0.71 \pm 0.07$. For D2357, $D_0 = 1.2 \pm 1.0$, $E_s = 1.4 (\pm 1.5) \times 10^2$, $r_0 = 0.72 \pm 0.08$. *The data for Be was calculated using Equation 1 in Burnham and O'Neill (2016) in order to better constrain the fit, however the samples in this study contained no Be. The square with the downward facing arrow marks the maximum partition coefficient of $Ge^{2+}$ in D2357. This is plotted at the ionic radius of $Ge^{2+}$ (in 6-fold coordination) listed in Shannon (1976). Note that Mn is likely in the 2+ valence state, as discussed in the text, and Ti probably in the 4+ valence state in D2413 and in the 3+ valence state in D2357 (Mallmann and O'Neill 2009).

## 5.4 Discussion

### *Partitioning and coordination of Ge$^{2+}$*

The XANES spectra presented in this work show clear evidence for the stability of Ge$^{2+}$ in silicate melts, and the partitioning data indicate that Ge$^{2+}$ is highly incompatible in olivine.

Our results indicate that tetrahedral coordination may be required to stabilise Ge$^{2+}$. Previous work found that Ge$^{2+}$ occurs in a distorted tetrahedral coordination in phosphate compounds (Cempírek and Groat 2013). The bond lengths obtained from EXAFS in this study are also consistent with a tetrahedral coordination of Ge$^{2+}$ in silicate melt. Furthermore, in olivine, Ge$^{2+}$ probably occupies the tetrahedral site, because its partition coefficient is much lower than would be expected if it substituted on the octahedral site Figure 5.13.

The highly incompatible behaviour of Ge$^{2+}$ can be explained in light of this, as it is too large to be comfortably accommodated on the tetrahedral site in olivine. In contrast, in the silicate melt structure is flexible enough to accommodate the large cation in a distorted tetrahedral coordination. Therefore Ge$^{2+}$ is preferentially partitioned into the melt phase. If this line of reasoning holds, Ge$^{2+}$ is likely to be incompatible in all rock-forming silicate minerals, because none of these minerals contain suitably large tetrahedral sites.

Finally, if tetrahedral coordination is required in the melt for the stability of Ge$^{2+}$, this raises the question of whether Ge$^{2+}$ will remain stable at high pressures. Ge$^{2+}$ was still observed at 1 GPa in this study, but this is not enough pressure to substantially alter the coordination number of Ge$^{4+}$ (Chapter 2). Further work at higher pressures is needed to test whether or not Ge$^{2+}$ will remain stable or not, and this question is important for models of Earth's core formation, as will be discussed.

### *The* f$O_2$ *of the* $Ge^{4+}$*–*$Ge^{2+}$ *transition*

The XANES spectra show that the transition from primarily $Ge^{4+}$ to primarily $Ge^{2+}$ occurs between approximately ΔIW +2 and ΔIW -2. The scatter in the sigmoid (Figure 5.9) is larger than what has been observed in similar studies (e.g. Cr valence state; Berry and O'Neill 2004). The scatter is not likely to be due to the uncertainties in determining the speciation represented by a spectrum using linear combination fitting, because the changes in the shape of the Ge spectra are substantial around the transition (Figure 5.5), and the linear combination fits are very good (Figure 5.7). R-factor values are <0.005 for all fits shown in Figure 5.9 (note that the reduced chi-squared is not a meaningful statistic in this context, because the number of independent points in a spectrum cannot be quantified). Therefore, this scatter in the sigmoid is likely to result from the complexity of the experimental design. The 1-atm experiments depend on establishing a steady state between Ge acquired from the vapour of the source at the bottom of the silicate tube (Figure 5.2), and Ge lost by vaporization. Since the vapour species is $Ge^{2+}O$ (Barton and Heil, 1970), the preferential loss of $Ge^{2+}$ might upset the equilibrium between $Ge^{2+}$ and $Ge^{4+}$. This does not explain, however, the discrepancy in apparent $Ge^{2+}/\sum Ge$ in the experiments in air, which may be due to beam damage, nor the deviations from the sigmoid among the high-pressure experiments.

The observation that the $Ge^{4+}$–$Ge^{2+}$ transition occurs at around IW is consistent with the hypothesis based on metal–silicate partitioning data from literature studies (Schmitt et al. 1989; Capobianco et al. 1999; Kegler and Holzheid 2011; Siebert et al. 2011). However, in detail, just as these studies mostly do not agree with each other, the data presented in the present study also does not agree with any of the literature data. This could simply be because $Ge^{2+}$ stability is different depending on the composition, temperature and pressure.

However, the width of the transition between $Ge^{4+}/\sum Ge = 0.1$ to 0.9 is defined thermodynamically from its stoichiometry to be around four log units (Equation 5.6). Regardless of the location of the transition in log$fO_2$ space, reconciling these literature data with this width is not easy. To calculate valence states from metal–silicate partitioning experiments requires data over an adequate range of $fO_2$. Yet the ranges in the literature studies are somewhat restricted (Figure 5.1). The method described in this chapter, despite its difficulties, has the advantage that the speciation is determined for each individual sample. Thus, it is suggested that the data presented here are a better estimate for the $Ge^{4+}$–$Ge^{2+}$ transition than any of the previous studies.

Whether the partitioning data presented in this study support or contradict the XANES data is unclear, because of the difficulty in retrospectively estimating the $fO_2$. The Ge partition coefficients of samples D2368-i and D2368-ii lie in between those in samples equilibrated at lower $fO_2$ (D2270 and D2357) and at higher $fO_2$ (C4444 and D2413). This observation suggests that a mixture of $Ge^{2+}$ and $Ge^{4+}$ is present in samples D2368-i and D2368-ii. If the $fO_2$ of these samples are known, a sigmoid can be fit to the data (Figure 5.12) and directly compared to the XANES results. However, the two methods for calculating $fO_2$ produced results that differed by about 3 log units. Using V olivine–melt partitioning to calculate $fO_2$ gives values of $\Delta$IW +2.47 ± 0.05 for D2368-i, and $\Delta$IW +2.26 ± 0.10 for D2368-ii. At these $fO_2$ values, $Ge^{4+}$ is the only species expected to be stable based on the XANES data, and so using this method, the partitioning data contradict the results from XANES. However, using the Co–CoO equilibrium, the $fO_2$ of both samples was estimated to be $\Delta$IW -0.7 ± 0.2; using this $fO_2$ value, the partitioning data agree well with the results from XANES spectroscopy.

The cause of the discrepancy between the methods of calculating $fO_2$ is unclear. A number of assumptions were made in these calculations that could affect the result. For example, in the calculations based on the Co–CoO equilibrium, the presence of dissolved Si in the metal phase was assumed to have no effect on the activity of Co, and the composition of the metal phase was assumed to be that of the largest, or several largest blobs in the sample, whereas smaller metal nuggets were not analysed. In the calculations based on V partitioning, the equation was calibrated on compositions that differ to the one studied here. Any of these factors may affect the results, and so which method gives more accurate results is unknown.

### *Implications*

#### **Models of Earth's core formation**

It is possible that the metal–silicate partitioning of $Ge^{2+}$ during core formation has influenced the present-day Ge distribution in the Earth. Our results indicate that $Ge^{2+}$ is the stable species below ~$\Delta$IW -2, and is dominant over $Ge^{4+}$ up to IW.

Core formation in the Earth is classically thought to have occurred at an $fO_2$ of ~ΔIW -2 (Wood et al. 2006). If metal and silicate equilibrated in a deep magma ocean (e.g. Li and Agee 1996; Rubie et al. 2003) the high-pressure stability and partitioning behaviour of $Ge^{2+}$ is of critical importance, and nothing is yet known about the high-pressure stability of $Ge^{2+}$. Other recent models of core formation suggest that metal and silicate may have equilibrated in highly reducing planetesimals, which subsequently accreted to the proto-Earth and did not necessarily equilibrate fully with the silicate part of the proto-Earth (e.g. Dahl and Stevenson 2010; Rubie et al. 2015; Fischer et al. 2017; Marchi et al. 2018). If so, the behaviour of $Ge^{2+}$ at low pressure in these planetesimals will have influenced its subsequent distribution.

In addition to the partitioning-based models of Earth's core formation, recent work has attempted to use Ge isotopes to trace this process. The $\Delta^{74/70}$Ge fractionation factor between the silicate Earth and magmatic iron meteorites (a proxy for the Earth's core) is $\Delta^{74/70}$Ge +0.85 ‰. This is at odds with the theoretical prediction of a negative fractionation factor between metal and silicate, assuming $Ge^{4+}$ in the silicate (Luais 2012; Rouxel and Luais 2017). Luais (2012) suggested the discrepancy indicated that the isotopic composition measured for silicate materials is a poor estimated for the bulk silicate Earth, due to the lack of samples from the deep or ancient mantle. Our work suggests another factor to be taken into account: the predictions of fractionation factors would change if $Ge^{2+}$ were assumed to be the stable species, because the calculations depend on oxidation state, coordination number and bond lengths (Li et al. 2009). The work presented in this study may therefore provide important information for interpreting Ge isotopic data.

### Lunar and planetary magmatism

As well as being the stable oxidation state in the early Earth, $Ge^{2+}$ is likely to be the stable species on the moon. The $fO_2$ at which lunar basalts crystallised, as well as the $fO_2$ of the lunar mantle, is thought to be at or below IW (Wieczorek et al. 2006). Ge is very depleted in the moon, but there are large enrichments in KREEP basalts (Dickinson et al. 1989; Haskin and Warren 1991). KREEP refers to the last, highly evolved magma to crystallise from the lunar magma ocean, which was enriched in K, REE and P. This material was then sampled by the 'KREEP basalts' which erupted onto the surface. The unusual enrichment of Ge in KREEP was a puzzle to

Dickinson et al. (1989), because, working with a partition coefficient of ~0.7 for $Ge^{4+}$ (Capobianco and Watson 1982), there would be very little Ge enrichment through processes like fractional crystallization. Dickinson et al. (1989) therefore proposed a model involving lunar mantle metasomatism, which transported and concentrated Ge. However, the data presented here indicate that $Ge^{2+}$ is probably the stable species on the moon, and unlike $Ge^{4+}$, it is highly incompatible. $Ge^{2+}$ would therefore be enriched in KREEP simply as a result of its incompatibility, and models involving lunar mantle metasomatism are probably not required. Further work is needed to quantify $D_{Ge2+}$ for olivine and other minerals before a new model can be quantified.

Trace element geochemistry has also been used to investigate the magmatic histories of smaller planetary bodies, such as the howardite, eucrite and diogenite (HED) parent body, likely to be the asteroid 4 Vesta (McCord et al. 1970; Consolmagno and Drake 1977). Trace element analyses of the HED meteorites have been used to investigate the nature of Vesta's mantle, the extent of melting and the present-day structure of the asteroid (Consolmagno and Drake 1977; Barrat et al. 2010; Consolmagno et al. 2015; Hahn et al. 2017). There is some, albeit limited, data for Ge contents in eucrites (Kitts and Lodders 1998), indicating that eucrites, like lunar basalts, are depleted in Ge relative to terrestrial basalts and martian meteorites (Lodders 1998). Based on these data, and assuming a partition coefficient of Ge between silicate minerals and melts of ~1, Ruzicka et al. (2001) suggested that Ge was strongly depleted in the source regions of eucrite melts through the segregation of metal (i.e. during core formation). If $Ge^{2+}$ were the stable species in Vesta, the data presented in this study implies an even stronger depletion of Ge in the source regions of eucrites. However the overwhelming signal is likely the volatility of Ge, which is greater at low $fO_2$.

## 5.5 Conclusion

Germanium has not been analysed routinely with other trace elements in geochemical studies, because little variation in Ge concentration is observed in crustal and mantle rocks. This homogeneity is a result of the mineral–silicate melt partition coefficient of $Ge^{4+}$ being close to unity, preventing any significant fractionation during magmatic processes in the relatively oxidised conditions of the present-day upper mantle and crust of the Earth. However, in more reducing conditions, $Ge^{2+}$ may become stable, with the $Ge^{4+}$–$Ge^{2+}$ transition occurring over the range from IW +2 and IW -2. $Ge^{2+}$ behaves very differently to $Ge^{4+}$, being highly incompatible, although further experiments are needed to quantify $Ge^{2+}$ partitioning. $Ge^{2+}$ may have been the stable species in the reducing conditions of a magma ocean on the early Earth (and/or in the planetesimals that accreted to form the Earth), and in magmas generated on the moon. This work may be important in understanding Ge isotopic fractionation, and suggests that further work on Ge geochemistry could provide insights into magmatic processes in reducing environments.

# Chapter 6: Concluding remarks

## 6.1 Discussion

Despite the importance of trace element partitioning in models of magmatic processes, little research has been done so far to investigate the pressure-induced coordination changes of trace elements and how these affect partitioning. This thesis extends the previous work on $Ni^{2+}$, $Co^{2+}$ and $Lu^{3+}$ (Keppler and Rubie 1993; Jones 2012; de Grouchy et al. 2017) to include $Ge^{4+}$ and $Ga^{3+}$.

The work presented in Chapter 2 shows that both $Ge^{4+}$ and $Ga^{3+}$ undergo coordination changes with pressure, from around 1–2 GPa to at least 10 GPa in annealed glasses. The coordination change began at higher pressures (2–3 GPa) in quenched melts. Several compositions were studied for $Ge^{4+}$ and indicate that the coordination changes at a greater rate with pressure in more depolymerised compositions. Thus, pressure-induced coordination changes of these trace elements would be expected to occur in natural melts in the Earth's mantle.

The influence of these coordination changes on the partitioning behaviour of the trace elements is not well established. The olivine–melt partitioning behaviour of Ge is predicted to become more compatible with pressure using equations of state (that do not incorporate coordination changes). This is not observed; as shown in Chapter 4, $Ge^{4+}$ becomes slightly more incompatible with pressure (up to 4.5 GPa, the maximum pressure of the experiments). More work is needed to unravel the influence of the changing molar volumes, configurational entropy and enthalpy on the partition coefficients, as well as the influence of Al coordination changes, which may affect activity coefficients of trace elements.

In Chapter 3, the potential effect of major element coordination on that of trace elements is investigated. A strong correlation between $Ga^{3+}$ and $Al^{3+}$, and a weaker correlation between $Ge^{4+}$ and $Al^{3+}$, suggests that Al coordination changes might 'encourage' both trace elements to also change their coordination. This is the first evidence for a possible link between major and trace element coordination. Whether such a link would extend to other trace elements is unknown; $Ge^{4+}$ and $Ga^{3+}$, being network formers, might be influenced more strongly by modifications to the tetrahedral network than trace elements that are network modifiers. This is worth further investigation. If coordination changes of major elements do affect the coordination of many trace elements, this would be very important for interpreting and predicting changes in trace element partition coefficients with pressure.

Finally, the results presented in Chapter 5 show that $Ge^{2+}$ is indeed stable in silicate melts at low $fO_2$, and probably at the conditions of core formation in the Earth. Preliminary partitioning experiments show that $Ge^{2+}$ is highly incompatible. Whether $Ge^{2+}$ also undergoes pressure-induced coordination changes is unknown.

### *Limitations of the results*

A key unknown that may affect the results presented in this thesis is the volatile content of the samples. The presence of dissolved volatiles in the glasses studied in Chapters 2 and 3 may affect the glass transition temperature, and if this changes systematically with pressure, it may be obfuscating our interpretations of pressure-induced changes. Volatiles may also influence the partition coefficients found in Chapter 4 and 5. To ensure accurate interpretations of the results, future work will determine the amount of dissolved volatiles in the samples using infra-red spectroscopy.

### *Directions for future work*

There are several interesting results from this thesis that warrant further investigation, including the relationship between major and trace element coordination changes, the influence of coordination changes on trace element partitioning, and the stability and partitioning behaviour of $Ge^{2+}$.

The relationship between major and trace element coordination changes could be investigated further by determining coordination changes of several trace elements in glasses of CMAS7G composition, for which the pressure-dependence of Al coordination is now known. As a starting point, I suggest investigating Lu coordination state to validate the results obtained from *in situ* X-ray diffraction by de Grouchy et al. (2017). Further work on Ni, Co and W coordination at pressures >4.5 GPa would also be valuable (Jones 2012). Similar work on more basaltic melt compositions would also be of interest, since Al and Ge coordination changes appear to increase more steeply with pressure in more depolymerised compositions (Chapter 2; Wolf and McMillan 1995).

Partitioning experiments, in principle, could provide valuable information about silicate melt structure. Chemical diffusion is too slow to change upon quenching the experiment, so the measured partition coefficients should reflect the structure of the melt at high pressure and temperature. However, interpreting the relationship between melt structure and partition coefficients is difficult. Studying the structure of glasses directly as an analogue for the melt can help with this interpretation, but suffers from the limitation that the compositions studied usually differ. Melt compositions used in olivine–melt partitioning experiments are MgO-rich, but MgO-rich melts have high liquidus temperatures and do not easily quench to glass from high pressure and temperature. This means that synthesising ‘quenched melts’ of these compositions from high pressures is not possible. However, if glasses of an MgO-rich composition could be quenched at ambient pressure, perhaps these glasses could be annealed near $T_g$ to provide information on their high-pressure structures. To my knowledge, no previous studies have investigated the structure of a glass that has the same composition as a melt used in a partitioning experiment. This would be very valuable.

A better thermodynamic treatment of the effect of pressure on partition coefficients, taking coordination changes into account is also needed. As described in Chapter 3, most existing equations of state do not account for coordination changes.

The stability of $Ge^{2+}$ also needs further investigation, because so far, the stability of this species has only been determined for one composition, pressure and temperature. Furthermore, given the likelihood that $Ge^{2+}$ was the stable species at the time of core formation in the Earth, it would be important to determine whether $Ge^{2+}$ undergoes pressure-induced coordination changes. This could be determined relatively easily up to pressures around 5 GPa by synthesising melts in graphite capsules as described for the $Ge^{2+}$ partitioning experiments. Further work to determine the olivine–melt partition coefficient of $Ge^{2+}$ is also needed.

## 6.2 Conclusion

There is a great deal we do not know about how trace elements are incorporated into silicate melts, and the effect of coordination changes on trace element partitioning. This thesis extends the limited work on trace element coordination environments in silicate melts to $Ge^{4+}$ and $Ga^{3+}$. Both of these cations increase their coordination number with pressure, and their coordination changes may be affected by changes in $Al^{3+}$ coordination. This is the first evidence for a link between major and trace element coordination changes. The pressure-dependence of the partitioning behaviour of $Ge^{4+}$ is likely to be affected by its coordination change, and possibly also by the coordination change of $Al^{3+}$, but predicting the pressure-dependence of trace element partitioning is not possible with existing equations of state. Finally, $Ge^{2+}$ was likely to be the stable species at the time of Earth's core formation, and is probably also stable on the Moon and other planetary bodies. The highly incompatible nature of $Ge^{2+}$ can explain Ge enrichments in lunar KREEP basalts without invoking lunar mantle metasomatism.

# References

Abe Y (1997) Thermal and chemical evolution of the terrestrial magma ocean. Physics of the Earth and Planetary Interiors 100:27–39. doi: 10.1016/S0031-9201(96)03229-3

Adam J, Green T (2006) Trace element partitioning between mica- and amphibole-bearing garnet lherzolite and hydrous basanitic melt: 1. Experimental results and the investigation of controls on partitioning behaviour. Contributions to Mineralogy and Petrology 152:1–17. doi: 10.1007/s00410-006-0085-4

Ahrens LH (1952) The use of ionization potentials Part 1. Ionic radii of the elements. Geochimica et Cosmochimica Acta 2:155–169. doi: 10.1016/0016-7037(52)90004-5

Alessi DS, Uster B, Borca CN, Grolimund D, Bernier-Latmani R (2013) Beam-induced oxidation of monomeric U(IV) species. Journal of Synchrotron Radiation 20:197–199. doi: 10.1107/S0909049512041763

Allwardt JR, Poe BT, Stebbins JF (2005a) The effect of fictive temperature on Al coordination in high-pressure (10 GPa) sodium aluminosilicate glasses. American Mineralogist 90:1453–1457. doi: 10.2138/am.2005.1736

Allwardt JR, Stebbins JF, Schmidt BC, Frost DJ (2005b) The effect of composition, compression, and decompression on the structure of high-pressure aluminosilicate glasses: an investigation utilizing $^{17}O$ and $^{27}Al$ NMR. In: Chen J, Wang Y, Duffy TS, Shen G, Dobrzhinetskaya LF (eds) Advances in High-Pressure Technology for Geophysical Applications. Elsevier B.V., pp 211–240

Allwardt JR, Stebbins JF, Schmidt BC, Frost DJ, Withers AC, Hirschmann MM (2005c) Aluminum coordination and the densification of high-pressure aluminosilicate glasses. American Mineralogist 90:1218–1222. doi: 10.2138/am.2005.1836

Allwardt JR, Stebbins JF, Terasaki H, Du LS, Frost DJ, Withers AC, Hirschmann MM, Suzuki A, Ohtani E (2007) Effect of structural transitions on properties of high-pressure silicate melts: $^{27}Al$ NMR, glass densities, and melt viscosities. American Mineralogist 92:1093–1104. doi: 10.2138/am.2007.2530

Angeli F, Gaillard M, Jollivet P, Charpentier T (2007) Contribution of $^{43}Ca$ MAS NMR for probing the structural configuration of calcium in glass. Chemical Physics Letters 440:324–328. doi: 10.1016/j.cplett.2007.04.036

Bagdassarov N, Golabek GJ, Solferino G, Schmidt MW (2009) Constraints on the Fe–S melt connectivity in mantle silicates from electrical impedance measurements. Physics of the Earth and Planetary Interiors 177:139–146. doi: 10.1016/J.PEPI.2009.08.003

Baldini M, Aquilanti G, Mao H, Yang W, Shen G, Pascarelli S, Mao WL (2010) High-pressure EXAFS study of vitreous $GeO_2$ up to 44 GPa. Physical Review B 81:024201. doi: 10.1103/PhysRevB.81.024201

Barrat JA, Yamaguchi A, Zanda B, Bollinger C, Bohn M (2010) Relative chronology of crust formation on asteroid Vesta: Insights from the geochemistry of diogenites. Geochimica et Cosmochimica Acta 74:6218–6231. doi: 10.1016/j.gca.2010.07.028

Barton L, Heil CA (1970) The reduction of germanium dioxide with graphite at high temperatures. Journal of the Less-Common Metals 22:11–17. doi: 10.1016/0022-5088(70)90171-2

Bayense CR, Kentgens APM, de Haan JW, van de Ven LJM, van Hoof JHC (1992) Determination of gallium in H Ga)ZSM5 zeolites by $^{71}Ga$ MAS NMR spectroscopy. The Journal of Physical Chemistry 96:775–782. doi: 10.1021/j100181a047

Belissont R, Muñoz M, Boiron M-C, Luais B, Mathon O (2016) Distribution and oxidation state of Ge, Cu and Fe in sphalerite by μ-XRF and K-edge μ-XANES: Insights into Ge incorporation, partitioning and isotopic fractionation. Geochimica et Cosmochimica Acta 177:298–314. doi: 10.1016/j.gca.2016.01.001

Belkebir A, Rocha J, Esculcas AP, Berthet P, Poisson S, Gilbert B, Gabelica Z, Llabres G, Wijzen F, Rulmont A (2000) Structural characterization of glassy phases in the system $Na_2O$-$Ga_2O_3$-$P_2O_5$ by MAS-NMR, EXAFS and vibrational spectroscopy. I. Cations coordination. Spectrochimica Acta - Part A: Molecular and Biomolecular Spectroscopy 56:423–434. doi: 10.1016/S1386-1425(99)00279-6

Berry AJ, O'Neill HStC (2004) A XANES determination of the oxidation state of chromium in silicate glasses. American Mineralogist 89:790–798. doi: 10.2138/am-2004-5-613

Berry AJ, O'Neill HStC, Jayasuriya KD, Campbell SJ, Foran GJ (2003a) XANES calibrations for the oxidation state of iron in a silicate glass. American Mineralogist 88:967–977. doi: 10.2138/am-2003-0704

Berry AJ, Shelley JMG, Foran GJ, O'Neill HStC, Scott DR (2003b) A furnace design for XANES spectroscopy of silicate melts under controlled oxygen fugacities and temperatures to 1773 K. Journal of Synchrotron Radiation 10:332–336. doi: 10.1107/S0909049503007556

Berry AJ, Walker AM, Hermann J, O'Neill HStC, Foran GJ, Gale JD (2007) Titanium substitution mechanisms in forsterite. Chemical Geology 242:176–186. doi: 10.1016/j.chemgeo.2007.03.010

Bezanson J, Edelman A, Karpinski S, Shah VB (2017) Julia: A fresh approach to numerical computing. SIAM Review 59:65–98. doi: 10.1137/141000671

Bista S, Stebbins JF, Hankins WB, Sisson TW (2015) Aluminosilicate melts and glasses at 1 to 3 GPa: temperature and pressure effects on recovered structural and density changes. American Mineralogist 100:2298–2307. doi: 10.2138/am-2015-5258

Blanchard I, Badro J, Siebert J, Ryerson FJ (2015) Composition of the core from gallium metal–silicate partitioning experiments. Earth and Planetary Science Letters 427:191–201. doi: 10.1016/j.epsl.2015.06.063

Blundy J, Wood B (2003) Partitioning of trace elements between crystals and melts. Earth and Planetary Science Letters 210:383–397. doi: 10.1016/S0012-821X(03)00129-8

Blundy J, Wood B (1994) Prediction of crystal–melt partition coefficients from elastic moduli. Nature 372:452–454. doi: 10.1038/372452a0

Bonnet J, Cauzid J, Testemale D, Kieffer I, Proux O, Lecomte A, Bailly L (2017) Characterization of germanium speciation in sphalerite (ZnS) from central and eastern Tennessee, USA, by X-ray absorption spectroscopy. Minerals 7:79. doi: 10.3390/min7050079

Bottinga Y, Weill DF (1972) The viscosity of magmatic silicate liquids: A model for calculation. American Journal of Science 272:438–475. doi: 10.2475/ajs.272.5.438

Bouhifd MA, Andrault D, Fiquet G, Richet P (1996) Thermal expansion of forsterite up to the melting point. Geophysical Research Letters 23:1143–1146. doi: 10.1029/96GL01118

Bouhifd MA, Jephcoat AP (2003) The effect of pressure on partitioning of Ni and Co between silicate and iron-rich metal liquids: A diamond-anvil cell study. Earth and Planetary Science Letters 209:245–255. doi: 10.1016/S0012-821X(03)00076-1

Bouhifd MA, Jephcoat AP (2011) Convergence of Ni and Co metal–silicate partition coefficients in the deep magma-ocean and coupled silicon–oxygen solubility in iron melts at high pressures. Earth and Planetary Science Letters 307:341–348. doi: 10.1016/j.epsl.2011.05.006

Bower DJ, Wicks JK, Gurnis M, Jackson JM (2011) A geodynamic and mineral physics model of a solid-state ultralow-velocity zone. Earth and Planetary Science Letters 303:193–202. doi: 10.1016/j.epsl.2010.12.035

Brice JCC (1975) Some thermodynamic aspects of the growth of strained crystals. Journal of Crystal Growth 28:249–253. doi: 10.1016/0022-0248(75)90241-9

Burnham AD, O'Neill HStC (2016) The effect of melt composition on mineral-melt partition coefficients: The case of beryllium. Chemical Geology 442:139–147. doi: 10.1016/j.chemgeo.2016.09.012

Burnham CW (1975) Water and magmas; a mixing model. Geochimica et Cosmochimica Acta 39:1077–1084. doi: 10.1016/0016-7037(75)90050-2

Cameron AGW, Benz W (1991) The origin of the moon and the single impact hypothesis IV. Icarus 92:204–216. doi: 10.1016/0019-1035(91)90046-V

Capobianco CJ, Drake MJ, De'Aro J (1999) Siderophile geochemistry of Ga, Ge, and Sn: cationic oxidation states in silicate melts and the effect of composition in iron–nickel alloys. Geochimica et Cosmochimica Acta 63:2667–2677. doi: 10.1016/S0016-7037(99)00085-X

Capobianco CJ, Watson EB (1982) Olivine/silicate melt partitioning of germanium: an example of a nearly constant partition coefficient. Geochimica et Cosmochimica Acta 46:235–240. doi: 10.1016/0016-7037(82)90250-2

Carlson RW (1994) Mechanisms of Earth differentiation: Consequences for the chemical structure of the mantle. Reviews of Geophysics 32:337–361. doi: 10.1029/94RG01874

Carlson RW, Garnero E, Harrison TM, Li J, Manga M, Mcdonough WF, Mukhopadhyay S, Romanowicz B, Rubie D, Williams Q, Zhong S (2014) How did early Earth become our modern world? Annual Review of Earth and Planetary Sciences 42:151–178. doi: 10.1146/annurev-earth-060313-055016

Caron A, Doumert B, Tricot G (2014) The $xGa_2O_3$–(100 – x)$NaPO_3$ glass system: Preparation, properties and structural analysis by solid state NMR. Materials Chemistry and Physics 147:1165–1170. doi: 10.1016/j.matchemphys.2014.06.074

Cempírek J, Groat LA (2013) Note on the formula of brunogeierite and the first bond-valence parameters for $Ge^{2+}$. Journal of Geosciences 58:71–74. doi: 10.3190/jgeosci.130

Coltice N, Moreira M, Hernlund J, Labrosse S (2011) Crystallization of a basal magma ocean recorded by Helium and Neon. Earth and Planetary Science Letters 308:193–199. doi: 10.1016/j.epsl.2011.05.045

Coltice N, Schmalzl J (2006) Mixing times in the mantle of the early Earth derived from 2-D and 3-D numerical simulations of convection. Geophysical Research Letters 33:L23304. doi: 10.1029/2006GL027707

Consolmagno GJ, Drake MJ (1977) Composition and evolution of the eucrite parent body: evidence from rare earth elements. Geochimica et Cosmochimica Acta 41:1271–1282. doi: 10.1016/0016-7037(77)90072-2

Consolmagno GJ, Golabek GJ, Turrini D, Jutzi M, Sirono S, Svetsov V, Tsiganis K (2015) Is Vesta an intact and pristine protoplanet? Icarus 254:190–201. doi: 10.1016/j.icarus.2015.03.029

Cook N, Etschmann B, Ciobanu C, Geraki K, Howard D, Williams T, Rae N, Pring A, Chen G, Johannessen B, Brugger J (2015) Distribution and substitution mechanism of Ge in a Ge-(Fe)-bearing sphalerite. Minerals 5:117–132. doi: 10.3390/min5020117

Cormier L, Ferlat G, Itié JP, Galoisy L, Calas G, Aquilanti G (2007) Amorphous-amorphous transformation at high pressure in gallo-germanosilicate tetrahedral network glasses. Physical Review B 76:134204. doi: 10.1103/PhysRevB.76.134204

Cottrell E, Walter MJ, Walker D (2009) Metal–silicate partitioning of tungsten at high pressure and temperature: Implications for equilibrium core formation in Earth. Earth and Planetary Science Letters 281:275–287. doi: 10.1016/j.epsl.2009.02.024

Czjzek G, Fink J, Götz F, Schmidt H, Coey JMD, Rebouillat J-P, Liénard A (1981) Atomic coordination and the distribution of electric field gradients in amorphous solids. Physical Review B 23:2513–2530. doi: 10.1103/PhysRevB.23.2513

Dahl TW, Stevenson DJ (2010) Turbulent mixing of metal and silicate during planet accretion - And interpretation of the Hf-W chronometer. Earth and Planetary Science Letters 295:177–186. doi: 10.1016/j.epsl.2010.03.038

Daniel I, McMillan PF, Gillet P, Poe BT (1996) Raman spectroscopic study of structural changes in calcium aluminate ($CaAl_2O_4$) glass at high pressure and high temperature. Chemical Geology 128:5–15. doi: 10.1016/0009-2541(95)00159-X

Davis FA, Humayun M, Hirschmann MM, Cooper RS (2013) Experimentally determined mineral/melt partitioning of first-row transition elements (FRTE) during partial melting of peridotite at 3GPa. Geochimica et Cosmochimica Acta 104:232–260. doi: 10.1016/j.gca.2012.11.009

de Argollo R, Schilling J-G (1978) Ge/Si and Ga/Al variations along the Reykjanes Ridge and Iceland. Nature 276:24–28. doi: 10.1017/CBO9781107415324.004

de Grouchy CJL, Sanloup C, Cochain B, Drewitt JWE, Kono Y, Crépisson C (2017) Lutetium incorporation in magmas at depth: Changes in melt local environment and the influence on partitioning behaviour. Earth and Planetary Science Letters 464:155–165. doi: 10.1016/j.epsl.2017.02.017

de Vries J, Nimmo F, Melosh HJ, Jacobson SA, Morbidelli A, Rubie DC (2016) Impact-induced melting during accretion of the Earth. Progress in Earth and Planetary Science 3:7. doi: 10.1186/s40645-016-0083-8

Deschamps T, Martinet C, Neuville DR, de Ligny D, Coussa-Simon C, Champagnon B (2009) Silica under hydrostatic pressure: A non continuous medium behavior. Journal of Non-Crystalline Solids 355:2422–2424. doi: 10.1016/j.jnoncrysol.2009.08.031

Deubener J, Müller R, Behrens H, Heide G (2003) Water and the glass transition temperature of silicate melts. Journal of Non-Crystalline Solids 330:268–273. doi: 10.1016/S0022-3093(03)00472-1

Dickinson T, Taylor GJ, Keil K, Bild RW (1989) Germanium abundances in lunar basalts: Evidence of mantle metasomatism? In: Proceedings of the 19th Lunar and Planetary Science Conference. pp 189–198

Dingwell DB, Knoche R, Webb SL (1993) A volume temperature relationship for liquid $GeO_2$ and some geophysically relevant derived parameters for network liquids. Physics and Chemistry of

Minerals 19:445–453. doi: 10.1007/BF00203184

Dobson DP, Brodholt JP (2005) Subducted banded iron formations as a source of ultra-low velocity zones at the core-mantle boundary. Nature 434:371–374. doi: 10.1038/nature03385.1.

Dupree R, Howes AP, Kohn SC (1997) Natural abundance solid state $^{43}$Ca NMR. Chemical Physics Letters 276:399–404. doi: 10.1016/S0009-2614(97)00863-4

Durandurdu M, Drabold DA (2002) Simulation of pressure-induced polyamorphism in a chalcogenide glass GeSe2. Physical Review B 65:104208. doi: 10.1103/PhysRevB.65.104208

Durben DJ, Wolf GH (1991) Raman spectroscopic study of the pressure-induced coordination change in $GeO_2$ glass. Physical Review B 43:2355–2363. doi: 10.1103/PhysRevB.43.2355

Edén M (2015) $^{27}$Al NMR studies of aluminosilicate glasses. In: Webb GA (ed) Annual Reports on NMR Spectroscopy. Academic Press, pp 237–331

Edwards T, Endo T, Walton JH, Sen S (2014) Observation of the transition state for pressure-induced $BO_3 \rightarrow BO_4$ conversion in glass. Science 345:1027–1030. doi: 10.1126/science.1256224

Elkins-Tanton LT (2012) Magma Oceans in the Inner Solar System. Annual Review of Earth and Planetary Sciences 40:113–139. doi: 10.1146/annurev-earth-042711-105503

Farnan I, Stebbins JF (1990) High-temperature $^{29}$Si NMR investigation of solid and molten silicates. Journal of the American Chemical Society 112:32–39. doi: 10.1021/ja00157a008

Fei H, Hegoda C, Yamazaki D, Wiedenbeck M, Yurimoto H, Shcheka S, Katsura T (2012) High silicon self-diffusion coefficient in dry forsterite. Earth and Planetary Science Letters 345–348:95–103. doi: 10.1016/j.epsl.2012.06.044

Fernandes A, Moran RF, Sneddon S, Dawson DM, McKay D, Bignami GPM, Blanc F, Whittle KR, Ashbrook SE (2018) $^{17}$O solid-state NMR spectroscopy of $A_2B_2O_7$ oxides: quantitative isotopic enrichment and spectral acquisition? RSC Advances 8:7089–7101. doi: 10.1039/C8RA00596F

Ferreira PG, de Ligny D, Lazzari O, Jean A, Gonzalez OC, Neuville DR (2013) Photoreduction of iron by a synchrotron X-ray beam in low iron content soda-lime silicate glasses. Chemical Geology 346:106–112. doi: 10.1016/j.chemgeo.2012.10.029

Fiquet G, Auzende AL, Siebert J, Corgne A, Bureau H, Ozawa H, Garbarino G (2010) Melting of peridotite to 140 GPa. Science 329:1516–1518. doi: 10.1126/science.1192448

Fiquet G, Gillet P, Richet P (1992) Anharmonicity and high-temperature heat capacity of crystals: the examples of $Ca_2GeO_4$, $Mg_2GeO_4$ and $CaMgGeO_4$ olivines. Physics and Chemistry of Minerals 18:469–479. doi: 10.1007/BF00200970

Fischer RA, Campbell AJ, Ciesla FJ (2017) Sensitivities of Earth's core and mantle compositions to accretion and differentiation processes. Earth and Planetary Science Letters 458:252–262. doi: 10.1016/j.epsl.2016.10.025

Fischer RA, Nakajima Y, Campbell AJ, Frost DJ, Harries D, Langenhorst F, Miyajima N, Pollok K, Rubie DC (2015) High pressure metal–silicate partitioning of Ni, Co, V, Cr, Si, and O. Geochimica et Cosmochimica Acta 167:177–194. doi: 10.1016/j.gca.2015.06.026

Fleet ME, Herzberg CT, Henderson GS, Crozier ED, Osborne MD, Scarfe CM (1984) Coordination of Fe, Ga and Ge in high pressure glasses by Mössbauer, Raman and X-ray absorption spectroscopy, and geological implications. Geochimica et Cosmochimica Acta 48:1455–1466. doi: 10.1016/0016-7037(84)90402-2

Freitas D, Manthilake G, Schiavi F, Chantel J, Bolfan-Casanova N, Bouhifd MA, Andrault D (2017) Experimental evidence supporting a global melt layer at the base of the Earth's upper mantle. Nature Communications 8:2186. doi: 10.1038/s41467-017-02275-9

Frost DJ, McCammon CA (2008) The redox state of earth's mantle. Annual Review of Earth and Planetary Sciences 36:389–420. doi: 10.1146/annurev.earth.36.031207.124322

Frost RB (1991) Introduction to oxygen fugacity and its petrologic importance. Reviews in Mineralogy 25:1–9.

Funakoshi K-I, Suzuki A, Terasaki H (2002) *In situ* viscosity measurements of albite melt under high pressure. Journal of Physics Condensed Matter 14:11343–11347. doi: 10.1088/0953-8984/14/44/479

Funamori N, Yamamoto S, Yagi T, Kikegawa T (2004) Exploratory studies of silicate melt structure at high pressures and temperatures by in situ X-ray diffraction. Journal of Geophysical Research 109:B03203. doi: 10.1029/2003JB002650

Gambuzzi E, Pedone A, Menziani MC, Angeli F, Florian P, Charpentier T (2015) Calcium environment in silicate and aluminosilicate glasses probed by $^{43}$Ca MQMAS NMR experiments and MD-GIPAW calculations. Solid State Nuclear Magnetic Resonance 68–69:31–36. doi: 10.1016/j.ssnmr.2015.04.003

Gan Z (2007) $^{13}$C/$^{14}$N heteronuclear multiple-quantum correlation with rotary resonance and REDOR dipolar recoupling. Journal of Magnetic Resonance 184:39–43. doi: 10.1016/j.jmr.2006.09.016

Gaudio SJ, Edwards TG, Sen S (2015a) An in situ high-pressure NMR study of sodium coordination environment compressibility in albite glass. American Mineralogist 100:326–329. doi: 10.2138/am-2015-5081

Gaudio SJ, Lesher CE, Maekawa H, Sen S (2015b) Linking high-pressure structure and density of albite liquid near the glass transition. Geochimica et Cosmochimica Acta 157:28–38. doi: 10.1016/j.gca.2015.02.017

Ghiorso MS (2004) An equation of state for silicate melts. I. Formulation of a general model. American Journal of Science 304:637–678. doi: 10.2475/ajs.304.8-9.637

Goldschmidt VM (1937) The principles of distribution of chemical elements in minerals and rocks. The seventh Hugo Müller Lecture, delivered before the Chemical Society on March 17th, 1937. Journal of the Chemical Society 0:655–673. doi: 10.1039/JR9370000655

Guillot B, Sator N (2007) A computer simulation study of natural silicate melts. Part II: High pressure properties. Geochimica et Cosmochimica Acta 71:4538–4556. doi: 10.1016/j.gca.2007.05.029

Guitreau M, Blichert-Toft J, Mojzsis SJ, Roth ASG, Bourdon B (2013) A legacy of Hadean silicate differentiation inferred from Hf isotopes in Eoarchean rocks of the Nuvvuagittuq supracrustal belt (Québec, Canada). Earth and Planetary Science Letters 362:171–181. doi: 10.1016/j.epsl.2012.11.055

Hahn M, Behrens H, Tegge-Schüring A, Koepke J, Horn I, Rickers K, Falkenberg G, Wiedenbeck M (2005) Trace element diffusion in rhyolitic melts: comparison between synchrotron radiation X-ray fluorescence microanalysis (μ-SRXRF) and secondary ion mass spectrometry (SIMS). European Journal of Mineralogy 17:233–242. doi: 10.1127/0935-1221/2005/0017-0233

Hahn TM, Lunning NG, McSween Jr. HY, Bodnar RJ, Taylor LA (2017) Dacite formation on Vesta: Partial melting of the eucritic crust. Meteoritics & Planetary Science 52:1173–1196. doi: 10.1111/maps.12870

Haines J, Léger JM, Chateau C, Pereira AS (2000) Structural evolution of rutile-type and $CaCl_2$-type germanium dioxide at high pressure. Physics and Chemistry of Minerals 27:575–582. doi: 10.1007/s002690000092

Halliday AN (2013) The origin and earliest history of the Earth. In: Holland H, Turekian K (eds) Treatise on Geochemistry: Second Edition. Elsevier Ltd., pp 149–211

Haskin L, Warren P (1991) Lunar chemistry. In: Heiken GH, Vaniman DT, French BM (eds) Lunar Sourcebook: A User's Guide to the Moon. Cambridge University Press, pp 357–474

Henderson GS, de Groot FMF, Moulton BJA (2014) X-ray absorption near-edge structure (XANES) spectroscopy. Reviews in Mineralogy and Geochemistry 78:75–138. doi: 10.2138/rmg.2014.78.3

Hermann J, O'Neill HS., Berry AJ (2005) Titanium solubility in olivine in the system $TiO_2$-MgO-$SiO_2$: No evidence for an ultra-deep origin of Ti-bearing olivine. Contributions to Mineralogy and Petrology 148:746–760. doi: 10.1007/s00410-004-0637-4

Hier-Majumder S, Courtier A (2011) Seismic signature of small melt fraction atop the transition zone. Earth and Planetary Science Letters 308:334–342. doi: 10.1016/j.epsl.2011.05.055

Hier-Majumder S, Keel EB, Courtier AM (2014) The influence of temperature, bulk composition, and melting on the seismic signature of the low-velocity layer above the transition zone. Journal of Geophysical Research: Solid Earth 119:971–983. doi: 10.1002/2013JB010314

Hillgren VJ, Drake MJ, Rubie DC (1996) High pressure and high temperature metal-silicate partitioning of siderophile elements: The importance of silicate liquid composition. Geochimica et Cosmochimica Acta 60:2257–2263. doi: 10.1016/0016-7037(96)00079-8

Hirschmann MM (2006) Water, melting, and the deep earth $H_2O$ cycle. Annual Review of Earth and Planetary Sciences 34:629–653. doi: 10.1146/annurev.earth.34.031405.125211

Hochella MF, Brown GE (1985) The structures of albite and jadeite composition glasses quenched from high pressure. Geochimica et Cosmochimica Acta 49:1137–1142. doi: 10.1016/0016-7037(85)90004-3

Holland TJB, Powell R (1998) An internally consistent thermodynamic data set for phases of petrological interest. Journal of Metamorphic Geology 16:309–343. doi: 10.1111/j.1525-1314.1998.00140.x

Holland TJB, Powell R (2011) An improved and extended internally consistent thermodynamic dataset for phases of petrological interest, involving a new equation of state for solids. Journal of Metamorphic Geology 29:333–383. doi: 10.1111/j.1525-1314.2010.00923.x

Holzapfel C, Courtial P, Dingwell DB, Chakraborty S, Palme H (2001) Experimental determination of partial molar volumes of $Ga_2O_3$ and $GeO_2$ in silicate melts: implications for the pressure dependence of metal–silicate partition coefficients. Chemical Geology 174:33–49. doi: 10.1016/S0009-2541(00)00305-3

Holzheid A, Kegler P, Frost D, Rubie DC, Palme H (2007) Partitioning behaviour of copper and germanium: Implications for terrestrial core formation scenarios. In: 38th Lunar and Planetary Science Conference. p 2090

Hong X, Newville M, Duffy TS, Sutton SR, Rivers ML (2014) X-ray absorption spectroscopy of $GeO_2$ glass to 64 GPa. Journal of Physics: Condensed Matter 26:035104. doi: 10.1088/0953-8984/26/3/035104

Huang PY, Kurasch S, Srivastava A, Skakalova V, Kotakoski J, Krasheninnikov A V., Hovden R, Mao Q, Meyer JC, Smet J, Muller DA, Kaiser U (2012) Direct imaging of a two-dimensional silica glass on graphene. Nano Letters 12:1081–1086. doi: 10.1021/nl204423x

Imai T, Takahashi E, Suzuki T, Hirata T (2012) Element partitioning between olivine and melt up to 10 GPa: Implications for the effect of pressure. Physics of the Earth and Planetary Interiors 212–213:64–75. doi: 10.1016/j.pepi.2012.09.001

Itié JP, Polian A, Calas G, Petiau J, Fontaine A, Tolentino H (1989) Pressure-induced coordination changes in crystalline and vitreous GeO2. Physical Review Letters 63:398–401. doi: 10.1103/PhysRevLett.63.398

Jakobsen HJ, Skibsted J, Bildsbe H, Nielsen N (1989) Magic-angle spinning NMR spectra of satellite transitions for quadrupolar nuclei in solids. Journal of Magnetic Resonance 85:173–180. doi: 10.1016/0022-2364(89)90333-8

Jana D, Walker D (1997a) The influence of silicate melt composition on distribution of siderophile elements among metal and silicate liquids. Earth and Planetary Science Letters 150:463–472. doi: 10.1016/S0012-821X(97)00079-4

Jana D, Walker D (1997b) The impact of carbon on element distribution during core formation. Geochimica et Cosmochimica Acta 61:2759–2763. doi: 10.1016/S0016-7037(97)00091-4

Jollands MC, O'Neill HStC, Hermann J (2014) The importance of defining chemical potentials, substitution mechanisms and solubility in trace element diffusion studies: the case of Zr and Hf in olivine. Contributions to Mineralogy and Petrology 168:1055. doi: 10.1007/s00410-014-1055-x

Jones J (2012) Experimental constraints on the thermodynamic modeling of siderophile element distribution during core-segregation and basalt petrogenesis. PhD thesis, Australian National University

Jones JH, Drake MJ (1986) Geochemical constraints on core formation in the Earth. Nature 322:221–228. doi: 10.1038/322221a0

Kanehashi K, Stebbins JF (2007) In situ high temperature $^{27}$Al NMR study of structure and dynamics in a calcium aluminosilicate glass and melt. Journal of Non-Crystalline Solids 353:4001–4010. doi: 10.1016/j.jnoncrysol.2007.06.030

Kanzaki M, Stebbins JF, Xue X (1992) Characterization of crystalline and amorphous silicates quenched from high pressure by 29Si MAS NMR spectroscopy. In: Syono Y, Manghnani MH (eds) High-Pressure Research: Application to Earth and Planetary Sciences. Tokyo, pp 89–100

Karki BB (2010) First-principles molecular dynamics simulations of silicate melts: Structural and dynamical properties. Reviews in Mineralogy and Geochemistry 71:355–389. doi: 10.2138/rmg.2010.71.17

Kegler P, Holzheid A (2011) Determination of the formal Ge-oxide species in silicate melts at oxygen fugacities applicable to terrestrial core formation scenarios. European Journal of Mineralogy 23:369–378. doi: 10.1127/0935-1221/2011/0023-2097

Kegler P, Holzheid A, Frost DJ, Rubie DC, Dohmen R, Palme H (2008) New Ni and Co metal–silicate partitioning data and their relevance for an early terrestrial magma ocean. Earth and Planetary Science Letters 268:28–40. doi: 10.1016/j.epsl.2007.12.020

Kelsey KE, Stebbins JF, Mosenfelder JL, Asimow PD (2009) Simultaneous aluminum, silicon, and sodium coordination changes in 6 GPa sodium aluminosilicate glasses. American Mineralogist 94:1205–1215. doi: 10.2138/am.2009.3177

Kennedy AK, Lofgren GE, Wasserburg GJ (1993) An experimental study of trace element partitioning between olivine, orthopyroxene and melt in chondrules: Equilibrium values and kinetic effects. Earth and Planetary Science Letters 115:177–195. doi: 10.1016/0012-821X(93)90221-T

Keppler H, Rubie DC (1993) Pressure-induced coordination changes of transition-metal ions in silicate melts. Nature 364:54–56. doi: 10.1038/364054a0

Kitts K, Lodders K (1998) Survey and evaluation of eucrite bulk compostitons. Meteoritics & Planetary Science 33:A197–A213. doi: 10.1111/j.1945-5100.1998.tb01334.x

Kojitani H, Többens DM, Akaogi M (2013) High-pressure Raman spectroscopy, vibrational mode calculation, and heat capacity calculation of calcium ferrite-type $MgAl_2O_4$ and $CaAl_2O_4$. American Mineralogist 98:197–206. doi: 10.2138/am.2013.4095

Kono Y (2018) Viscosity measurement. In: Kono Y, Sanloup C (eds) Magmas Under Pressure. Elsevier, pp 261–280

Kress VC, Carmichael ISE (1991) The compressibility of silicate liquids containing $Fe_2O_3$ and the effect of composition, temperature, oxygen fugacity and pressure on their redox states. Contributions to Mineralogy and Petrology 108:82–92. doi: 10.1007/BF00307328

Kroeker S, Stebbins JF (2000) Magnesium coordination environments in glasses and minerals: New insight from high-field magnesium-25 MAS NMR. American Mineralogist 85:1459–1464. doi: 10.2138/am-2000-1015

Labrosse S, Hernlund JW, Coltice N (2007) A crystallizing dense magma ocean at the base of the Earth's mantle. Nature 450:866–869. doi: 10.1038/nature06355

Lange RA, Carmichael ISE (1987) Densities of $Na_2O$-$K_2O$-CaO-MgO-FeO-$Fe_2O_3$-$Al_2O_3$-$TiO_2$-$SiO_2$ liquids: New measurements and derivated partial molar properties. Geochimica et Cosmochimica Acta 51:2931–2946. doi: 10.1016/0016-7037(87)90368-1

Laurenz V, Rubie DC, Frost DJ, Vogel AK (2016) The importance of sulfur for the behaviour of highly-siderophile elements during Earth's differentiation. Geochimica et Cosmochimica Acta 194:123–138. doi: 10.1016/j.gca.2016.08.012

Le Losq C, Neuville DR, Florian P, Henderson GS, Massiot D (2014) The role of $Al^{3+}$ on rheology and structural changes in sodium silicate and aluminosilicate glasses and melts. Geochimica et Cosmochimica Acta 126:495–517. doi: 10.1016/j.gca.2013.11.010

Le Roux V, Dasgupta R, Lee C-TA (2015) Recommended mineral-melt partition coefficients for FRTEs (Cu), Ga, and Ge during mantle melting. American Mineralogist 100:2533–2544. doi: 10.2138/am-2015-5215

Lee SK, Cody GD, Fei Y, Mysen BO (2004) Nature of polymerization and properties of silicate melts and glasses at high pressure. Geochimica et Cosmochimica Acta 68:4189–4200. doi: 10.1016/j.gca.2004.04.002

Lee SK, Eng PJ, Mao H -k. (2014) Probing of pressure-induced bonding transitions in crystalline and amorphous Earth materials: Insights from X-ray raman scattering at high pressure. Reviews in Mineralogy and Geochemistry 78:139–174. doi: 10.2138/rmg.2014.78.4

Lee SK, Yi YS, Cody GD, Mibe K, Fei Y, Mysen BO (2012) Effect of network polymerization on the pressure-induced structural changes in sodium aluminosilicate glasses and melts: $^{27}$Al and $^{17}$O solid-state NMR study. The Journal of Physical Chemistry C 116:2183–2191. doi: 10.1021/jp206765s

Leinenweber KD, Tyburczy JA, Sharp TG, Soignard E, Diedrich T, Petuskey WB, Wang Y, Mosenfelder JL (2012) Cell assemblies for reproducible multi-anvil experiments (the COMPRES assemblies). American Mineralogist 97:353–368. doi: 10.2138/am.2012.3844

Lesher CE, Hervig RL, Tinker D (1996) Self diffusion of network formers (silicon and oxygen) in naturally occurring basaltic liquid. Geochimica et Cosmochimica Acta 60:405–413. doi: 10.1016/0016-7037(95)00400-9

Li D, Secco RA, Bancroft GM, Fleet ME (1995) Pressure induced coordination change of Al in silicate melts from Al K edge XANES of high pressure $NaAlSi_2O_6$-$NaAlSi_3O_8$ glasses. Geophysical Research Letters 22:3111–3114. doi: 10.1029/95GL03175

Li J, Agee CB (1996) Geochemistry of mantle–core differentiation at high pressure. Nature 381:686–689. doi: 10.1038/381686a0

Li X, Zhao H, Tang M, Liu Y (2009) Theoretical prediction for several important equilibrium Ge isotope fractionation factors and geological implications. Earth and Planetary Science Letters 287:1–11. doi: 10.1016/j.epsl.2009.07.027

Liebermann RC (1975) Elasticity of olivine (α), beta (ß), and spinel (γ) polymorphs of germanates and silicates. Geophysical Journal of the Royal Astronomical Society 42:899–929. doi: 10.1111/j.1365-246X.1975.tb06458.x

Lodders K (1998) A survey of shergottite, nakhlite and chassigny meteorites whole-rock compositions. Meteoritics & Planetary Science 33:A183–A190. doi: 10.1111/j.1945-5100.1998.tb01331.x

Luais B (2012) Germanium chemistry and MC-ICPMS isotopic measurements of Fe-Ni, Zn alloys and silicate matrices: Insights into deep Earth processes. Chemical Geology 334:295–311. doi: 10.1016/j.chemgeo.2012.10.017

MacKenzie KJD, Meinhold RH (1994) $^{25}$Mg nuclear magnetic resonance spectroscopy of minerals and related inorganics: A survey study. American Mineralogist 79:250–260.

Magi M, Lippmaa E, Samoson A, Engelhardt G, Grimmer A-R (1984) Solid-state high-resolution silicon-29 chemical shifts in silicates. The Journal of Physical Chemistry 88:1518–1522. doi: 10.1021/j150652a015

Majérus O, Cormier L, Itié JP, Galoisy L, Neuville DR, Calas G (2004) Pressure-induced Ge coordination change and polyamorphism in $SiO_2$–$GeO_2$ glasses. Journal of Non-Crystalline Solids 345–346:34–38. doi: 10.1016/j.jnoncrysol.2004.07.039

Malfait WJ, Verel R, Ardia P, Sanchez-Valle C (2012) Aluminum coordination in rhyolite and andesite glasses and melts: Effect of temperature, pressure, composition and water content. Geochimica et Cosmochimica Acta 77:11–26. doi: 10.1016/j.gca.2011.11.011

Mallmann G, O'Neill HStC (2013) Calibration of an empirical thermometer and oxybarometer based on the partitioning of Sc, Y and V between olivine and silicate melt. Journal of Petrology 54:933–949. doi: 10.1093/petrology/egt001

Mallmann G, O'Neill HStC (2009) The crystal/melt partitioning of V during mantle melting as a function of oxygen fugacity compared with some other elements (Al, P, Ca, Sc, Ti, Cr, Fe, Ga, Y, Zr and Nb). Journal of Petrology 50:1765–1794. doi: 10.1093/petrology/egp053

Malvin DJ, Drake MJ (1987) Experimental determination of crystal/melt partitioning of Ga and Ge in the system forsterite-anorthite-diopside. Geochimica et Cosmochimica Acta 51:2117–2128. doi: 10.1016/0016-7037(87)90260-2

Mann U, Frost DJ, Rubie DC, Becker H, Audétat A (2012) Partitioning of Ru, Rh, Pd, Re, Ir and Pt between liquid metal and silicate at high pressures and high temperatures - Implications for the origin of highly siderophile element concentrations in the Earth's mantle. Geochimica et Cosmochimica Acta 84:593–613. doi: 10.1016/j.gca.2012.01.026

Manning CE (2018) The influence of pressure on the properties and origins of hydrous silicate liquids in Earth's interior. In: Kono Y, Sanloup C (eds) Magmas Under Pressure. Elsevier, pp 83–113

Mao H, Sundman B, Wang Z, Saxena SK (2001) Volumetric properties and phase relations of silica - thermodynamic assessment. Journal of Alloys and Compounds 327:253–262. doi: 10.1016/S0925-8388(01)01465-7

Marchi S, Canup RM, Walker RJ (2018) Heterogeneous delivery of silicate and metal to the Earth by large planetesimals. Nature Geoscience 11:77–81. doi: 10.1038/s41561-017-0022-3

Massiot D, Farnan I, Gautier N, Trumeau D, Trokiner A, Coutures JP (1995) $^{71}$Ga and $^{69}$Ga nuclear magnetic resonance study of β-$Ga_2O_3$: resolution of four- and six-fold coordinated Ga sites in static conditions. Solid State Nuclear Magnetic Resonance 4:241–248. doi: 10.1016/0926-2040(95)00002-8

Massiot D, Fayon F, Capron M, King I, Le Calvé S, Alonso B, Durand J-O, Bujoli B, Gan Z, Hoatson G (2002) Modelling one- and two-dimensional solid-state NMR. Magnetic Resonance in Chemistry 40:70–76. doi: 10.1002/mrc.984

Mastelaro VR, Zanotto ED (2018) X-ray absorption fine structure (XAFS) studies of oxide glasses-A 45-year overview. Materials 11:204. doi: 10.3390/ma11020204

Matsui M (1996) Molecular dynamics simulation of structures, bulk moduli, and volume thermal expansivities of silicate liquids in the system CaO-MgO-$Al_2O_3$-$SiO_2$. Geophysical Research Letters 23:395–398. doi: 10.1029/96GL00260

McCord TB, Adams JB, Johnson T V (1970) Asteroid vesta: spectral reflectivity and compositional implications. Science 168:1445–1447. doi: 10.1126/science.168.3938.1445

McFarlane EA (1994) Differentiation in the early Earth: An experimental investigation. PhD thesis, The University of Arizona

Meade C, Hemley RJ, Mao HK (1992) High-pressure x-ray diffraction of $SiO_2$ glass. Physical Review Letters 69:1387–1390. doi: https://doi.org/10.1103/PhysRevLett.69.1387

Médard E, McCammon CA, Barr JA, Grove TL (2008) Oxygen fugacity, temperature reproducibility, and $H_2O$ contents of nominally anhydrous piston-cylinder experiments using graphite capsules. American Mineralogist 93:1838–1844. doi: 10.2138/am.2008.2842

Meiboom S, Gill D (1958) Modified spin-echo method for measuring nuclear relaxation times. Review of Scientific Instruments 29:688–691. doi: 10.1063/1.1716296

Micoulaut M, Cormier L, Henderson GS (2006) The structure of amorphous, crystalline and liquid $GeO_2$. Journal of Physics: Condensed Matter 18:R753–R784. doi: 10.1088/0953-8984/18/45/R01

Mikhail S, Heap MJ (2017) Hot climate inhibits volcanism on Venus: Constraints from rock deformation experiments and argon isotope geochemistry. Physics of the Earth and Planetary Interiors 268:18–34. doi: 10.1016/J.PEPI.2017.05.007

Mills KC (1993) The influence of structure on the physico-chemical properties of slags. ISIJ International 33:148–155. doi: 10.2355/isijinternational.33.148

Morin EI, Stebbins JF (2016) Separating the effects of composition and fictive temperature on Al and B coordination in Ca, La, Y aluminosilicate, aluminoborosilicate and aluminoborate glasses. Journal of Non-Crystalline Solids 432:384–392. doi: 10.1016/j.jnoncrysol.2015.10.035

Morizet Y, Vuilleumier R, Paris M (2015) A NMR and molecular dynamics study of $CO_2$-bearing basaltic melts and glasses. Chemical Geology 418:89–103. doi: 10.1016/j.chemgeo.2015.03.021

Moulton BJA, Henderson GS, Sonneville C, O'Shaughnessy C, Zuin L, Regier T, de Ligny D (2016) The structure of haplobasaltic glasses investigated using X-ray absorption near edge structure (XANES) spectroscopy at the Si, Al, Mg, and O K-edges and Ca, Si, and Al $L_{2,3}$-edges. Chemical Geology 420:213–230. doi: 10.1016/j.chemgeo.2015.11.016

Moynihan CT (1995) Structural relaxation and the glass transition. Reviews in Mineralogy 32:1–19. doi: 10.2138/rmg.1995.32.1

Moynihan CT, Easteal AJ, Wilder J, Tucker J (1974) Dependence of the glass transition temperature on heating and cooling rate. Journal of Physical Chemistry 78:2673–2677. doi: 10.1021/j100619a008

Mukhopadhyay S (2012) Early differentiation and volatile accretion recorded in deep-mantle neon and xenon. Nature 486:101–104. doi: 10.1038/nature11141

Mungall JE, Dingwell DB, Chaussidon M (1999) Chemical diffusivities of 18 trace elements in granitoid melts. Geochimica et Cosmochimica Acta 63:2599–2610. doi: 10.1016/S0016-7037(99)00209-4

Muniz RF, de Ligny D, Martinet C, Sandrini M, Medina AN, Rohling JH, Baesso ML, Lima SM, Andrade LHC, Guyot Y (2016) In situ structural analysis of calcium aluminosilicate glasses under high pressure. Journal of Physics Condensed Matter 28:315402. doi: 10.1088/0953-8984/28/31/315402

Mysen BO, Virgo D, Seifert FA (1982) The structure of silicate melts: Implications for chemical and physical properties of natural magma. Reviews of Geophysics and Space Physics 20:353–383.

Neuville DR, Cormier L, Massiot D (2004) Al environment in tectosilicate and peraluminous glasses: A $^{27}$Al MQ-MAS NMR, Raman, and XANES investigation. Geochimica et Cosmochimica Acta 68:5071–5079. doi: 10.1016/j.gca.2004.05.048

Newville M (2014) Fundamentals of XAFS. Reviews in Mineralogy and Geochemistry 78:33–74. doi: 10.2138/rmg.2014.78.2

Norris CA, Wood BJ (2017) Earth's volatile contents established by melting and vaporization. Nature 549:507–510. doi: 10.1038/nature23645

O'Neill HStC, Berry AJ (2006) Activity coefficients at low dilution of CrO, NiO and CoO in melts in the system $CaO$-$MgO$-$Al_2O_3$-$SiO_2$ at 1400 °C: Using the thermodynamic behaviour of transition metal oxides in silicate melts to probe their structure. Chemical Geology 231:77–89. doi: 10.1016/j.chemgeo.2006.01.004

O'Neill HStC, Eggins SM (2002) The effect of melt composition on trace element partitioning: An experimental investigation of the activity coefficients of FeO, NiO, CoO, $MoO_2$ and $MoO_3$ in silicate melts. Chemical Geology 186:151–181. doi: 10.1016/S0009-2541(01)00414-4

O'Neill HStC, Navrotsky A (1983) Simple spinels: crystallographic parameters, cation radii, lattice energies, and cation distribution. American Mineralogist 68:181–194.

O'Neill HStC, Nell J (1997) Gibbs free energies of formation of RuO2, $IrO_2$, and $OsO_2$: A high-temperature electrochemical and calorimetric study. Geochimica et Cosmochimica Acta 61:5279–5293. doi: 10.1016/S0016-7037(97)00317-7

Ohtaka O, Arima H, Fukui H, Utsumi W, Katayama Y, Yoshiasa A (2004) Pressure-induced sharp coordination change in liquid germanate. Physical Review Letters 92:155506. doi: 10.1103/PhysRevLett.92.155506

Ohtaka O, Yoshiasa A, Fukui H, Murai K, Okube M, Katayama Y, Utsumi W, Nishihata Y (2001) Structural changes of quartz-type crystalline and vitreous $GeO_2$ under pressure. Journal of Synchrotron Radiation 8:791–793.

Ohtaka O, Yoshiasa A, Fukui H, Murai K, Okube M, Takebe H, Katayama Y, Utsumi W (2002) XAFS study of $GeO_2$ glass under pressure. Journal of Physics: Condensed Matter 14:10521–10524. doi: 10.1088/0953-8984/14/44/326

Onuma N, Higuchi H, Wakita H, Nagasawa H (1968) Trace element partition between two pyroxenes and the host lava. Earth and Planetary Science Letters 5:47–51. doi: 10.1016/S0012-821X(68)80010-X

Osborn EF (1959) Role of oxygen pressure in the crystallization and differentiation of basaltic magma. American Journal of Science 257:609–647.

Østergaard MB, Youngman RE, Svenson MN, Rzoska SJ, Bockowski M, Jensen LR, Smedskjaer MM (2015) Temperature-dependent densification of sodium borosilicate glass. RSC Advances 5:78845–78851. doi: 10.1039/C5RA16219J

Penner-Hahn JE (1999) X-ray absorption spectroscopy in coordination chemistry. Coordination Chemistry Reviews 190–192:1101–1123. doi: 10.1016/S0010-8545(99)00160-5

Peters BJ, Carlson RW, Day JMD, Horan MF (2018) Hadean silicate differentiation preserved by anomalous $^{142}Nd/^{144}Nd$ ratios in the Réunion hotspot source. Nature 555:89–93. doi: 10.1038/nature25754

Petitgirard S (2017) Density and structural changes of silicate glasses under high pressure. High Pressure Research 37:200–213. doi: 10.1080/08957959.2017.1302444

Pető MK, Mukhopadhyay S, Kelley KA (2013) Heterogeneities from the first 100 million years recorded in deep mantle noble gases from the Northern Lau Back-arc Basin. Earth and Planetary Science Letters 369–370:13–23. doi: 10.1016/j.epsl.2013.02.012

Poe BT, Romano C, Zotov N, Cibin G, Marcelli A (2001) Compression mechanisms in aluminosilicate melts: Raman and XANES spectroscopy of glasses quenched from pressures up to 10 GPa. Chemical Geology 174:21–31. doi: 10.1016/S0009-2541(00)00304-1

Pohlenz J, Rosa AD, Mathon O, Pascarelli S, Belin S, Landrot G, Murzin V, Veligzhanin A, Shiryaev A, Irifune T, Wilke M (2018) Structural controls of $CO_2$ on Y, La and Sr incorporation in sodium-rich silicate - carbonate melts by in-situ high P-T EXAFS. Chemical Geology 486:1–15. doi: 10.1016/J.CHEMGEO.2017.12.023

Pugsley AJ, Bull CL, Sella A, Sankar G, McMillan PF (2011) XAS/EXAFS studies of Ge nanoparticles produced by reaction between $Mg_2Ge$ and $GeCl_4$. Journal of Solid State Chemistry 184:2345–2352. doi: 10.1016/j.jssc.2011.06.020

Ravel B, Newville M (2005) ATHENA, ARTEMIS, HEPHAESTUS: Data analysis for X-ray absorption spectroscopy using IFEFFIT. Journal of Synchrotron Radiation 12:537–541. doi: 10.1107/S0909049505012719

Ren J, Eckert H (2014) Intermediate role of gallium in oxidic glasses: solid state NMR structural studies of the $Ga_2O_3$–$NaPO_3$ system. The Journal of Physical Chemistry 118:15386–15403. doi: 10.1021/jp504023k

Revenaugh J, Sipkin SA (1994) Seismic evidence for silicate melt atop the 410-km mantle discontinuity. Nature 369:474–476. doi: 10.1038/369474a0

Ridgway MC, Azevedo G de M, Glover CJ, Elliman RG, Llewellyn DJ, Cheung A, Johannessen B, Brett DA, Foran GJ (2004) EXAFS characterisation of Ge nanocrystals in silica. Nuclear Instruments and Methods in Physics Research B 218:421–426. doi: 10.1016/j.nimb.2004.01.004

Riebling EF (1963) Structure of molten oxides. II. A density study of binary germanates containing $Li_2O$, $Na_2O$, $K_2O$, and $Rb_2O$. The Journal of Chemical Physics 39:3022–3030. doi: 10.1063/1.1734137

Rigden SM, Ahrens TJ, Stolper EM (1988) Shock compression of molten silicate: results for a model basaltic composition. Journal of Geophysical Research 93:367–382. doi: 10.1029/JB093iB01p00367

Righter K, Danielson L, Drake MJ, Domanik K (2014) Partition coefficients at high pressure and temperature. In: Holland H, Turekian K (eds) Treatise on Geochemistry: Second Edition. Elsevier Inc., pp 425–449

Righter K, King C, Danielson L, Pando K, Lee CT (2011) Experimental determination of the metal/silicate partition coefficient of Germanium: Implications for core and mantle differentiation. Earth and Planetary Science Letters 304:379–388. doi: 10.1016/j.epsl.2011.02.015

Righter K, Nickodem K, Pando K, Danielson L, Boujibar A, Righter M, Lapen TJ (2017) Distribution of Sb, As, Ge, and In between metal and silicate during accretion and core formation in the Earth. Geochimica et Cosmochimica Acta 198:1–16. doi: 10.1016/j.gca.2016.10.045

Ringwood AE (1970) Phase transformations and the constitution of the mantle. Physics of the Earth and Planetary Interiors 3:109–155. doi: 10.1016/0031-9201(70)90047-6

Robie R, Hemingway B (1995) Thermodynamic properties of minerals and related substances at 298.15 K and 1 bar (105 pascals) pressure and at higher temperatures.

Rouxel OJ, Luais B (2017) Germanium isotope geochemistry. Reviews in Mineralogy and Geochemistry 82:601–656. doi: 10.2138/rmg.2017.82.14

Rubie DC, Jacobson SA, Morbidelli A, O'Brien DP, Young ED, de Vries J, Nimmo F, Palme H, Frost DJ (2015) Accretion and differentiation of the terrestrial planets with implications for the compositions of early-formed Solar System bodies and accretion of water. Icarus 248:89–108. doi: 10.1016/j.icarus.2014.10.015

Rubie DC, Melosh HJ, Reid JE, Liebske C, Righter K (2003) Mechanisms of metal-silicate equilibration in the terrestrial magma ocean. Earth and Planetary Science Letters 205:239–255. doi: 10.1016/S0012-821X(02)01044-0

Ruzicka A, Snyder GA, Taylor LA (2001) Comparative geochemistry of basalts from the moon, earth, HED asteroid, and mars: Implications for the origin of the moon. Geochimica et Cosmochimica Acta 65:979–997. doi: 10.1016/S0016-7037(00)00599-8

Ryan JG, Chauvel C (2014) The subduction-zone filter and the impact of recycled materials on the evolution of the mantle. In: Turekian K, Holland H (eds) Treatise on Geochemistry: Second Edition. Elsevier, pp 479–508

Sakamaki T, Suzuki A, Ohtani E, Terasaki H, Urakawa S, Katayama Y, Funakoshi K, Wang Y, Hernlund JW, Ballmer MD (2013) Ponded melt at the boundary between the lithosphere and asthenosphere. Nature Geoscience 6:1041–1044. doi: 10.1038/ngeo1987

Salmon PS, Zeidler A (2015) Networks under pressure: The development of in situ high-pressure neutron diffraction for glassy and liquid materials. Journal of Physics Condensed Matter 27:133201. doi: 10.1088/0953-8984/27/13/133201

Sanloup C, Cochain B, De Grouchy C, Glazyrin K, Konôpkova Z, Liermann HP, Kantor I, Torchio R, Mathon O, Irifune T (2018) Behaviour of niobium during early Earth's differentiation: Insights from its local structure and oxidation state in silicate melts at high pressure. Journal of Physics Condensed Matter 30:084004. doi: 10.1088/1361-648X/aaa73e

Sanloup C, Drewitt JWE, Konôpková Z, Dalladay-Simpson P, Morton DM, Rai N, Van Westrenen W, Morgenroth W (2013) Structural change in molten basalt at deep mantle conditions. Nature 503:104–107. doi: 10.1038/nature12668

Schmitt W, Palme H, Wänke H (1989) Experimental determination of metal/silicate partition coefficients for P, Co, Ni, Cu, Ga, Ge, Mo, and W and some implications for the early evolution of the Earth. Geochimica et Cosmochimica Acta 53:173–185. doi: 10.1016/0016-7037(89)90284-6

Sen S, Aitken BG, Khalid S (2005) Short-range structure and chemical order in In-Ge sulfide and selenide glasses by X-ray absorption fine structure spectroscopy. Journal of Non-Crystalline Solids 351:1710–1715. doi: 10.1016/j.jnoncrysol.2005.04.004

Shanavas K V., Garg N, Sharma SM (2006) Classical molecular dynamics simulations of behavior of $GeO_2$ under high pressures and at high temperatures. Physical Review B 73:094120. doi: 10.1103/PhysRevB.73.094120

Shannon MC, Agee CB (1996) High pressure constraints on percolative core formation. Geophysical Research Letters 23:2717–2720. doi: 10.1029/96GL02817

Shannon RD (1976) Revised effective ionic radii and systematic studies of interatomic distances in halides and chalcogenides. Acta Crystallographica A32:751–767. doi: 10.1107/S0567739476001551

Shimoda K, Nemoto T, Saito K (2008) Local structure of magnesium in silicate glasses: a $^{25}$Mg 3QMAS NMR study. The Journal of Physical Chemistry B 112:6747–6752. doi: 10.1021/jp711417t

Shimoda K, Tobu Y, Hatakeyama M, Nemoto T, Saito K (2007) Structural investigation of Mg local environments in silicate glasses by ultra-high field $^{25}$Mg 3QMAS NMR spectroscopy. American Mineralogist 92:695–698. doi: 10.2138/am.2007.2535

Siebert J, Badro J, Antonangeli D, Ryerson FJ (2012) Metal-silicate partitioning of Ni and Co in a deep magma ocean. Earth and Planetary Science Letters 321–322:189–197. doi: 10.1016/j.epsl.2012.01.013

Siebert J, Corgne A, Ryerson FJ (2011) Systematics of metal–silicate partitioning for many siderophile elements applied to Earth's core formation. Geochimica et Cosmochimica Acta 75:1451–1489. doi: 10.1016/j.gca.2010.12.013

Smith GS, Isaacs PB (1964) The crystal structure of quartz-like $GeO_2$. Acta Crystallographica 17:842–846. doi: 10.1107/S0365110X64002262

Smith KA, Kirkpatrick RJ, Oldfield E, Henderson DM (1983) High-resolution silicon-29 nuclear magnetic resonance spectroscopic study of rock-forming silicates. American Mineralogist 68:1206–1215.

Smith J V., Anderson AT, Newton RC, Olsen EJ, Wyllie PJ, Crewe A V., Isaacson MS, Johnson D (1970) Petrologic history of the moon inferred from petrography, mineralogy, and petrogenesis of Apollo 11 rocks. In: Levinson AA (ed) Geochimica et Cosmochimica Acta Supplement, Volume 1. Proceedings of the Apollo 11 Lunar Science Conference. Pergamon Press, Houston, TX, pp 897–925

Stebbins JF (2016) Glass structure, melt structure and dynamics: some concepts for petrology. American Mineralogist 101:753–768. doi: 10.2138/am-2016-5386

Stebbins JF (1991) NMR evidence for five-coordinated silicon in a silicate glass at atmospheric pressure. Nature 351:638–639. doi: 10.1038/351638a0

Stebbins JF (1987) Identification of multiple structural species in silicate glasses by $^{29}$Si NMR. Nature 330:465–467. doi: 10.1038/330465a0

Stebbins JF, Dubinsky E V., Kanehashi K, Kelsey KE (2008) Temperature effects on non-bridging oxygen and aluminum coordination number in calcium aluminosilicate glasses and melts. Geochimica et Cosmochimica Acta 72:910–925. doi: 10.1016/j.gca.2007.11.018

Stebbins JF, Ellsworth SE (1996) Temperature effects on structure and dynamics in borate and borosilicate liquids: High-resolution and high-temperature NMR results. Journal of the American Ceramic Society 79:2247–2256. doi: 10.1111/j.1151-2916.1996.tb08969.x

Stebbins JF, Farnan I (1992) Effects of high temperature on silicate liquid structure: A multinuclear NMR study. Science 255:586–589. doi: 10.1126/science.255.5044.586

Stebbins JF, Kanzaki M (1991) Local structure and chemical shifts for six-coordinated silicon in high-pressure mantle phases. Science 251:294–298. doi: 10.1126/science.251.4991.294

Stebbins JF, McMillan P (1989) Five- and six-coordinated Si in $K_2Si_4O_9$ glass quenched from 1.9 GPa and 1200°C. American Mineralogist 74:965–968.

Stebbins JF, Xue X (2014) NMR spectroscopy of inorganic earth materials. Reviews in Mineralogy and Geochemistry 78:605–653. doi: 10.2138/rmg.2014.78.15

Steenstra ES, Rai N, Knibbe JS, Lin YH, van Westrenen W (2016) New geochemical models of core formation in the Moon from metal-silicate partitioning of 15 siderophile elements. Earth and Planetary Science Letters 441:1–9. doi: 10.1016/j.gca.2016.01.002

Stevenson DJ (1990) Fluid dynamics of core formation. In: LPI Conference on the Origin of the Earth. pp 231–249

Stixrude L, de Koker N, Sun N, Mookherjee M, Karki BB (2009) Thermodynamics of silicate liquids in the deep Earth. Earth and Planetary Science Letters 278:226–232. doi: 10.1016/j.epsl.2008.12.006

Sutton SR, Karner J, Papike J, Delaney JS, Shearer C, Newville M, Eng P, Rivers M, Dyar MD (2005) Vanadium K edge XANES of synthetic and natural basaltic glasses and application to microscale oxygen barometry. Geochimica et Cosmochimica Acta 69:2333–2348. doi: 10.1016/j.gca.2004.10.013

Suzuki A, Ohtani E, Terasaki H, Funakoshi K (2005) Viscosity of silicate melts in $CaMgSi_2O_6$–$NaAlSi_2O_6$ system at high pressure. Physics and Chemistry of Minerals 32:140–145. doi: 10.1007/s00269-005-0452-0

Suzuki T, Hirata T, Yokoyama TD, Imai T, Takahashi E (2012) Pressure effect on element partitioning between minerals and silicate melt: Melting experiments on basalt up to 20 GPa. Physics of the Earth and Planetary Interiors 208–209:59–73. doi: 10.1016/j.pepi.2012.07.008

Tan CZ, Arndt J (1999) X-ray diffraction of densified silica glass. Journal of Non-Crystalline Solids 249:47–50. doi: 10.1016/S0022-3093(99)00245-8

Taura H, Yurimoto H, Kurita K, Sueno S (1998) Pressure dependence on partition coefficients for trace elements between olivine and the coexisting melts. Physics and Chemistry of Minerals 25:469–484. doi: 10.1007/s002690050138

Tauzin B, Debayle E, Wittlinger G (2010) Seismic evidence for a global low-velocity layer within the Earth’s upper mantle. Nature Geoscience 3:718–721. doi: 10.1038/ngeo969

Taylor GJ, Norman MD (1992) Evidence for magma oceans on asteroids, the moon, and Earth. In: In Lunar and Planetary Inst., Workshop on the Physics and Chemistry of Magma Oceans from 1 Bar to 4 Mbar. pp 58–65

The MathWorks Inc. (2015) MATLAB 2015b.

Timken HKC, Oldfield E (1987) Solid-state gallium-69 and gallium-7 1 nuclear magnetic resonance spectroscopic studies of gallium analogue zeolites and related systems. Journal of the American Chemical Society 109:7669–7673. doi: 10.1021/ja00259a015

Tomkins AG, Weinberg RF, Schaefer BF, Langendam A (2013) Disequilibrium melting and melt migration driven by impacts: Implications for rapid planetesimal core formation. Geochimica et Cosmochimica Acta 100:41–59. doi: 10.1016/j.gca.2012.09.044

Tonks WB, Melosh HJ (1993) Magma ocean formation due to giant impacts. Journal of Geophysical Research: Planets 98:5319–5333. doi: 10.1029/92JE02726

Trail D, Bruce Watson E, Tailby ND (2012) Ce and Eu anomalies in zircon as proxies for the oxidation state of magmas. Geochimica et Cosmochimica Acta 97:70–87. doi: 10.1016/j.gca.2012.08.032

Tricot G, Lafon O, Trébosc J, Delevoye L, Méar F, Montagne L, Amoureux J-P (2011) Structural characterisation of phosphate materials: new insights into the spatial proximities between phosphorus and quadrupolar nuclei using the D-HMQC MAS NMR technique. Physical Chemistry Chemical Physics 13:16786–16794. doi: 10.1039/c1cp20993k

Tricot G, Trébosc J, Pourpoint F, Gauvin R, Delevoye L (2014) The D-HMQC MAS-NMR technique: An efficient tool for the editing of through-space correlation spectra between quadrupolar and spin-1/2 ($^{31}P$, $^{29}Si$, $^{1}H$, $^{13}C$) nuclei. In: Webb GA (ed) Annual Reports on NMR Spectroscopy. Academic Press, pp 145–184

Vaccari M, Aquilanti G, Pascarelli S, Mathon O (2009) A new EXAFS investigation of local structural changes in amorphous and crystalline $GeO_2$ at high pressure. Journal of Physics: Condensed Matter 21:145403. doi: 10.1088/0953-8984/21/14/145403

Waff HS (1975) Pressure-induced coordination changes in magmatic liquids. Geophysical Research Letters 2:193–196. doi: 10.1029/GL002i005p00193

Wagner J, Haigis V, Künzel D, Jahn S (2017) Trace element partitioning between silicate melts – A molecular dynamics approach. Geochimica et Cosmochimica Acta 205:245–255. doi: 10.1016/j.gca.2017.02.017

Walker D, Norby L, Jones JH (1993) Superheating effects on metal–silicate partitioning of siderophile elements. Science 262:1858–1861. doi: 10.1126/science.262.5141.1858

Walter MJ (1998) Melting of garnet peridotite and the origin of komatiite and depleted lithosphere. Journal of Petrology 39:29–60. doi: 10.1093/petroj/39.1.29

Walter MJ, Trønnes RG (2004) Early earth differentiation. Earth and Planetary Science Letters 225:253–269. doi: 10.1016/j.epsl.2004.07.008

Wang Y, Sakamaki T, Skinner LB, Jing Z, Yu T, Kono Y, Park C, Shen G, Rivers ML, Sutton SR (2014) Atomistic insight into viscosity and density of silicate melts under pressure. Nature Communications 5:3241. doi: 10.1038/ncomms4241

Warren PH, Taylor GJ (2014) The Moon. In: Turekian K, Holland H (eds) Treatise on Geochemistry: Second Edition. Elsevier, pp 493–538

Weill DF, Drake MJ (1973) Europium anomaly in plagioclase feldspar: Experimental results and semiquantitative model. Science 180:1059–1060. doi: 10.1126/science.180.4090.1059

Wicks JK, Jackson JM, Sturhahn W (2010) Very low sound velocities in iron-rich (Mg,Fe)O: Implications for the core-mantle boundary region. Geophysical Research Letters 37:L15304. doi: 10.1029/2010GL043689

Wieczorek MA, Jolliff BL, Khan A, Pritchard ME, Weiss BP, Williams JG, Hood LL, Righter K, Neal CR, Shearer CK, McCallum IS, Tompkins S, Hawke BR, Peterson C, Gillis JJ, Bussey B (2006) The constitution and structure of the lunar interior. Reviews in Mineralogy and Geochemistry 60:221–364. doi: 10.2138/rmg.2006.60.3

Wilke M, Farges F, Petit P-E, Brown GE, Martin F (2001) Oxidation state and coordination of Fe in minerals: An Fe K-XANES spectroscopic study. American Mineralogist 86:714–730. doi: 10.2138/am-2001-5-612

Wilke M, Jugo PJ, Klimm K, Susini J, Botcharnikov R, Kohn SC, Janousch M (2008) The origin of S4+ detected in silicate glasses by XANES. American Mineralogist 93:235–240. doi: 10.2138/am.2008.2765

Williams Q, Garnero EJ (1996) Seismic evidence for partial melt at the base of Earth's mantle. Science 273:1528–1530. doi: 10.2307/2891048

Wolf GH, McMillan PF (1995) Pressure effects on silicate melt structure and properties. Reviews in Mineralogy and Geochemistry 32:505–561.

Wong J, Lytle FW, Messmer RP, Maylotte DH (1984) K-edge absorption spectra of selected vanadium compounds. Physical Review B 30:5596–5610. doi: 10.1103/PhysRevB.30.5596

Wood BJ, Blundy JD (2014) Trace element partitioning: the influences of ionic radius, cation charge, pressure, and temperature. In: Holland H, Turekian K (eds) Treatise on Geochemistry: Second Edition. Elsevier Ltd., pp 421–448

Wood BJ, Walter MJ, Wade J (2006) Accretion of the Earth and segregation of its core. Nature 441:825–833. doi: 10.1038/nature04763

Wood JA, Dickey, J. S. J, Marvin UB, Powell BN (1970) Lunar anorthosites and a geophysical model of the moon. In: A. A. Levinson (ed) Geochimica et Cosmochimica Acta Supplement, Volume 1. Proceedings of the Apollo 11 Lunar Science Conference. Pergamon Press, Houston, TX, pp 965–988

Wu J, Stebbins JF (2010) Quench rate and temperature effects on boron coordination in aluminoborosilicate melts. Journal of Non-Crystalline Solids 356:2097–2108. doi: 10.1016/j.jnoncrysol.2010.08.015

Xue X, Kanzaki M (2008) Structure of hydrous aluminosilicate glasses along the diopside-anorthite join: A comprehensive one- and two-dimensional $^{1}$H and$^{27}$Al NMR study. Geochimica et Cosmochimica Acta 72:2331–2348. doi: 10.1016/j.gca.2008.01.022

Xue X, Stebbins JF, Kanzaki M, McMillan PF, Poe B (1991) Pressure-induced silicon coordination and tetrahedral structural changes in alkali oxide-silica melts up to 12 GPa: NMR, Raman, and infrared spectroscopy. American Mineralogist 76:8–26.

Xue X, Stebbins JF, Kanzaki M, Trønnes RG (1989) Silicon coordination and speciation changes in a silicate liquid at high pressures. Science 245:962–964. doi: 10.1126/science.245.4921.962

Yarger JL, Smith KH, Nieman RA, Diefenbacher J, Wolf GH, Poe BT, McMillan PF, Yarger AJL, Smith KH, Nieman RA, Diefenbacher J, Wolf GH, Poe BT, McMillan PF (1995) Al coordination changes in high-pressure aluminosilicate liquids. Science 270:1964–1967. doi: 10.1126/science.270.5244.1964

Yildirim C, Micoulaut M, Boolchand P, Kantor I, Mathon O, Gaspard J-P, Irifune T, Raty J-Y (2016) Universal amorphous-amorphous transition in $Ge_xSe_{100-x}$ glasses under pressure. Scientific Reports 6:27317. doi: 10.1038/srep27317

Yu S, Garnero EJ (2018) Ultralow velocity zone locations: A global assessment. Geochemistry, Geophysics, Geosystems 19:396–414. doi: 10.1002/2017GC007281

Zachariasen WH (1932) The atomic arrangement in glass. Journal of the American Chemical Society 54:3841–3851. doi: doi:10.1021/ja01349a006

Zhang Z, Dorfman SM, Labidi J, Zhang S, Li M, Manga M, Stixrude L, Mcdonough WF, Williams Q (2016) Primordial metallic melt in the deep mantle. Geophyscal Research Letters 43:3693–3699. doi: 10.1002/2016GL068560

Zhou W, Paesler M, Sayers DE (1991) Structure of germanium-selenium glasses: An x-ray-absorption fine-structure study. Physical Review B 43:2315–2321. doi: 10.1103/PhysRevB.43.2315

# Chapter 7: Supplementary Material

## 7.1 Preparation of model compounds

$GeO_2$ in the quartz form (q-$GeO_2$) was synthesized by firing $GeO_2$ powder at 1060 °C for 24 h in a box furnace. $GeO_2$ in the rutile form was synthesized from q-$GeO_2$ in a silver capsule at 2.0 GPa and 900 °C for 24 h.

$Mg_2GeO_4$ in the olivine form was synthesized from stoichiometric proportions of MgO and $GeO_2$. The powders were mixed under acetone and fired as a pellet at 1000°C for 6 days in a box furnace. The ol-$Mg_2GeO_4$ was converted to a spinel form (spl-$Mg_2GeO_4$) in a graphite capsule at 1150 °C, and 2.5 GPa for 14 h.

$CaGeO_3$ in the wollastonite form was synthesized from stoichiometric proportions of $CaCO_3$ and $GeO_2$, mixed thoroughly under acetone, and then fired as a pellet at 1200 °C for 24 h to decarbonate. Wollastonite-$CaGeO_3$ was converted to the garnet form in a graphite capsule at 900 °C and 2.0 GPa for 20 h.

$MgGeO_3$ enstatite was synthesized from stoichiometric proportions of MgO and $GeO_2$. The powders were mixed under acetone and fired in a box furnace for 12 h at 1200 °C.

$\beta$-$Ga_2O_3$ was synthesized from reagent grade $Ga_2O_3$ by firing it in air at 1300 °C for 12 hours.

A sample of $ZnGa_2O_3$ spinel (that had been synthesised using a lead-borate flux) was annealed at 800 °C for one week, to ensure as much as possible of the Ga was on the octahedral site.

The gallium albite $NaGaSi_3O_8$ was made by dissolving Ga metal (1.4847g) and $Na_2CO_3$ (1.1285g) in dilute $HNO_3$ and adding TEOS (tetraethyl orthosilicate, 13.3087 g), along with a small amount of ethanol and $NH_3$. The mixture was left overnight, and then heated on a hot plate for 24 h. The powder was then heated over a Bunsen burner in a platinum crucible to burn off most of the nitrate, and then heated in a box furnace at ~800 °C overnight to ensure no nitrate was left.

For the an-$CaAl_2Si_2O_8$, stoichiometric proportions of $Al_2O_3$ and $SiO_2$ were mixed under acetone. 0.0106 g Ga metal was dissolved in 6 drops of concentrated nitric acid (70%) and some water in a volumetric flask. The flask was left on a hot plate for several h and put in an ultrasonic bath for a few min until the Ga was dissolved. Distilled water was added to make up the volume to 25 ml. 4.7 ml of this solution was added to the powdered oxide mix, and this was mixed for 15 min and left to dry overnight in a fume hood. The dry mix was heated slowly as a pellet to 500° C, and then powdered again, and $CaCO_3$ was mixed in under acetone. The resulting mix was pelletised and decarbonated by firing at 1050 °C. The sample was reground and pelletised once more, and fired at 1500 °C in air for 24 hours. The signal-to-noise of the XRD pattern is poor, but the only phase present is an-$CaAl_2Si_2O_8$.

The Ga-doped corundum was synthesised as a by-product of an attempt to synthesise Ga-doped kyanite. Stoichiometric proportions of $Al_2O_3$ and $SiO_2$ powders were mixed with the Ga nitrate solution previously made for the anorthite. This mixture was left to dry overnight, then pressed into a pellet and fired at 1050 °C overnight. The pellet was crushed and the powder loaded into a graphite capsule, which was run in a piston cylinder apparatus at 1000 °C and 2.0 GPa for 24 h.

## 7.2 Major element compositions of glass samples

This section contains compositional analyses, made using FE-SEM, of glass samples prepared for Chapters 2 and 3.

Table 7.1. Compositions (wt%) of selected samples (CMAS7G) prepared for Chapter 2.

| | C4485 | C4486 | D1585 | D1591 | D1572 |
|---|---|---|---|---|---|
| *n* | 3 | 3 | 3 | 3 | 3 |
| $SiO_2$ | 58.4 (2) | 58.7 (3) | 58.2 (3) | 58.2 (2) | 56.8 (2) |
| $Al_2O_3$ | 12.31 (8) | 12.33 (8) | 12.19 (4) | 12.15 (1) | 11.7 (1) |
| MgO | 2.26 (6) | 2.47 (7) | 2.23 (5) | 2.28 (1) | 2.23 (2) |
| CaO | 24.39 (4) | 24.6 (1) | 24.2 (2) | 24.5 (2) | 23.29 (6) |
| Total | 97.3 (3) | 98.2 (4) | 96.8 (4) | 97.1 (2) | 94.1 (3) |
| | uhppc-251 | uhppc-250 | MA1117 | MA1118 | MA1121 |
| *n* | 3 | 3 | 8 | 5 | 3 |
| $SiO_2$ | 56.5 (4) | 58.1 (3) | 60.7 (6) | 60 (2) | 61 (1) |
| $Al_2O_3$ | 11.80 (8) | 12.1 (1) | 12.7 (3) | 13.0 (8) | 13.5 (5) |
| MgO | 2.17 (8) | 2.24 (2) | 2.45 (8) | 2.4 (2) | 2.4 (1) |
| CaO | 23.5 (1) | 24.2 (1) | 23.5 (4) | 24.0 (5) | 22.9 (4) |
| Total | 93.9 (4) | 96.7 (5) | 99.4 (9) | 100 (2) | 100.3 (7) |

Note MA1117, MA1118 and MA1121 are annealed glass samples; all others are quenched melts. *n* is the number of analyses. One standard deviation on the last digit is given in parentheses.

Table 7.2. Compositions (wt%) of selected samples (CMAS7G) prepared for Chapter 3.

| | C4901 | D1842 | C4900 | C4904 | D1840 | C4892 | C4905 |
|---|---|---|---|---|---|---|---|
| *n* | 2 | 2 | 1 | 1 | 1 | 1 | 1 |
| $SiO_2$ | 58.3 (6) | 57 (1) | 57.44 | 58.13 | 57.63 | 57.60 | 56.96 |
| $Al_2O_3$ | 11.81 (0.8) | 11.8 (2) | 11.71 | 11.69 | 11.84 | 11.76 | 11.84 |
| MgO | 2.23 (5) | 2.30 (3) | 2.08 | 2.31 | 2.73 | 2.26 | 2.23 |
| CaO | 23.8 (1) | 22.5 (2) | 22.46 | 22.38 | 22.89 | 22.40 | 22.79 |
| Total | 96.1 (5) | 94 (1) | 93.70 | 94.50 | 95.09 | 94.02 | 93.82 |

All are quenched melts. *n* is the number of analyses. One standard deviation on the last digit is given in parentheses.

Table 7.3. Compositions (wt%) of selected samples in the CMAS7A pressure series prepared for Chapter 1.

| | D1602 | C4493 | D1590 | D1592 | C4506 |
|---|---|---|---|---|---|
| *n* | 3 | 3 | 3 | 3 | 3 |
| $SiO_2$ | 53.9 (12) | 54.3 (2) | 52 (2) | 49.3 (1) | 50.6 (4) |
| $Al_2O_3$ | 14.98 (1) | 14.98 (3) | 14.4 (7) | 13.63 (8) | 13.94 (8) |
| MgO | 11.46 (7) | 11.62 (7) | 11.0 (5) | 15.09 (9) | 10.71 (8) |
| CaO | 14.54 (4) | 14.52 (9) | 14.0 (6) | 13.16 (7) | 13.7 (2) |
| Total | 94.8 (2) | 95.41 (3) | 91 (4) | 91.2 (2) | 89.0 (7) |

All are quenched melts. *n* is the number of analyses. One standard deviation on the last digit is given in parentheses.

Table 7.4. Compositions (wt%) of samples in the NHPG-1 pressure series prepared for Chapter 2.

| | E131113 | D1637 | D1635 | D1368 | C4563 | uhppc253 |
|---|---|---|---|---|---|---|
| *n* | 3 | 2 | 1 | 1 | 1 | 1 |
| $SiO_2$ | 59.1 (9) | 58.2 (4) | 59.29 | 58.32 | 58.58 | 58.11 |
| $Al_2O_3$ | 14.07 (9) | 14.52 (6) | 14.63 | 14.54 | 14.89 | 14.62 |
| MgO | 6.1 (1) | 6.61 (3) | 6.62 | 6.66 | 6.77 | 6.76 |
| CaO | 7.9 (3) | 8.3 (2) | 8.31 | 8.17 | 8.23 | 8.33 |
| $TiO_2$ | 3.8 (2) | 3.82 (7) | 3.94 | 3.63 | 3.84 | 3.71 |
| $Na_2O$ | 2.84 (5) | 3.2 (2) | 3.37 | 3.86 | 3.95 | 3.98 |
| $K_2O$ | 1.61 (2) | 1.72 (6) | 1.81 | 1.91 | 1.97 | 1.80 |
| $P_2O_5$ | 0.52 (2) | 0.44 (6) | 0.40 | 0.44 | 0.47 | 0.42 |
| Total | 95.8 (5) | 96.8 (1) | 98.37 | 97.52 | 98.69 | 97.73 |

All are quenched melts. *n* is the number of analyses. One standard deviation on the last digit is given in parentheses.

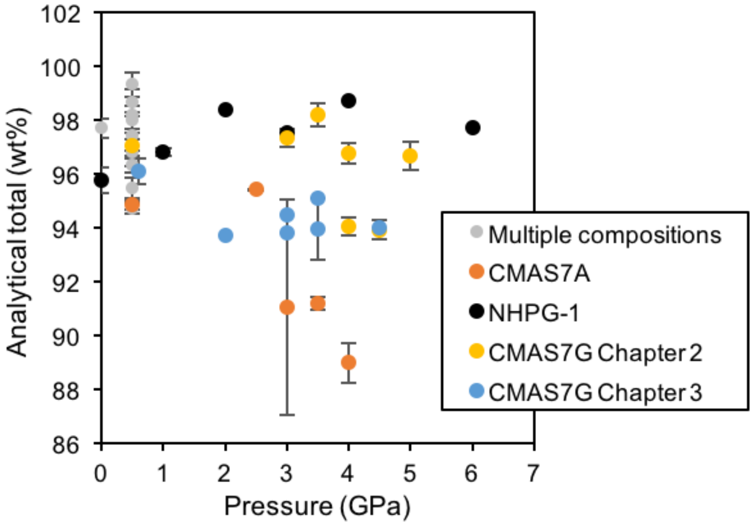

Figure 7.1. Analytical totals plotted against pressure for quenched melts, as an estimate of how water content might vary with pressure. Where there are no error bars on a data point, only one analysis was made for that sample.

## 7.3 Ge and Ga concentrations in glasses

Ge and Ga concentrations and presence or absence of vesicles in glass samples prepared for Chapter 2.

Table 7.5. Ge and Ga concentrations and presence of vesicles in glass samples.

| Sample Name | *n* | Ga (ppm) | sd | Ge (ppm) | sd | Vesicles observed? |
|---|---|---|---|---|---|---|
| **Quenched melts doped with Ge** | | | | | | |
| C4496 | 3 | 14 | 0 | 2108 | 14 | no |
| D1602 | 3 | 17 | 0 | 2679 | 14 | yes |
| D1601 | 3 | 7 | 0 | 2041 | 24 | yes |
| D1591 | 3 | 11 | 0 | 2444 | 34 | yes |
| D1597 | 4 | 20 | 0 | 2783 | 16 | yes |
| D1598 | 4 | 15 | 0 | 2435 | 25 | yes |
| C4503 | 4 | 19 | 0 | 2320 | 17 | yes |
| D1605 | 5 | 18 | 0 | 2474 | 9 | yes |
| D1611 | 5 | 18 | 0 | 2346 | 42 | no |
| C4519 | 4 | 8 | 0 | 2255 | 13 | yes |
| D1609 | 4 | 18 | 0 | 2805 | 19 | yes |
| D1608 | 3 | 11 | 0 | 2901 | 32 | yes |
| **Quenched melts doped with Ga** | | | | | | |
| E16/11/13A | 3 | 2456 | 30 | 6 | 1 | N/A |
| E16/11/13B | 3 | 1956 | 2 | 3 | 0 | N/A |
| E16/11/13C | 4 | 2291 | 27 | 3 | 1 | N/A |
| E16/11/13D | 3 | 1928 | 9 | 5 | 1 | N/A |
| E16/11/13E | 3 | 2181 | 46 | 4 | 0 | N/A |
| E16/11/13F | 3 | 2469 | 25 | 11 | 0 | N/A |
| E19/11/13D | 3 | 1950 | 14 | 2 | 0 | N/A |
| E19/11/13E | 3 | 1845 | 7 | 2 | 0 | N/A |
| E19/11/13F | 3 | 2424 | 16 | 2 | 0 | N/A |
| E23/10/13A | 3 | 1912 | 158 | 2825 | 133 | N/A |

Table 7.5. (Continued)

| Sample Name | n | Ga (ppm) | sd | Ge (ppm) | sd | Vesicles observed? |
|---|---|---|---|---|---|---|
| **Quenched melts doped with Ge** | | | | | | |
| *NHPG-1 pressure series* | | | | | | |
| E13/11/13 | 3 | 10 | 0 | 2189 | 191 | no |
| D1637 | 3 | 11 | 0 | 2216 | 22 | no |
| D1635 | 3 | 11 | 0 | 2248 | 23 | no |
| D1638 | 3 | 11 | 0 | 2062 | 11 | no |
| C4563 | 3 | 11 | 0 | 2088 | 18 | no |
| uhppc253 | 3 | 11 | 0 | 2208 | 5 | no |
| *CMAS7A pressure series* | | | | | | |
| E15/10/13 | 5 | 16 | 0 | 2665 | 82 | N/A |
| D1602* | 3 | 17 | 0 | 2679 | 14 | no |
| D1588 | 3 | 17 | 0 | 2855 | 15 | yes |
| C4491 | 3 | 17 | 0 | 2761 | 36 | yes |
| D1589 | 3 | 18 | 0 | 2950 | 16 | yes |
| C4493 | 3 | 16 | 0 | 2791 | 12 | yes |
| D1590 | 4 | 17 | 0 | 2861 | 10 | no |
| D1592 | 3 | 17 | 0 | 3764 | 3 | yes |
| C4506 | 4 | 16 | 0 | 3357 | 25 | no |
| *CMAS7G pressure series* | | | | | | |
| E23/10/13B | 2 | 10 | 0 | 2566 | 86 | N/A |
| B1-080316 | 6 | 2051 | 97 | 2883 | 87 | N/A |
| C110416 | 3 | 2179 | 189 | 2832 | 90 | N/A |
| D05/04/16 | 8 | 2376 | 254 | 2905 | 110 | N/A |
| D1591 | 3 | 11 | 0 | 2444 | 34 | no |
| C4490 | 3 | 12 | 0 | 2477 | 27 | no |
| D1586 | 3 | 9 | 0 | 2028 | 10 | no |
| D1584 | 3 | 12 | 0 | 2544 | 39 | no |
| C4484 | 3 | 11 | 0 | 2439 | 22 | no |
| D1576 | 3 | 2134 | 15 | 2538 | 23 | no |
| uhppc271 | 1 | 10 | – | 2464 | – | no |
| C4485 | 4 | 10 | 0 | 2426 | 27 | no |
| C4486 | 3 | 11 | 0 | 2456 | 8 | no |
| D1585 | 3 | 11 | 0 | 2515 | 7 | no |
| D1572 | 5 | 1838 | 38 | 975 | 87 | no |
| uhppc-251 | 3 | 11 | 0 | 2543 | 32 | no |
| uhppc-367 | 1 | 2226 | – | 2669 | – | no |
| uhppc-369 | 1 | 2257 | – | 2769 | – | no |
| uhppc-250 | 4 | 11 | 0 | 2616 | 20 | no |
| uhppc-258 | 3 | 2189 | 9 | 2678 | 13 | no |
| uhppc-365 | 5 | 2284 | 8 | 2719 | 10 | no |
| uhppc-370 | 1 | 2226 | – | 2731 | – | no |

Table 7.5. (Continued)

| Sample Name | n | Ga (ppm) | sd | Ge (ppm) | sd | Vesicles observed? |
|---|---|---|---|---|---|---|
| **Quenched melts doped with Ga** | | | | | | |
| *CMAS7G pressure series* | | | | | | |
| E23/10/13A* | 3 | 1912 | 158 | 2825 | 133 | N/A |
| B1-080316* | 6 | 2051 | 97 | 2883 | 87 | N/A |
| D1604 | 5 | 2095 | 10 | 2550 | 13 | yes |
| D1580 | 3 | 2105 | 4 | 2613 | 11 | yes |
| D1578 | 3 | 2049 | 14 | 2501 | 16 | yes |
| D1576 | 3 | 2134 | 15 | 2538 | 23 | yes |
| D1574 | 4 | 1855 | 9 | 2307 | 11 | no |
| D1577 | 3 | 2171 | 30 | 2586 | 35 | yes |
| D1572* | 5 | 1838 | 38 | 975 | 87 | no |
| uhppc-367 | 1 | 2226 | – | 2669 | – | no |
| uhppc-369 | 1 | 2257 | – | 2769 | – | no |
| uhppc-258 | 3 | 2189 | 9 | 2678 | 13 | no |
| uhppc-365 | 5 | 2284 | 8 | 2719 | 10 | no |
| uhppc-370 | 1 | 2226 | – | 2731 | – | no |
| **Annealed glasses doped with Ge and Ga, unless specified** | | | | | | |
| D2210 | 1 | 2066 | – | 2885 | – | N/A |
| D2212 | 3 | 2035 | 18 | 2911 | 104 | N/A |
| D2208 | 1 | 2218 | – | 2842 | – | N/A |
| C5232 | 1 | 2140 | – | 2838 | – | N/A |
| D2209 | 1 | 2215 | – | 2811 | – | N/A |
| C5199 | 4 | 2171 | 63 | 2990 | 46 | N/A |
| C5231 | 1 | 2409 | – | 2827 | – | N/A |
| D2125 | 4 | 3475 | 182 | 2351 | 211 | N/A |
| D2189 (Ge scan only) | 5 | 2168 | 55 | 2910 | 119 | N/A |
| D2213 | 1 | 2095 | – | 2889 | – | N/A |
| D2173 | 4 | 2136 | 60 | 2954 | 29 | N/A |
| D2207 | 1 | 2243 | – | 3181 | – | N/A |
| C5228 | 1 | 2246 | – | 2936 | – | N/A |
| uhppc357 (Ga only) | 4 | 1915 | 81 | 431 | 139 | N/A |
| uhppc358 (Ga only) | 6 | 1855 | 448 | 685 | 387 | N/A |
| uhppc372 | 1 | 2032 | – | 2968 | – | N/A |
| MA-1117 | 3 | 2166 | 53 | 3020 | 47 | N/A |
| MA-1121 | 1 | 2155 | – | 2905 | – | N/A |
| MA-1118 | 2 | 2063 | 52 | 2943 | 7 | N/A |

*n* is the number of analyses. Vesicle observations are only for high-pressure samples (all ambient-pressure samples are expected to contain vesicles).

## 7.4 $Ge^{2+}$ in annealed glasses

In this appendix I will present a more detailed justification for my interpretation that $Ge^{2+}$ is present in the annealed glasses, and my approach for processing the data.

The spectra of all annealed glasses exhibit a shoulder on the low-energy side of the absorption edge (Figure 7.2). This shoulder is only observed in the spectrum of a single quenched melt sample (Figure 7.2B, D1572).

Let's begin by discussing the most anomalous sample: D2125. The spectrum of D2125 shows a large peak at ~11108.3 eV, and the spectrum is similar to spectra containing a mixture of $Ge^{2+}$ and $Ge^{4+}$ presented in Chapter 5 (Figure 5.5, e.g. sample D14/04/16). Indeed, linear combination fitting (Figure 7.3) produces a good match to the spectrum of D2125 by combining 67.1 % of the $Ge^{2+}$–endmember spectrum (D12/04/16, Chapter 5), 28.2 % of the $^{[4]}Ge^{4+}$–endmember spectrum (B1-080316), and 0.5% of the $^{[6]}Ge^{4+}$–endmember spectrum (rt-$GeO_2$).

If D2125 does contain 67.1% $Ge^{2+}$, the Ge in the sample must have been reduced at some point during sample synthesis. Probably, this reduction occurred during the synthesis of the quenched melt B1-030216, which was used as the starting material for D2125. This starting material was synthesised by melting an oxide mixture (CMAS7G composition) in a graphite crucible for 15 minutes at 1300 °C. The graphite crucible may have imposed a low $fO_2$ on the melt, leading to reduction of Ge from 4+ to 2+, as well as more rapid volatile loss of Ge. This could explain the large inferred $Ge^{2+}$ component in the XANES spectrum of the resulting annealed glass (D2125), as well as explaining the lower concentration of Ge in D2125 (~2300 ppm) compared with the other annealed glasses (typically ~ 2900 ppm, see Table 7.5). The loss of Ge due to melting the starting material in a graphite capsule was also observed for annealed glasses uhppc357 and uhppc358, which contained only 400–600 ppm Ge. Ge XANES spectra for these glasses were not recorded, but it would be expected that these samples would also contain a $Ge^{2+}$ component. All other annealed glass samples were prepared from starting materials melted in alumina crucibles to avoid this problem.

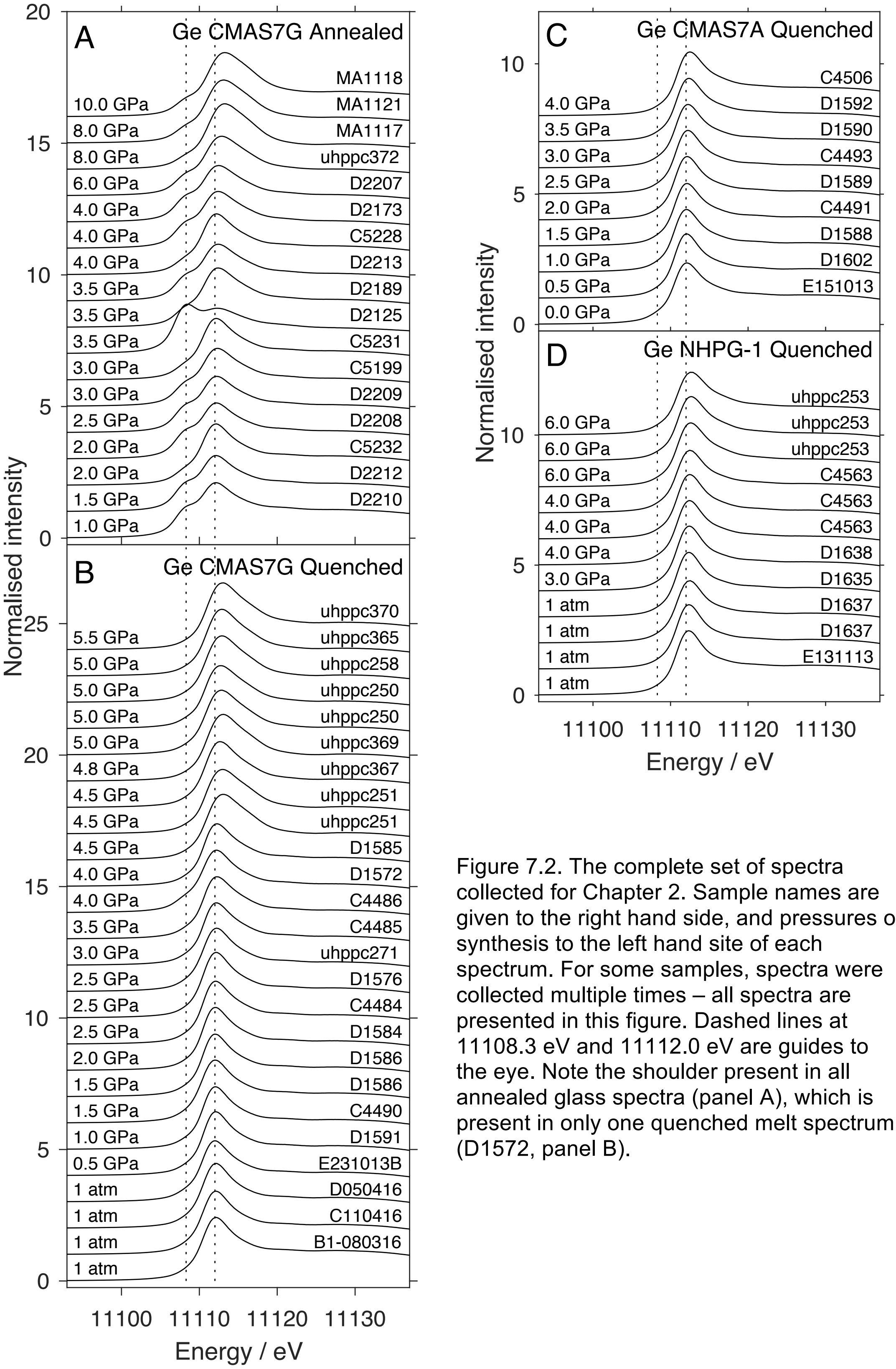

Figure 7.2. The complete set of spectra collected for Chapter 2. Sample names are given to the right hand side, and pressures of synthesis to the left hand site of each spectrum. For some samples, spectra were collected multiple times – all spectra are presented in this figure. Dashed lines at 11108.3 eV and 11112.0 eV are guides to the eye. Note the shoulder present in all annealed glass spectra (panel A), which is present in only one quenched melt spectrum (D1572, panel B).

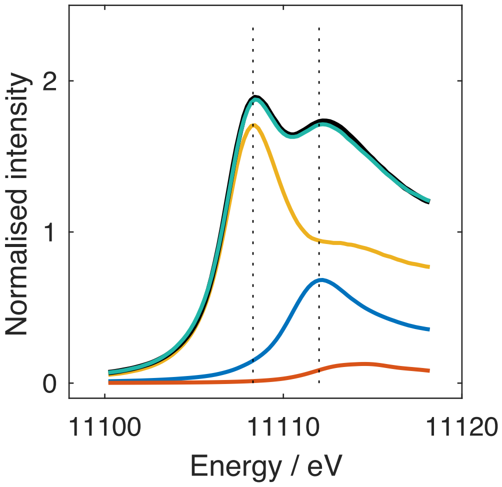

Figure 7.3. Linear combination fit (green) to the Ge XANES spectrum (black) of sample D2125, showing components in the fit – $Ge^{2+}$ (D12/04/16, yellow), $^{[4]}Ge^{4+}$ (B1-080316, blue) and $^{[6]}Ge^{4+}$ (rt-$^{[6]}Ge^{4+}O_2$, red). Dotted lines at 11108.3 eV and 11112.0 eV are guides to the eye.

Nevertheless, the other annealed glasses also show a shoulder at the same position as the peak in D2125. Once again, these spectra can be fit using a combination of three endmember spectra representing $Ge^{2+}$, $^{[4]}Ge^{4+}$ and $^{[6]}Ge^{4+}$ (Figure 2.7). Fits to all $Ge^{2+}$-bearing spectra are shown in Figure 7.4A.

The interpretation that the shoulders represent $Ge^{2+}$ implies that Ge partially reduced during the sample synthesis even when alumina crucibles were used for the starting material. In this case, it would be surprising if this reduction occurred during melting of the starting material. Instead it is more likely that Ge reduction occurred during annealing of the glasses at high pressure. No oxygen buffer was used in these high-pressure experiments, because it was assumed that at such low temperatures, including a solid-state oxygen buffer would be ineffective. Therefore, the $fO_2$ in these experiments was not controlled. In contrast, the $fO_2$ was controlled in the quenched melt samples using a Ru–$RuO_2$ buffer. Sample D1572 was the only quenched melt sample that definitely reduced during the run, because only Ru metal (and no $RuO_2$) was observed in the run product. The other run products of quenched melts contained either both Ru and $RuO_2$, or $RuO_2$ only (with the exception of D1592, which had no buffer exposed at the surface and could not be checked). Sample D1572 is therefore the only quenched melt sample that I can be confident had a lower $fO_2$ than that of the Ru–$RuO_2$ buffer, and is also the only quenched melt sample that exhibits a shoulder on the absorption edge of the XANES spectrum that is at the same energy as the white line of $Ge^{2+}$. The interpretation that the shoulders observed in the XANES spectra of annealed glasses and one quenched melt are a $Ge^{2+}$ component in the spectra is therefore consistent with the sample synthesis procedures.

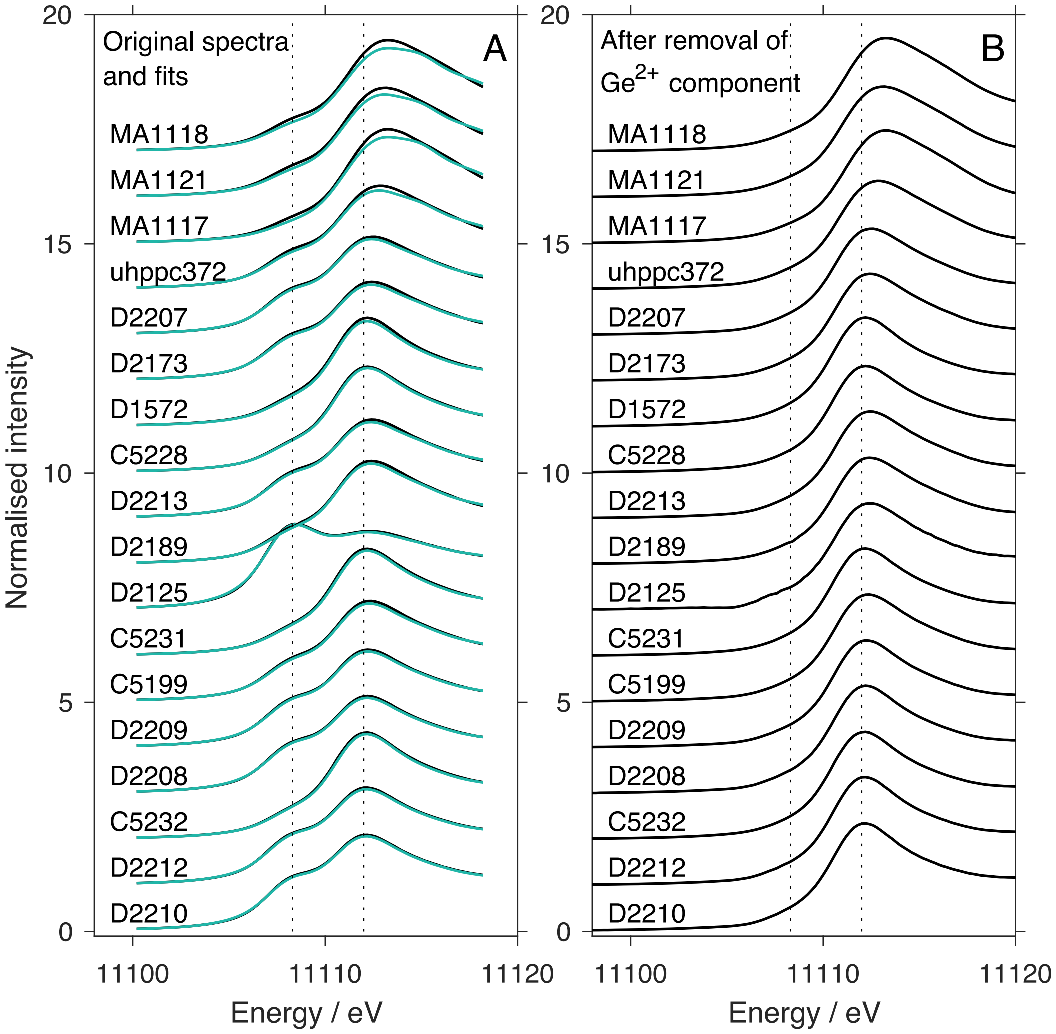

Figure 7.4. (A) Linear combination fits (green) to the Ge XANES spectra (black) of samples indicated. Fit components are not shown in this figure but numerical values are given in Table 2.8. (B) Spectra obtained after removal of the $Ge^{2+}$ component and renormalisation.

The $Ge^{2+}$ component seems to vary systematically with pressure, as shown in Figure 7.5. Discounting D2125, which had a very high $Ge^{2+}$ component because of the starting material used, the fits to the spectra indicate that the $Ge^{2+}$ component decreases with pressure, from about 30% to 10% over the 10 GPa. The reason for this is unknown.

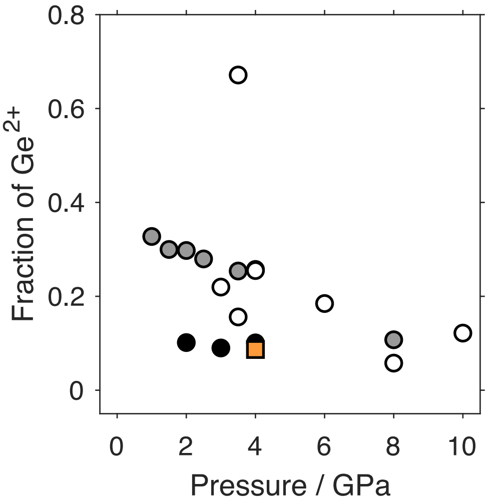

Figure 7.5. The variation in $Ge^{2+}$ with pressure. Circles are annealed glass samples, with different annealing temperatures indicated by their shade: white = 760–780 °C, grey = 700–730 °C, black = 600 °C. Orange square is the quenched melt sample D1572.

Figure 7.4B shows the spectra after the $Ge^{2+}$ component was removed and the spectra renormalised. The shoulder at 11108.3 eV is minimised in these spectra, although small shoulders are still present in some of the spectra: D2125, which contained a large fraction of $Ge^{2+}$, and the three highest-pressure spectra, for which the linear combination fits were poorer due to the larger fraction of the $^{[6]}Ge^{2+}$ component. While this approach is not perfect, it was the best that could be done with the information available.

## 7.5 $^{27}$Al fit parameters

Table 7.6. Parameters obtained by fitting $^{27}$Al MAS and MQMAS NMR spectra. All fits are to spectra collected at 14.1 T unless indicated otherwise.

|  | Exp | $AlO_4$ |  |  |  | $AlO_5$ |  |  |  | $AlO_6$ |  |  |  |
|---|---|---|---|---|---|---|---|---|---|---|---|---|---|
|  |  | $\delta_{iso}$ | dCSA | CQ | % | $\delta_{iso}$ | dCSA | CQ | % | $\delta_{iso}$ | dCSA | CQ | % |
|  |  | ppm | ppm | MHz | Int | ppm | ppm | MHz | Int | ppm | ppm | MHz | Int |
| C5232 | MAS | 62.4 | 11.6 | 6.7 | 76.3 | 31 | 10 | 6.5 | 5.9 | -0.5 | 8.6 | 6.3 | 6.8 |
|  |  |  |  |  |  | 24.5 | 4 | 5.3 | 4.7 |  |  |  |  |
|  |  |  |  |  |  | 16 | 3 | 3.2 | 6.3 |  |  |  |  |
|  | MQMAS | 62.8 | 13.1 | 6.8 |  | 31 | 10 | 6.5 |  | -0.5 | 10 | 6.3 |  |
|  |  |  |  |  |  | 24.5 | 5 | 6.1 |  |  |  |  |  |
| C5231 | MAS | 62.8 | 12.2 | 6.5 | 67.8 | 28.5 | 10 | 6.4 | 16.4 | -0.5 | 10.6 | 5.8 | 7.6 |
|  |  |  |  |  |  | 15.6 | 4.7 | 2.6 | 6.4 | 5.9 | 17.8 | 3.6 | 1.8 |
|  | MQMAS | 61.4 | 16.5 | 6.5 |  | 30 | 13.7 | 6.4 |  | -0.5 | 15 | 5.7 |  |
|  |  |  |  |  |  |  |  |  |  | 5.9 | 17.8 | 3.6 |  |
| C5228 | MAS | 62.9 | 13.2 | 6.5 | 63.2 | 32 | 8 | 6.6 | 9.6 | 2 | 6 | 4 | 3.2 |
|  |  |  |  |  |  | 25.6 | 6 | 6.1 | 10 | -5 | 3 | 6.9 | 7.3 |
|  |  |  |  |  |  | 16.8 | 3 | 3.9 | 6.7 |  |  |  |  |
|  | MQMAS | 62.9 | 13.5 | 6.7 |  | 32 | 10 | 6.6 |  | 2 | 6 | 3.9 |  |
|  |  |  |  |  |  | 25 | 6 | 5.7 |  | -5 | 3 | 6.7 |  |
| D2210 | MAS | 62.6 | 12.5 | 6.5 | 83.5 | 31 | 12 | 6.5 | 7.2 | 3.5 | 8 | 5.5 | 3.2 |
|  |  |  |  |  |  | 15.3 | 7 | 2.1 | 6 |  |  |  |  |
|  | MQMAS | 62.8 | 13 | 6.7 |  | 31 | 12 | 6.5 |  | 2 | 6 | 3.4 |  |
| D2212 | MAS | 63 | 13 | 6.3 | 79 | 32 | 3 | 6.5 | 3.3 | -3 | 11.7 | 4.1 | 2.6 |
|  |  |  |  |  |  | 25 | 8 | 5.9 | 8.6 | 7 | 6 | 2 | 1 |
|  |  |  |  |  |  | 15.3 | 5 | 1.9 | 5.1 |  |  |  |  |
|  | MQMAS | 61.1 | 13 | 6.3 |  | 32 | 3 | 6.5 |  | -2.6 | 9.7 | 4.6 |  |
|  |  |  |  |  |  | 25 | 8 | 5.9 |  |  |  |  |  |
| D2209 | MAS | 63.5 | 12.5 | 6.6 | 71 | 34 | 10 | 5 | 4.3 | 0.5 | 6 | 5.3 | 2.2 |
|  |  |  |  |  |  | 28 | 10 | 7.3 | 14.1 | -1.5 | 3 | 6 | 8.5 |
|  | MQMAS | 62.8 | 12.5 | 6.6 |  | 34 | 15 | 5 |  | 1 | 6 | 5.3 |  |
|  |  |  |  |  |  | 28 | 10 | 7.2 |  | -3 | 3 | 6 |  |
| D2213 | MAS | 63.5 | 13 | 6.5 | 48.3 | 32 | 20 | 6.6 | 11.5 | -0.7 | 6 | 5.1 | 11.7 |
|  |  |  |  |  |  | 27 | 6 | 6.3 | 11.6 | -5 | 15 | 6.9 | 9.8 |
|  | MQMAS | 60 | 11 | 6.5 |  | 32 | 6 | 6.6 |  | -0.6 | 6 | 5.5 |  |
|  |  |  |  |  |  | 25 | 8 | 6.5 |  | -0.5 | 15 | 6.9 |  |
| C5199 | MAS | 62.9 | 12.1 | 6.5 | 58.2 | 29 | 5 | 6 | 16.5 | -1 | 3.5 | 6.1 | 18.9 |
|  |  |  |  |  |  | 19 | 5.7 | 6.2 | 6.5 |  |  |  |  |
|  | MQMAS | 62.5 | 16 | 6.5 |  | 30 | 10 | 6 |  | -0.5 | 12 | 5.5 |  |
| D2189 | MAS | 63.5 | 12 | 6.6 | 44.7 | 28 | 12 | 6 | 23.2 | -1 | 11 | 5.9 | 25.5 |
|  |  |  |  |  |  | 15.5 | 6.9 | 2.1 | 6.7 |  |  |  |  |
|  | MQMAS | 62.8 | 13 | 6 |  | 30 | 13 | 7.3 |  | 2.6 | 13.6 | 4.9 |  |
|  |  |  |  |  |  |  |  |  |  | -2.6 | 6.8 | 5.9 |  |
| D2208 | MAS | 62.8 | 11 | 6.7 | 76.3 | 28 | 5.2 | 5.5 | 7.7 | -2 | 6 | 6 | 8.2 |
|  |  |  |  |  |  | 20 | 10 | 6.3 | 7.8 |  |  |  |  |
|  | MQMAS | 62.8 | 12 | 6.2 |  | 34 | 10 | 6 |  | -1.5 | 13 | 2 |  |
|  |  |  |  |  |  | 25 | 10 | 6 |  |  |  |  |  |

| | Exp | AlO$_4$ | | | | AlO$_5$ | | | | AlO$_6$ | | | |
|---|---|---|---|---|---|---|---|---|---|---|---|---|---|
| | | δ$_{iso}$ | dCSA | CQ | % | δ$_{iso}$ | dCSA | CQ | % | δ$_{iso}$ | dCSA | CQ | % |
| | | ppm | ppm | MHz | Int | ppm | ppm | MHz | Int | ppm | ppm | MHz | Int |
| D2207 | MAS | 63.2 | 13.1 | 6.2 | 44 | 29 | 12 | 7.2 | 37.5 | -1.5 | 8 | 5.3 | 18.5 |
| | MQMAS | 62.8 | 13.1 | 6.6 | | 30 | 12 | 7.2 | | -0.7 | 12 | 5.4 | |
| D2125 | MAS | 62.3 | 18 | 4.8 | 49.12 | 30 | 20 | 5.7 | 29.33 | 1.2 | 9.6 | 6 | 21.55 |
| D2173 | MAS | 64.5 | 15 | 6.7 | 52.44 | 31 | 11.1 | 8.7 | 32.69 | 1.0 | 7.4 | 6.4 | 14.88 |
| MA1125 | 9.4T | | | | | | | | | | | | |
| | MAS | 55 | 30.9 | 4.7 | 3.6 | 34.9 | 19.8 | 11.9 | 67.7 | 5 | 10.1 | 5.8 | 28.7 |
| | MAS | 59.5 | 30.9 | 4.7 | 7 | 34.5 | 19.2 | 12.2 | 60.9 | 3.8 | 10.1 | 6.1 | 32.1 |
| | MQMAS | | | | | 30 | 18 | 7.2 | | 2.5 | 10.1 | 5.1 | |
| B3-180615 | MAS | 63.6 | 12.4 | 7.06 | 100 | | | | 0 | | | | 0 |
| | MQMAS | 62.24 | 12.4 | 7.06 | | | | | | | | | |
| C4794 | MAS | 64.3 | 12.8 | 6.9 | 92.8 | 30.4 | 14.8 | 6 | 3.4 | 7.7 | 0.45 | 1.3 | 3.8 |
| | MQMAS | 62.7 | 11 | 6.4 | | | | | | | | | |
| C4900 | MAS | 62.7 | 13.4 | 5.2 | 87.4 | 31.3 | 9 | 5.1 | 5.3 | 0.4 | 9.2 | 3.2 | 4.3 |
| | | | | | | 19.3 | 8.5 | 2.8 | 0.7 | -8.1 | 12.3 | 4.7 | 2.7 |
| | MQMAS | 61.8 | 13.5 | 5.4 | | 31 | 10 | 4.6 | | 1.3 | 7 | 3.1 | |
| | | | | | | 19.2 | 9.7 | 2.9 | | | | | |
| C4896 | MAS | 62.8 | 12.5 | 5.6 | 77.9 | 33 | 10 | 6.9 | 11.6 | 2.2 | 7.5 | 5.2 | 10.4 |
| | MQMAS | 63.6 | 12 | 5.6 | | 33 | 10 | 6.9 | | 1.5 | 7.5 | 5.4 | |
| C4904-C4905 | MAS | 62.7 | 12 | 5.2 | 69.4 | 31.5 | 9.8 | 5.6 | 9.1 | 1.8 | 8.6 | 4.4 | 8.9 |
| | | | | | | 19.3 | 9.9 | 2.2 | 0.7 | 1.6 | 5.8 | 6.8 | 11.9 |
| | MQMAS | 62.5 | 12 | 5.3 | | 30.8 | 10.2 | 5.7 | | 2.2 | 8.9 | 4.4 | |
| | | | | | | | | | | 1.6 | 5.9 | 6.9 | |
| D1840-D1842 | MAS | 63.4 | 14.6 | 4.9 | 62.4 | 31.6 | 9.5 | 6 | 11.9 | 2.6 | 6.7 | 5.6 | 25.7 |
| | MQMAS | 63.7 | 11.2 | 4.9 | | 31.6 | 9.6 | 6 | | 3.4 | 7.7 | 5.5 | |
| C4878-C4879 | MAS | 62.8 | 12.9 | 5.3 | 56.1 | 32.8 | 8.7 | 7.6 | 18.8 | 2.7 | 7 | 5.3 | 25.05 |
| | MQMAS | 62.7 | 12.9 | 5.2 | | 30.8 | 11.3 | 5.7 | | 1.3 | 8.4 | 3.8 | |
| C4892-C4924 | MAS | 63.4 | 13 | 5.4 | 41.8 | 32.7 | 8.3 | 7 | 15 | 2.9 | 10 | 6.1 | 42.9 |
| | | | | | | 19 | 6.05 | 1.9 | 0.3 | | | | |
| | MQMAS | 62.7 | 14.3 | 5.3 | | 29.8 | 12 | 7 | | 2 | 10 | 5.6 | |
| uhppc -269-314 | MAS | 63.5 | 10 | 5.3 | 26.7 | 30.5 | 8 | 5.5 | 15 | 1 | 7 | 5.1 | 57.2 |
| | | | | | | 18 | 9 | 1.5 | 1.2 | | | | |
| | MQMAS | 62.6 | 11 | 5.5 | | 29.9 | 11 | 6.1 | | 1 | 7 | 4.3 | |
| uhppc-333 | MAS | 62.7 | 14.5 | 5.8 | 40.3 | 29.6 | 8.2 | 6.8 | 32.33 | 0.2 | 9.5 | 5.4 | 27.4 |
| | MQMAS | 63.2 | 14.1 | 5.8 | | 29.7 | 10 | 6.6 | | 0 | 10 | 5.4 | |

## 7.6 $^{17}$O fit parameters

Table 7.7. Fit parameters used in fits to $^{17}$O spectra.

| | BO | | | | NBO | | | | 3rd peak | | | |
|---|---|---|---|---|---|---|---|---|---|---|---|---|
| | pos | dCSA | CQ | % | pos | dCSA | CQ | % | pos | dCSA | CQ | % |
| **D1679** | | | | | | | | | | | | |
| MAS | 53 | 28.08 | 3.73 | 79.56 | 105 | 15 | 3.33 | 20.44 | | | | |
| MQMAS | 63.76 | 28.08 | 4.75 | | 102.31 | 40.55 | 0.93 | | | | | |
| **uhppc269** | | | | | | | | | | | | |
| MAS | 64 | 26.51 | 4.52 | 79.72 | 100.31 | 37.41 | 1.01 | 16.77 | 84.76 | 7.43 | 3.1 | 3.51 |
| MQMAS | 62.91 | 18.63 | 4.45 | | 100.86 | 37.48 | 1.1 | | 79.63 | 20.07 | 3.38 | |

## 7.7 Analyses of partitioning experiments

Major and trace element analyses of experimental olivine and melt phases from partitioning experiments described in Chapter 4.

Table 7.8. Major and trace element analyses of experimental olivines.

| | D1515 | sd | C4444 | sd | D2413 | sd | C4396(3) | sd |
|---|---|---|---|---|---|---|---|---|
| Major elements by FE-SEM (wt%) | | | | | | | | |
| *n* | **7** | | 6 | | 9 | | 4 | |
| MgO | 57.3 | 0.4 | 57.2 | 0.4 | 57 | 0.9 | 57 | 0.1 |
| $SiO_2$ | 42.6 | 0.3 | 42.7 | 0.2 | 42.9 | 0.6 | 42.4 | 0.2 |
| Total | 99.8 | 0.7 | 99.9 | 0.5 | 100 | 1 | 99.3 | 0.3 |
| Trace elements by LA-ICPMS (ppm, unless specified) | | | | | | | | |
| *n* | 18 | | 7 | | 10 | | 13 | |
| Na | bdl | | 1.3 | 0.2 | bdl | | 10 | 7 |
| Al | 158 | 9 | 165 | 10 | 214 | 7 | 315 | 220 |
| P | | | 42 | 2 | 53 | 6 | | |
| K | | | bdl | | bdl | | | |
| Ca | 530 | 55 | 441 | 22 | 581 | 115 | 595 | 250 |
| Sc | 29.2 | 0.7 | 26 | 0.5 | 42 | 1 | 24 | 2 |
| Ti | | | 3 | 0.2 | 23 | 2 | | |
| V | | | 4 | 1 | 2.2 | 0.1 | | |
| Cr | | | 2.6 | 0.2 | 1.2 | 0.2 | | |
| Mn | | | 8.9 | 0.4 | 634 | 11 | | |
| Fe | | | 74 | 7 | 49 | 5 | | |
| Co | | | 22.6 | 0.2 | 3.53 | 0.09 | | |
| Ni | | | 359 | 5 | 45 | 3 | | |
| Zn | | | 17 | 1 | 254 | 5 | | |
| Ge | 2077 | 51 | 1759 | 36 | 1275 | 32 | 1795 | 36 |
| Sr | | | 0.02 | 0.03 | 0.3 | 0.3 | | |
| Y | 61 | 2 | 50 | 1 | 17.6 | 0.7 | 79 | 67 |
| Zr | 0.16 | 0.04 | 0.14 | 0.03 | 1.03 | 0.09 | 1 | 2 |
| Ba | | | bdl | | 0.5 | 0.5 | | |
| Hf | | | 0.009 | 0.003 | 2.3 | 0.2 | | |

| | D2374 | sd | D1517 | sd | C5299 | sd | C4396(4) | sd |
|---|---|---|---|---|---|---|---|---|
| Major elements by FE-SEM (wt%) | | | | | | | | |
| *n* | 7 | | 4 | | 10 | | 8 | |
| MgO | 56 | 1 | 57 | 0.3 | 57 | 0.6 | 55.9 | 0.8 |
| $SiO_2$ | 42.2 | 0.9 | 42.5 | 0.3 | 42.5 | 0.5 | 41.7 | 0.5 |
| Total | 98 | 2 | 99.6 | 0.5 | 99 | 1 | 98 | 1 |
| Trace elements by LA-ICPMS (ppm, unless specified) | | | | | | | | |
| *n* | 7 | | 3 | | 11 | | 7 | |
| Na | 3.4 | 0.3 | 4.9 | 0.5 | 8 | 1 | 5 | 1 |
| Al | 269 | 6 | 321 | 20 | 401 | 18 | 364 | 10 |
| P | 41 | 2 | | | 44 | 8 | 43 | 3 |
| K | bdl | | | | bdl | | bdl | |
| Ca | 486 | 128 | 529 | 29 | 508 | 101 | 573 | 177 |
| Sc | 23 | 1 | 20.5 | 0.4 | 21.8 | 0.5 | 21.9 | 0.3 |
| Ti | 2.2 | 0.7 | | | 0.8 | 0.1 | 1.8 | 0.6 |
| V | 4.1 | 0.2 | | | 5.6 | 0.8 | 0.05 | 0.01 |
| Cr | 2.1 | 0.3 | | | 2 | 0.4 | 1.7 | 0.3 |
| Mn | 5.2 | 0.2 | | | 5.1 | 0.3 | 5.4 | 0.2 |
| Fe | 83 | 9 | | | 83 | 10 | 70 | 9 |
| Co | 5 | 0.2 | | | 3.24 | 0.09 | 19.8 | 0.7 |
| Ni | 297 | 38 | | | 15 | 3 | 107 | 12 |
| Zn | 13.3 | 0.6 | | | | | 14.3 | 0.9 |
| Ge | 1661 | 53 | 1622 | 9 | 1651 | 30 | 1685 | 51 |
| Sr | 0.011 | 0.008 | | | | | 0.3 | 0.3 |
| Y | 50 | 3 | 50 | 6 | 43 | 3 | 47 | 10 |
| Zr | 0.17 | 0.03 | 0.22 | 0.05 | | | 0.19 | 0.03 |
| Ba | bdl | | | | | | bdl | |
| Hf | 0.03 | 0.01 | | | | | 0.034 | 0.003 |

Table 7.8. *(Continued).*

| | D2411 | sd | D2427 | sd | C4451 | sd | C4735 | sd |
|---|---|---|---|---|---|---|---|---|
| Major elements by FE-SEM (wt%) | | | | | | | | |
| *n* | 8 | | 6.00 | | 7.00 | | 6 | 8 |
| MgO | 55.4 | 0.3 | 54.7 | 0.2 | 54.4 | 0.4 | 53.6 | 55.4 |
| $SiO_2$ | 42.3 | 0.3 | 42.1 | 0.1 | 41.9 | 0.3 | 41.8 | 42.3 |
| FeO* | 2.04 | 0.08 | 2.5 | 0.1 | 2.06 | 0.06 | 3.41 | 2.04 |
| Total | 99.7 | 0.6 | 99.3 | 0.4 | 98.4 | 0.7 | 98.7 | 99.7 |
| Trace elements by LA-ICPMS (ppm, unless specified) | | | | | | | | |
| *n* | 9 | | 9 | | 8 | | 11 | |
| Na | 150 | 10 | 229 | 28 | 305 | 4 | 398 | 25 |
| Al | 165 | 20 | 248 | 59 | 334 | 11 | 348 | 15 |
| P | 195 | 51 | 293 | 137 | 204 | 21 | 191 | 17 |
| K | bdl | | 56 | 52 | bdl | | bdl | |
| Ca | 2281 | 169 | 2025 | 86 | 1774 | 104 | 1872 | 179 |
| Sc | 24.6 | 0.5 | 25 | 1 | 19.5 | 0.5 | 21.9 | 1 |
| Ti | 165 | 34 | 189 | 86 | 131 | 7 | 115 | 20 |
| V | 0.4 | 0.2 | 0.9 | 0.7 | 0.61 | 0.07 | 0.9 | 0.7 |
| Cr | 64 | 18 | 122 | 79 | 123 | 4 | 135 | 4 |
| Mn | 424 | 10 | 408 | 8 | 307 | 3 | 393 | 10 |
| FeO wt% | 1.4 | 0.08 | 1.63 | 0.09 | 1.67 | 0.02 | 2.7 | 0.1 |
| Co | 1241 | 32 | 1244 | 31 | 1043 | 19 | 1197 | 38 |
| Ni | 2390 | 89 | 2442 | 74 | 2341 | 82 | 2286 | 45 |
| Zn | 37 | 1 | 36 | 2 | | | | |
| Ge | 826 | 31 | 785 | 31 | 961 | 31 | 800 | 31 |
| Sr | 0.012 | 0.002 | 0.05 | 0.04 | | | | |
| Y | 5.8 | 0.4 | 5.9 | 0.9 | 5.2 | 0.2 | 5.2 | 0.5 |
| Zr | 0.1 | 0.06 | 0.3 | 0.4 | | | | |
| Ba | 0.05 | 0.04 | 0.21 | 0.08 | | | | |
| Hf | 0.07 | 0.04 | 0.2 | 0.1 | | | | |

Table 7.8. *(Continued)*

| | D1715 | sd | D1703 | sd | D2472 | sd | C4650 | sd |
|---|---|---|---|---|---|---|---|---|
| Major elements by FE-SEM (wt%) | | | | | | | | |
| *n* | 6 | | 7 | | 4 | | 6 | |
| MgO | 54.1 | 0.4 | 53.6 | 0.4 | 53.2 | 0.4 | 53.9 | 0.4 |
| $SiO_2$ | 42.2 | 0.4 | 41.8 | 0.3 | 41.1 | 0.4 | 41.6 | 0.2 |
| FeO* | 3.3 | 0.1 | 3.08 | 0.07 | 2.61 | 0.05 | 2.71 | 0.08 |
| Total | 99.6 | 0.9 | 98.5 | 0.8 | 96.9 | 0.7 | 98.2 | 0.8 |
| Trace elements by LA-ICPMS (ppm, unless specified) | | | | | | | | |
| *n* | 5 | | 10 | | 8 | | 11 | |
| Na | 489 | 26 | 420 | 7 | 400 | 8 | 230 | 152 |
| Al | 391 | 15 | 337 | 6 | 362 | 12 | 278 | 163 |
| P | 220 | 30 | 184 | 29 | 218 | 7 | 155 | 53 |
| K | 46 | 31 | bdl | | bdl | | 540 | 559 |
| Ca | 2006 | 254 | 1668 | 86 | 1619 | 72 | 1773 | 621 |
| Sc | 29.2 | 0.5 | 20 | 0.3 | 20.9 | 0.4 | 19 | 1 |
| Ti | 149 | 16 | 96 | 4 | 102 | 6 | 211 | 238 |
| V | 1.1 | 0.5 | 0.68 | 0.06 | 0.58 | 0.03 | 2 | 3 |
| Cr | 100 | 3 | 119 | 3 | 114 | 4 | 117 | 9 |
| Mn | 550 | 8 | 371 | 4 | 315 | 4 | 322 | 7 |
| FeO wt% | 2.74 | 0.06 | 2.56 | 0.06 | 1.79 | 0.04 | 2.3 | 0.1 |
| Co | 1628 | 42 | 1192 | 20 | 1137 | 17 | 970 | 17 |
| Ni | 2802 | 61 | 2323 | 67 | 2490 | 51 | 1935 | 50 |
| Zn | 71 | 3 | | | 33.6 | 0.9 | | |
| Ge | 970 | 28 | 794 | 15 | 653 | 9 | 765 | 14 |
| Sr | 0.3 | 0.3 | | | bdl | | | |
| Y | 8 | 2 | 4.2 | 0.1 | 3.9 | 0.1 | 7 | 8 |
| Zr | 0.2 | 0.1 | | | 0.09 | 0.01 | | |
| Ba | 0.4 | 0.2 | | | Bdl | | | |
| Hf | 0.10 | 0.02 | | | 0.045 | 0.008 | | |

Table 7.8. *(Continued)*

| | D1718 | sd | D1758 | sd | C4757 | sd | C4521 | sd |
|---|---|---|---|---|---|---|---|---|
| | | | Major elements by FE-SEM (wt%) | | | | | |
| n | 7 | | 8 | | 7 | | 4 | |
| MgO | 54.4 | 0.7 | 54.4 | 0.4 | 54.4 | 0.4 | 53.5 | 0.7 |
| $SiO_2$ | 41.9 | 0.4 | 41.7 | 0.4 | 41.9 | 0.3 | 41.6 | 0.4 |
| FeO* | 2.6 | 0.2 | 2.26 | 0.06 | 2.06 | 0.06 | 3 | 0.1 |
| Total | 99 | 1 | 98.4 | 0.8 | 98.4 | 0.7 | 98.2 | 1 |
| | | | Trace elements by LA-ICPMS (ppm, unless specified) | | | | | |
| n | 4 | | 8 | | 2 | | 2 | |
| Na | 248 | 12 | 250 | 10 | 269 | 20 | 452 | 13 |
| Al | 306 | 17 | 272 | 14 | 274.9 | 0.3 | 367 | 22 |
| P | 168 | 43 | 138 | 19 | 194 | 28 | 228 | 37 |
| K | 15 | 18 | bdl | | bdl | | bdl | |
| Ca | 1285 | 43 | 1127 | 97 | 1052 | 85 | 1109 | 68 |
| Sc | 17.5 | 0.5 | 13.3 | 0.7 | 14 | 0.05 | 19.8 | 0.8 |
| Ti | 128 | 25 | 170 | 99 | 89 | 3 | 94 | 6 |
| V | 0.9 | 0.3 | 1.6 | 1 | 1 | 0.4 | 1 | 0.2 |
| Cr | 109 | 10 | 114 | 15 | 85 | 6 | 60 | 27 |
| Mn | 265 | 6 | 239 | 3 | 254 | 8 | 330 | 13 |
| FeO wt% | 2 | 0.05 | 1.82 | 0.03 | 2.4 | 0.2 | 2.11 | 0.07 |
| Co | 903 | 22 | 894 | 8 | 953 | 48 | 1111 | 41 |
| Ni | 1999 | 16 | 2128 | 43 | 2299 | 99 | 1978 | 26 |
| Zn | | | | | | | 506 | 23 |
| Ge | 641 | 16 | 630 | 17 | 653 | 7 | 625 | 35 |
| Sr | | | | | | | bdl | |
| Y | 4 | 0.4 | 3.1 | 0.6 | 3.53 | 0.09 | 3.5 | 0.2 |
| Zr | | | | | | | 0.12 | 0.03 |
| Ba | | | | | | | bdl | |
| Hf | | | | | | | bdl | |

Table 7.9. Major and trace element analyses of experimental melt.

| | D1515 | sd | C4444 | sd | D2413 | sd | C4396 (3) | sd |
|---|---|---|---|---|---|---|---|---|
| Major elements by FE-SEM (wt%) | | | | | | | | |
| *n* | 9 | | 8 | | 8 | | 6 | |
| MgO | 30.8 | 0.2 | 36.6 | 0.5 | 30.5 | 0.4 | 34.2 | 0.1 |
| $Al_2O_3$ | 9.9 | 0.1 | 7.4 | 0.3 | 9.9 | 0.3 | 8.9 | 0.2 |
| $SiO_2$ | 50.8 | 0.4 | 47.1 | 0.3 | 48.4 | 0.7 | 49 | 0.1 |
| CaO | 4.79 | 0.09 | 3.37 | 0.08 | 4.4 | 0.1 | 4.07 | 0.08 |
| $Y_2O_5$ | 1.68 | 0.04 | 1.09 | 0.03 | 0.1 | 0.2 | 1.46 | 0.05 |
| BaO | | | | | 1.39 | 0.06 | | |
| Total | 97.9 | 1 | 95.6 | 0.5 | 95 | 1 | 97.5 | 0.5 |
| Cl* | 0.56 | 0.02 | 0.46 | 0.02 | | | 0.39 | 0.02 |
| Trace elements by LA-ICPMS (ppm, unless specified) | | | | | | | | |
| *n* | 11 | | 8 | | 9 | | 6 | |
| Na | 459 | 6 | 359 | 7 | 466 | 15 | 388 | 13 |
| $Al_2O_3$ (wt%) | 2.5 | 0.02 | 1.75 | 0.06 | 2.33 | 0.05 | 2.2 | 0.06 |
| P | | | 64.4 | 0.7 | 181 | 6 | | |
| K | | | 191 | 5 | 320 | 21 | | |
| CaO (wt%) | 3.19 | 0.06 | 2.24 | 0.07 | 2.86 | 0.09 | 2.8 | 0.08 |
| Sc | 233 | 3 | 170 | 2 | 304 | 10 | 209 | 4 |
| Ti | | | 52 | 2 | 3218 | 46 | | |
| V | | | 919 | 22 | 765 | 19 | | |
| Cr | | | 12.2 | 0.3 | 3 | 0.5 | | |
| Mn | | | 25.4 | 0.7 | 1321 | 39 | | |
| Fe | | | 636 | 24 | 383 | 10 | | |
| Co | | | 22.2 | 0.3 | 2.72 | 0.05 | | |
| Ni | | | 175 | 6 | 16 | 3 | | |
| Zn | | | 33.6 | 0.4 | 336 | 17 | | |
| Ge | 3428 | 42 | 3090 | 25 | 2176 | 21 | 3233 | 17 |
| Sr | | | 13 | 0.4 | 1594 | 40 | | |
| Y | 9830 | 192 | 7239 | 181 | 2627 | 91 | 8834 | 290 |
| Zr | 224 | 3 | 159 | 3 | 1336 | 32 | 198 | 5 |
| Ba | | | 12.8 | 0.4 | 7324 | 184 | | |
| Hf | | | 3.7 | 0.1 | 1791 | 35 | | |

Table 7.9 *(Continued).*

| | D2374 | sd | D1517 | sd | C5299 | sd | C4396 (4) | sd |
|---|---|---|---|---|---|---|---|---|
| | | | | Major elements by FE-SEM (wt%) | | | | |
| *n* | 8 | | 10 | | 6 | | 8 | |
| MgO | 35.1 | 0.9 | 36 | 0.6 | 32.6 | 0.3 | 34.4 | 0.8 |
| $Al_2O_3$ | 8.7 | 0.3 | 8.3 | 0.2 | 9.2 | 0.2 | 8.6 | 0.2 |
| $SiO_2$ | 48.4 | 0.6 | 48.4 | 0.5 | 49.7 | 0.6 | 48.8 | 0.3 |
| CaO | 3.68 | 0.07 | 3.69 | 0.08 | 4.3 | 0.2 | 3.78 | 0.09 |
| $Y_2O_5$ | 1.29 | 0.04 | 1.2 | 0.1 | 1.4 | 0.1 | 1.39 | 0.07 |
| Total | 97 | 1 | 97.6 | 0.9 | 97.3 | 0.9 | 96.9 | 0.8 |
| Cl* | | | 0.4 | 0.03 | | | 0.11 | 0.06 |
| | | | | Trace elements by LA-ICPMS (ppm, unless specified) | | | | |
| *n* | 7 | | 15 | | 6 | | 6 | |
| Na | 396 | 51 | 325 | 106 | 432 | 87 | 275 | 93 |
| $Al_2O_3$ (wt%) | 1.9 | 0.3 | 2.02 | 0.1 | 2.5 | 0.2 | 2.1 | 0.04 |
| P | 74 | 2 | | | 78 | 1 | 73 | 5 |
| K | 34 | 2 | | | 52 | 18 | 128 | 57 |
| CaO (wt%) | 2.4 | 0.4 | 2.5 | 0.2 | 3 | 0.3 | 2.4 | 0.2 |
| Sc | 179 | 17 | 197 | 6 | 230 | 18 | 195 | 11 |
| Ti | 53 | 6 | | | 64 | 5 | 28 | 3 |
| V | 937 | 123 | | | 1123 | 132 | 3.3 | 0.3 |
| Cr | 8.3 | 0.5 | | | 6.1 | 0.3 | 5.5 | 0.4 |
| Mn | 13.5 | 0.6 | | | 12.3 | 0.4 | 13.2 | 0.6 |
| Fe | 539 | 77 | | | 327 | 21 | 308 | 12 |
| Co | 5.1 | 0.4 | | | 2.5 | 0.2 | 17.7 | 0.6 |
| Ni | 160 | 35 | | | 7 | 2 | 49 | 3 |
| Zn | 20 | 1 | | | | | 17 | 0.9 |
| Ge | 3114 | 113 | 3190 | 45 | 3430 | 112 | 3456 | 44 |
| Sr | 14 | 2 | | | | | 10 | 3 |
| Y | 7619 | 1272 | 7772 | 471 | 9648 | 890 | 8342 | 487 |
| Zr | 172 | 22 | 176 | 11 | | | 179 | 9 |
| Ba | 15 | 2 | | | | | 7 | 4 |
| Hf | 4.3 | 0.5 | | | | | 4.5 | 0.2 |

Table 7.9. *(Continued)*

| | D2411 | sd | D2427 | sd | C4451 | sd | C4735 | sd |
|---|---|---|---|---|---|---|---|---|
| Major elements by FE-SEM (wt%) | | | | | | | | |
| n | 8 | | 7 | | 9 | | 6 | |
| MgO | 13.4 | 0.2 | 13.5 | 0.2 | 17.4 | 0.3 | 14.44 | 0.03 |
| $Al_2O_3$ | 7.21 | 0.07 | 7.12 | 0.06 | 6.44 | 0.07 | 7.1 | 0.2 |
| $SiO_2$ | 40.3 | 0.3 | 39.7 | 0.4 | 39.3 | 0.5 | 39.6 | 0.4 |
| CaO | 9.35 | 0.1 | 9.19 | 0.08 | 8.3 | 0.1 | 8.83 | 0.09 |
| FeO | 11.6 | 0.1 | 11.7 | 0.2 | 11.7 | 0.2 | 11.8 | 0.2 |
| $TiO_2$ | 4.9 | 0.1 | 4.9 | 0.1 | 4.6 | 0.1 | 4.86 | 0.05 |
| $Na_2O$ | 4.33 | 0.08 | 4.28 | 0.05 | 3.77 | 0.07 | 4.27 | 0.04 |
| $P_2O_5$ | 1.08 | 0.05 | 1.08 | 0.09 | 1.01 | 0.06 | 1.1 | 0.1 |
| $K_2O$ | 4.11 | 0.07 | 4.05 | 0.08 | 3.66 | 0.04 | 4.17 | 0.04 |
| Total | 96.2 | 0.5 | 95.5 | 0.9 | 96 | 1 | 96.2 | 0.8 |
| Cl* | n.d. | | n.d. | | 0.33 | 0.02 | n.d | |
| Trace elements by LA-ICPMS (ppm, unless specified) | | | | | | | | |
| n | 7 | | 11 | | 7 | | 6 | |
| $Na_2O$ (wt%) | 4.46 | 0.01 | 4.4 | 0.03 | 3.77 | 0.01 | 4.199 | 0.007 |
| $Al_2O_3$ (wt%) | 6.87 | 0.03 | 6.88 | 0.03 | 6.56 | 0.02 | 7.38 | 0.02 |
| P | 4478 | 49 | 4477 | 77 | 3957 | 10 | 4482 | 12 |
| $K_2O$ (wt%) | 9.6 | 0.1 | 9.08 | 0.1 | 7.47 | 0.04 | 8.49 | 0.02 |
| CaO (wt%) | 8.6 | 0.1 | 8.7 | 0.2 | 8.07 | 0.01 | 8.58 | 0.06 |
| Sc | 150.5 | 0.9 | 155 | 2 | 147.2 | 0.5 | 155.1 | 0.5 |
| $TiO_2$ (wt%) | 4.228 | 0.01 | 4.26 | 0.09 | 4.237 | 0.009 | 4.55 | 0.01 |
| V | 264.4 | 0.9 | 262 | 4 | 249.8 | 0.7 | 272.2 | 0.5 |
| Cr | 157 | 8 | 204 | 4 | 464 | 3 | 402 | 2 |
| Mn | 505 | 5 | 511 | 5 | 532 | 1 | 548 | 1 |
| Fe | 7.77 | 0.06 | 7.4 | 0.2 | 9.15 | 0.02 | 9.33 | 0.02 |
| Co | 550 | 4 | 559 | 2 | 680 | 2 | 613 | 1 |
| Ni | 353 | 8 | 372 | 7 | 643 | 9 | 460 | 10 |
| Zn | 43.7 | 0.8 | 41 | 1 | | | | |
| Ge | 1127 | 4 | 1130 | 6 | 1424 | 3 | 1211 | 4 |
| Sr | 31.5 | 0.4 | 31.3 | 0.7 | | | | |
| Y | 920 | 4 | 931 | 14 | 864 | 4 | 965 | 5 |
| Zr | 202 | 1 | 203 | 3 | | | | |
| Ba | 60.8 | 0.9 | 61 | 1 | | | | |
| Hf | 66.2 | 0.8 | 67.6 | 0.8 | | | | |

Table 7.9. *(Continued)*

| | D1715 | sd | D1703 | sd | D2472 | sd | C4650 | sd |
|---|---|---|---|---|---|---|---|---|
| | | | | Major elements by FE-SEM (wt%) | | | | |
| n | 7 | | 8 | | 4 | | 6 | |
| MgO | 12.9 | 0.1 | 14.9 | 0.2 | 16.4 | 0.2 | 16.61 | 0.05 |
| $Al_2O_3$ | 7.71 | 0.06 | 6.99 | 0.06 | 6.4 | 0.1 | 6.44 | 0.07 |
| $SiO_2$ | 38.9 | 0.4 | 39.4 | 0.4 | 38.5 | 0.3 | 38.8 | 0.1 |
| CaO | 7.89 | 0.07 | 8.8 | 0.1 | 8.2 | 0.06 | 8.23 | 0.07 |
| FeO | 11.3 | 0.2 | 11.8 | 0.2 | 11.48 | 0.02 | 11.7 | 0.1 |
| $TiO_2$ | 5.48 | 0.05 | 4.9 | 0.1 | 4.4 | 0.2 | 4.53 | 0.08 |
| $Na_2O$ | 4.92 | 0.06 | 3.9 | 0.3 | 3.74 | 0.09 | 3.69 | 0.04 |
| $P_2O_5$ | 1.39 | 0.06 | 1.13 | 0.02 | 0.97 | 0.03 | 1.01 | 0.03 |
| $K_2O$ | 5.36 | 0.08 | 4.11 | 0.07 | 3.7 | 0.1 | 3.53 | 0.07 |
| Total | 95.9 | 0.7 | 95.9 | 0.9 | 94 | 1 | 94.6 | 0.4 |
| Cl* | n.d | | n.d | | n.d | | n.d | |
| | | | | Trace elements by LA-ICPMS (ppm, unless specified) | | | | |
| n | 7 | | 6 | | 8 | | 6 | |
| $Na_2O$ (wt%) | 6.31 | 0.05 | 3.99 | 0.02 | 3.86 | 0.02 | 3.74 | 0.01 |
| $Al_2O_3$ (wt%) | 9.38 | 0.03 | 7.11 | 0.03 | 6.16 | 0.04 | 6.35 | 0.02 |
| P | 7031 | 35 | 4307 | 26 | 3974 | 23 | 3931 | 25 |
| $K_2O$ (wt%) | 15.6 | 0.1 | 8.11 | 0.06 | 8.09 | 0.1 | 7.52 | 0.03 |
| CaO (wt%) | 9.25 | 0.03 | 8.53 | 0.03 | 7.71 | 0.05 | 7.97 | 0.06 |
| Sc | 179 | 0.9 | 157.6 | 0.9 | 139.1 | 0.9 | 142 | 1 |
| $TiO_2$ (wt%) | 5.93 | 0.04 | 4.56 | 0.02 | 3.87 | 0.05 | 4.11 | 0.03 |
| V | 411 | 2 | 269 | 1 | 228 | 1 | 268 | 1 |
| Cr | 277 | 4 | 385 | 3 | 413 | 4 | 381 | 4 |
| Mn | 712 | 8 | 544 | 2 | 502 | 2 | 498 | 5 |
| Fe | 9.51 | 0.07 | 9.12 | 0.06 | 7.39 | 0.05 | 8.73 | 0.06 |
| Co | 743 | 5 | 629 | 2 | 642 | 2 | 566 | 4 |
| Ni | 471 | 5 | 491 | 5 | 582 | 4 | 413 | 8 |
| Zn | 79 | 2 | | | 41.3 | 0.6 | | |
| Ge | 1575 | 11 | 1225 | 6 | 1074 | 4 | 1110 | 4 |
| Sr | 45.2 | 0.8 | | | 27.5 | 0.4 | | |
| Y | 1323 | 13 | 944 | 5 | 824 | 5 | 864 | 8 |
| Zr | 276 | 2 | | | 178 | 1 | | |
| Ba | 104 | 2 | | | 53 | 1 | | |
| Hf | 98 | 1 | | | 59.5 | 0.8 | | |

Table 7.9. *(Continued).*

| | D1718 | sd | D1758 | sd | C4757 | sd | C4521 | sd |
|---|---|---|---|---|---|---|---|---|
| Major elements by FE-SEM (wt%) | | | | | | | | |
| n | 6 | | 6 | | 9 | | 9 | |
| MgO | 17.5 | 0.2 | 20.6 | 0.3 | 17.4 | 0.3 | 14.8 | 0.3 |
| $Al_2O_3$ | 6.07 | 0.02 | 5.52 | 0.06 | 6.44 | 0.07 | 6.2 | 0.1 |
| $SiO_2$ | 38.1 | 0.5 | 38.4 | 0.3 | 39.3 | 0.5 | 36.3 | 0.6 |
| CaO | 7.63 | 0.1 | 6.78 | 0.08 | 8.3 | 0.1 | 7.5 | 0.1 |
| FeO | 11.4 | 0.2 | 10.4 | 0.2 | 11.7 | 0.2 | 11.3 | 0.3 |
| $TiO_2$ | 4.16 | 0.08 | 3.77 | 0.09 | 4.6 | 0.1 | 4.5 | 0.2 |
| $Na_2O$ | 3.13 | 0.09 | 2.68 | 0.03 | 3.77 | 0.07 | 3.4 | 0.1 |
| $P_2O_5$ | 0.92 | 0.09 | 0.74 | 0.02 | 1.01 | 0.06 | 1 | 0.1 |
| $K_2O$ | 3.38 | 0.07 | 3.05 | 0.06 | 3.66 | 0.04 | 5.7 | 0.4 |
| Total | 92.3 | 1 | 92 | 1 | 96 | 1 | 91 | 1 |
| Cl* | n.d | | n.d | | 0.01 | 0.02 | n.d. | |
| Trace elements by LA-ICPMS (ppm, unless specified) | | | | | | | | |
| n | 11 | | 11 | | 5 | | 5 | |
| $Na_2O$ (wt%) | 3.3 | 0.2 | 2.5 | 0.3 | 2.9 | 0.2 | 3.4 | 0.4 |
| $Al_2O_3$ (wt%) | 5.95 | 0.07 | 5.62 | 0.07 | 5.62 | 0.07 | 5.88 | 0.07 |
| P | 3339 | 371 | 2100 | 438 | 3588 | 52 | 4666 | 609 |
| $K_2O$ (wt%) | 6.9 | 0.1 | 6.37 | 0.07 | 6.42 | 0.04 | 8.8 | 0.7 |
| CaO (wt%) | 7.2 | 0.3 | 6.3 | 0.1 | 6.9 | 0.2 | 6.7 | 0.2 |
| Sc | 134 | 1 | 125.2 | 0.8 | 130 | 0.5 | 128 | 3 |
| $TiO_2$ (wt%) | 3.76 | 0.04 | 3.58 | 0.03 | 3.5 | 0.06 | 3.8 | 0.2 |
| V | 216 | 15 | 193 | 44 | 171 | 25 | 158 | 28 |
| Cr | 394 | 5 | 432 | 4 | 344 | 3 | 297 | 10 |
| Mn | 469 | 14 | 433 | 8 | 471 | 6 | 491 | 21 |
| Fe | 8.25 | 0.09 | 8.32 | 0.05 | 9.41 | 0.09 | 7.5 | 0.1 |
| Co | 581 | 3 | 619 | 3 | 626 | 5 | 532 | 3 |
| Ni | 476 | 13 | 645 | 11 | 646.2 | 0.5 | 391 | 7 |
| Zn | | | | | | | 535 | 26 |
| Ge | 1104 | 7 | 1060 | 6 | 1082 | 9 | 968 | 9 |
| Sr | | | | | | | 37 | 3 |
| Y | 780 | 27 | 645 | 37 | 761 | 18 | 827 | 31 |
| Zr | | | | | | | 187 | 7 |
| Ba | | | | | | | 62 | 5 |
| Hf | | | | | | | 61 | 2 |